DETERMINATION DE LA COMPOSITION DES SURFACES PLANETAIRES PAR SPECTROSCOPIE GAMMA ET NEUTRON

Benedicte Diez

▶ **To cite this version:**

THÈSE

En vue de l'obtention du

DOCTORAT DE L'UNIVERSITÉ DE TOULOUSE

Délivré par l'Université Toulouse III - Paul Sabatier
Discipline ou spécialité : Planétologie

Présentée et soutenue par **Bénédicte Diez**
Le 25/06/2009

DETERMINATION DE LA COMPOSITION DES SURFACES PLANETAIRES

PAR SPECTROSCOPIE GAMMA ET NEUTRON

DETERMINATION OF PLANETARY SURFACES ELEMENTAL COMPOSITION BY

GAMMA AND NEUTRON SPECTROSCOPY

JURY

Pr. Henri Reme	professeur à l'université Toulouse III	Président
Dr. Johannes Brückner	senior scientist au Max Planck Institut, Mainz	Rapporteur
Dr. Eric Chassefière	directeur de recherche à l'université Paris 6	Rapporteur
Pr. Philippe Paillou	professeur à l'université Bordeaux I	Examinateur
Dr. David J. Lawrence	research scientist à l'APL, Laurel, USA	Examinateur
Dr. Francis Rocard	ingénieur CNES	Examinateur
Dr. Mike Toplis	directeur de recherche à l'université Toulouse III	Examinateur
Dr. Sylvestre Maurice	astronome à l'université Toulouse III	Directeur

Ecole doctorale : Sciences de l'Univers, de l'Environnement et de l'Espace
Unité de recherche : Centre d'Etude Spatiale des Rayonnements
Directeur de Thèse : Dr. Sylvestre Maurice
Rapporteurs : Dr. Johannes Brückner et Dr. Eric Chassefière

Avant propos

Les premiers mots de cette thèse, qui sont chronologiquement les derniers, ne seront pas scientifiques. Je m'autorise une parenthèse de français, que de toute façon la plupart de mes amis anglophones comprennent mieux que je n'écris l'anglais. Le présent manuscrit constitue un résumé des travaux que j'ai effectué au cours de ces trois années de thèse. Que ce soit d'un point de vue professionnel ou personnel, il n'est le récit que de la partie émergée de ce qu'a été pour moi l'iceberg de ces trois ans.

La description de la démarche scientifique ne reflète rien de ce qu'on pu être les collaborations avec nombre de chercheurs, que je peux maintenant non sans fierté nommer collègues. Je pense en premier lieu à mes amis de Los Alamos : Rick, Tom, David et surtout Bill, dont la patience, la disponibilité et l'infatigable ténacité au travail ont fait un mentor exemplaire. Si je peux, au fil des ans qui me restent pour rejoindre son âge respectable, acquérir un tant soit peu de sa vivacité intellectuelle et de ses qualités humaines, alors je m'estimerai la plus récompensée des créatures. Je pense également à mes amis d'Orsay : François, Véronique, Nicolas, Ana, Damien, Sandrine et Sylvain qui m'ont épaulé pendant mon passage à Paris. Contrairement à ce que laissaient présager les premiers mois de pataugeage complet, mon séjour chez les géologues s'est avéré très riche d'enseignements et a donné l'un des chapitres les plus aboutis de ma thèse. Je pense aussi à mes amis japonais, et il sera difficile de les nommer tous ici… La communication n'a pas été facile entre notre équipe et la leur, mais les liens se sont progressivement affirmés, et l'arrivée prochaine de Yuki est pleine de promesses pour l'avenir.

Je pense enfin et surtout à l'équipe surfaces planétaires de Toulouse, dont je me sens membre à part entière aujourd'hui et qu'il va être difficile de devoir quitter. Claude, Olivier F., Agnès, Nath (et puis Benoit et Erwan qui ont déjà pris leur envol) il fait bon travailler à vos côtés ! J'ai mis de côté Olivier G. et Sylvestre pour des raisons qui dépassent le simple fait qu'on partage un même bureau… Olivier merci pour la constance de ta disponibilité et l'abondance de bons conseils que tu m'as divulgués. Sylvestre merci de m'avoir donné la latitude dont j'ai besoin, d'avoir su trouver les mots pour chacune des crises que j'ai traversée, bref d'avoir été là quand il fallait ! Même s'il y a eu des hauts et des bas au cours des trois ans et qu'il m'est arrivé de rechigner sur certains aspects de la recherche (tels que les corrections d'article que j'affectionne particulièrement…), je trouve le bilan plutôt très positif et j'ai le sentiment qu'on forme une bonne équipe !

D'un point de vue plus personnel, la thèse a aussi été l'occasion de nombreux voyages: Los Alamos, Berlin, Hawaï, Tucson, Noordwijk, Vienne, Tokyo, Münster… et de toutes les rencontres qui vont avec. Certaines très ponctuelles, et d'autres qui ont été amenées à durer quand j'ai réussi à faire taire les fourmis dans les pieds. Je pense aux doctorants

d'Orsay et de Toulouse qui sont trop nombreux pour être tous nommés. Mention spéciale pour quelques vieux de la veille avec qui j'ai plus particulièrement eu l'occasion de prendre des verres, manger des glaces ou fêter des anniversaires : Mathieu et Pat, Martatin, Pierrick, Céline et Nadège… Partout où j'ai été je me suis sentie bien entourée.

Hors du cadre des laboratoires, j'ai aussi connu au cours de ces trois ans plusieurs tournants significatifs. Certains me laissent encore un peu nostalgique, ils m'ont amené à faire cavalier solitaire une grande partie de la thèse (une pensée particulièrement affectueuse pour Nico). Mais il en est d'autres plus réjouissants, tels que la découverte du swing qui a été un puissant moteur d'épanouissement ces deux dernières années, ainsi que l'occasion de rencontrer des personnes à qui je tiens beaucoup. Je repenserai par ailleurs aux années de thèse comme étant celles de la colocation avec Steph et Mathieu. Mathieu t'es un autiste du pc un brin ronchon à tes heures, mais on t'aime bien quand même. Steph, Julien a beau essayer de te voler mesquinement à nous, on ne te laissera pas partir comme ça, faudra me passer sur le corps auparavant. Merci à tous les deux, je pourrais citer douze mille anecdotes, mais je crois qu'il suffit de dire qu'on est bien ensemble. J'espère qu'il nous reste de nombreuses réunions à venir avec toute la bande ! Et puis j'ai gardé ma famille pour la fin, en dépit du fait qu'elle soit plutôt à l'origine de l'aventure. Durant ces années des évènements majeurs ont eu lieu : le mariage de Laurent avec Hélène, celui d'Alice avec Austin, et puis l'annonce d'autres encore plus importants à venir… Espérons que de nombreuses occasions de célébration nous attendent. Merci à mes proches et surtout à papa, maman et frangin qui me supportent et me soutiennent depuis encore plus longtemps que tous les autres !

Table of contents

Introduction

Neutron and gamma ray spectrometers have been used for more than ten years in planetology to constrain the chemical composition of the surficial material of planets and smaller bodies deprived of (or with only tenuous) atmosphere. Neutrons and gamma rays are mostly produced by the interaction of galactic cosmic rays with planetary material.

Gamma ray spectroscopy consists in measuring energy spectra of the light in the gamma ray domain of the electromagnetic spectrum. The analysis of the spectra thus obtained is used to identify and quantify the gamma emitting nuclides contained in the material. The fluxes of gamma rays emitted by a planetary surface allow mapping many elements of interest for deriving the geological history of a body: radioactive incompatible elements (potassium, thorium and uranium), major elements (iron, calcium, silicium, titanium, oxygen, aluminium) and volatile elements (hydrogen, chlorine, sulfur).

Neutron spectroscopy consists in collecting neutrons and evaluating their flux in large energy bands. The analysis of the spectra of neutrons leaking outward a planetary surface allows detecting, quantifying and locating important volatiles such as hydrogen and carbon dioxide. Neutron spectroscopy also provides significant information on other major elements abundances. The elements that have high affinities of reaction with neutrons can thus be constrained.

The present work is in the framework of two experiments, the Mars Odyssey Neutron Spectrometer and the Selene Gamma Ray Spectrometer. The US mission Mars Odyssey carried in orbit a Neutron Spectrometer whose primary goals were to detect the presence of hydrogen, measure its abundance and constrain its location both geographically and in depth. The Japanese mission Selene possesses a Gamma Ray Spectrometer designed to collect the abundances of many elements fundamental to constrain the geological history of the Moon: radioactive elements, major elements and most importantly hydrogen.

Gamma ray and neutron spectroscopy are complex sciences that necessitate many steps before compositional information can be extracted from the data. From raw data to interpretation in terms of geological context, three important phases have to be undergone:

- Data reduction and processing, which consists in all corrections and manipulations that are applied to the datasets to extract the geochemical useful information from the other contributions (variations of external sources, instrumental contributions, spacecraft motion…)
- Data modeling, which consists in simulating the production of neutrons and gamma rays by a planetary surface bombarded with galactic cosmic rays, their transport in the planetary material and in the atmosphere and space environment up to the spacecraft altitude and finally the response of the instrument to these gamma ray and neutron fluxes in terms of counting rates

- Interpretation, which consists in confronting the measured data to the modeled data in order to convert the counting rates of the instrument in term of maps of the chemical abundances and finally to confront these maps to the contextual geological knowledge so as to improve the understanding the causes for the presence and proportion of these different elements

Because of the agenda of the missions (Mars Odyssey was launched in 2001 and Selene in September 2007), all these phases could not be studied in detail for each mission. Most of the neutron data had already been processed when the present work started. However, an in-depth understanding of the data was compulsory before any interpretation of its content could be drawn. This work therefore begun with reviewing all processing steps that had been applied to the neutron dataset.

After that could start an interpretation phase which focused on the following problematic: determining the depth of the hydrogen deposits below the Martian surface and confronting it to the models of ice stability; constraining the composition in major elements in water depleted regions. The methods acquired while studying the Martian neutron dataset reduction scheme have been used to process the lunar gamma ray dataset from Selene. Because of the paucity of data (nominal mission did not start before end of December 2007), innovative methods have also been explored. Thanks to these different tools, the raw data from the Selene GRS can be processed to maps of elemental abundances on the Moon.

The first chapter presents how gamma and neutron spectroscopy work, how these techniques can and have already been used for constraining the geochemistry of planetary surfaces. Specific knowledge needed for interpreting the Martian neutron dataset and the lunar gamma ray dataset are provided, which includes notions about Mars and the Moon.

The second chapter explains how information about the chemical composition of the planetary surface can be inferred from the Mars Odyssey Neutron Spectrometer data. After a proper data reduction, neutron spectra are interpreted in terms of water abundance, water depth and chemical abundances. The knowledge so far acquired on the red planet (thermal models of ice stability, geological context, elemental composition from the Mars Odyssey Gamma Ray Spectrometer data…) is used to assess the quality of the results, and thus determine the limitations of our dataset.

The third chapter explains how the raw spectra collected by the Selene Gamma Ray Spectrometer can be analyzed and processed into counting rates proportional to the abundances of the elements of interest. Several aspects of the processing are tackled: the mapping techniques, the tools developed to analyze the spectra and the analysis of the global lunar spectrum made of the accumulation of a major part of the dataset.

The manuscript ends with a conclusion that sum ups the results and derives the perspective and possible follow-up of this work.

Introduction (en français)

Les spectroscopies neutron et gamma sont utilisées en planétologie depuis plus d'une dizaine d'années pour contraindre la composition chimique des surfaces des planètes et petits corps dépourvus (ou presque) d'atmosphère. Les neutrons et les rayons gamma sont produits en grande partie par les interactions du rayonnement galactique cosmique avec les atomes du sol planétaire.

La spectroscopie gamma consiste à acquérir des spectres d'énergie dans le domaine gamma du spectre électromagnétique de la lumière. L'analyse de ces spectres permet d'identifier et de quantifier les nucléides à l'origine de ces émissions contenus dans les matériaux superficiels. Le flux de rayonnement gamma émis par une surface planétaire sert donc à cartographier de nombreux éléments fondamentaux pour reconstituer l'histoire géologique d'un corps : des éléments radioactifs (potassium, thorium et uranium), des éléments majeurs (fer, calcium, silicium, titane, oxygène, aluminium) et des éléments volatils (hydrogène, chlore, souffre).

La spectroscopie neutron consiste d'une part à détecter les neutrons et mesurer leur flux dans de larges bandes d'énergie. L'analyse des spectres de neutrons émis par une surface planétaire permet de détecter, de quantifier et de localiser d'importants éléments volatils tels que l'hydrogène ou le dioxyde de carbone. La spectroscopie neutron fournit aussi quantité d'informations sur d'autres éléments majeurs. L'abondance des éléments dotés d'une grande affinité de réaction avec les neutrons peut ainsi être déterminée.

Ces travaux de thèse s'inscrivent dans le cadre de deux expériences : le spectromètre neutron de Mars Odyssey et le spectromètre gamma de Selene. La mission américaine Mars Odyssey a transporté en orbite un spectromètre neutron dont les objectifs comprenaient : la détection de la présence d'hydrogène, la mesure de son abondance et la détermination de son emplacement (à la fois géographiquement et en profil vertical). La mission japonaise Selene comporte un spectromètre gamma conçu pour déterminer les abondances de nombreux éléments fondamentaux pour l'histoire de la Lune : des éléments radioactifs, des éléments majeurs et surtout l'hydrogène.

Les spectroscopies gamma et neutron sont des sciences complexes dont les données nécessitent de nombreuses étapes de traitement avant qu'une information géochimiques en soit extraite. Depuis les données brutes jusqu'à l'interprétation en terme de contexte géologique, trois grandes phases sont mises en jeu :

- La réduction et le traitement des données, qui sont constituées de toutes les corrections et manipulations appliquées aux jeux de données pour en extraire l'information géochimique utile des autres contributions (variations de sources externes, contributions des instruments, mouvement du satellite…)
- La modélisation des données, qui consiste à simuler la production de neutrons et rayons gamma par une surface planétaire soumise au bombardement du rayonnement galactique cosmique, leur transport au sein du sol planétaire dans un premier temps, puis leur transport dans l'atmosphère et l'environnement

spatial jusqu'à l'orbite du satellite et enfin la réponse de l'instrument aux flux de rayons gamma et courants de neutrons résultants

- L'interprétation, qui consiste à confronter les données mesurées aux données simulées afin de convertir le signal instrumental en cartes d'abondances géochimiques, puis à confronter ces cartes au contexte géologique pour affiner notre compréhension de ce dernier

En raison de l'agenda de ces deux missions (Mars Odyssey a été lancée en 2001 et Selene en septembre 2007), toutes ces phases n'ont pu être étudiées en détail pour chacune des missions. La majeure partie des données neutron avait déjà été traitée quand ces travaux de thèse ont commencé. Cependant une compréhension détaillée des données est impérative avant de pouvoir interpréter leur contenu. Cette étude a donc commencé par une revue détaillée de toutes les corrections appliquées au jeu de données neutron.

La phase d'interprétation a pu ensuite démarrer en se focalisant sur les problématiques suivantes : déterminer la profondeur des dépôts d'hydrogène sous la surface martienne et confronter les résultats aux modèles de stabilité thermique de la glace sur Mars ; contraindre la composition en éléments majeurs dans les régions dépourvues d'eau. Les méthodes utilisées pour la réduction des données neutron de Mars Odyssey ont été ensuite appliquées au jeu de données gamma de Selene. Cependant en raison du manque de données (la mission nominale a commencé seulement fin décembre 2007), des méthodes de traitement innovatrices ont aussi été examinées.

Le premier chapitre expose comment les spectroscopies neutron et gamma fonctionnent, comment ces techniques peuvent, et ont déjà contribué à contraindre la géochimie des surfaces planétaires. Les connaissances spécifiques à l'interprétation du jeu de données neutron martien et du jeu de données gamma lunaire sont ensuite abordées, sous forme de notions de géochimie de la Mars et de la Lune.

Le deuxième chapitre démontre comment l'information géochimique sur les surfaces planétaires peut être extraite des données du spectromètre neutron de Mars Odyssey. Après une analyse détaillée de la réduction des données, les spectres de neutrons sont interprétés en termes d'abondance d'eau, de profondeur des réservoirs et d'abondances d'autres éléments chimiques. Les connaissances préalablement acquises sur la planète rouge (modèles thermiques de stabilité de la glace, contexte géologique, composition élémentaire issue des données gamma de Mars Odyssey…) sont utilisées afin d'évaluer la qualité des résultats et de déterminer les limites de l'utilisation du jeu de données.

Le troisième chapitre explique comment les données brutes collectées par le spectromètre gamma de Selene sont analysées et traitées en signaux proportionnels aux abondances des éléments chimiques cibles. Différents aspects sont abordés : les techniques de cartographie, les outils d'analyse des spectres et enfin l'analyse du spectre global issu de l'accumulation d'une grande partie des données.

Le manuscrit finit par une conclusion qui rassemble les résultats et dérive les perspectives de ces travaux.

Chapter 1   Gamma ray and neutron spectroscopy in a planetary context

This first chapter presents how gamma and neutron spectroscopy work, how these techniques can and have already been used for constraining the geochemistry of planetary surfaces. The present work will focus on two experiments, the Mars Odyssey Neutron Spectrometer and the Selene GRS. Therefore, specific knowledge needed for interpreting these datasets will be provided here, which includes notions about Mars and the Moon.

A first section presents theoretic notions necessary to understand how planetary materials emit neutron and gamma rays. After a short definition of gamma rays and neutrons, the production of neutrons and gamma rays by planetary material are exposed. A brief history of planetary missions carrying neutron and gamma spectrometers concludes this part.

The second section presents the principles of the instrumentation dedicated to gamma ray and neutron spectroscopy. Gamma ray spectroscopy is presented first, followed by neutron spectroscopy. This section ends with an overview of the instruments based on one of the two techniques that have been so far flown for planetary sciences applications.

The third section focuses on the planets currently surveyed with gamma and neutron spectroscopy. These techniques, particularly appropriate for terrestrial planets deprived of atmosphere, or with a very tenuous one, are used in the context of the Mars Odyssey and Selene missions. Mars, observed by the Mars Odyssey Neutron Spectrometer, is presented first, followed by the Moon, which is subjected to the survey of the Selene GRS. After a short presentation of their exploration and general features, surface composition will be is particularly emphasized for both planets and a brief presentation of the atmosphere in the case of Mars will complement the outline.

1.1   Gamma ray and neutron spectroscopy principles

1.1.1 Gamma rays and neutrons

Gamma rays were discovered by Paul Villard, a French chemist and physicist, in 1900. Gamma rays are the electromagnetic radiations having the highest energy (above 100 keV) in the electromagnetic spectrum. X-rays overlap the energy range of gamma rays. The distinction between the two terms depends on the source of the radiation, not its wavelength. X-ray photons are generated by excitation and ejection of atomic electrons, gamma rays by excitation of atomic nuclei, including dissociation, or matter-antimatter annihilation.

Neutrons are subatomic particles with no electric charge and a slightly larger mass than that of a proton. Neutrons are usually found in atomic nuclei, where they can

be stable. When unbound to nuclei, neutrons are unstable. A neutron decays by β radioactivity into a proton, an electron and an electron antineutrino. The neutron lifetime is about 15 minutes (885.7 ± 0.8 s). Because free neutrons are unstable, they can only be obtained from nuclear reactions (spontaneous disintegration or caused by bombardment with high energy particles).

1.1.2 Neutron sources in planetary materials

In a planetary context, the main source of neutrons is the interaction between galactic cosmic rays (GCR) and the nuclear constituents of the surface material. GCR are high energy (typically ranging between 0.1 and 10 GeV) ions that penetrate the solar system. They mainly consist of protons (about 87%), but also of about 12% alpha particles, and about 1% heavier nuclei.

When they encounter a solid body, GCR particles begin to lose their energy through initiation of intra-nuclear cascades [Bertini, 1969]. Cosmic rays particle and planetary nuclei are subsequently transformed in a variety of secondary nucleons, mesons and residual nuclei. These secondary particles continue to lose energy, through initiation of further cascades, decay or Coulomb collisions. The resulting population of particles with energies below 100 MeV is dominated by neutrons. Neutrons newly created have rather high energies, and are referred to as fast neutrons.
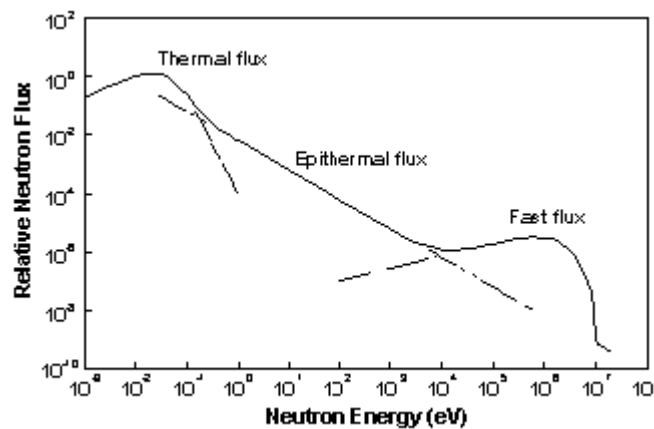
Figure 1.1: Theoretic neutron spectrum showing the different neutron distribution resulting from the neutron production, moderation and absorption.

Neutrons can be produced with two main mechanisms: direct interactions and evaporation from excited nuclei. Direct interactions (or spallation collisions) produce neutrons with a continuum of energies extending up to that of the incident cosmic ray. Neutron evaporations produce a Maxwellian energy spectrum whose average is about 1 MeV [Feldman et al., 1993]. Secondary neutrons can either moderate in the surrounding material or escape to space. They can undergo multiple elastic and non-elastic collisions with the nuclei of the material. The resultant neutron spectrum below 10 keV has two different regimes: epithermal and thermal (Figure 1.1).

The epithermal range of energies is below the energies at which neutrons are produced with the spallation or evaporation processes (which is known as the fast range). It is also above the energies where neutrons are scattered by ion thermal motion or lost by absorption (which is known as the thermal range). The resulting energy subdivision is roughly the following: thermal energies are below ~0.1 eV, epithermal energies range between ~0.1 and ~1000 eV, fast energies are above ~1000 eV.

1.1.3 Gamma ray sources in planetary materials

Gamma ray production in planetary materials can be due to natural or induced radioactivity. The first phenomenon consists in the deexcitation of radionuclides whose half-life is about the same as the age of the solar system. The second phenomenon consists in the interactions of secondary particles created by the energetic particles bombardment (either of solar or galactic cosmic ray origin) with nuclei of the surrounding planetary material.

GCR produced neutrons are the major source of gamma rays. Nuclei can be excited directly by cosmic-ray particles, by inelastic scattering and capture of neutrons, or in the decay of radioactive nuclei. The excited levels in each nucleus occur at specific quantized energies, and the energy of a gamma ray made by a transition between nuclear levels can usually identify which nucleus produced it.

Natural radioactivity

Energy (keV)	Decay chain	Element
238.6	^{232}Th	^{212}Pb
351.9	^{238}U	^{214}Pb
583.1	^{232}Th	^{208}Tl
609.3	^{238}U	^{214}Bi
911.1	^{232}Th	^{228}Ac
1120.3	^{238}U	^{214}Bi
1460.8	^{40}K	^{40}K
1764.5	^{238}U	^{214}Bi
2614.6	^{232}Th	^{208}Tl

Table 1.1: Example of gamma ray lines produced by natural radioactivity.

The isotopes that have half-lives long enough to allow observing their decay nowadays include: ^{40}K (half-life of 1.25 Ga), isotopes in the decay chains of ^{232}Th (half-life of 14.05 Ga), isotopes in the decay chains of ^{238}U (half-life of 4.47 Ga).

Table 1.1 displays examples of isotopes whose lines can be observed. If a naturally radioactive element is uniformly distributed in the top ~100 g/cm2 of a planet's surface, the fluxes of its decay gamma rays escaping the surface depend only on basic nuclear data, such as half-lives, gamma-ray yields, and the gamma-ray-transport property of overlying media [Boynton et al., 2004].

Inelastic scattering reactions occur when an excited level in a nucleus is populated by an energetic particle and then almost immediately decays to a lower level. This decay results in the emission of a gamma photon whose energy is the difference between the excited state of the atom and its final state. Almost all elements can produce inelastic-scattering gamma rays from neutron interactions, at the exception of very light elements like H and He that do not have gamma-ray-emitting excited levels.

Energy (keV)	Element
847	Fe
1014	Al
1238	Fe
1369	Mg
1779	Si
3737	Ca
6129	O

Table 1.2: Example of gamma ray lines produced by inelastic scattering.

Capture

Once moderated down to the thermal regime, neutrons have sufficiently low speed to be captured by environmental nuclei. Many elements have high cross sections for capture of neutrons at thermal energies. In most cases after the low-energy neutron is absorbed, one or more gamma rays are emitted. Table 1.3 displays a few examples of lines produced by this reaction. The thermal neutron flux affects a lot the emission of gamma rays through capture. This thermal neutron flux being dependent on the composition, the analysis of lines produced by capture is far from straightforward.

Energy (keV)	Element
2223	H
6111	Cl
6418-6760	^{48}Ti
7631-7646	^{56}Fe

Table 1.3: Example of gamma ray lines produced by capture.

Summary

A large variety of mechanisms induce the surface of a planet to produce gamma rays. However all mechanisms do not contribute to lines that identify uniquely the emitting nucleus. Many gamma photons are emitted by Bremsstrahlung radiation (which is produced when a very high-energy electron is deflected by the electric field of a nucleus). The decay of cosmic ray produced pions also produces gamma photons. Finally, some of the photons produced by the previously described mechanisms undergo

diffusion before escaping the planetary surface. In that case, they have lost their initial energy signature.

These effects contribute to a featureless continuum that is not useful for chemical abundance mapping. Only photons whose energies carry the information of their parent nuclei are used for gamma spectroscopy. Figure 1.2 synthesizes the mechanisms that produce neutrons and gamma rays allowing analysis in terms of chemical abundances.
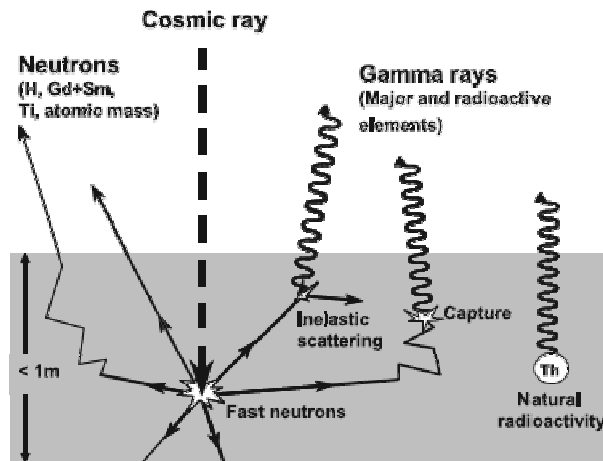
Figure 1.2: Scheme of the nuclear interactions in a planetary body useful for spectroscopy.

1.2   Instrumentation

1.2.1   Gamma ray spectroscopy

Gamma ray spectroscopy is the science that aims at measuring energy spectra of the light in the gamma ray domain of the electromagnetic spectrum. The measurement consists in counting the photons emitted by a material (either by natural radioactivity or by irradiation with an extern source) and measuring their energy. Figure 1.3 shows the type of spectrum that could be acquired with a high resolution instrument. The analysis of the spectra thus obtained is used to identify and quantify the gamma emitting nuclides contained in the material. Gamma ray spectrometers consist of a detector, electronics to collect and process the signals produced by the detector, and a computer with processing software to generate, display, and store the spectra.

Detectors are passive materials in which gamma interactions are susceptible to occur. Two types of detectors can be encountered: scintillation detectors and semi-conductors. Crystals used on scintillation detectors emit light when gamma rays interact with their atoms. The intensity of the light produced is proportional to the energy deposited in the crystal by the gamma ray. The detectors are joined to photomultipliers that convert the light into electrons and then amplify the electrical signal provided by those electrons. Common scintillators include sodium iodide (NaI) and bismuth

germanate (BGO). NaI-based detectors have a rather poor resolution which makes them unsuitable for the identification of complicated mixtures of gamma ray-producing materials.
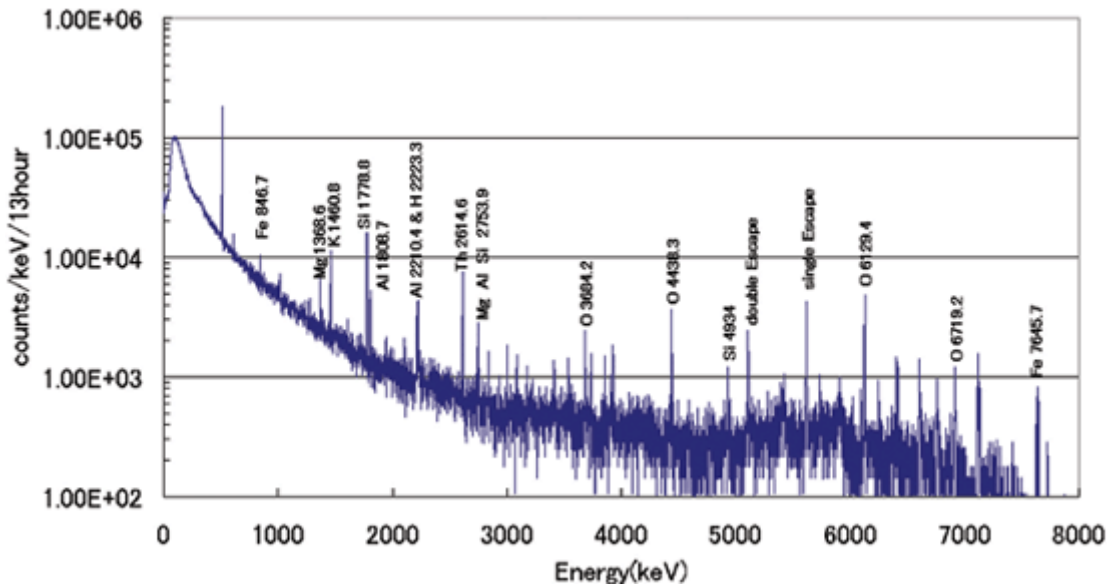
Figure 1.3: Typical spectrum collected by a high energy resolution gamma ray spectrometer. Several lines have been identified as produced by major elements.

In semiconductor detectors, gamma rays are measured by counting the number of free charge carriers. Gamma rays produce electron-hole pairs in the detector volume. An electric field is applied to induce electrons and holes to migrate towards the electrodes. The arrival of an electron at the positive contact and of a hole at the negative contact produces an electrical signal that is sent to the preamplifier. The amount of energy required to create an electron-hole pair is known, so measuring the number of electron-hole pairs allows estimating the energy of the incident gamma ray. Common semiconductor-based detectors include germanium, cadmium telluride, and cadmium zinc telluride. Germanium detectors produce the highest energy resolution commonly available today.

For both detector types, the voltage pulse produced is shaped by a multichannel analyzer (MCA). The multichannel analyzer takes the very small voltage signal produced by the detector, reshapes it into a Gaussian or trapezoidal shape, and converts this analog signal into a digital one. The analog-to-digital converter (ADC) sorts the pulses by their height. ADCs have specific numbers of "bins", or channels, into which the pulses can be sorted. The choice of the number of channels depends on the resolution of the system and the energy range being studied. The multichannel analyzer output is sent to a computer, which stores, displays, and analyzes the data.

1.2.2 Neutron spectroscopy

Neutron spectroscopy consists in the effective detection of neutrons entering a detector coupled to an electronic box. Neutron detection is used for varying purposes outside planetary sciences: nuclear reactor instrumentation (the neutron flux measures the power involved in reactors), radiation safety (measurement of the neutron radiation hazard anywhere irradiation sources are involved), cosmic ray monitoring (through measurement of secondary neutrons)…

Neutrons do not respond to electric fields, which makes it hard to direct their course towards a detector. Neutrons also do not ionize atoms except by direct collision. Neutron detection is therefore not an easy science. Instrumentation also faces the problem of the noise background produced by high energy photons and α particles. Coincidence and anticoincidence methods have been developed to discriminate between real neutron events and other radiations.

Different detectors allow measuring neutrons depending on their energy range [Feldman et al., 1993]:

- Moderated thermal neutron detectors: a polyethylene moderated, ^{3}He gas proportional counter is used to detect neutrons in the energy range 1 eV – 10 MeV
- Proton recoil detectors: a boron-loaded plastic scintillator allows measuring the energy deposited by a fast neutron through multiple proton recoils and identifies the particle as being a neutron thanks to the unique activation energy of the ^{10}B$(n, \alpha)^7$Li reaction
- Nonelastic scatter: a cooled germanium crystal allows detecting fast neutrons at different energies thanks to the identification of Ge (n,nγ) inelastic lines

1.2.3 History of gamma and neutron spectrometers onboard planetary missions

Some of the planetary missions carrying gamma or neutron spectrometers are presented here. Table 1.4 provides an insight of all missions launched towards planetary objects since the beginning of the use of this technique.

Because the composition of the planet modulates the production and transport of neutrons and gamma rays, neutron and gamma spectroscopy were proposed to study the composition of planetary surfaces [Lingenfelter et al., 1961; Arnold et al., 1962; Van Dilla et al., 1962]. The Apollo 15 and 16 missions carried NaI(Tl) scintillation gamma-ray spectrometers to the Moon in 1971 and 1972. The spectra accumulated on about 10% of the lunar surface allowed determining abundances of magnesium, potassium, iron, titanium, and thorium, at that time confirming that gamma ray spectroscopy was an appropriate tool for constraining the elemental composition of planetary surfaces.

In 1998 Lunar Prospector flew both a bismuth germanate (BGO) gamma-ray instrument and a ^{3}He based neutron instrument (Figure 1.4) on a spacecraft in a low polar orbit around the Moon [Feldman et al., 1999]. The data provided by the gamma ray spectrometer was used to make geochemical maps of the entire Moon [Lawrence et

al., 1999; Lawrence et al., 2002; Prettyman et al., 2006b] while the neutron spectrometer provided strong evidence for hydrogen near the lunar poles [Feldman et al., 2001], probably in the form of ice trapped on the permanently-shadowed floors of polar impact craters.

Mission	Year	Reference	Detector	Objective
Ranger 3-5	1962	[Arnold et al., 1962]	CsI:Tl (sci)	Moon
Luna 10 et 12	1966	[Vinogradov et al., 1967]	NaI:Tl (sci)	Moon
Apollo 15 et 16	1971-72	[Harrington et al., 1974]	NaI:Tl (sci)	Moon
Mars 4 et 5	1973	[Surkov et al., 1981]	CsI:Tl (sci)	Mars
Phobos 1 et 2 / APEX	1988	[Surkov et al., 1989]	CsI:Tl (sci)	Mars
Mars Observer / GRS	1992	[Boynton et al., 1992]	HPGe (sem)	Mars
Mars 96 / HGRS	1996	[Mitrofanov et al., 1996]	2 HPGe (sem)	Mars
NEAR	1996	[Trombka et al., 1997]	BGO (sci)	Eros
Lunar Prospector / GRS	1998	[Feldman et al., 2004a]	BGO (sci)	Moon
Mars Odyssey / GRS	2001	[Boynton et al., 2004]	HPGe (sem)	Mars
MESSENGER / GRS	2004	[Gold et al., 2001]	HPGe (sem)	Mercury
DAWN / GRaND	2006	[Prettyman et al., 2006a]	CZT + BGO	Asteroids
SELENE	2007	[Hasebe et al., 1999]	HPGe (sem)	Moon
Bepi-Colombo / MGNS	2013	[Schulz et Benkhoff, 2006]	LaBr3:Ce (sci)	Mercury

Table 1.4: Characteristics from past, current and future planetary mission carrying gamma spectroscopy instruments [adapted from Pirard 2006].
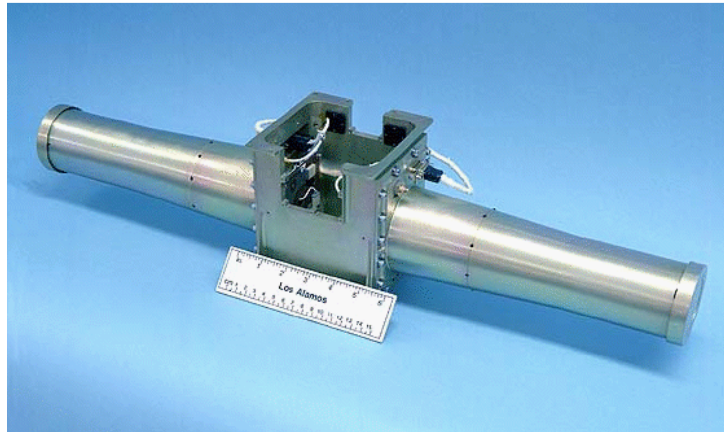
Figure 1.4: Neutron Spectrometer with 3He tubes onboard Lunar Prospector.

Initially launched in 1995, the gamma-ray spectrometer flown as part of the NEAR (Near Earth Asteroid Rendezvous) mission reached the asteroid Eros in 2001 [Trombka et al., 2000, Trombka et al., 2001]. This instrument was similar in many respects to the Apollo GRS instrument. The NEAR GRS produced only limited compositional results, due to the low gamma-ray emission rate from the asteroid. However, the mission was ended by a soft landing of the spacecraft on the asteroid,

which allowed direct physical contact with its regolith and improved significantly the counting statistics. This configuration gathered over 200 hours of gamma ray data, providing information on the elemental composition of the asteroid at the landing location [Evans et al., 2001].

Although considered for many years [Metzger and Arnold, 1970], survey of Mars with gamma ray spectroscopy was not really achieved before the launch of Mars Odyssey. Mars-5 [Surkov et al., 1981] [Vinogradov et al., 1976] and Phobos [d'Uston et al., 1989] [Surkov et al., 1989] included CsI(Tl) scintillators that obtained limited but quantitative results on elemental abundances. Mars Observer, launched in 1992, carried a combined gamma and neutron spectrometer [Boynton et al., 1992]. Unfortunately, the mission was lost three days prior to orbit insertion. Beside Mars Observer, high purity germanium detectors were later carried by Mars 96. However this mission also ended tragically.

So the GRS onboard Mars Odyssey became in 2002 the first instrument to successfully measure elemental abundances in orbit around Mars [Boynton et al., 2004]. The experiment flown by Mars Odyssey is very similar to that previously carried by Mars Observer. The high purity Ge crystal allows collecting high resolution gamma ray spectra. Over 300 lines were thus identified, among whom about 60 were useful for geochemical mapping. Maps of Fe, H, Si, Cl, K, Th, Al and Ca have been published thanks to this dataset. In addition to the gamma subsystem, Mars Odyssey carries a neutron spectrometer that continuously measures the neutron flux leaking outward the Martian surface. More details on the Mars Odyssey GRS suite of instruments will be given in 2.1.

Since Lunar Prospector, new missions have been launched in direction of the Moon. Among them, the Japanese mission Selene (SELenological Engineering Explorer) carried into lunar orbit in 2007 the first high resolution spectrometer [Hasebe et al., 2008]. The Selene GRS instrument allows mapping the abundances of many elements: O, Mg, Si, S, K, Ca, Ti, Fe, Th and U over the entire lunar surface. More details on the Selene GRS mission will be given in 3.1.

Also launched in September 2007, the spacecraft of the Dawn mission is on its way to Vesta and Ceres (the two most important bodies of the asteroids belt). Onboard the spacecraft, the GRaND experiment (Gamma Ray and Neutron spectrometer) will measure elemental abundances of the surface of these objects when Dawn reaches Vesta in 2011 and later Ceres in 2015.

And finally the American mission Messenger will be inserted in orbit around Mercury in 2011 after 3 flybys. Its European counterpart BepiColombo, whose launch is planned for 2013, should not reach Mercury before 2019. Both missions carry gamma ray and neutron spectrometers (instruments respectively named GRNS and MGNS). For both missions, collecting gamma rays will provide abundances of geologically important elements such as H, Mg, Si, O, Fe, Ti, Na, and Ca. It may also detect naturally radioactive elements such as K, Th, and U. The neutron detection will complement this information and provide more specifically the composition in light elements such as H. From now on, missions dedicated to the study of the surfaces of Mars and the Moon will be focused on.

1.3   Planets of interest

1.3.1 Mars

Exploration

Although observations of Mars have started as soon as Antiquity, the first decisive studies can be considered to happen with the invention of telescopes at the 17th century. At that time, the first drawings of Mars have been realized by Huygens and Cassini. Herschel postulated the existence of seasons and of a tenuous atmosphere around 1777. By the 19th century, the technology of telescopes reached a level sufficient to resolve surface features. Consequently, Phobos and Deimos were discovered in 1877 by Hall. At that same time, the Italian astronomer Schiaparelli observed straight linear structures that he named *canali*. Interpreted as an evidence of the existence of Martian intelligent life by Lowell, these so-called canals nourished fantasies of a populated Mars for years. It was not until 1909 that the channels were proven to be optical illusions, thanks to the observations of Flammarion. However the belief that Mars contained vast seas and vegetation remained longer held.

The arrival of the space area dispelled many myths about Mars. The first flyby of Mars occurred in 1965 with Mariner 4. Back then, it was a great disappointment to discover that the surface of Mars did harbor neither life, nor any liquid water. The first spacecraft to orbit around Mars was Mariner 9 in 1971. This same year, the two probes Mars 2 and Mars 3 successfully landed on the surface, but lost contact within seconds after landing. They were followed in 1976 by Viking 1 and Viking 2, two missions made of the conjunction of an orbiter with a lander. Viking 1 remained operational for six years and Viking 2 for three, relaying a considerable amount of pictures both from orbit and from surface.

The following years were filled with failed missions. The red planet indeed resisted fiercely to exploration, and Russian missions proved especially unlucky (Table 1.5). Renewed luck stroke Martian missions in 1996 with the launch of Mars Global Surveyor. This mission was a complete success and kept working until late 2006 although its primary mapping mission finished in early 2001. Shortly after the launch of Surveyor, Mars Pathfinder left with the objective of carrying the vehicle Sojourner onto the surface. The mission successfully landed in Ares Vallis in 1997 and harvested many images from the surface.

	URSS	*USA*	*Other*
Launch failure	1960 Marsnik 1 et 2 1969 Mars 1969 A et B	1964 Mariner 3 1971 Mariner 8	
Failure in terrestrial orbit	1962 Spuntnik 22 et 24 1971 Kosmos 419 1996 Mars 96		
Lost during the Earth-Mars transfer	1962 Mars 1 1964 Zond 2 1965 Zond 3 1988 Phobos 1		
Failure in Martian orbit	1973 Mars 4	1992 Mars Observer 1998 Mars Climate Orbiter	1998 Nozomi
Crash	1971 Mars 2 lander 1973 Mars 6 et 7	1999 Mars Polar Lander 1999 Deep Space 2	2003 Beagle 2
Premature failure	1971 Mars 3 lander 1973 Mars 5 1988 Phobos 2		
Success		1964 Mariner 4 1969 Mariner 6 et 7 1971 Mariner 9 1975 Viking 1 et 2 1996 Mars Global Surveyor 1996 Mars Pathfinder 2001 Mars Odyssey 2003 Spirit et Opportunity 2005 MRO 2007 Phoenix	2003 Mars Express

Table 1.5: Overview of past and current mission to Mars classified by degree of achievement.

Missions sent subsequently are still in operation around or at the surface of Mars. Launched in 2001, the Mars Odyssey mission (Figure 1.5) is to be extended till 2010 and collected very nice results such as the detection of hydrogen in the upper meter of regolith, interpreted as large deposits of water ice. The European mission Mars Express launched in 2003 also proved successful. This same year were also launched the twin Mars Exploration Rovers: Spirit and Opportunity. They landed in January 2004 respectively in the Gusev Crater and Meridiani Planum and exceedingly met their objectives. Among the most significant scientific returns has been conclusive evidence that liquid water existed at some time in the past at both landing sites. The Mars Reconnaissance Orbiter launched in 2005 conducts a survey of suitable landing sites thanks to mapping of increased resolution. The most recently launched mission is the Phoenix Mars lander that arrived in the north polar region in May 2008 to confirm the presence of water ice buried at high latitudes.

Figure 1.5: Conceptual drawing of Mars Odyssey.

Future mission include Mars Science Laboratory, planned for 2011, onboard which ChemCam will be the first instrument capable of remotely determining the composition of rocks thanks to Laser-Induced Breakdown Spectrometry. The joint Russian and Chinese mission Phobos-Grunt scheduled for 2009 intends to return samples of Mars's moon Phobos. The first European rover is planned for 2013 with ExoMars which should be capable of drilling 2 m into the soil in search for organic molecules. The American mission MAVEN, also announced for 2013, should provide information about Mars' atmosphere. And finally the Finnish-Russian MetNet mission will land tens of small vehicles on the Martian surface to establish a widespread network to investigate the planet's atmosphere.

General features

Mars is the fourth planet of the Solar System. Also referred to as the "red planet", Mars has a reddish appearance caused by the global presence of oxidized iron-bearing minerals on its surface. Mars is a terrestrial planet that has a tenuous atmosphere. Surface features visible from space include impact craters, volcanoes (such as Olympus Mons, the highest mountain of the Solar System), canyons (such as Valles Marineris, the largest canyon), valleys and polar ice caps. They reveal that the planet has known volcanic, tectonic, fluvial and glacial activity along its history.

Mars has approximately half the radius of Earth and is ten times less massive. A Martian year equals 1 Earth year and 320 days. The solar day on Mars is only slightly longer than a day on Earth: 24 hours, 39 minutes and 35 seconds. Seasonal cycles are quite similar to those of Earth because the axial tilt of Mars (angle between the axis of Mars and the direction perpendicular to the ecliptic plane) is currently about the same: 25.19°. The Martian eccentricity is among the greatest of the Solar System: 0.09. Mars has two tiny natural moons: Phobos and Deimos, which orbit very close to the planet. Both satellites are thought to be captured asteroids.
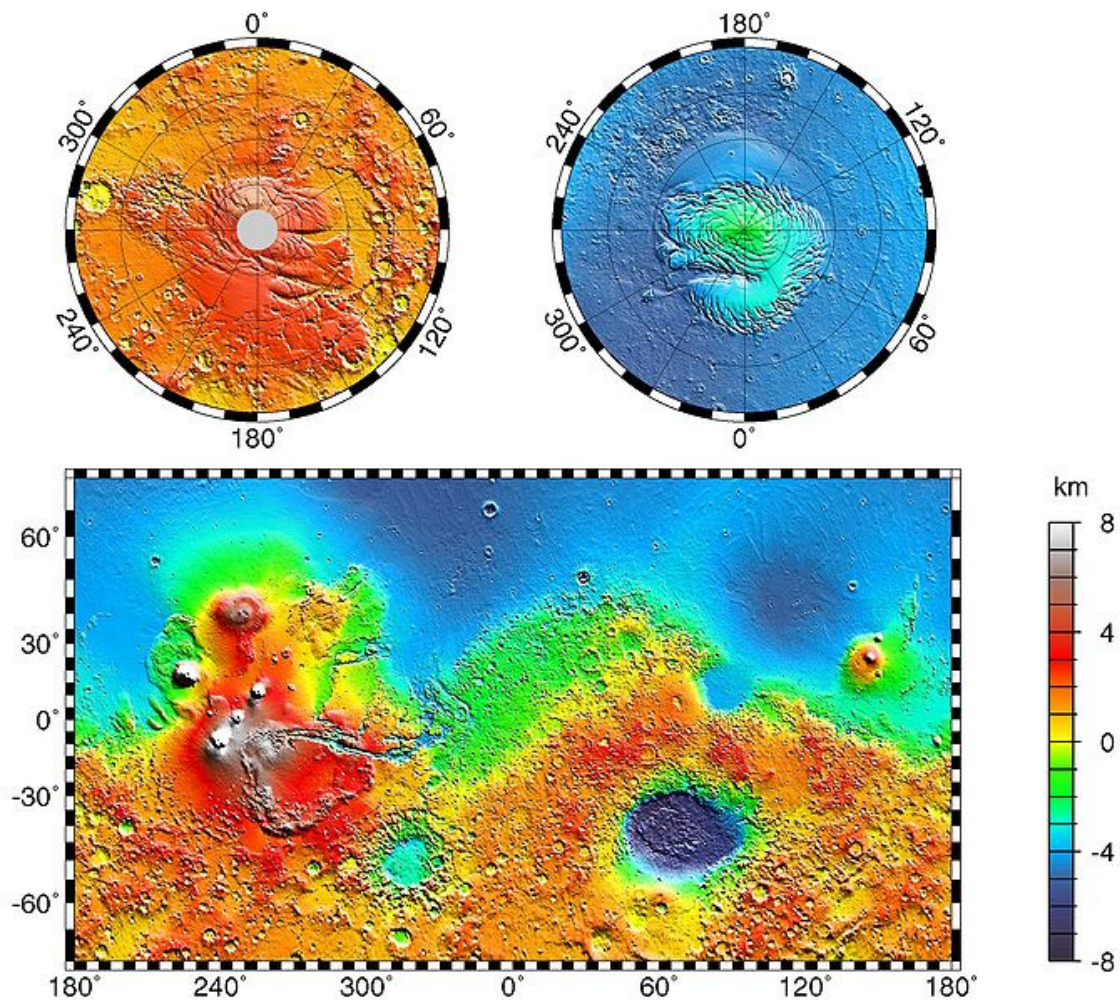
Figure 1.6: Topographic map of Mars acquired by MGS MOLA [Smith et al., 1999].

The Martian surface exhibits a very striking dichotomy: northern plains flattened by lava flows (in blue on Figure 1.6) contrast with the southern highlands (in orange on Figure 1.6), deeply cratered by ancient impacts. The surface of Mars as seen from Earth is consequently divided into two terrains of different albedo. The paler plains covered with dust and sand rich in reddish iron oxides were once thought to be Martian continents whereas the dark features were thought to be seas. This dichotomy is inherited from the geological history of Mars, which can be roughly split into three main epochs (Figure 1.7):

- Noachian epoch (3.8 billion years ago to 3.5 billion years ago): formation of the oldest surfaces of Mars, easily recognized by their large number of impact craters; formation of the Tharsis volcanic bulge; extensive flooding by liquid water
- Hesperian epoch (3.5 billion years ago to 1.8 billion years ago): formation of the extensive lava plains.
- Amazonian epoch (1.8 billion years ago to present): with few meteorite impact craters; formation of Olympus Mons along with lava flows elsewhere on Mars.

Figure 1.7: Geologic epochs of the Martian history.

Composition of the surface

Earth-based and orbital observations as long as geochemical measurements of meteorites and in situ samples provide decisive information on the composition and physical properties of the Martian crust. Due to its smaller radius than that of Earth, Mars cooled off more quickly, restra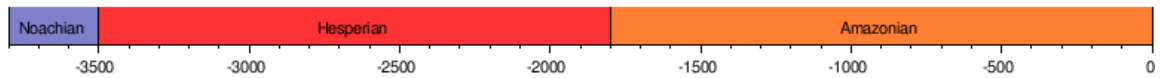ining the geological activity to volcanism and tectonism without motion of surface plates. The surface is composed of a mixture of relatively pristine igneous rocks overlain by highly oxidized weathering products that constitute the relatively bright dust and soils.

Major breakthroughs in the study of the mineralogy of materials constituting the surface have been brought by the space area. The Viking landers revealed the likely presence of peroxide, a reactive oxidant. The Thermal Emission Spectrometer (TES) onboard Mars Global Surveyor identified and mapped two end members of low-albedo materials: a basalt-rich component in the southern highlands and an andesite-rich (or altered basalt) component in the northern lowlands [Bandfield et al., 2000]. TES also discovered an accumulation of crystalline hematite that covers an area centered on Sinus Meridiani [Christensen et al., 2000]. Following missions flew spectrometers of higher spatial resolution that provided additional details on the mineralogy of the Martian surface. The Thermal Emission imaging System (THEMIS) onboard Mars Odyssey allows identifying lithologically different layers by collecting daytime and nighttime infrared to visible images [Christensen et al., 2003].

The Observatoire pour la Minéralogie, l'Eau, les Glaces, et l'Activité (OMEGA) onboard Mars Express is mapping the surface composition with visible and near-infrared imagery. OMEGA identified mafic iron-bearing silicates, localized concentrations of hydrated phyllosilicates and sulfates but no carbonates [Bibring et al., 2005]. The Compact Reconnaissance Imaging Spectrometer for Mars (CRISM) onboard Mars Reconnaissance Orbiter expanded the study of phyllosilicate-rich regions preidentifed by OMEGA thanks to a higher spatial resolution. The phyllosilicate mineralogy proved very diverse with the identification of kaolinite, chlorite and illite or muscovite, and a new class of hydrated silicate. Fe/Mg-OH phyllosilicates and smectites such as nontronite and saponite have been found to be the most common, but chlorites were also present in some locations [Mustard et al., 2008].

Composition of the atmosphere

Although the detailed analysis of the atmosphere exceeds the objectives of the present study, basic understanding of its structure and composition is needed to anticipate how it will affect the fluxes of neutrons and gamma rays. The atmosphere of Mars is very tenuous compared to that of Earth. In spite of its thinness, the Martian atmosphere is a very complex system that is subjected to both space and time variations.

The pressure at the surface varies with the topography from as low as 30 Pa on Olympus Mons up to 1155 Pa in Hellas Planitia, the average being around 600 Pa. The Martian atmosphere consists most of all of carbon dioxide with traces of oxygen and water (Table 1.6). It also contains a non negligible fraction of dust, which explains the orange color of the sky. The presence of methane in still debated, and occurs anyway at concentrations which make it irrelevant for gamma and neutron spectroscopy.

element	abundance
CO_2	95,32%
N_2	2,7%
Ar	1,6%
O_2	0,13%
CO	0,07%
H_2O	~0,03%

Table 1.6: Composition of the gaseous fraction of the Martian atmosphere.

Due to its tilted axis, Mars possesses Earthlike seasons. However the cycles triggered by the variations of temperature are very different from that of Earth: because of the presence of large quantities of CO_2 and dust, atmospheric variations are not mostly governed by water. During northern winter, the pole lies continuously in the dark and the temperatures drop down to -125°C, causing large amounts of CO_2 to condense into a thick veneer of ice. When spring exposes again the polar cap to sunlight, the frozen CO_2 sublimes back to the atmosphere. Northern summer corresponds to southern winter, during which the same sequence of events occurs for the southern polar cap. The sudden sublimation of massive quantities of CO_2 gives rise to strong winds that transport large amounts of dust and water vapor.

In addition to the cycle of CO_2, the atmosphere is subjected to variations of the dust concentration. The opacity of the atmosphere is intimately connected to its mean temperature. Numerous local storms occur daily on the planet. They refill the atmosphere with particles of dust that tend to fall on the surface when atmospheric conditions are calm. The additional dust in the atmosphere modifies the equilibrium of the system in adding a source of heat. Sometimes this additional energy can cause the storms to become regional, or even global. The dustier the atmosphere is, the more it is warmed by sunlight, which induces storms to last for quite a long time (months).

Finally the water component of the atmosphere is also subjected to seasonal variations. The cycle of water on Mars is made of complex exchanges in between three different reservoirs: the polar caps which contain water ice, the atmosphere that contains water vapor and clouds and the regolith that contains water vapor, water ice, and maybe liquid water at appropriate conditions of depth and latitude. The seasonal and latitudinal distribution of water is controlled by the sublimation and condensation of ice deposits and by the meridional transport of water vapor. The northern hemisphere contains a large permanent ice cap recharged during wintertime, and alimenting the atmosphere in

water vapor during summertime. Finally the distribution of water between atmosphere and regolith obeys to a pressure equilibrium.

Although presented separately, the three described cycles – CO_2, dust and water – are closely interconnected and each variation in the concentration and distribution of one of these components induces feedback in the distribution of the other components.

Stakes of gamma ray and neutron spectroscopy for Martian science

Knowledge of the elemental composition of its surface, and most particularly the abundance of water, is a necessary preliminary to understanding the formation and evolution of Mars. Like presented in the history, there have been several missions prior to Mars Odyssey that were carried out to determine the composition of the surface of Mars. In addition to Earth-based reflectance spectroscopy observations, orbital studies were carried out using visible and infrared imaging [e.g., Bandfield et al., 2000; Christensen et al., 2000; Bandfield, 2002; Bibring et al., 2005; Gendrin et al., 2005].

Due to the presence of an atmosphere and to layering in the first centimeters of soil, techniques of spectroscopy in the infrared region of the electromagnetic spectrum are not very adapted to constraining the composition of the surface: infrared spectroscopy tend to be very influenced by an atmospheric contribution and only reveals the mineralogy of the top micrometers of soil. In spite of also being complicated by the presence of atmosphere, gamma ray and neutron spectroscopy have the major advantage of surveying a thicker layer of material (the upper few tens of centimeters).

Neutron spectroscopy can be used to survey planetary bodies for hydrogen [Lingenfelter et al., 1961]. Epithermal neutrons are most sensitive for this purpose. Thermal and epithermal neutron fluxes also provide unique information about the distribution and thickness of deposits of CO_2 [Feldman et al., 1993] that cover both polar caps during their respective winter months.

Gamma ray spectroscopy can be used to determine the composition of a planetary body [Evans et al., 1993; and references therein]. The gamma rays spectroscopy allow detecting radioactive elements (the isotope ^{40}K and the elements U and Th with their daughter isotopes) and elements producing gamma rays by the scattering of fast neutrons from a nucleus or by the capture of thermal neutrons, such as H, Si, Cl, Fe.

1.3.2 The Moon

Exploration

Like for the exploration of Mars, the first breakthrough in lunar observation was concomitant with the invention of the telescope. Galilei observed mountains and craters on the Moon surface thanks to this instrument. Hevelius published in 1647 the first treaty devoted to the Moon: *Selenographia*. Further major steps of exploration were brought by the space area (Table 1.7). The exploration of the Moon gave birth to a passionate race in between the Soviet Union and the United States. Both nations alternatively obtained scientifically important firsts.

Flyby and impact probes were sent to the Moon very soon after the first flights in space had been performed. The Russian Luna program was the first unmanned spacecraft to reach the Moon. In 1959 Luna 1 was the first object to escape Earth's gravity and pass near the Moon, Luna 2 was the first object to impact the lunar surface and Luna 3 acquired the first photographs of the far side. Later, Luna 9 managed the first soft landing on the surface and Luna 10 the first orbiting mission. Luna 16, 20 and 24 brought samples of lunar material back to Earth.

However the American missions brought considerably larger amounts of samples back to Earth. The Apollo program (a picture taken during Apollo 17 is shown in Figure 1.8) did not only bring first man on Moon, but also contributed to exploring several landing sites of the surface. Apollo mission 11 to 17 (at the exception of the aborted mission Apollo 13) collected multiple samples, which amount to 382 kg of lunar material when the Luna missions only brought 326 g. The culmination of Apollo was nevertheless the first steps of Neil Armstrong on the Moon during Apollo 11. Apollo missions carried scientific payload on the surface of the Moon containing heat flow probes, seismometers, magnetometers, LLR (Lunar Laser Ranging) stations…

Figure 1.8: Harrison Schmitt (the only geologist to have set foot on the Moon, and incidentally my advisor's hero!) standing next to a large boulder during Apollo 17.

From the mid-1960s to the mid-1970s, 65 human-made objects reached the Moon, after what the frenetic race for the Moon dampened. The Japanese spacecraft Hiten orbited the Moon in 1990, becoming the third country to place a spacecraft into

lunar orbit. No further American probe was sent again to the Moon before Clementine in 1994. This mission acquired the first global topographic map and multispectral images of the lunar surface. Clementine was followed by Lunar Prospector in 1998, onboard of which a neutron spectrometer allowed the detection of hydrogen at the poles, interpreted as water ice in the upper few meters of the regolith within permanently shadowed craters.

Mission	Year	Nationality	Description
Luna 1-2-3	1959	Russian	1st flyby, 1st impact with surface, 1st photographs of the far side
Ranger 6-7	1964	American	detailed photographs
Luna 9	1966	Russian	1st soft landing, photographs of the surface
Lunar Orbiter 1-2-3-4-5	1965-1966	American	Unmanned orbiter designed to map the lunar surface at high resolution (tens of meters)
Surveyor 1-3-5-6-7	1966-1968	American	Soft landing training, photographs of the surface
Apollo 8 à 17	1968-1972	American	Manned flybys, manned lunar landing from Apollo 11, remote geochemistry, surface geochemistry
Luna 17-21 + Lunakhods	1970-1973	Russian	Spacecraft + rover destined to explore surface and return pictures
Hiten	1990	Japanese	Lunar orbiter
Clementine	1994	American	Topography and global geochemical mapping
Lunar Prospector	1998	American	Global geochemical mapping, search for water ice
Smart 1	2003	European	Test of ion propulsion, IR and X ray imaging
Selene	2007	Japanese	Topography, gravity map of the far side, geochemical mapping
Chang'e 1	2007	Chinese	3D imaging, geochemical mapping, search for ^{3}He
Chandrayaan 1	2008	Indian	3D imaging, geochemical mapping

Table 1.7: Past and present exploration missions to the Moon.

The first European spacecraft, Smart 1, was launched in 2003 and remained in lunar orbit from November 15, 2004 to September 3, 2006. Japan launched Selene in 2007. Around the same time was launched the Chinese mission Chang'e 1. These two successes were imitated a year after by India with the launch of Chandrayaan I. The three competitive countries are reviving the technologic race for space conquest. Although these missions have not harvested many revolutionary scientific facts so far, they contribute considerably to boosting the exploration of the Moon.

The next mission towards the Moon is the American Lunar Reconnaissance Orbiter planned for a launch in 2009. LRO will take high resolution imagery of the moon's surface and investigate the possible existence of water in the Shackleton crater. China plans to land a rover in 2012 and to conduct a sample return mission in 2017. India expects to launch further missions, including a rover, around 2011 and a manned flight by 2014. Japan should launch Lunar A in 2010. All nations announced their intention to send a manned lunar landing around 2020.

General features

The Moon is the Earth only natural satellite. With a diameter of 3474 km, it is the fifth largest satellite in the Solar System. The center of the Moon is distant from that of the Earth of about 384 400 km. The orbital period lasts 27.3 days and the synodic period (which is responsible for the lunar phases) 29.5 days. The rotation of the Moon about its axis is synchronized on the rotation around Earth which explains why the same face (the near side, in opposition to the far side) is always turned towards the Earth. The initial rotation was at a faster rate, but was slowed down and locked as a result of the tidal deformations caused by Earth.

The Moon also exhibits two main types of terrains. The dark and relatively smooth plains called *maria* consist of solidified basaltic lavas. They result from the flow of lavas into depressions caused by meteoric impacts. Maria are found almost exclusively on the near side of the Moon. They cover about 31% of the surface of the near side against only 2% of that of the far side. Regions with a higher albedo are known as *terrae* or *highlands*. Generally higher than mare, they are notably populated by mountains along the periphery of impact basin which are thought to be surviving remnants of outer rims. The surface of the Moon, especially on the highlands, is deeply marked by impact craters. Since the end of the cataclysmic bombardment, impact craters accumulate at a nearly constant rate, so the number of craters per unit area can be used to estimate the age of the surface. The Moon possesses the largest known impact basin of the solar system: the South Pole Aitken basin (2240 km in diameter and 13 km in depth).

Composition of the surface

The Moon is a differentiated body, i.e. composed of a geochemically distinct crust, mantle, and core. This structure is thought to have resulted from the fractional crystallization of a magma ocean shortly after its formation, which would have given rise to a mafic mantle and a plagioclase-rich crust. The magma ocean hypothesis is consistent with the geochemical mapping from orbit that revealed a predominance of anorthositic composition [Warren, 1985], that involves the following elements: O, Si, Mg, Fe, Ca and Al. On the basis of geochemical mapping from orbit (Clementine multispectral data and Lunar Prospector gamma ray data), Jolliff [Jolliff et al., 2000] identifies three distinct geological terrains:

- The Procellarum KREEP Terrain (PKT): provinces whose composition is mafic (in other words rich in Mg and Fe, due to the following dominant minerals:

olivine, orthopyroxene and clinopyroxene) with a very high concentration of heat producing elements (Th, U and K) resulting from resurfacing events

- The Feldspathic Highlands Terrain (FHT): provinces whose composition is anorthositic (that is to say very rich in plagioclase feldspar) resulting from crust produced during early lunar differentiation (see Figure 1.9)
- The South Pole Aitken Terrain (SPAT): large impact basin whose composition is much more mafic than the surrounding terrains, probably a mix of lower crust and upper mantle.

The composition of the crust revealed by remote geochemistry is consistent with that derived with the use of the lunar rock samples available on Earth. Different sources exist: samples collected by Apollo and Luna missions; and rocks that were ejected naturally from the lunar surface by cratering events and subsequently fell to Earth as lunar meteorites. Nearly all lunar rocks are depleted in volatiles. Moon rocks fall into two main categories, the ones found in the lunar highlands and those of the maria. Highlands are composed of three distinct groups: the ferroan anorthosite suite, the magnesian suite, and the alkali suite (Table 1.8). Mare basalts have relatively high iron values and come in three distinct series depending on their Ti concentration (in the form of ilmenite): high-Ti basalts, low-Ti basalts, and very low-Ti basalts.

	Plagioclase	*Pyroxene*	*Olivine*	*Ilmenite*
Anorthosite	90%	5%	5%	0%
Norite	60%	35%	5%	0%
Troctolite	60%	5%	35%	0%
High-Ti basalt	30%	54%	3%	13%
Low-Ti basalt	30%	60%	5%	5%
Very low-Ti basalt	35%	55%	8%	2%

Table 1.8: Mineral composition of highlands and mare basalts.

Figure 1.9: Sample of anorthosite (igneous rock mostly composed of plagioclase and forming the light-toned lunar highlands).

The top of the Moon crust is highly fragmented into small particles due to the constant bombardment by meteoritic activity. This surface layer is known as the regolith. Its thickness varies depending on the age of the surface: from 3-5 meters in maria, up to 10-20 meters in highlands. Underlying the regolith is less finely grained layer referred to as the megaregolith. The size of fragments progressively increases with depth, until reaching the bedrock. Due to the absence of atmosphere, the dust produced at a location is not much transported (except by subsequent meteoritic bombardment) and is therefore representative of the bedrock it is originating from.

Stakes of gamma ray spectroscopy for lunar science

Like for Mars, the elemental composition of the surface of the Moon is needed to understand its formation and evolution. Prior to Selene, many observations contributed to constraining the composition of the Moon, both remotely and with the help of samples as described in the previous paragraph. Several of these observations were made during the flyby of the Moon by spacecraft carrying gamma ray and neutron spectrometers. However it was not until Lunar Prospector that such instruments did orbit the planet, allowing global mapping.

Lunar Prospector carried both a gamma-ray spectrometer (GRS) and a neutron spectrometer (NS). The GRS, consisting of a cylinder of bismuth germanate (BGO), provided global maps of the major element (Si, Fe, Ti, and perhaps Mg, Al, and Ca) and trace element (U, Th and K) composition of the lunar surface. The NS consisted of a matched pair of ^{3}He gas proportional counters, one of which covered by a 0.63mm thick sheet of Cd and responding only to epithermal neutrons, and the other covered by a 0.63mm thick sheet of Sn and responding to both thermal and epithermal neutrons. This system allowed sorting out thermal and epithermal neutrons. Special emphasis was placed on the search for polar water-ice deposits as implied by the H abundances [Feldman et al., 1999].

The Selene mission carries a more efficient type of GRS than the scintillator of Lunar Prospector. The detector consists of a germanium crystal that will allow obtaining very high energy resolution, granting a chance to identify additional chemical elements to those already identified with the Lunar Prospector GRS [Hasebe et al., 2008]. Although this instrument is not expected to harvest revolutionary science facts in comparison to its predecessor, it is of primary importance from the technological point of view. This instrument is indeed the first Japanese gamma ray spectrometer and also the first Ge crystal flown to the Moon.

The Moon is a very good laboratory for testing remote sensing techniques (crater counting, different types of spectrometry…) before using them for other bodies of the solar system. First, the proximity of the Moon makes it very convenient to reach. Then the possession of samples (Apollo missions and meteorites) provides ground truth that can compare to the orbital measurements. Finally the absence of atmosphere and the constant gardening operated by micrometeorites bombardment that homogenizes the surface materials makes it a relatively simpler object of study (in comparison to other bodies of the solar system).

Chapter 2　Constraints on the composition of the Martian surface provided by the Mars Odyssey Neutron Spectrometer

Among the many objectives pursued by Mars Odyssey, determining the composition and more specifically the abundance in hydrogen is of primary importance. Over the last few years, consigns of NASA regarding the exploration of Mars have been quite explicit: "Follow the water!" Neutron spectroscopy's capability to detect hydrogen, as long with that of other volatiles, such as carbon dioxides in the Martian context, is well known. The goals of the neutron spectrometer were not restricted to measuring the abundances of these two elements over the planet, but also included determining the depth at which the water lies.

Chapter 1 exposed the principle of neutron spectrometers, and how they could detect neutrons leaking outward a planetary surface, providing their energy in addition to their counts. The present chapter will now explain how information about the chemical composition of the planetary surface can be inferred from these measurements. Before being interpreted in terms of water abundance, and then water depth, neutron data have to undergo proper data reduction. Most of the data (Mars Odyssey is still acquiring measurements to date) had already been processed when the present work started. However, an in-depth understanding of the data, and of all corrections applied to it, is compulsory before any interpretation of its content can be drawn. In addition to this necessary step, the knowledge so far acquired on the red planet helps to assess the quality of the information extracted from the measurements, and thus to determine the limitations of our dataset.

After a short presentation of the scope of the Mars Odyssey mission and most particularly of the Neutron Spectrometer, this chapter presents in detail the data reduction, which consists in all corrections and manipulations that have been applied to the dataset. A third part shows how to obtain abundances of hydrogen deposits and their depth on the basis of the neutron dataset. Besides, a detailed assessment of the limitations of the results is performed. The composition appears to play a strong role in the process of constraining the water depth. This observation invited to explore what abundances in chemical elements other than hydrogen could be extracted from the dataset. The problem being too complex to be solved on the global scale, a hydrogen depleted region was analyzed: the Central Elysium Planitia. A fourth part presents the results of this analysis, how they compare to other datasets, and how to reconstitute a scheme of the processes at stake in this region.

2.1 Scope of the Mars Odyssey Neutron Spectrometer mission

2.1.1 The Mars Odyssey mission

Launched on April 7th 2001, Mars Odyssey was originally designed for a prime mission of 917 days. The mapping phase started on February 19th 2002. Due to the availability of spacecraft resources, the prime mission was extended to achieve communications relay for the Mars Exploration Rovers and science observations. The spacecraft was injected on a near circular orbit by aerobraking. The average height of the satellite is 400 km (370 to 432 km because of eccentricity) and the inclination 93 degrees.

The science objectives of this mission are to: globally map the elemental composition of the surface, determine the abundance of hydrogen in the shallow subsurface, acquire high spatial and spectral resolution images of the surface mineralogy, provide information on the morphology of the surface, and characterize the Martian near-space radiation environment as related to radiation-induced risk to human explorers.

Instrument	Description
THEMIS (Thermal Emission Imaging System)	Determines the mineralogy of the Martian surface using multispectral, thermal-infrared images that have 9 spectral bands between 6.5 and 14.5 µm. Also acquires visible-light images with 18 m pixel resolution in either monochrome or color.
GRS (Gamma Ray Spectrometer)	Performs full-planet mapping of elemental abundance, at a spatial resolution of about 600 km, by remote gamma ray spectroscopy, and full-planet mapping of H (with depth of water inferred) and CO_2 abundances by combined gamma ray and neutron spectroscopy.
MARIE (Martian Radiation Environment Experiment)	Measures the accumulated absorbed dose and tissue dose rate as a function of time, determines the radiation quality factor, determines the energy deposition spectrum from 0.1 keV/µm to 40 keV/µm, and separates the contribution of protons and of high energy particles to these quantities.

Table 2.1: Mars Odyssey Instruments [adapted from Saunders et al., 2004].

The payload consists in a Gamma Ray Spectrometer (GRS), a multi-spectral Thermal Emission Imaging System (THEMIS) and a radiation detector, the Martian Radiation Environment Experiment (MARIE) (see Table 2.1). The position of these instruments on the spacecraft is shown in Figure 2.1. At the exception of the gamma sensor head that is located on a 6 m boom, all instruments are sitting on the spacecraft bus.
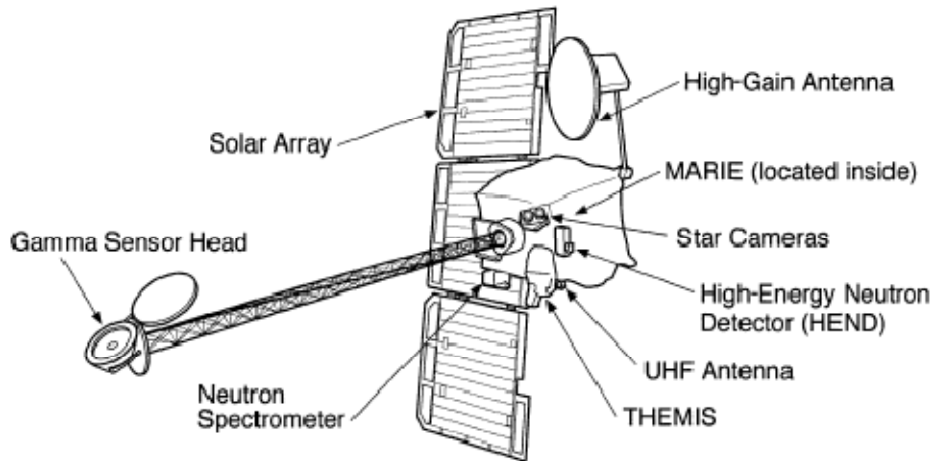
Figure 2.1: Scheme of the Mars Odyssey spacecraft in mapping configuration [extracted from Saunders et al., 2004].

The GRS suite of instruments includes the Gamma Ray Subsystem [Boynton et al., 2002], the Neutron Spectrometer [Feldman et al., 2002b] and the High Energy Neutron Detector [Mitrofanov et al., 2002]. The instruments work together [sic] to measure the currents of neutrons and fluxes of gamma rays produced by the interaction of galactic cosmic rays with planetary material. The neutron instruments have a greater sensitivity to low amounts of hydrogen whereas the gamma ray spectrometer is sensitive to small differences in hydrogen content when hydrogen is very abundant [Boynton et al., 2004].

THEMIS investigates the surface mineralogy and physical properties of the Martian surface. THEMIS is mapping the entire planet in both day and night multi spectral infrared images. Its spectral coverage allows detecting numerous geological material including carbonates, silicates, sulfates, phosphates and hydroxides. THEMIS follows the Mars Global Surveyor Thermal Emission Spectrometer (TES) and Mars Orbiter Camera (MOC), providing higher spatial resolution infrared multispectral images and regional visible images at scales intermediate between Viking and MOC [Christensen et al., 2004].

MARIE was designed to measure the radiation levels at Mars including the contributions of protons, neutrons and heavy ions. It acquires energy spectra of the galactic cosmic ray and solar energetic particles within the energy range from 15 to 500 MeV/n. Constraining the propagation and radial dependence in the Earth-Mars space is an important prerequisite to human exploration [Badhwar et al., 2004].

2.1.2 The Mars Odyssey Neutron Spectrometer (MONS)

The MONS detector consists of a cubical block of boron-loaded plastic scintillator [Boynton et al., 2004]. It is segmented into four prism-shaped quadrants as shown in Figure 2.2. The prism segments are optically isolated from one another, and each is viewed by a separate 3.8 cm diameter photomultiplier tube (PMT). Both ends of the scintillator assembly are covered with a 0.069 cm thick sheet of cadmium to shield

the ends of all prisms from thermal neutrons coming from those directions. In addition, the downward looking prism has its face covered by another cadmium sheet so that it only responds to neutrons having energies larger than about 0.4 eV, which corresponds to the epithermal and fast neutron energy ranges.

Neutrons lose energy in the neutron detector through multiple elastic scattering collisions with the hydrogen and carbon nuclei that comprise the scintillator. Most of the energy is lost to proton recoils because protons and neutrons have close to the same mass and the cross section for (n,p) scattering is about four times larger than that for (n,^{12}C) at low energies. As the recoil protons slow down in the scintillator, they produce multiple ion-electron pairs that eventually recombine to produce photons.

Collection of these photons by the PMTs produces pulses of charge that are then amplified and digitized by the neutron detector analog electronics to generate histograms. If the neutrons deposit all of their energy in the scintillator, they will eventually be captured by a ^{10}B nucleus to produce a second pulse in the electronics. Although the Q-value of the ^{10}B(n,α)^{7}Li reaction is about 2.8 MeV; 478 keV of this energy goes to the gamma-ray de-excitation of the first excited state of ^{7}Li, which is populated 94% of the time in this reaction, and the remaining 2.3 MeV is split between the α and ^{7}Li recoils.

The sequence of events just described, is shown schematically in the upper part of Figure 2.2. The signature of a thermal or epithermal neutron in the scintillator, is therefore a single pulse that has an amplitude that is characteristic of the ^{10}B(n,α)^{7}Li reaction. The signature of a fast neutron that has lost all of its energy in the scintillator is a time-correlated double pulse. The amplitude of the first pulse provides a measure of the energy of the neutron and that of the second pulse is the same as that for a thermal or epithermal neutron.

The orientation of the outward normals to each of the four prism elements of the neutron spectrometer is shown in Figure 2.2. One face will view forward, one backward, one downward and one upward. Separation of the thermal and epithermal components is possible using the relative counting rates of the forward and backward-directed prisms and a Doppler-filter technique [Feldman and Drake, 1986].

Such a separation is made possible by the fact that the Mars Odyssey spacecraft travels faster (3.4 km.s^{-1}) than a thermal neutron (2.2 km.s^{-1}) while in mapping orbit. The forward directed prism therefore scoops up thermal neutrons and the backward directed one will outrun them. The difference in counting rates between forward- and backward-directed faces thus yields a measure of the flux of thermal neutrons. A measure of epithermal neutrons is provided by the downward facing prism because it is completely shielded from the outside by sheets of cadmium and the other three prisms.
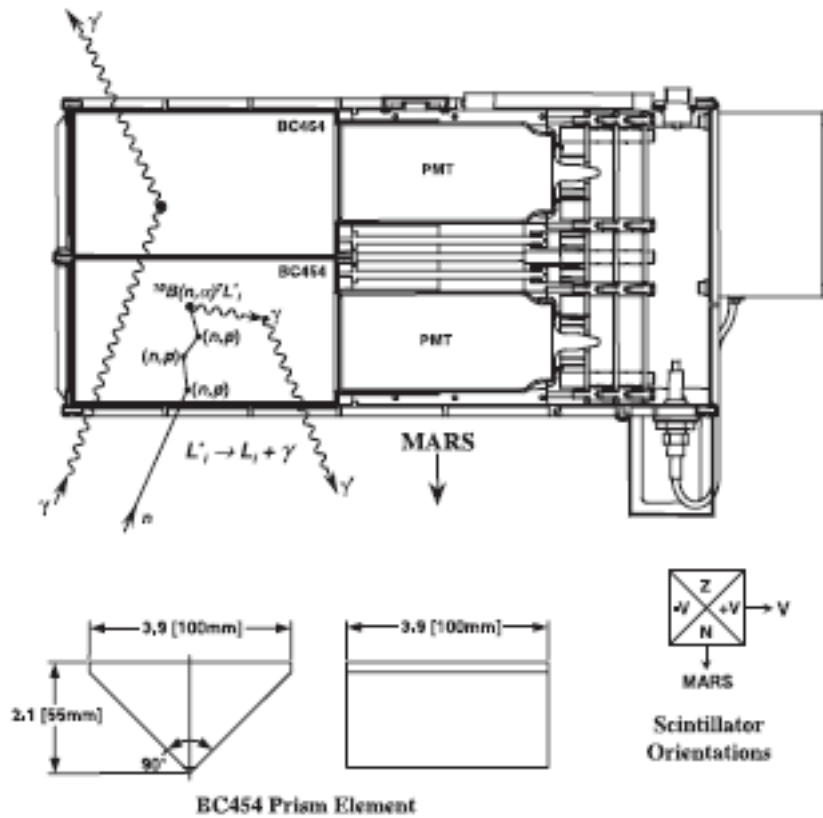
Figure 2.2: Drawing of the GRS neutron spectrometer sensor head.

The neutron dataset

Three codes have been developed to reduce raw data measured using MONS, to thermal, epithermal, and fast neutron counts per second. The reduction of neutron data consists in all steps allowing the transformation of raw counting rates collected by the instrument into mapping of neutron emission in different energy ranges, and eventually, mapping of hydrogen content of the top ~meter of Mars.

The first was written by Tokar and was used for the initial discovery articles [Tokar et al., 2002]. The next was written by T. Prettyman [Prettyman et al., 2004a, 2004b], and was used for all articles published through 2004. This code is used to deliver Level 1 Derived Neutron Data (DND) to the PDS. It consists of time series of corrected neutron counting data that can be used for scientific investigations. The Level 1 data set also includes Averaged Neutron Data (AND), which consists of maps of neutron counting rates determined from DND time series data. The last code, written by S. Maurice, produced the dataset to be used here. It has been used for all publications that included the LANL team as coauthors, after 2004.

2.2 Reduction of neutron data from Mars Odyssey

2.2.1 Overview of the data reduction

Data available at the different levels of processing

To organize the entire data reduction procedures for neutrons, different levels of processing have been defined. Level 0 comprises all science and housekeeping data returned by the spacecraft. Data consist of a set of time records with a 19.75 sec resolution time baseline. Level 0 data are binary packets, formatted on board the spacecraft and relayed to the Los Alamos National Laboratory through the NASA Ames Research Center.

For level 1 data, corrupted and unusable records have been removed. Additional information also has been introduced to level 1 data, such as spacecraft position (altitude, latitude, longitude). At level 2, data have been corrected for observational biases and the response function of the instrument. In addition, several normalizations have been made to obtain normalized counting rates. Within levels 0-1-2, the data remain organized sequentially with time. Finally, level 3 data contain parameters that have been summed and mapped onto Mars.

Two categories of events are recognized by the front-head electronics [Feldman et al., 2002a]. A category 1 event is a first scintillator interaction having energy in the range 40 keVeq < E1 < 630 keVeq (equivalent light output) that is not followed by a second interaction within 25.6 ms. Another characteristic is that the interaction should be registered in only one or two prism segments of the neutron sensor. Any prompt interaction having energy greater than 2.55 MeVeq (regardless of the number of sensor elements that register energy above threshold) will be identified as a galactic cosmic ray (GCR). After detection, no second interaction is looked for, and the event is counted in a dedicated GCR scaler.

A category 2 event is a prompt scintillator interaction having energy in the range 40 keVeq < E1 < 2.55 MeVeq that deposits energy in one or two prism segments only and that is followed by a second interaction that is detected in one or two prism segments within a 25.6 ms gate window beginning with the time of the first interaction. The second interaction must have energy in the range 40 keVeq < E2 < 630 keVeq. Any event that does not satisfy these criteria is ignored but is nevertheless accounted for in a dedicated dead-time counter.

For every category 2 event identified by onboard classification firmware, information used in the present study to determine the energy spectrum of fast neutrons aboard Mars Odyssey consist of (1) a 5-bit prompt Analog to Digital Converter (ADC) address, (2) a 6-bit delayed ADC address, (3) a 4-bit prompt interaction sensor ID, (4) a 1-bit delayed interaction sensor ID, and (5) an 8-bit digitized time to second pulse. The prompt and delayed ADC addresses give the pulse height of the prompt and delayed interactions, respectively. Each of the four prompt interaction ID bits identifies a unique prism that detects energy deposition above threshold. Only one or two prisms are allowed for analysis. The delayed ID bit identifies only whether the second interaction occurred in one or two prisms. Here again, three- and four-prism events are rejected by the onboard event classifier. Event-mode data consist of the first 84 3-byte events in

each accumulation time interval. All succeeding events are counted without recording details of the separate interactions.

To build up our Level 0 data, we collect: the initial time series counting rates and additional information about the collection of this data. Data have been collected through two different modes: events mode and category 1 mode. Category 1 is also referred to as the histogram mode. For each prism the counts are collected during an integration time of 19.75 seconds and shared in 64 channels that correspond to different energy levels. The acquired spectra (see Figure 2.3) are merged into (4,64)-sized tables of integers. The events mode collects the history of events. For each measurement are collected: the detection of an interaction, the prism concerned by the interaction, the type of interaction (first or second interaction). The resulting information is coded in 252 bits.
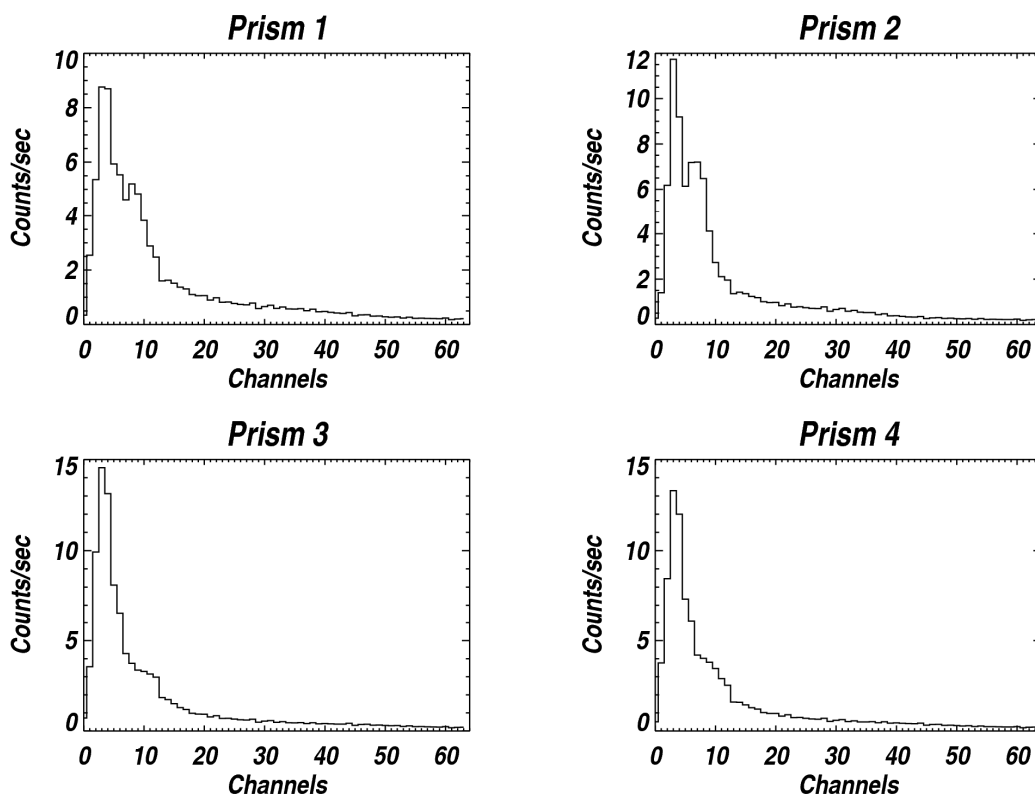

Figure 2.3: Histogram of counts in prism 1, 2, 3 and 4 averaged on measurements acquired during 1st term of 2003 and normalized in counts/sec.

The support data include a time baseline (coordinated universal time (utc) plus time in Julian and martian days), orbital information (longitude, latitude, height of satellite), satellite attitude information and proxies of the measurement quality (amount of dead time during measurement, galactic cosmic ray intensity). The data is formatted into IDL structures that contain: a header, data and orbital information. The variables contained by these three categories are displayed in Table 2.2.

	Variable	Type	Description
header	pixel	integer	number of pixel associated
	orbit	integer	number of orbit
	UTC	byte array (24)	UTC time
	jtime	float	Julian time
data	dead_cnt	integer	dead time count
	gcr_cnt	integer	galactic cosmic ray count
	cat2_cnt	integer	
	events	byte array (252)	byte coded information on events
	cat1_hist	integer array (64,5)	count rates in the 64 channels for each four prism + over load
orbit	latitude	float	latitude [-90°, 90°]
	longitude	float	longitude [0°, 360°]
	altitude	float	altitude of spacecraft above reference radius in km [386, 456]
	scpos_mars	float array (3)	spacecraft position
	instrboresite_mars	float array (3)	instrument pointing direction
	mars_sol	float	longitude of Mars on solar orbit
	day_index	integer	day since beginning of mission
	local_hour	integer	hour in the day
	local_min	integer	minute in the day
	pointing	byte	boolean telling if spacecraft is pointing towards Mars
	intersecting	byte	boolean

Table 2.2: Summary of available variables.

Data reduction scheme

The transformation from level 0 to level 1 consists of checking for corrupted data. Records that are obviously erroneous are removed. We proceed in applying flags to the measurements that are considered unfit: during Solar Energetic Particle (SEP) events, when the overload channel (which records the most energetic events) has significantly higher values than usual or when the nadir spacecraft is pointing off Mars. Once these anomalies are identified, the data is reformatted without them. This operation is performed while respecting the homogeneity of data: when one point is corrupted, other data at the same time are also removed in order to keep a single time baseline for the whole dataset.
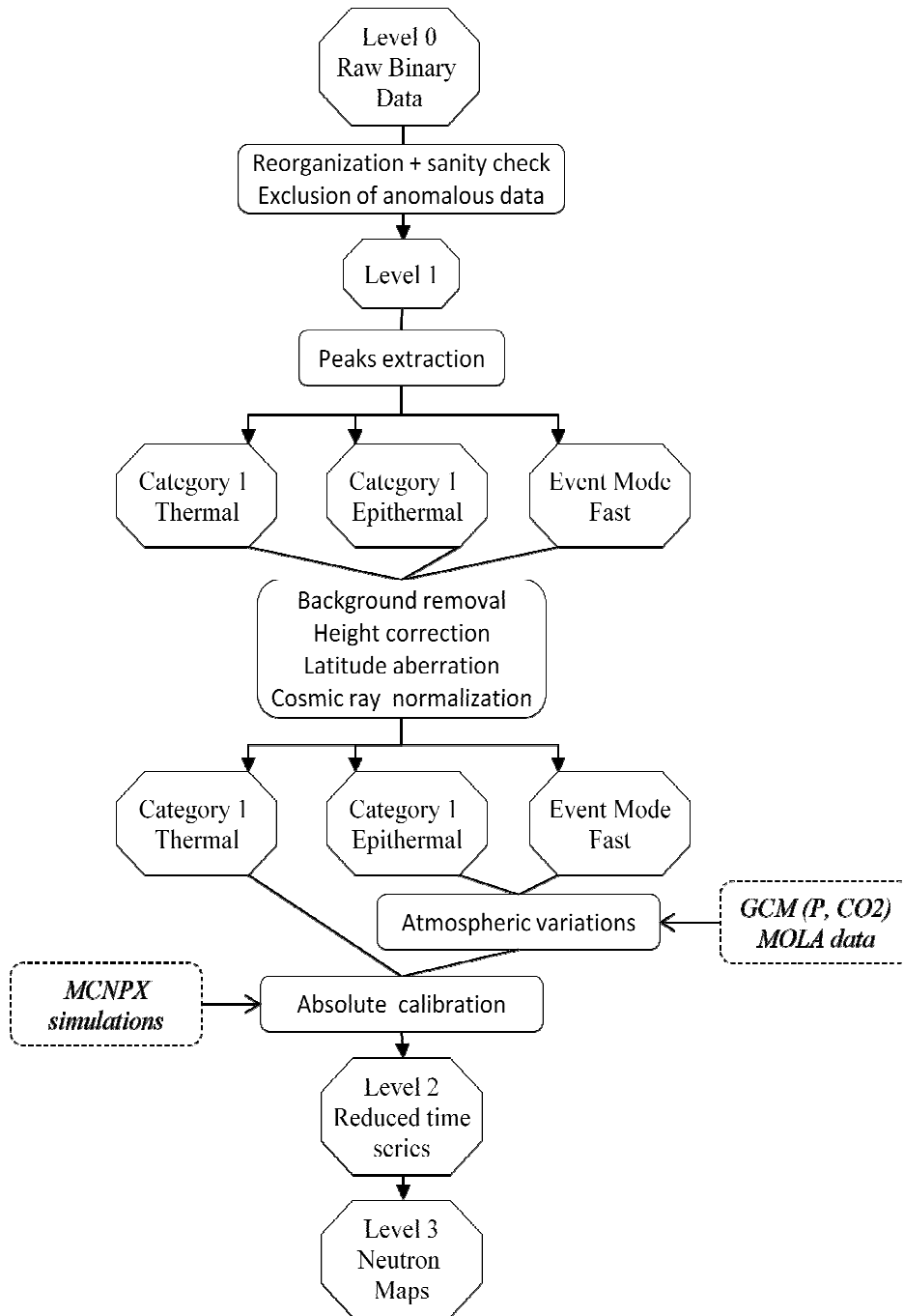
Figure 2.4: General scheme of data reduction from level 0 to level 3.

Passing from level 1 to level 2 includes a higher number of actions. The first step is the extraction of the peaks in the spectra. This operation is performed with different methods regarding the type of data considered: category 1 or events mode. The objective is to isolate the counts in three energy ranges: thermal, epithermal and fast. It can be done through use of the event mode in prism 1 (fast), category 1 mode in prism 1 (epithermal) and a combination of category 1 in prism 2 and 4 (thermal). The transformation from level 1 to level 2 also requires a number of corrections: background removal, satellite height correction, removal of latitudinal aberrations, cosmic ray normalization, correction for atmospheric variations, and final normalization.

42

After all these operations, we have time series of the neutron data corrected for all observational biases and normalized. The transformation from level 2 to level 3 consists in mapping these time dependent data onto Mars. That implies associating the latitude and longitude of a measure to a pixel on the planet. In addition to gridding the data with a resolution of 2 degrees, the maps are convolved with a Gaussian function to smooth the data at the resolution of the instrument. All the steps previously described are summed up in Figure 2.4.

2.2.2 Initial Processing

Solar Energetic Particle (SEP) events

Events	Start	Stop
1	2002-03-13 21:00	2002-03-18 12:24
2	2002-03-11 00:27	2002-03-20 07:59
3	2002-04-17 10:32	2002-04-19 10:56
4	2002-04-22 16:31	2002-05-02 17:46
5	2002-05-21 19:29	2002-05-28 21:45
6	2002-07-15 20:04	2002-07-27 12:58
7	2002-07-30 16:12	2002-08-06 17:15
8	2002-08-16 10:00	2002-08-19 08:57
9	2002-08-27 00:38	2002-08-30 01:34
10	2002-09-06 04:39	2002-09-08 06:23
11	2002-10-14 11:35	2002-10-18 02:43
12	2002-10-25 02:52	2002-11-03 19:37
13	2002-12-02 21:44	2002-12-04 16:11
14	2003-03-18 12:24	2003-03-21 11:21
15	2003-05-29 18:56	2003-06-02 03:50
16	2003-10-26 18:00	2003-11-25 00:00
17	2003-12-02 12:00	2003-12-05 06:00
18	2004-07-06 00:00	2004-07-11 18:00
19	2004-08-09 00:00	2004-08-12 12:00
20	2004-09-05 18:00	2004-09-16 06:00
21	2004-11-10 18:00	2004-11-18 18:00
22	2005-01-18 00:00	2005-02-03 18:00
23	2005-05-13 12:00	2005-05-19 18:00
24	2005-06-16 12:00	2005-06-21 06:00
25	2005-07-14 08:00	2005-08-05 12:00
26	2005-08-22 06:00	2005-09-26 12:00
27	2006-11-03 18:00	2006-11-05 12:00
28	2006-11-06 18:00	2006-11-09 00:00
29	2006-12-06 00:00	2006-12-21 00:00
30	2007-01-25 00:00	2007-01-27 00:00

Table 2.3: List of SEP events recorded.

Two processes are implemented to get rid of SEP events contaminated data. The first one consists in identifying the data obviously corrupted. We use the GCR count rates to visualize the time intervals where the instrument saturates. This proxy indeed records energetic particles regardless of their origin: galactic or solar. Figure 2.5 displays this counter during the second term of 2002. Windows of time are defined manually to be excluded from measurements. In the example displayed, one time interval has been identified. All measurements within this period are removed from datasets. The second process consists in setting boundary limits to the galactic cosmic ray counts. An average value of galactic cosmic ray counts is calculated. The maximum is set at 1.2 times this average value and the minimum at 0.8 times. All records outside the window thus defined are thrown away.
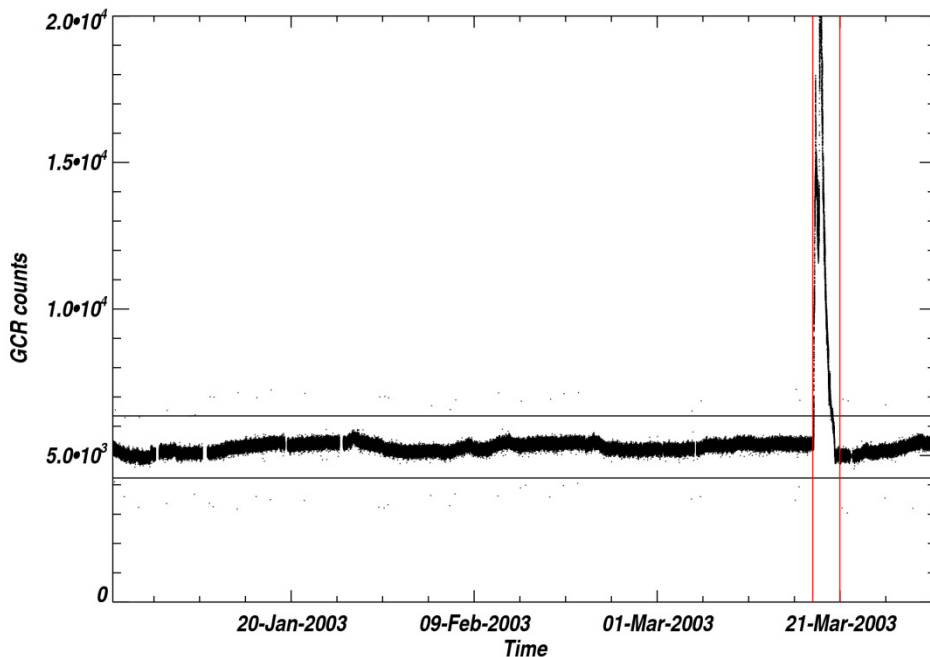

Figure 2.5: Galactic cosmic ray count rates during 1st term of 2003. The vertical colored lines indicate manually defined windows. The horizontal black lines indicate the window defined by [0.8 mean GCR, 1.2 mean GCR].

Off limits

Occasional out-of-range data can be observed in the dataset. The major part of them corresponds to SEP events, but other reasons can cause measurements to be anomalously high, such as variations of the instrument gain. The corresponding records are distributed randomly within the dataset. In order to track them, the sum of the channels is calculated for each prism. A limit is set over which all records are removed from dataset, as represented on Figure 2.6. The total amount of records concerned represents 7.5% of initial data. However only a very small fraction of the data excluded (0.18%) does not coincide with data acquired during SEP events.
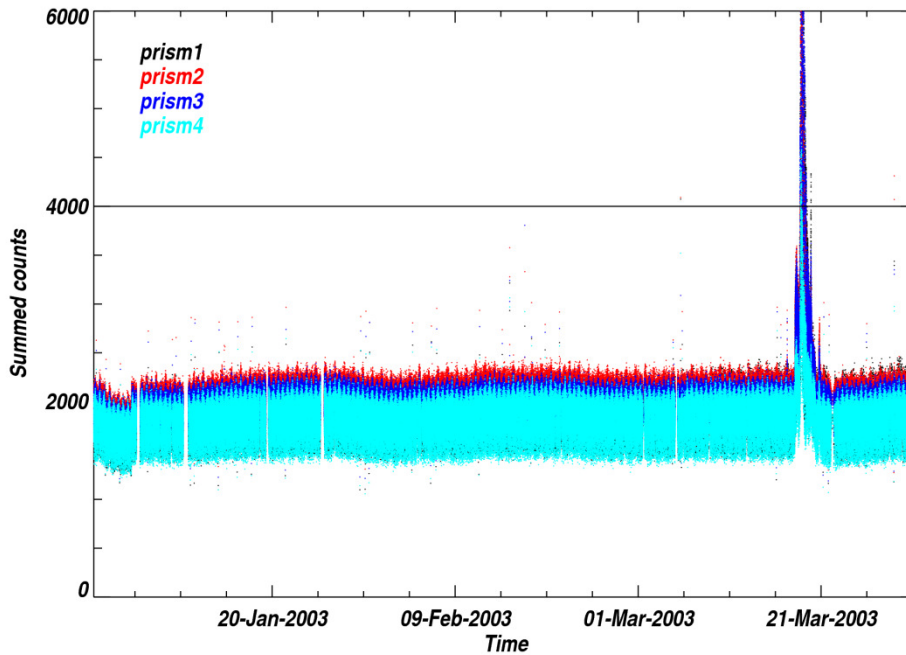
Figure 2.6: Sum of counts in the 64 channels for each prism during 1st term of 2003. The horizontal line represents the upper limit authorized.

Spacecraft orientation anomalies

A very simple test to assess the data consists in checking that the spacecraft attitude was compatible with the measurement. It implies that the instrument is oriented towards the planet. Three different processes are implemented to get rid of anomalies. First, data deprived of orientation information are flagged. Another method consists in using the boolean *intersect* (see Table 2.2 for definition) which tells for every record whether the spacecraft is pointing at the planet or not. And finally, the angle between the pointing direction of the instrument and the spacecraft-Mars direction is calculated. All records whose angle is greater than 0.2 rad are flagged. This routine is redundant with the second process most of the time, except in cases where the satellite is not completely pointing out of Mars, but is still far from the nominal measurement point.

Anomalous dead time

After the different operations described, one last analysis of the data is performed in order to look for anomalous records. The dead time counter measures the fraction of time where no action can be recorded. Dead time occurs when an event has just been recorded and is due to the fact that the electronics cannot instantaneously record another event. When the number of events increases, dead time can get quite high, inducing many counts to get lost. Figure 2.7 displays the histogram of dead time recorded during first term of 2003. A routine has been implemented to remove all records that belong to the wings of this histogram. The residual data has a dead time comprised between 90 and 140 µs. In regard to the integration time (19.75), that interval represents only 0.5 to 0.7 %. Therefore it was decided that the removal of extreme points was sufficient and no additional correction has been performed.
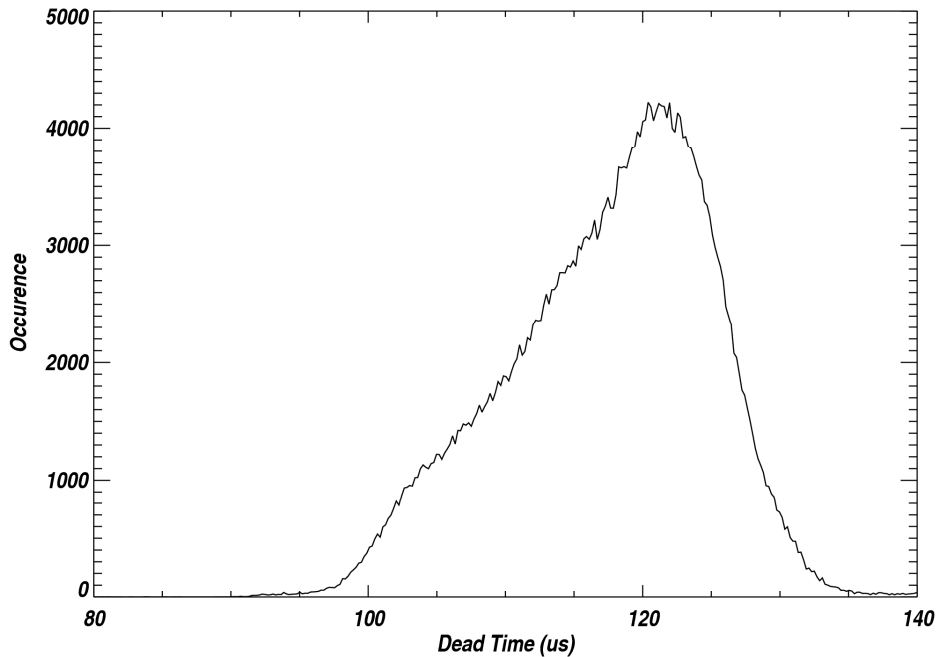
Figure 2.7: Histogram of dead time in µs during 1st term of 2003.

Summary

All these steps led to flagging data for different anomalies. The number of records treated for the four different operations presented: SEP events, off limits, orientation and dead time is presented in Table 2.4. The reader might notice that the total percentage of corrected points does not equal the difference between final and initial number of records. A same record can indeed be flagged for different reasons. In the end, a common flag is assigned to the data to identify all unwanted records.

	Number of records	Percentage of initial
Total time interval	7769438	
Initially available	7693063	99%
Total SEP	980096	12.7%
Number of SEP windows	30	
SEP Manually rejected	466186	6.1%
SEP Automatically rejected	513910	6.7%
Off limits	307017	4.0%
Total orientation	83263	0.9%
No pointing information	68931	1.1%
Not intersecting Mars	73665	1%
Bad orientation	9508	0.1%
Dead time	211	0.003%
Finally available	6756941	87.8%

Table 2.4: Summary of the number of records flagged by the different operations while processing from level 0 to level 1.

2.2.3   Peak extraction of event mode

2nd interaction

The data collected in the event mode is analyzed in order to decode the different events registered by the instrument. The event mode contains details about every recorded event. It is used to determine the fast neutron count rates. The signature of a fast neutron is a time correlated double pulse. The amplitude of the first pulse provides a measure of the energy of the neutron and that of the second pulse is the same as that for a thermal or epithermal neutron. The event mode records these pulses in separate channels. The first and second interaction can therefore be analyzed separately.

Time-correlated double pulses can also occur when cosmic rays interact with the plastic scintillators. These pulses can distort the shape of the fast-neutron spectrum if they are not eliminated. They are caused when an energetic particle deposits energy in the plastic, causing a large pulse of light. The associated photomultiplier tube can emit a characteristic "after pulse" caused by the production of secondary electrons through the impact of ions on the photocathode, dynodes, or the residual gas in the tubes. The drift of ions occurs on the time scale of the neutron die-away time. So, time discrimination is ineffective in suppressing these events. However, the second pulse is usually well below the pulse height of the ^{10}B(n,α) peak, and setting a lower level threshold is sufficient to eliminate after-pulsing.

As a first step, the original information stored in the 252 - byte array corresponding to the second interaction is reformatted into an individual 64 - integer array for each prism. The spectra thus reconstituted are shown in Figure 2.8. Spectra contain a low energy peak associated with after-pulsing, a peak at 93 keV associated with the recoil of the reaction products following neutron capture by ^{10}B, and a continuum which is caused by additional energy deposition by the 478 keV gamma ray produced by the decay of ^{7}Li* produced by neutron capture on ^{10}B. The relatively low continuum underneath the 93 keV peak enables accurate determination of the peak centroid.

The signal to noise ratio of a spectrum acquired during a single time interval is not sufficient to allow peak integration. Therefore we process spectra summed over 360 measurements. The main goal of the analysis of the second interaction is to identify the channels contaminated by after pulse. In order to determine the threshold between the after pulse and the signal due to capture of neutron by ^{10}B, we fit this latter peak by a Gaussian function and extract a threshold value of this fit valid for the 360 measurements analyzed. The Gaussian function is searched under the form:

$$f(x) = A\,e^{-\frac{1}{2}\left(\frac{x-B}{C}\right)^2} + D + Ex$$

After this operation (shown in Figure 2.9), only the center of the peak is kept for future use.
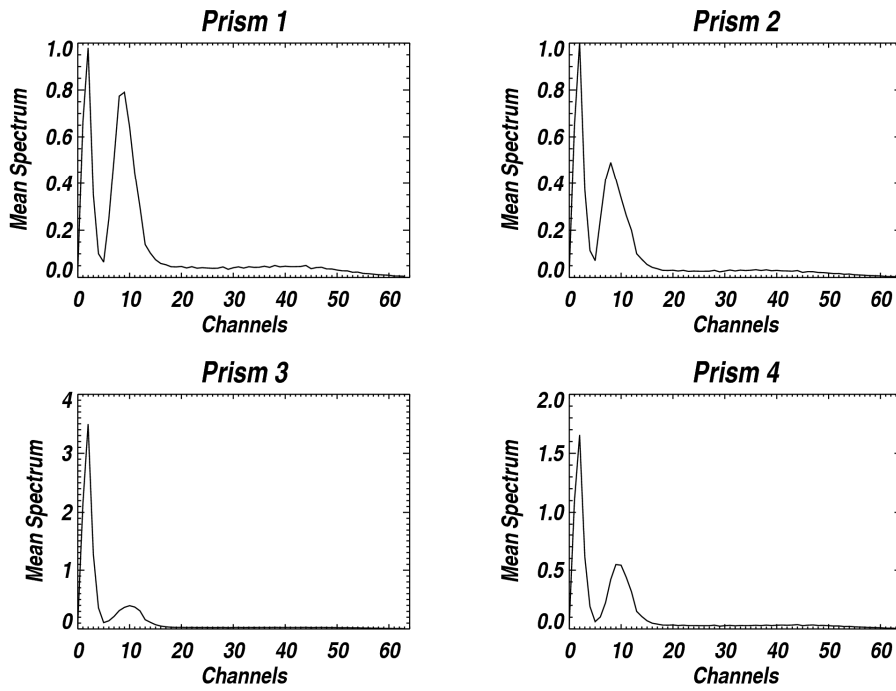
Figure 2.8: Spectra of second interactions in prism 1, 2, 3 and 4 averaged on measurements acquired during 1st term of 2003.
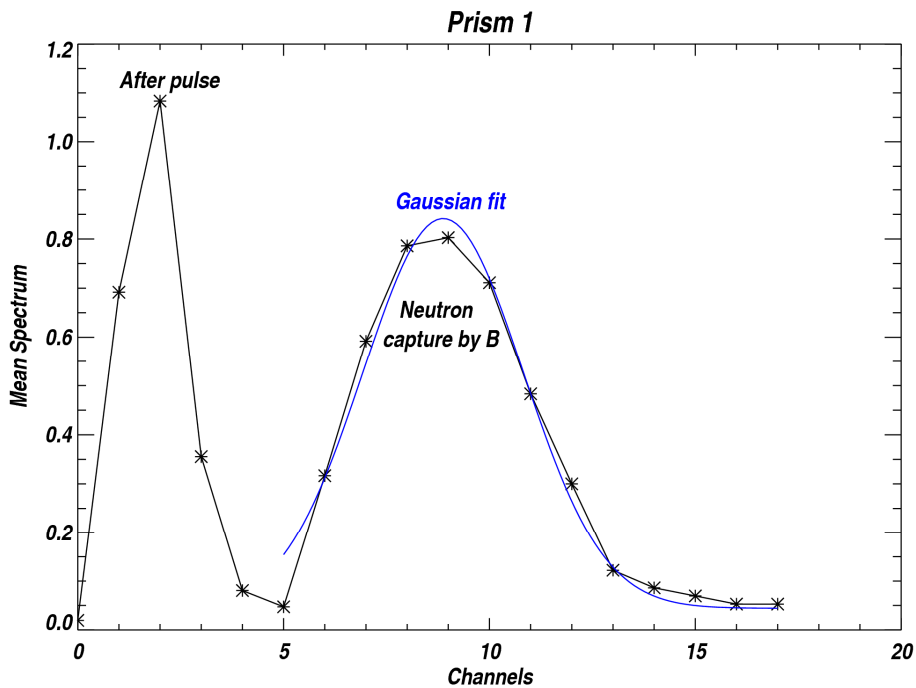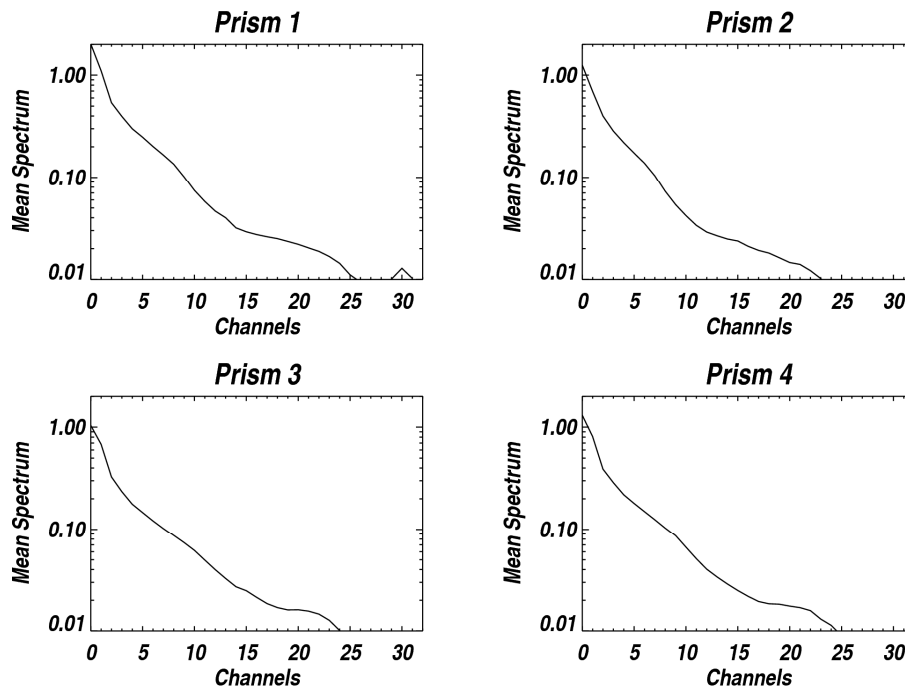

Figure 2.9: Spectrum of second interactions in prism 1 summed over the 360 first measurements of 1st term of 2003. In blue is represented the Gaussian function that fits the second interaction peak.

48

1st interaction

We process the first interaction as the second one: the original information stored in the 252 - byte array corresponding to the first interaction is reformatted into an individual 64 - integer array for each prism. However we need to remove the channels contaminated by after pulse. We set the energy lower level threshold 3 channels before the center of the peak previously determined. All channels under this level are removed. The spectra thus reconstituted are shown in Figure 2.10.

Figure 2.10: Spectra of first interactions in prism 1, 2, 3 and 4 averaged on measurements acquired during 1st term of 2003.

The first pulse corresponds to the scattering of the neutron by the scintillator. The integration of the spectrum of the prism over the channels of the appropriate energy provides the fast neutron count rates. Any prism can be chosen to perform the calculation; however the use of the nadir pointing prism (prism 1) provides the simplest geometry and therefore the lightest corrections. We defined the lower energy limit to avoid counts that can interfere with after pulse. On the contrary the definition of the upper energy limit is arbitrary. Fast neutrons of more or less high energy can be collected. The choice of the upper limit is a compromise between collecting neutron of relatively high energy and degrading the signal to noise ratio. The higher the energy is, the higher the noise is. Therefore we decided to restrain our integration of the spectrum to 4 channels, which provides the best signal to noise ratio. The integration consists in summing the counts in the channels as shown in Figure 2.11.
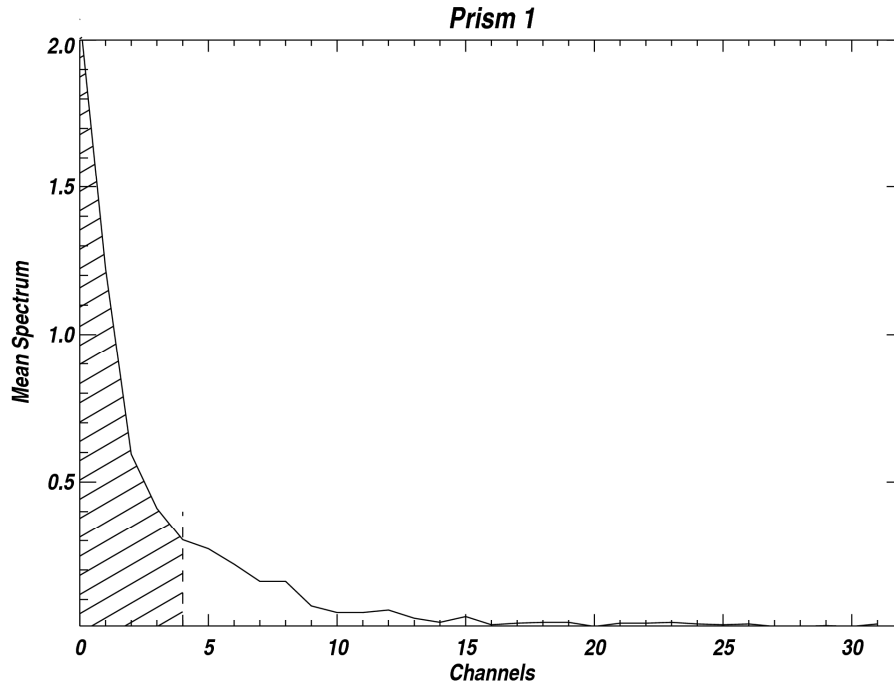
Figure 2.11: Spectrum of first interactions in prism 1 summed over 360 first measurements of 1st term of 2003. The hatched zone provides the fast count rates.

2.2.4 Peak extraction of category 1

ADC (Analog-Digital Converter) correction

The Category 1 data for each prism consists of a 64 channels pulse height spectrum which contains a peak at 93 keVeq corresponding to the capture of a neutron with energy less than about 700 keV by ^{10}B. This mode is used to determine the count rates of epithermal (determined through use of prism 1) and thermal neutrons (determined through use of prism 2 and 4). Figure 2.12 displays the spectrum obtained within prism 1 during 1st term of 2003. Underneath the peak is a background continuum caused by the interaction of gamma rays originating from Mars and the spacecraft as well as by Compton scattering and escape of the 478 keV gamma ray produced by the decay of ^{7}Li*, which is produced by neutron capture on boron. Category 1 spectrum processing is done by extracting the net peak area from the spectrum.

The conversion of data from analog to digital introduces non linearities. A correction is applied to each spectrum to remove artifacts of the differential nonlinearity of the analog to digital converter from the spectrum. The differential nonlinearity was determined by averaging spectra from Prism 3 poleward of 85°N over a long time period. The correction coefficients calculated on the basis of these measurements are applied to the rest of the dataset. This operation is performed for each prism. The resulting spectrum for prism 1 is compared to the initial histogram in Figure 2.12. The delineation of the peak seems to be better after shifting counts that had been attributed to the wrong channels.
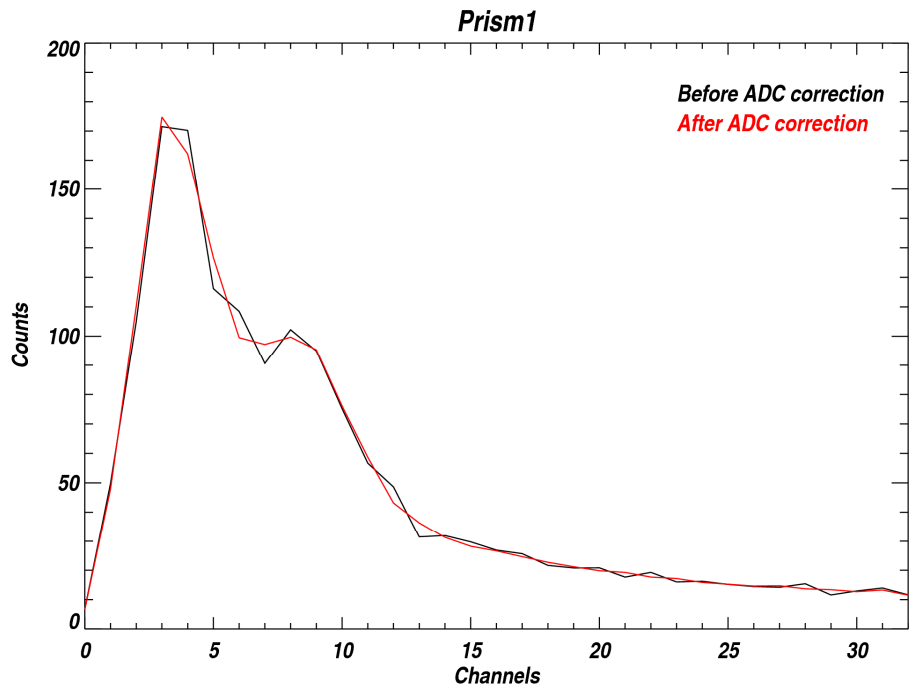
50

Figure 2.12: Histogram of counts in prism 1 averaged over 1st term of 2003. Superposed in red is the same histogram after ADC correction.
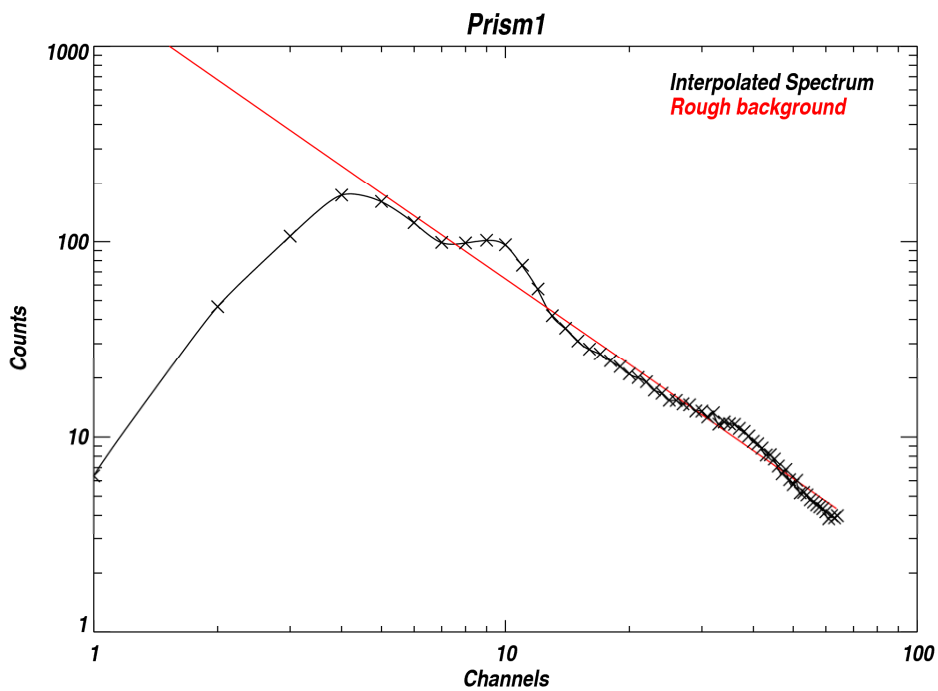

Figure 2.13: Histogram of counts in prism 1 summed over 360 first measurements of 1st term of 2003 in logarithm scale. Black crosses indicate the original counts and black line the interpolated function. Superposed in red is the rough background.

51

Determination of peak position

After applying the ADC correction, the next step consists in determining the position of the peak associated with the capture of neutrons by ^{10}B. Instead of trying to fit raw counts, we take the logarithm of the counts in order to simplify the calculations. As for the event mode, data are summed over 360 consecutive measurements in order to obtain sufficient signal to noise ratio to extract peak information. Besides, spectra are refined by spline interpolation to allow mathematical fit. An example of spectrum thus obtained is shown in Figure 2.13. The spectrum is the superposition of the capture peak and of a background.

The Gaussian fit is rendered difficult because of the orientation of the peak. In order to obtain a horizontal function, which is easier to fit, the linear fraction of the spectrum has to be removed. Background is calculated for the portion of spectrum following the maximum. At this step, we do not need a precise evaluation of the background so we perform a simple linear fit of the counts. The background thus determined (displayed in red in Figure 2.13) is subtracted from the spectrum, which rotates it to a horizontal position. The spectrum obtained is shown in Figure 2.14.
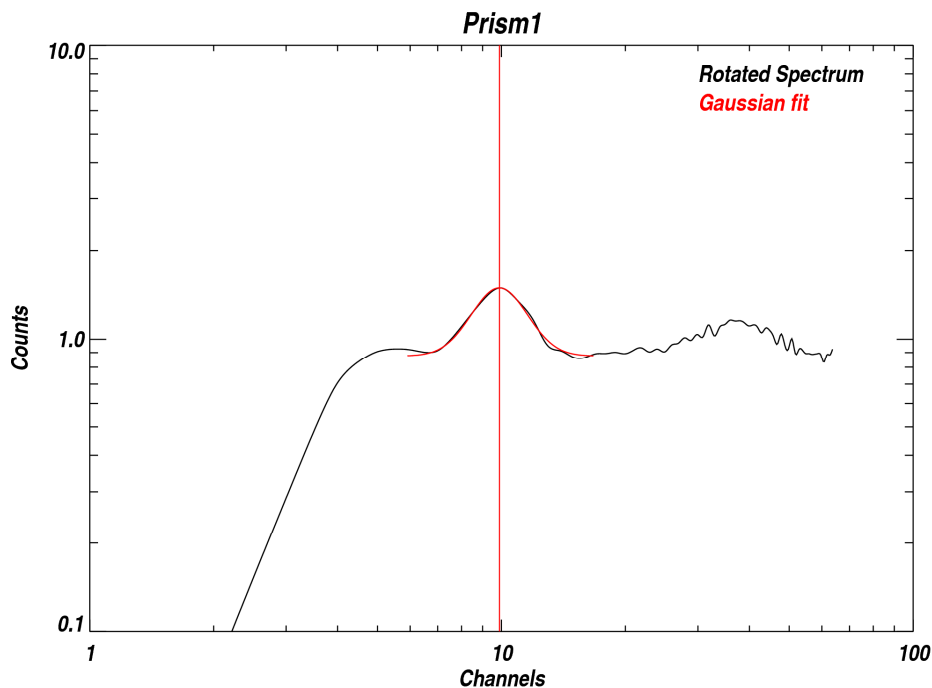

Figure 2.14: Histogram of counts in prism 1 summed over 360 first measurements of 1st term of 2003 with background subtracted in logarithm scale. Superposed in red is the Gaussian function that fits the peak. The line indicates the position of the peak.

Once the spectrum has been transformed by the described operations, the position of the peak can be determined. The spectrum displayed in Figure 2.14 shows that multiple regions of the signal can be interpreted as peaks by an automatic detection. Therefore we proceed cautiously in determining the position of the peak. The first step consists in detecting all local maxima within the spectrum. Those candidates are

52

submitted to Gaussian fit. A routine excludes the inappropriate peaks in agreement with arbitrary criterions. The standards are the following:

- Gaussian fit convergent
- Width of the Gaussian function within the interval [0.08, 0.2]
- Position of the center within 10% of a reference value
- Position of the center within 25 first channels

In spite of these selective conditions, several cases can be obtained. The program ends up with one single peak or with no peak at all or with several peaks. An iteration is considered successful only if it results in the determination of a single peak.

Gain correction

Because of the variations of voltage within the supply of power of the instrument, the gain does not remain constant over a period of time. The energy corresponding to a given channel is subsequently drifting. The observable consequence in measurements is that the position of the peak is changing. Figure 2.15 displays spectra acquired respectively around 06/27/2002 and 04/05/2002 by prism 2. There is a significant drift of the peak position (of almost two channels).
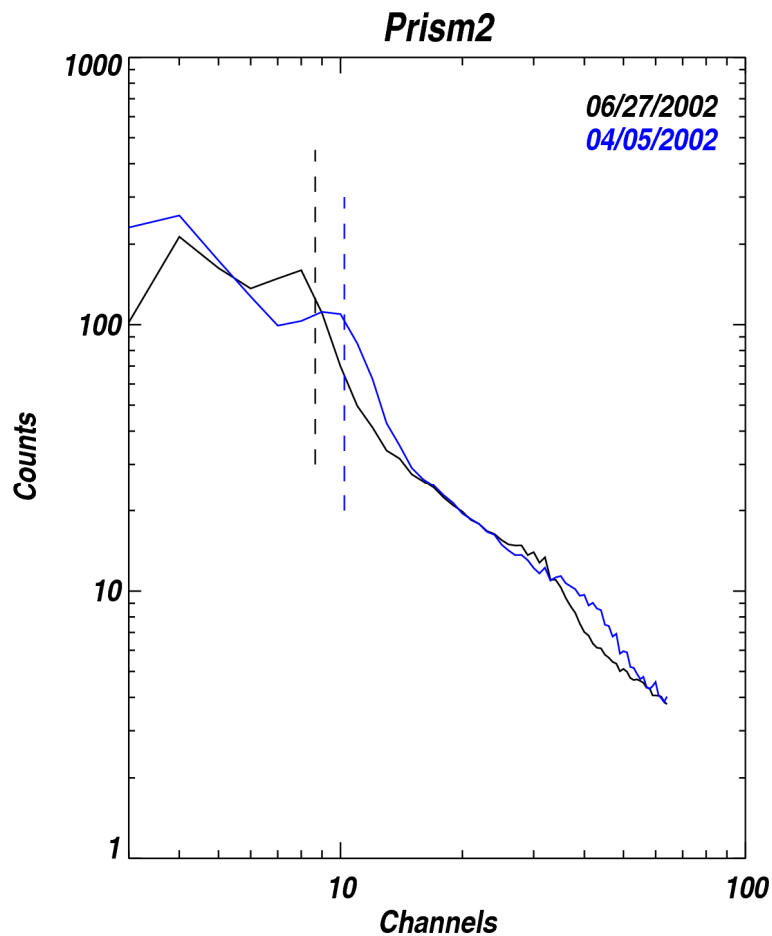

Figure 2.15: Spectra obtained respectively around 06/27/2002 and 04/05/2002 with prism 2. Dashed lines indicate the position of the peak centers determined with the Gaussian fit.

The gain correction is performed on time intervals of 360 measurements. The positions of the peaks have been calculated for these tiles at the precedent step. They are used to align all measurements on a common gain value. The measurements thus obtained are energy-wise consistent and independent of the high voltage drifts. Figure 2.16 shows the spectra before and after gain correction for the four prisms during 1st term of 2003. The peaks are generally thinner and higher, demonstrating that the correction reduced the energy dispersion of the acquisitions.
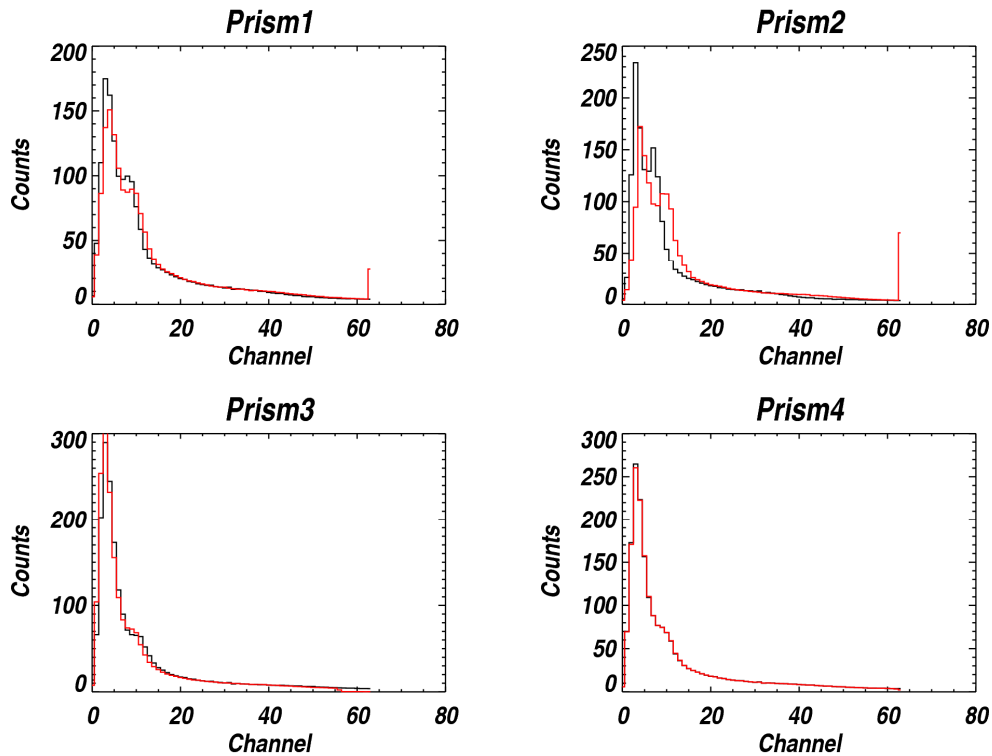

Figure 2.16: Histograms of counts before (black) and after (red) gain correction.

Peak integration

Now the centroid of the peak is known and identical for all measurements. Figure 2.17 displays the gain variations across the whole mission. This knowledge is used to set two intervals: one which only contains the peak and one where the background is to be estimated. These intervals are materialized respectively by blue crosses (peak) and red crosses (background) in Figure 2.18. Instead of processing a single spectrum to determine the background, we process an accumulation of spectra done with a sliding window. Every spectrum is averaged with two of his predecessors and two of his successors.

The background is fitted with a linear function on the basis of this averaged spectrum restricted on the background interval. This method processes a signal with a better signal to noise ratio and avoids the peak region, thus providing a more precise estimation of the true background. The fitted background is displayed in red in Figure 2.18. Once the background is properly defined, the extraction of the signal consists in

54

integrating the area between the background and the spectrum. This area is shown by the hatched region in Figure 2.18.
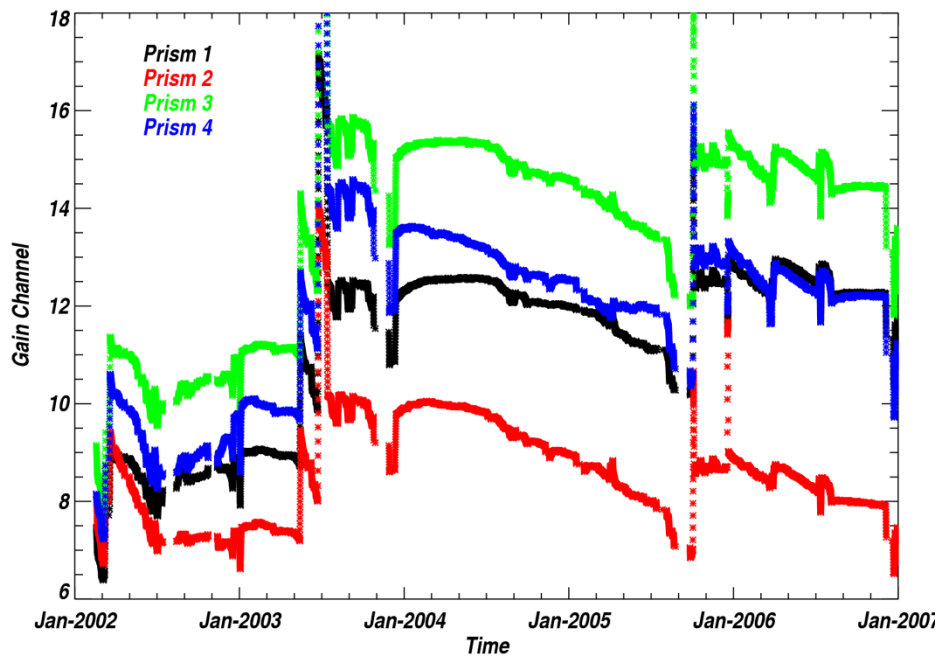

Figure 2.17: Variation of gains within the different prisms as a function of time.
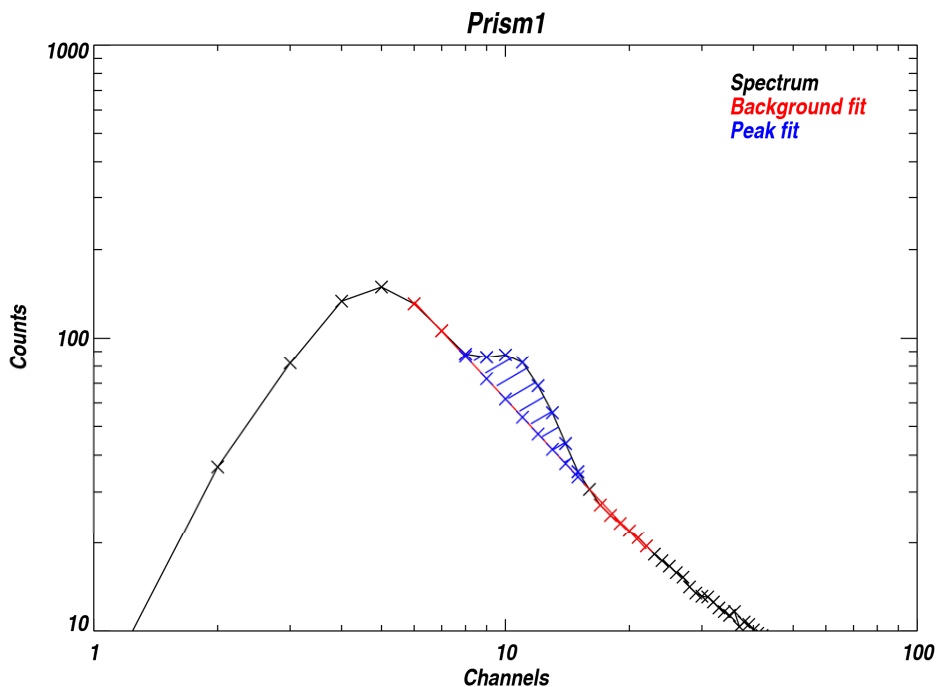

Figure 2.18: Spectrum of category 1 in prism 1 summed over 360 first measurements of 1st term of 2003 in logarithm scale. Superposed in red is the fit of background and in blue the fit of the peak.

However the method of the sliding window introduces some issues. Two successive measurements can be separated by a long interval of time (if for instance acquisitions have been removed from the dataset because of a solar particle energetic event). A flag that compares the length of the time period where the background is estimated to the length of a regular window was therefore created. All data flagged with abnormal windows are suppressed from the dataset.

2.2.5   Reduction of systematic uncertainties

Registration

The clock onboard the CPU of the instrument defines the time where the acquisition begins and ends. Times of acquisition correspond to different tiles of the planet, measured in longitude and latitude. Each time the spacecraft crosses the equator while heading towards the North there is a recalibration, thanks to what measurements are always associated with nominal pixels. However this setting of the clock introduces systematic errors of attribution of counts. Figure 2.19 displays the counts collected by prism 4 averaged on all longitudes and measurements as a function of latitude for the equatorial region. It reveals that the counts within the window comprised between -3° and 3° of latitude are mixed up when the spacecraft is heading northward. All measurements of this window were consequently removed to prevent from count errors.
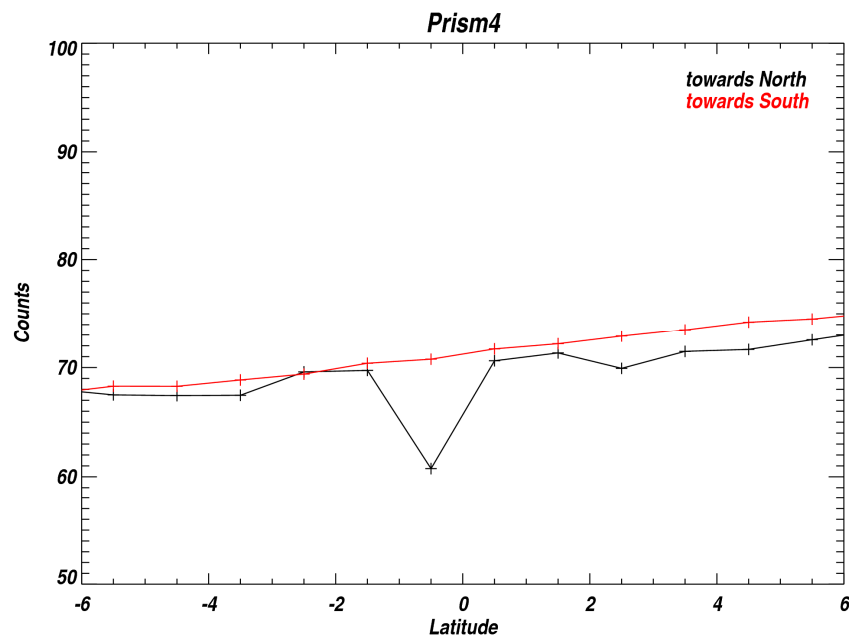

Figure 2.19: Counts in prism 4 as a function of latitude. Black curve is acquired while spacecraft heads northward and red curve southward.

Another problem with the clock lies in randomly distributed anomalies of registration. Time tags are settled to the middle of the acquisition range. Figure 2.20 displays this time as a function of latitude. In addition to slight oscillations of time, we notice that many measurements are not acquired at their nominal latitude. The nominal latitude is defined as the average of all latitudes associated with a given pixel. We

manually remove periods of time where measurements are messed up. Three instances of such intervals can be seen at the beginning of the mission, respectively around mid February, mid March and mid May. Figure 2.20 shows that the clock was behaving anomalously at these times. In addition to this correction, we automatically reject acquisitions whose latitude is far from nominal (the upper limit is set to 0.15°).
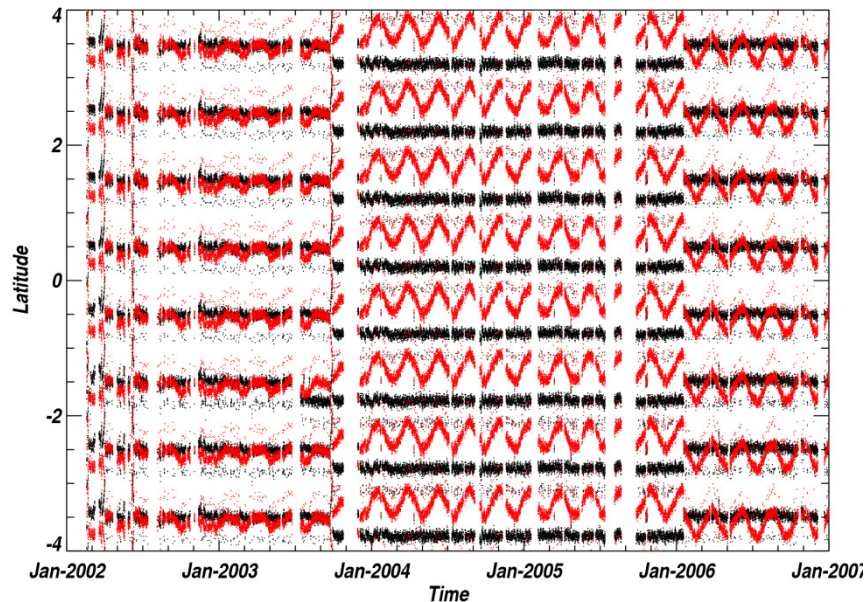

Figure 2.20: Latitude of acquisitions as a function of time. Black points are acquired while spacecraft heads northward and red points southward.

The last problem with the clock is about the acquisition time. Variations of time induce variations of the acquisition length. The count rates acquired by the prisms depend strongly on the integration time. In order to remove anomalous measurements, we filter the integration times outside the interval: [19.7;19.8]. Once these abnormal values are eliminated, the different signals are divided by the acquisition interval 19.75 s in order to normalize the data into counts per second.

Spacecraft altitude

The orbit of the spacecraft is not perfectly circular but slightly elliptical. The altitude of the satellite is therefore changing with time. Figure 2.21 displays the variation of the height of the spacecraft over April 6th and 7th of 2002. The spacecraft is evolving at an altitude comprised between 384 and 459 km above surface.

Variations of count rates with distance to the source are important. To avoid deviations of count rates due to spacecraft altitude we have modeled their variations as a function of the distance to the planetary body. The neutron production at the surface is computed from the Monte Carlo code MCNPX. Runs have been performed with several distances to the surface. Simulation points have been fitted to a simple solid-angle law. See details of these simulations in Maurice et al. [2004a].
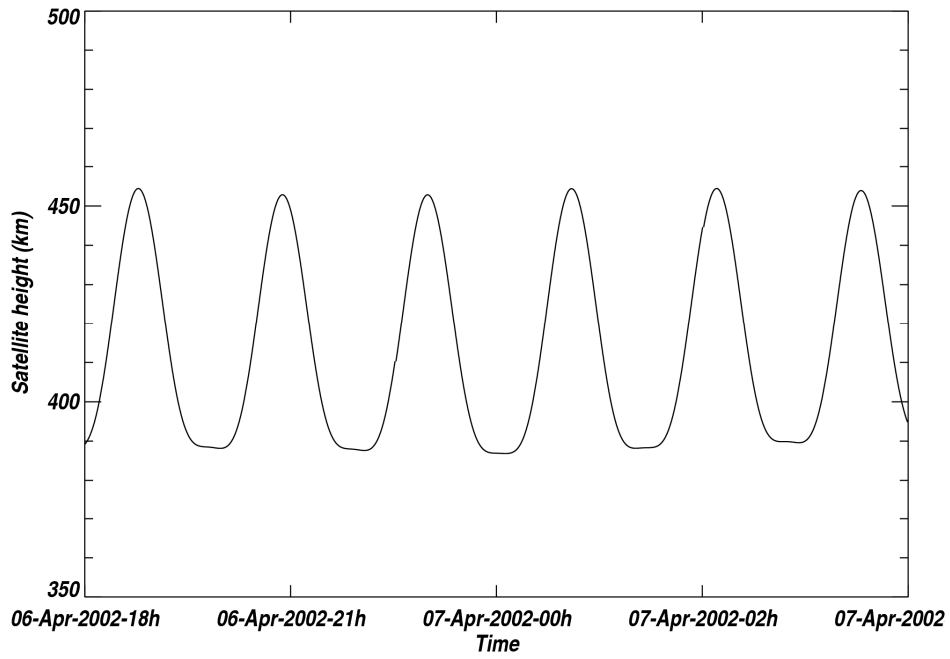
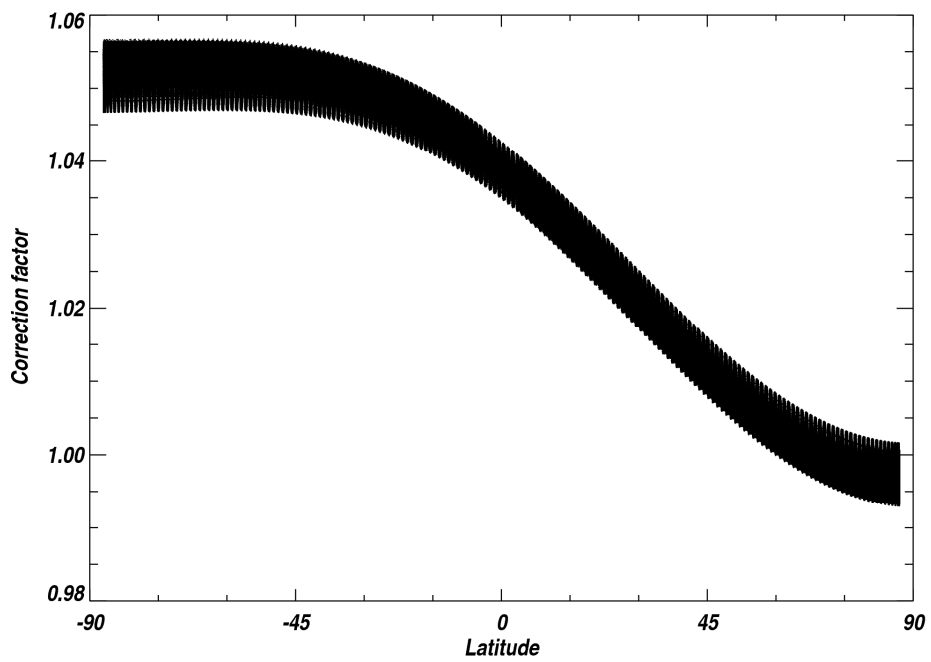Figure 2.21: Height of the satellite as a function of time.

Figure 2.22: Correction coefficient as a function of latitude.

In order to clear data from the contribution of the spacecraft height, we define a reference altitude: 450 km. The correction coefficient is then defined as the ratio of the solid angle of the measurement altitude over the solid angle at the altitude 450 km. This correction coefficient calculated for all measurements is shown as a function of latitude in Figure 2.22. The estimated correction factor is applied to the signals in all prisms, and to the estimated background.

Background

The background is constituted of neutrons generated by interactions between galactic cosmic rays and the Mars Odyssey spacecraft. The opportunity to evaluate its contribution to the signals acquired by the instrument has been plenty provided between the first activation of the Neutron Spectrometer on 2 May 2001 and the insertion of Mars Odyssey into orbit on 23 October 2001. During most of this time the interplanetary medium has been relatively quiet, thereby allowing the determination the baseline energy spectrum of neutrons produced on a spacecraft of the Mars Odyssey class by galactic cosmic rays.

The detailed study of the spectrum of fast neutron during cruise can be found in Feldman et al. [2002b]. The correction for background is only applied to the fast neutron currents. The thermal and epithermal neutron ranges of energy are indeed not significantly affected by neutrons produced by the spacecraft. The integration of the fast neutron spectrum over the energy range at which the fast signal is evaluated provides the background amount. It was thus determined that the background accounts for 0.12 counts per second on the fast neutron counting rate. This value is therefore subtracted from the signal.

Shift latitude

Because of the instrument configuration, all prisms are not pointing exactly towards the nadir of the spacecraft. In addition, the celerity of the spacecraft induces the latitude of the spacecraft to vary during an acquisition. These effects cause the latitude where the measurement is acquired to be different from the real latitude of the spacecraft. Prism 1 is looking slightly "forward", prism 2 is looking well forward and prism 4 is looking backward. We compare the signal averaged on all longitudes while satellite is moving northward and that when moving southward in Figure 2.23. Consequently to the effect previously described, there is a shift.

The signals obtained while the spacecraft is heading northward are compared to those while the spacecraft is heading southward for each prism. The latitudinal shift between the two is assumed to be twice the angle from nadir at which the prism is pointing. Once this angle has been calculated, we do a separate correction for latitude on each prism. Further manipulation of data is complicated by this operation. We indeed end up with 3 different latitude datasets: one associated with each prism that acquires data useful for neutron current determination: prism 1, 2 and 4 (prism 3 is not oriented towards the planet).
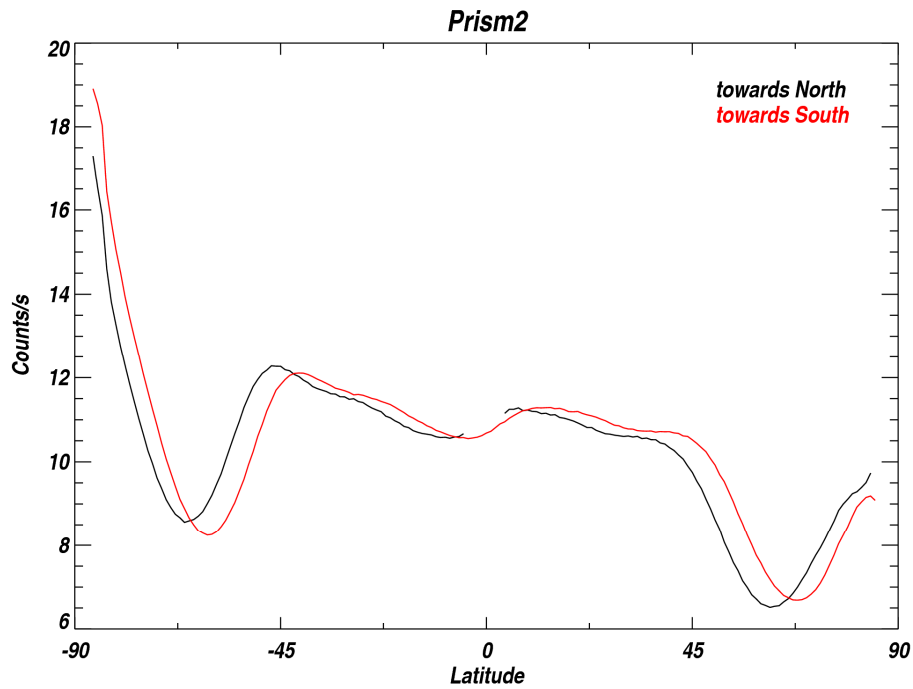
Figure 2.23: Signal measured in prism 2 averaged over all longitudes of the whole mission as a function of latitude. Black curve is acquired while spacecraft heads northward and red curve southward. Note: consequently to the registration correction, measurements at the equator when spacecraft is heading north have been excluded from dataset.
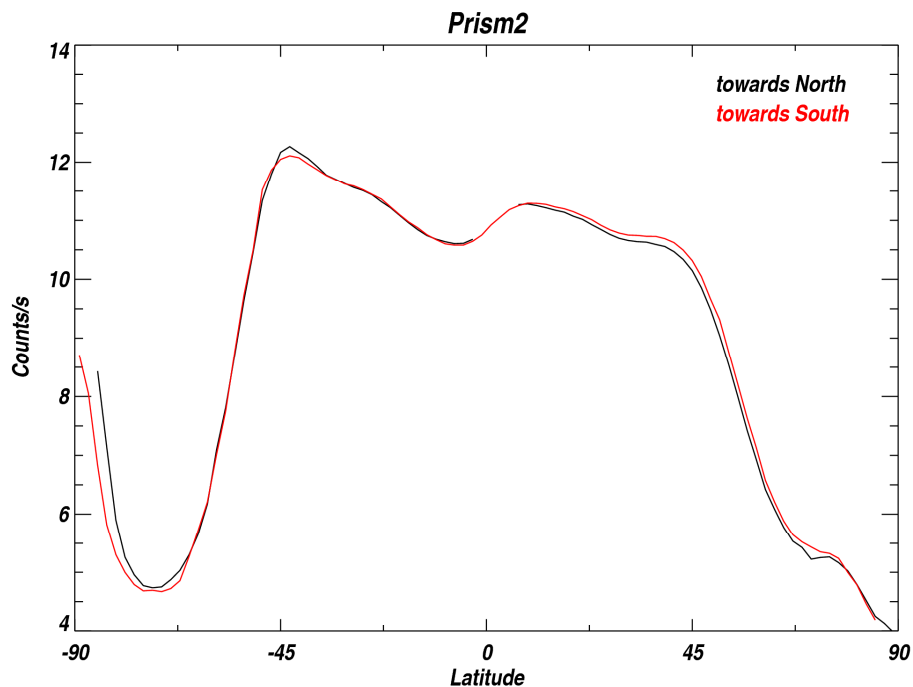

Figure 2.24: Frost free signal measured in prism 2 averaged over all longitudes of the whole mission as a function of latitude after shift correction. Black curve is acquired while spacecraft heads northward and red curve southward.

Prism 1 is looking 0.54° ahead of the spacecraft, prism 2: 2.46° and prism 4: 1.43° in the opposite direction of the spacecraft. To correct from these offsets, the signal in each prism is divided into northward heading and southward heading data. The latitude associated with this prism is augmented (if heading northward) or subtracted (if heading southward) from the shift value previously calculated. After doing this correction, there is not latitude shift left between signals acquired when the spacecraft heads northward and that when the spacecraft heads southward (Figure 2.24).

In addition to the latitudinal aberration, there is a slight longitudinal aberration because the planet is rotating while the spacecraft is acquiring a measurement. Consequently, longitude has been corrected for the shift due to the composition of the spacecraft motion and planet motion. This correction is a function of the latitude of the measurement, so the resulting longitude of acquisition is different in each prism.

Cosmic Rays

The flux of cosmic rays is known to vary over the course of the solar cycle. Between February 2002 and January 2007 the variation was significant enough (the average intensity varied by more than 30%) to bring about variations of the neutron count rates measured by our instrument. The dataset description provided in part 2.2.1 mentions the existence of a galactic cosmic ray counter. However, the variable geometry of the different prisms makes it impossible to use a single GCR proxy to account for the cosmic ray variations in all prisms. In addition, this proxy contains a non negligible fraction of variations due to gain variability.
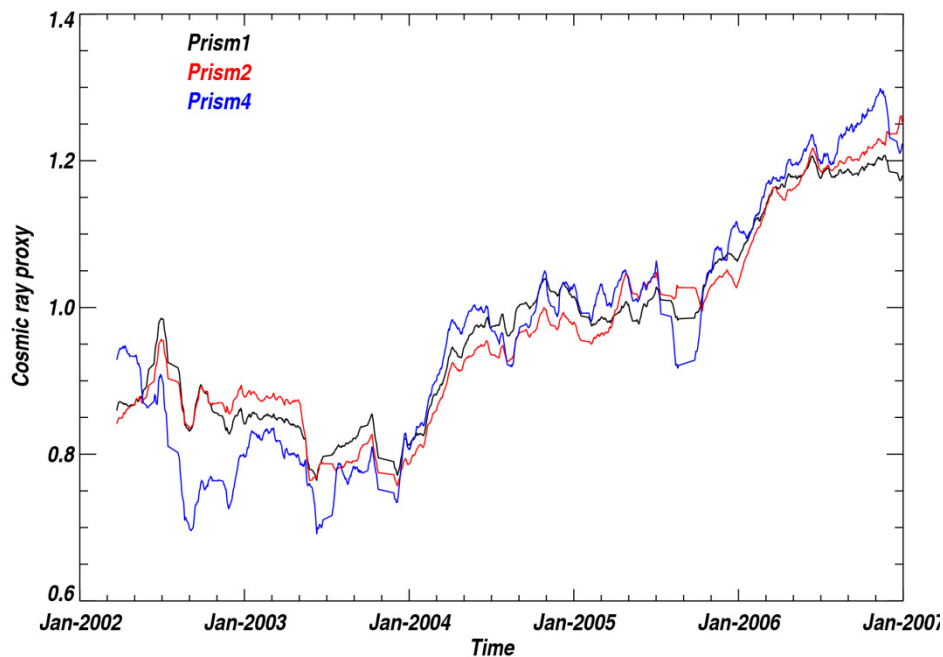

Figure 2.25: Normalized GCR proxy for prism 1, 2 and 4.

Therefore we build up a specific proxy of the cosmic ray variations for each prism. We take advantage of the fact that in absence of cosmic ray, gain and

atmospheric variations, the neutron signal measured above a pixel is supposed to be constant with time. We therefore use the variations of neutron signal across time within each prism to eliminate the cosmic ray contribution.

We consider the region comprised between -30° and 30° of latitude. We average all longitudes of this bellyband at the exclusion of regions with high topographic variations. Since the mean water content of this region is less than 10%, counting rates can be considered as independent of atmospheric pressure. Besides, the signals have been corrected for gain variation at this stage (see paragraph 2.4.3). The variation of count rates within the bellyband therefore constitutes a very good proxy of cosmic rays in each prism. These proxies are calculated for prism 1, 2 and 4. Prism 3 is not corrected for cosmic ray variation because only prism 1, 2 and 4 are used for determination of neutron currents. The results are normalized in order to form dividing factors. Figure 2.25 displays the resulting normalized GCR variations across time.

Residual anomalies

All the corrections so far performed intended to remove the systematic errors present in the datasets. However after correcting the data for average variations over the time, we still have suspicious measurements. Anomalous data are identified thanks to the variations at the equator. We calculate again the mean variation of count rates at the equator, within the bellyband previously defined. We set an interval around this average value. All measurements outside this interval are flagged as unwanted. Figure 2.26 shows count rates averaged within the bellyband for prism 1 over the whole mission. The allowed window is materialized by black lines. The boundary conditions are defined with fraction of the mean count rates.
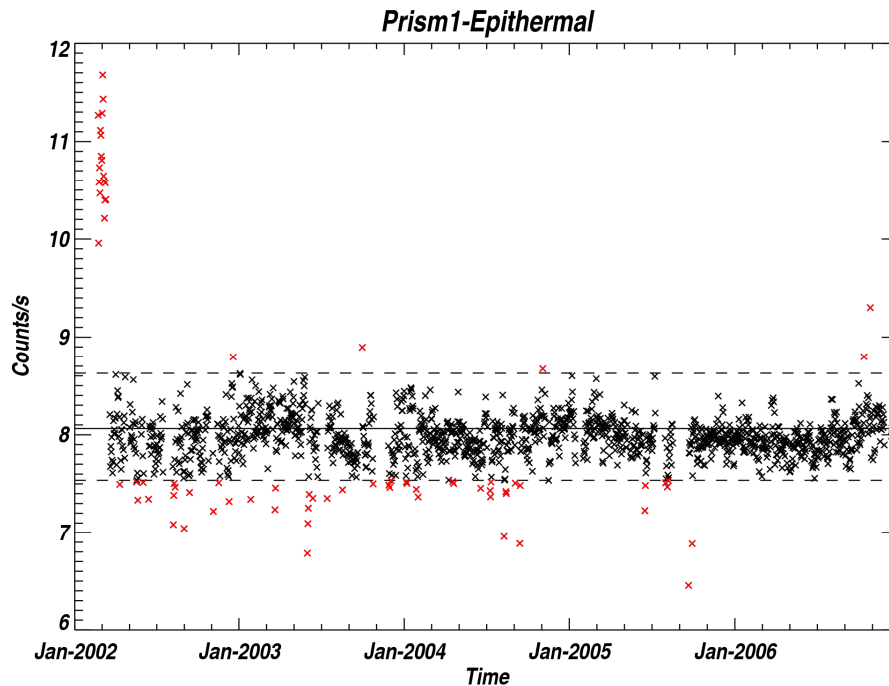

Figure 2.26: Epithermal count rates averaged within the bellyband. Black lines represent the authorized interval around average value. Red crosses are flagged unwanted.

	Number of unwanted
Prism 1 - Epis	296781
Prism 2	304122
Prism 4	277260
Prism 1 - Fast	90010
Total	528357

Table 2.5: Summary of measurements flagged unwanted.

For epithermal neutrons the authorized interval is [-1.07, 1.07] times the average epithermal count rate. For prism 2 it is [-1.15, 1.15] times the average prism 2 count rate. For prism 4 it is [-1.09, 1.09] times the average prism 4 count rate. And for fast neutrons it is [-1.15, 1.15] times the average fast count rate. The number of measurements flagged as unwanted by this routine is summed up in Table 2.5.

CO2 frost contribution

The polar caps were early determined to consist almost entirely of carbon dioxide [Leighton and Murray, 1966]. Carbon dioxide is indeed the major constituent of the martian atmosphere. A quantitative estimation of the variation of atmospheric pressure was allowed by the Viking mission [Hess et al., 1980]. It provided constraints to the carbon dioxide cycle, in particular about the deposition of carbon dioxide on the polar caps along the seasons. This data has been used to constraint the general circulation models of the martian atmosphere [Forget et al., 1999]. We use the predictions of these models in terms of CO_2 ice deposition [Forget et al., 2002] to identify measurements contaminated by carbon.
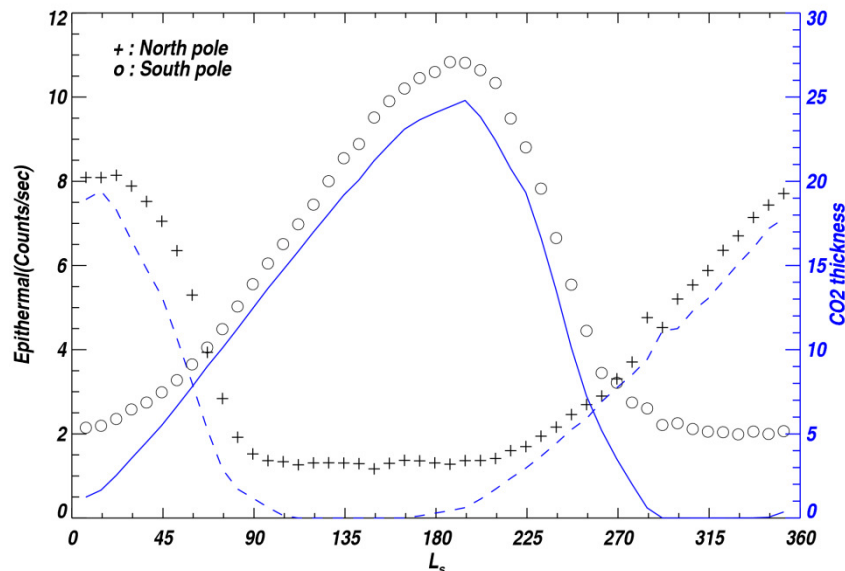

Figure 2.27: Epithermal count rates averaged within north pole (crosses) and south pole (circles) as a function of areocentric sun longitude Ls. Superposed in blue are the CO2 deposits thicknesses within north pole (dashed line) and south pole (continuous line).

Neutron emissions are indeed very sensitive to the presence of carbon in the material. Figure 2.27 shows the mean variation of epithermal count rates within north pole (latitude greater than 85°) and south pole (latitude lower than -85°) over a martian year. Superposed on this figure are the estimated thicknesses of CO_2 snow deposits averaged on the same regions. There is a very strong correlation between the thickness of CO_2 and the epithermal count rates. The same correlation is observed in all energy ranges. This observation confirms the prediction of neutron currents simulations [Prettyman et al., 2004b].

The general circulation model predictions in terms of CO_2 snow deposition were used to determine the geographic regions and periods of time where the amount of CO2 deposited is greater than 0.8 (which is roughly the amount necessary to observe a sensitive variation on the neutron count rates). All data outside this definition were flagged as "frost free". The "frost free" term refers to the fact that no measurable effect of CO_2 is detectable in neutron fluxes. Because of the perennial CO_2 ice cap in the south, no frost free data is acquired in this region.

Normalization

In the end, the neutron count rates are meant to be interpreted in terms of water contents, or more generally in compositional properties of the upper meter of Martian soil. So far count rates are indicative of relative intensities of neutron emission. In order to have quantitative measurements, we need to calibrate our instrument.

Normalization requires modeling the neutron count rates emitted by the planetary surface and transported to spacecraft orbit. Simulations can be done thanks to a priori information on the source (intensity of galactic cosmic rays flux, dependence to energy), the planet (geometry, composition, atmosphere) and the spacecraft (production of background neutrons, efficiency of the detector to collect neutron regarding their energy and coming direction). Except for the composition, whose influence on the fluxes is complex (these effects will be detailed in part 2.4), most of these parameters are quite well constrained.

Compositional ground truth that is available was acquired on a very little scale compared to our signal. Therefore the use of composition measurements provided by the landers would not give reliable results. However the in situ measurements are not the only sources of information about the composition. Among the best constrained locations on the planet are the polar caps. Within winter, they are indeed made of pure carbon dioxide snow.

We have just seen that the presence of a CO_2 veneer increases significantly the emissions of neutron. At some point, the thickness of this deposit gets sufficient to saturate the fast neutron count rates (meaning that the fast neutron count rates stop increasing while the thickness keeps increasing). The polar caps at winter therefore constitute very helpful ground truth information for the calibration of the neutron count rates. The detailed description of the calibration principle can be found in Prettyman et al. [2004b].

Prettyman ran simulations that predict what neutron count rates are produced by a soil made of a layer of CO_2 ice on top of a layer of pure water ice. The CO_2 veneer

thickness is estimated with the use of the General Circulation Model. Figure 2.28 shows the superposition of the measured fast count rates with the simulated count rates. We define the normalization factor as the ratio of the simulated count rates taken in northern winter time (for Ls between 0° and 20°) over the measured neutron count rates. Once multiplied by this normalization factor, there is a generally good agreement between measured neutron count rates and simulations during northern winter.

However Figure 2.28 shows that the measurements do not coincide very well with the simulations for Ls comprised between 90 and 225. The explanation for this discrepancy is that the model is not faithful of the reality outside winter time. It is indeed formed of a CO_2 ice veneer on top of a water ice layer. Once the thickness of CO_2 decreases, the modeled surface consists of pure ice, which is not representative of the true water content of the soil.
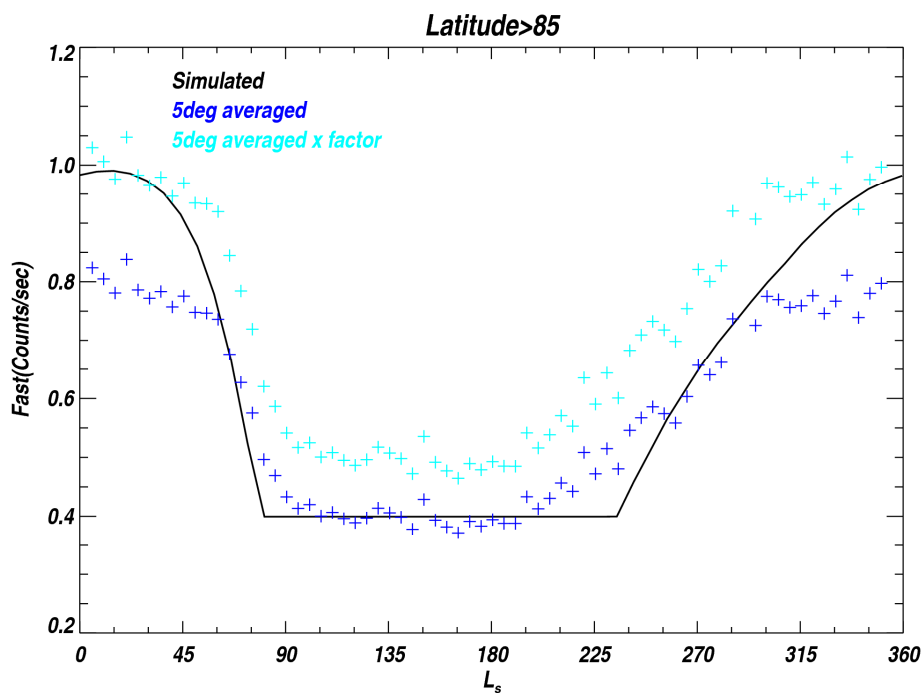

Figure 2.28: Fast neutron counting rates 5-degree averaged within north pole as a function of areocentric sun longitude Ls before (blue crosses) and after (turquoise crosses) multiplication by the normalization factor. Superposed in blue are the count rates obtained by simulations (see text for model description).

Atmospheric correction

The seasonal deposition of CO_2 ice in polar caps has been accounted for. However it is not the only contribution of the CO_2 cycle on the uncertainties of our data. It was previously said that the cycle could be characterized by the variations of atmospheric pressure within the martian year. The variations of CO_2 concentration across time induce variations of the neutron count rates. Epithermal and fast neutron count rates in particular depend on the column density of CO_2. We therefore detected a breathing in those count rates that was interpreted of atmospheric origin.
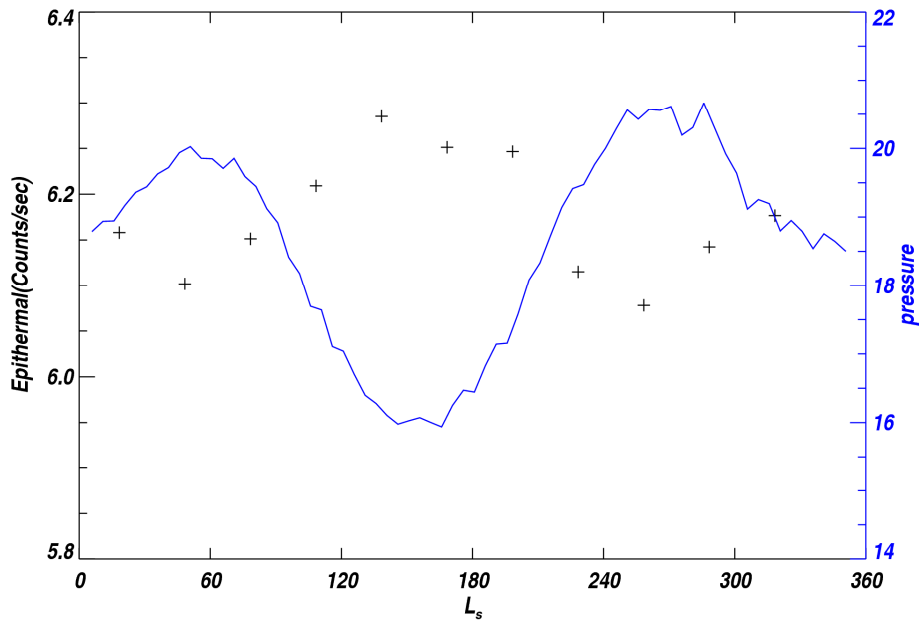
Figure 2.29: Epithermal count rates averaged within a square region near the equator (-10° < latitude < 10° and 180° < longitude < 200°) as a function of areocentric sun longitude L$_s$ tiled every 30°. Superposed in blue is the atmospheric pressure simulated by a general circulation model.

In addition to the variations of atmospheric pressure with time, there are some geographic variations of pressure. The pressure in a region is determined by its topography. Regions of low topography (such as the Hellas impact basin) have a high pressure because the column density of atmosphere is integrated over a higher range whereas regions of high topography (such as the Olympus Mons) have a low pressure. We therefore need to considerate both geographic and time dependent variations of pressure.

The variation of the epithermal count rates within a region is compared to the atmospheric pressure variation in Figure 2.29. Neutron measurements have been tiled on intervals of 30° of areocentric sun longitude. The pressure is derived from simulations performed with the general circulation model [Forget et al., 1999]. There is an obvious anticorrelation between these variables. The atmospheric correction routine consists in removing this contribution from the dataset.

In order to account for this effect, simulations of the count rates measured with varying atmospheric column density have been performed [Prettyman et al., 2004b]. However the evaluation of the atmospheric impact is complicated by the fact that it also depends on the composition of the material, and most particularly on the water content of the soil. Therefore simulations have been performed for different values of pressure and water content.

At this stage, the water content of the soil is not known yet. Simulations provide tables of thermal, epithermal and fast neutron count rates for different pressure and water content hypotheses. We use the neutron count rates measurements plus the

atmospheric pressure generated by the general circulation model as inputs for the determination of the rough water content of the soil. Obviously this is not the best water content we can obtain because the neutron count rates are not corrected for atmospheric contribution yet. However it provides a good preliminary estimation of the water content of the soil.

The next step consists in tiling the planet in pixels of 5 degrees by 5 degrees. The evaluation of the pressure correction factor is done pixel by pixel. For each pixel we calculate the mean counts rates of epithermal and fast neutrons (averaged in time and in space) and the associated water content estimation. We define the correction factor of an acquisition as the ratio of neutron count rates obtained with a pressure of 16 g/cm^2 over neutron count rates obtained with the pressure of the acquisition. We thus normalize all data to a common pressure of 16 g/cm^2. Figure 2.30 shows the correction factor as a function of pressure for epithermal and fast neutrons with different water content hypotheses.
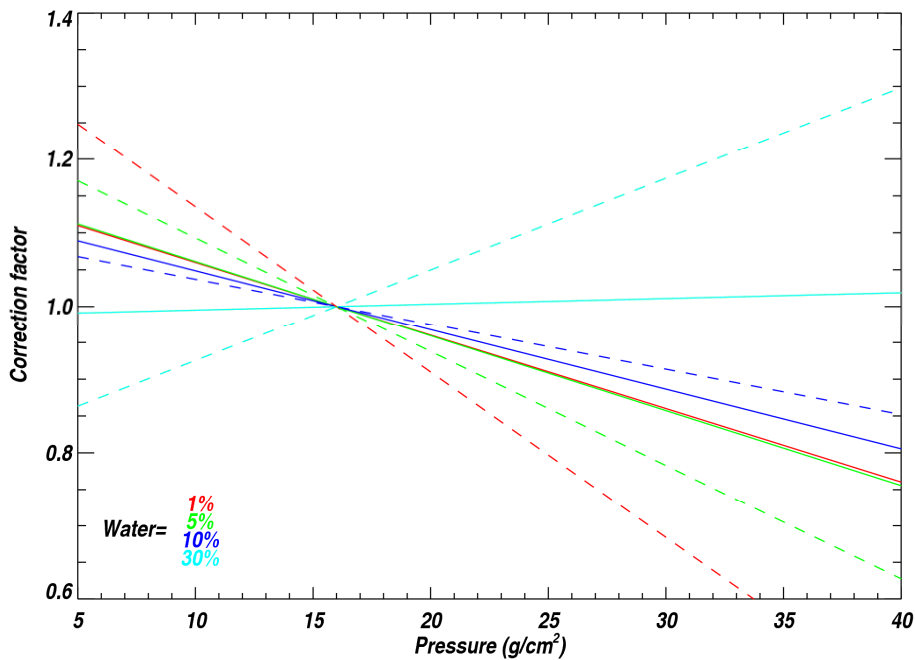

Figure 2.30: Atmospheric correction factor for fast (dashed lines) and epithermal (continuous line) neutron count rates for different water content hypotheses.

A given pixel is flown over several times by the spacecraft. All these acquisitions are done with identical water content in the material but with varying pressure in the atmosphere. The calculation of the correction factor of all these measurements is rendered easier because it is a linear function of the pressure for a given water content hypothesis. We constitute a table of the pressures associated with a pixel and calculate the associated correction factors. Fast and epithermal neutron count rates are then multiplied by the correction factors.

2.2.6 Final data

Mapping techniques

After all corrections have been applied to the data, level 2 data should be, as much as possible, independent of observational biases. Data are in the form of neutron counting rates (in counts per second) organized by time. We have four products: fast neutron counting rates, epithermal neutron counting rates, Prism 2 counting rates and Prism 4 count rates. Thermal neutron counting rates are then derived from Prism 2 minus Prism 4. However these counting rates are associated with different geographic coordinates and therefore need to be mapped before the subtraction is done.

The number of records is not exactly inherited from level 1, because data with anomalies were removed earlier. Figure 2.31 shows the different counting rate products obtained as a function of time. The eliminated data is shown by the blank intervals. Except for the variations at the poles due to the seasonal caps, we see that no significant global variation remain in the data after the corrections. The objective of the routines described in the coming paragraphs is to create level 3 data, that is to say maps of the neutron count rates.
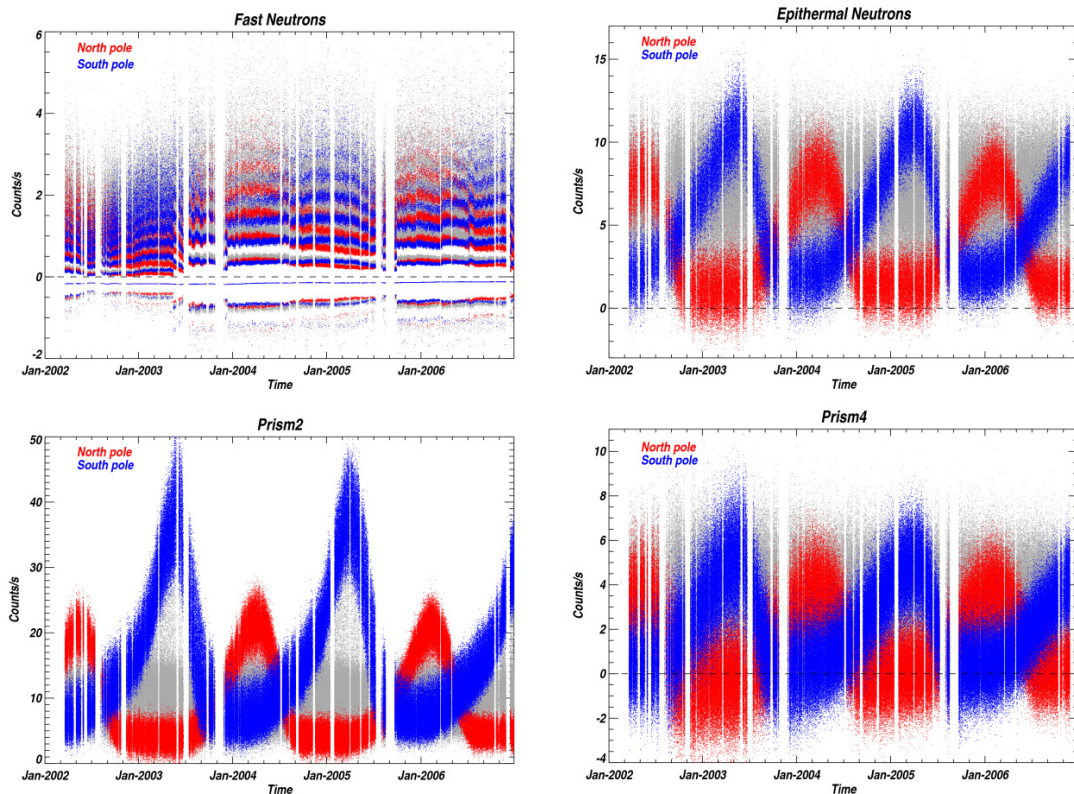

Figure 2.31: Counting rates as function of time for (a) fast, (b) epithermal, (c) prism 2 and (d) prism 4. Measurements in red are acquired within 5° of the north pole and measurements in blue of the south pole.

A comprehensive set of routines has been developed by the Lunar Prospector team to map neutron and gamma-ray data onto a planet [Gasnault et al., 2003]. This

toolkit is particularly suited to poor spatial resolution, and is therefore adapted to the data acquired by the neutron spectrometer onboard Mars Odyssey. A 0.5° cylindrical grid, i.e., 720 longitudes by 360 latitudes, is the basemap for all geographical projections. As a result, all projection routines (global or local, cylindrical, Mercator, or stereographic for instance) are coded onto that single basemap.

Thus level 3 products are 720° × 360° raster files, with a label for the color coding of the physical values. Because 0.5° pixels oversample the spatial resolution (which is roughly 600 km), two ways of mapping data onto the surface have been developed: straight mapping and smooth mapping. Straight mapping consists in averaging 0.5° tiles together to form larger pixels.

Two choices are possible: (1) Pixels have equal angular dimensions in latitude and longitude. This is the ''cylindrical mapping,'' with approximately equal statistics within each pixel. However, pixels have smaller areas toward the poles. (2) Pixels have the same angular dimension for the latitude, but the longitude extent is adjusted so that pixels have close to the same area. This is the ''equal area mapping,'' adapted to analyze the distribution of neutron fluxes over the planet, with no emphasis on the poles. For instance, at two-degree equal-angle resolution, a cylindrical map encompasses 16,200 pixels, whereas the equal-area map encompasses 10,538 pixels. In the first case, the pixel area varies from 0.07 at the poles to 4.00 square-degrees at the equator with a standard deviation of 1.23; in the second case, the pixel area varies from 3.14 to 4.41 with a standard deviation of only 0.23. The latter case has still small variations of the pixel area because pixel borders must match borders of the 0.5° basemap tiles.

Contrary to the straight mapping, smooth mapping takes into account the shape of the response function of the instrument. The value of a pixel in the basemap tile is calculated as the weighted average of nearby 0.5° pixels. The weight function is a Gaussian of the distance to the spacecraft nadir (which models quite well the response function of the instrument). It is given by its half-width-half-maximum (HWHM) value. As a result of this process, the signal-to-noise ratio increases and maps do not have a grainy aspect.

Determination of thermal neutron counting rates

Unlike epithermal neutron which are directly measured by Prism 1 (this latter is covered with cadmium, which does not let thermal neutrons through), thermal neutrons can only be determined with the combined use of Prism 2 and Prism 4. The removal of the epithermal neutrons counted in Prism 2 can be achieved by removing the counting rates of Prism 4. Because of the spacecraft velocity, the backward facing prism outruns the thermal neutron and therefore provides a good estimation of the epithermal neutron counting rates.

Counting rates measured in Prisms 2 and 4 were determined. The time series following from the processes described in section 2.5 are associated with different longitude and latitude coordinates regarding the prism considered. We therefore mapped the counting rates for each prism before subtracting Prism 4 from Prism 2 and obtain the thermal neutron counting rates. Once Prism 2 and Prism 4 counting rates are mapped,

thermal neutron counting rates can be mapped and normalized as described in section 6.8. The processing order is therefore slightly different from that of epithermal and fast neutron counting rates.

Dynamic range

Although each neutron product has its own spatial resolution (see next section), we use a common approximation of two degrees for all to allow comparisons. Thus we can calculate dynamic ranges and precisions of level 3 maps under the same conditions. The equal-area technique is chosen. Each map consists of 10,538 data points with associated latitude and longitude limits for each pixel. At this resolution there are no missing pixels. The maps are shown in Figure 2.32 with a color scale that ranges from the minimum to the maximum of each data set.
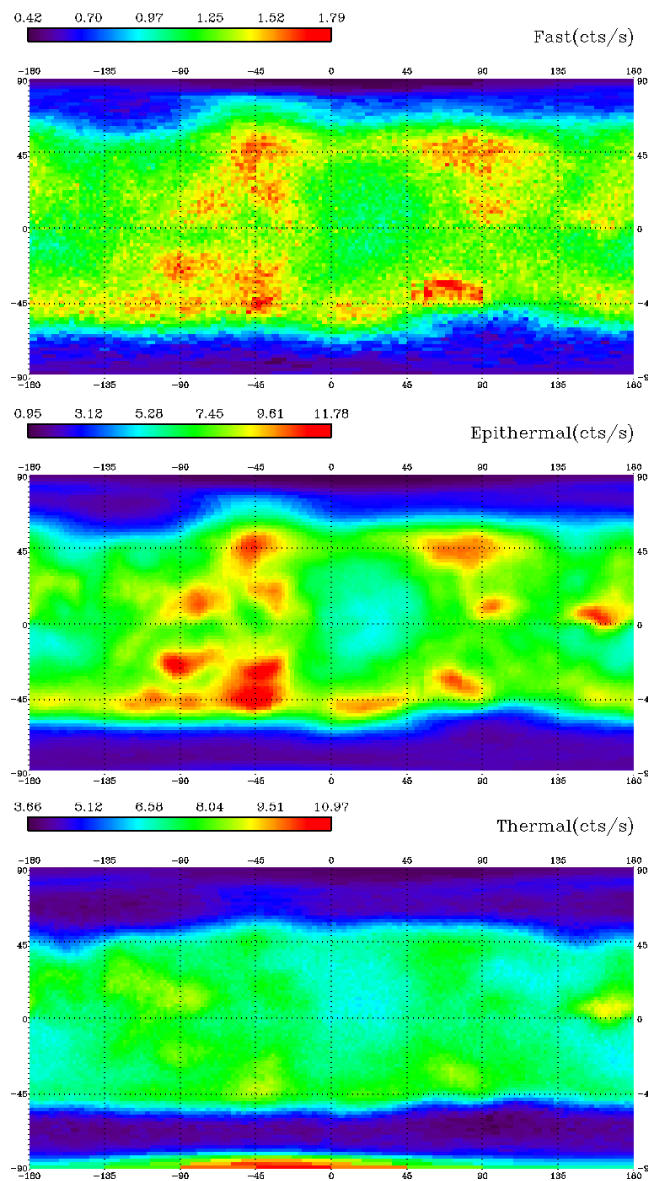

Figure 2.32: 2-degree equal area maps of (a) fast neutron, (b) epithermal neutron, and (c) thermal neutron counting rates.
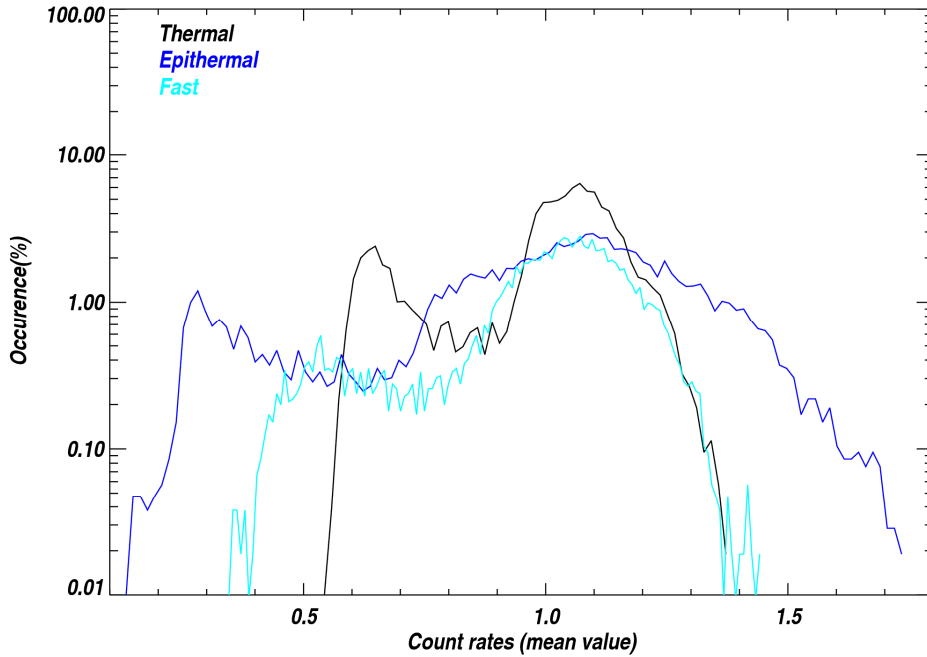
70

Figure 2.33: Histograms of the different 2° equal area maps: thermal neutron (black), epithermal neutron (blue) and fast neutron (turquoise). Occurrences are in percentage of the total number of pixels. Data are normalized to their average for comparison.

The dynamic range of neutron counting rates is defined as (max-min)/mean. Figure 2.33 presents histograms of each 2° map. The dynamic range of thermal neutron is 100%, that of epithermal neutron 160% and that of fast neutron 110%. High values of neutron counting rates (for all three energy ranges) distribute as a Gaussian. The shape of the low values of counting rates is not very well defined. The presence of features in these histograms is concomitant with the presence of features in the different maps shown in Figure 2.32.

Statistics

We evaluate the dispersion within each pixel, since the same quantity has been measured several times. When mapped onto the planet, the only information that is saved is the mean counting rate $\overline{x}$ for n measurements x_i taken at different times within a given pixel. Two quantities are meaningful to characterize the dispersion of the signal: the number of observations and the measured standard deviation of the population:

$$s_{\overline{x}} = \sqrt{\frac{\sum_i (x_i - \overline{x})^2}{n-1}}$$

We define the standard deviation within a pixel as the deviation of the population divided by the square root of the number of observations.
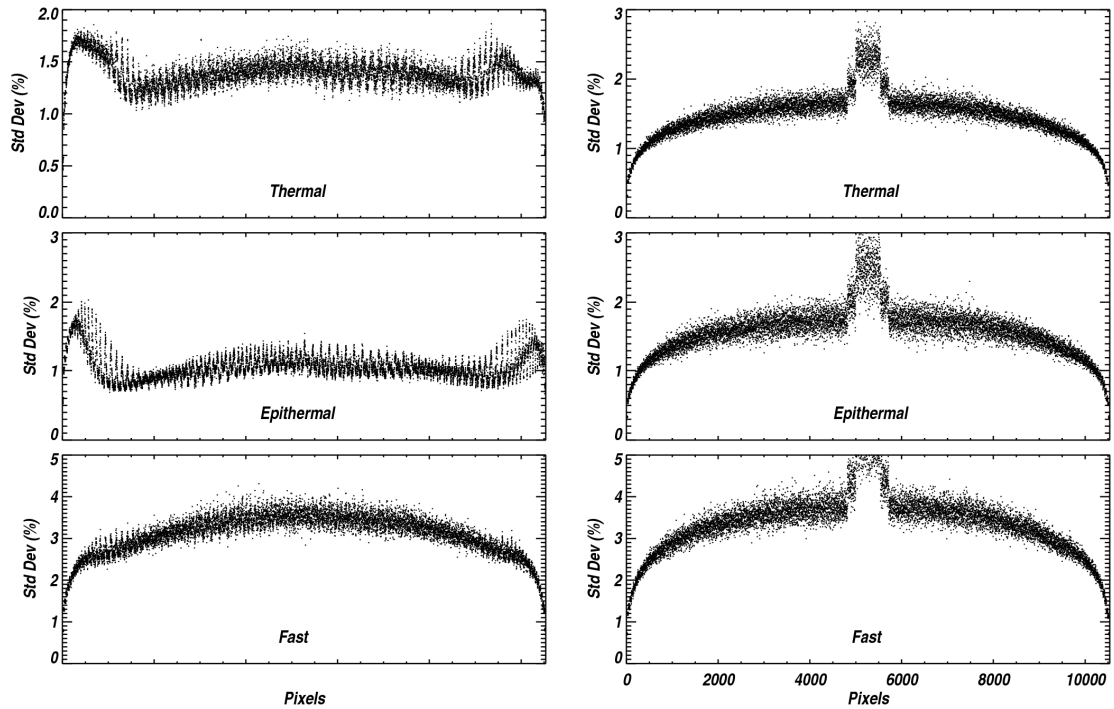
71

Figure 2.34: Standard deviations of thermal, epithermal and fast neutron counting rates from 2° equal-area maps of (a) level 1 (after peak extraction) and (b) level 2 (after reduction of systematic uncertainties). Standard deviations are expressed in percentage of the mean within each pixel. The averaged ordering of the pixels is by latitude from south to north.

The uncertainties in neutron counting rates have several contributions: statistical uncertainties in the average counting rates due to the random nature of counting experiments, systematic errors in the datasets and uncertainties in the normalization (due to uncertainties in models of neutron counting rates). As the reduction routines are applied to the datasets, the fraction of dispersion due to systematic errors is lowered.

We calculate the standard deviation within each pixel of a 2° equal-area map for data at different steps of processing. Figure 2.34a provides the standard deviations calculated for thermal, epithermal and fast neutron counting rates at level 1. Data have been picked after the step of peak extraction described in section 5. The x axis corresponds to 10,538 2°-pixels, which are ordered from south pole to north pole. The standard deviations have been divided by the average value of each pixel in order to be comparable. Figure 2.34b provides the standard deviations calculated for all neutron data product at level 2. At this step, datasets have been corrected for systematic uncertainties (see section 2.5).

As reduction of time-dependent biases in the data set progresses (SEP events, cosmic ray fluxes, altitude, background, gain, and temperature), we see a variation of the measured standard deviation. The standard deviation is found to decrease significantly at the poles and to increase at the equator. The reason for this higher dispersion is the removal of many measurement points at the equator due to registration problems. Therefore in spite of the improvement of the quality of the data, the loss of

72

many points makes the dispersion higher. As a general rule, the dispersion is not necessarily much smaller after data reduction because the processes applied remove many acquisitions, which reduces the total amount of measurements considered for statistics. However we notice that the standard deviation is smoother, because many variations were removed from the dataset. At the poles, the removal of the frost contaminated data leads to an impressive decrease of the dispersion of the data.

An average standard deviation has been calculated for the three neutron products. This average standard deviation tells us how reliable our estimate of the mean is per pixel. The mean standard deviation for thermal neutron counting rates is 1.97%, that for epithermal neutron counting rates 1.52% and that for fast is 0.71%.

Spatial resolution

Surface resolution is an important characteristic of neutron maps. A direct estimate of that parameter can be either derived from the shape and size of a signal due to an isolated point source on the surface or determined through numerical modeling of the response function of each sensor. The resolution depends on the directional capability of the sensors, on the satellite height and on the neutron energy.

The radiation transport code MCNPX was used to calculate the angular dependence of the current of neutrons at the top of the atmosphere and the response of a modeled cubical borated plastic block segmented in four prisms irradiated with neutrons. Prettyman et al. [2004b] details the hypotheses used for these simulations. The angular and energetic dependence of the sensors can be found in Feldman et al. [2002b] for the downward and upward looking prisms. The nadir facing sensor efficiency decreases as neutron incidence directions get far from normal to the prisms. This response profile tends to improve the resolution of the instrument.

Simulations show that the spatial response function of the instrument can be approximately modeled by a 2-D Gaussian function. The resolution of the instrument can be approximated as the FWHM (Full Width at Half Maximum) of this function. It has been determined to approximate 10°.

Smooth maps

Because a 2° pixels resolution oversamples the datasets, we smooth the maps to reintroduce the shape of the instrument response function. The convolution of the maps by a Gaussian function provides more natural maps (Figure 2.35), because it removes the pixelized aspect. In addition, the signal-to-noise ratio increases with this process.
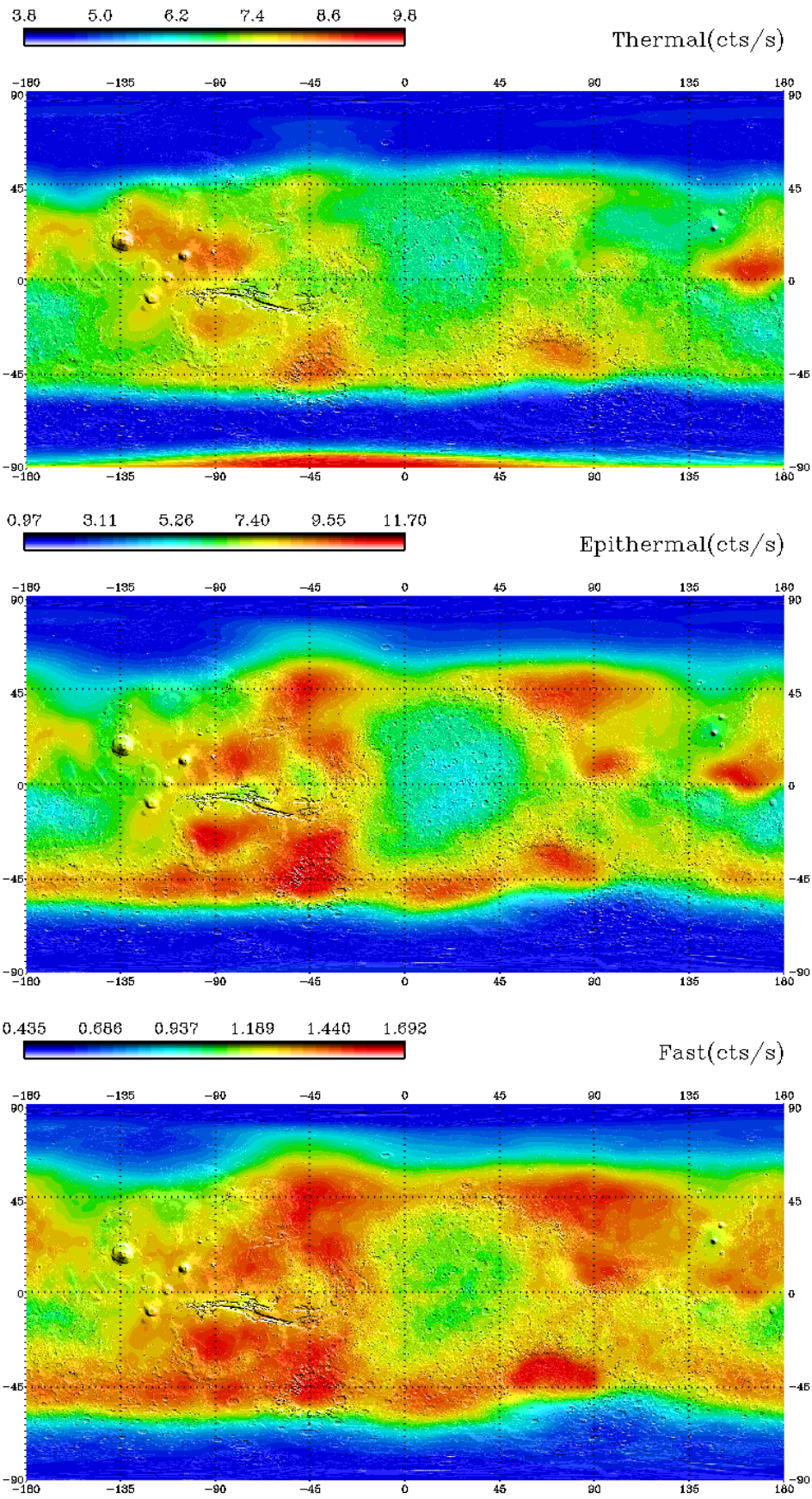
73

Figure 2.35: Smoothed map of (a) thermal, (b) epithermal and (c) fast neutron counting rates.

2.2.7 Conclusion

All steps of the Mars Odyssey neutron data reduction have been justified and documented and results are reproducible from raw data that are available from the Planetary Data System (PDS). Sources of errors have been minimized. The accumulation of acquisitions with time has allowed eliminating most of the instrument biases.

In addition to the processes of reduction, description of the neutron data products and of their statistical quality is given. Thanks to the long period of time covered by the mission, neutron counting rates yield average dispersions of 2% (thermal), 1.5% (epithermal) and 0.7% (fast). Improvements subsequent to level 3 can be achieved by signal processing in the form of a full spatial deconvolution of the signal with an accurate model of the instrument spatial response function at the surface.

Level 3 neutron data are used to put constrains on the composition. The systematic determination of elemental concentrations is rendered impossible by the fact that we only have three measurables. However the determination of the concentration of elements playing a major role in the neutron moderation and absorption is possible. The determination of the hydrogen content and depth, which is the primary objective of the mission, is described in next part.

Additional information on the composition of the soil can be achieved through use of the macroscopic cross sections which qualify the tendency of a soil to absorb or scatter neutrons. Interpreted with the use of the actual knowledge of Mars, they provide clues about the concentration of very strong absorbers such as chlorine, as will be shown in part 2.4, or on the contrary of very little absorbers such as carbon and oxygen. The detailed study of the carbon concentration can be found in Prettyman et al. [2004b]. A maximum science return can be obtained when the neutron products are exploited in conjunction with results from gamma-ray spectroscopy, X-ray spectroscopy, or spectral reflectance.

2.3 H layering in the top meter of Mars

[1]Centre d'Etude Spatiale des Rayonnements, Université Paul Sabatier, CNRS, Toulouse, France
[2]Planetary Science Institute, Tucson, AZ
[3]Los Alamos National Laboratory, Group ISR-1, Los Alamos, NM
[4]Laboratory for Atmospheric and Space Physics, University of Colorado, Boulder, CO
[5]Division of Geological and Planetary Sciences, Californian Institute of Technology, Pasadena, California, USA
[6]Institute for Astronomy, University of Hawaii at Manoa, Honolulu, Hawaii

2.3.1 Introduction

The Mars Odyssey Neutron Spectrometer provides considerable insight into the present state of the Martian water cycle. Maps of subsurface water content have been constructed using the Gamma Ray Spectrometer suite of instruments [Boynton et al., 2002; Feldman et al., 2002b; Mitrofanov et al., 2002].

We extend the work of Feldman et al. [2004b] which compares the neutron currents measured using the Mars Odyssey Neutron Spectrometer (MONS) with numerical simulations of these currents using the Monte Carlo code MCNPX [Waters, 1999]. We use a similar combination of measurements and simulations to explore the layering of hydrogen over the whole planet. Owing to the influence of elemental composition, most particularly through its effects on the thermal neutron current, the determination of layering will depend strongly on the chemical abundances of the soil. We consequently estimate the errors associated with the implemented method.

The neutron data used in this study extend between Feb 2002 and Sep 2005. The raw data has been processed with the reduction scheme described in part 2.2. Data have therefore been corrected for satellite altitude, cosmic ray variations and atmospheric pressure. Only measurements not contaminated by CO_2 frost were kept. This condition puts latitude-dependent constraints on seasonal time of year, Ls, and an annulus of avoidance, latitudes lower than -75°, because of thermal neutron current contamination from the south-pole residual CO_2 cap [Tokar et al., 2003]. We use data at level 3 that has been gridded with cylindrical projections with a 2-degree latitude and longitude resolution. However the true spatial resolution of the instrument is roughly 600km. Uncertainties in measured thermal, epithermal and fast neutron currents have been estimated previously [Prettyman et al., 2004b; Feldman et al., 2004b]. Uncertainties in fast neutrons can reach ±10% and that in thermal and epithermal neutrons, ±5%.

2.3.2 Detecting layering with the Mars Odyssey Neutron Spectrometer

The prediction of neutron currents stems from simulations that assume a layered model of the atmosphere and ground surface [Drake et al., 1988; Prettyman et al., 2004b]. The production of neutrons and their transport to the top of the atmosphere is simulated using the Monte Carlo Neutral Particle Code, MCNPX [Waters, 1999]. A second code is used to map these currents from the top of the atmosphere to the spacecraft and then convert them to counting rates using the energy-angle sensor response function [Prettyman et al., 2004b]. The Martian surface has been modeled with two layers in order to infer the vertical distribution of hydrogen [Maurice et al., 2004b]. The topmost layer is assumed to be relatively desiccated, chosen here to have a hydrogen content [H]up of one mass percent of Water Equivalent Hydrogen (WEH) and has a thickness D. The second layer is relatively rich in hydrogen ([H]dn) and is assumed to be semi-infinite in depth and extending uniformly to the horizon.

The neutron spectrometer provides three measurables, which correspond to three ranges of energy: thermal, epithermal and fast neutrons. Only thermal and epithermal neutron currents are used in our analysis. Fast neutron currents are not used here because their variation with hydrogen is not sufficiently different from that of epithermal neutron currents to provide additional useful discriminating information. A linear regression between epithermal and fast neutrons gives a correlation coefficient of R=0.84 [Feldman et al. 2002b]. Moreover the uncertainty in the determination of fast neutron currents is larger than that for thermal and epithermal neutron currents. However under the assumption of a uniform composition equal to that measured at the Pathfinder landing site, measured fast and epithermal neutron currents have been used to provide a rough average burial depth and permafrost hydrogen content of a discrete region of Mars near the equator [Feldman et al., 2004b].

Although the thermal and epithermal neutron currents should be sufficient to determine two of the three unknown parameters of a two-layered model (the thickness of the uppermost layer D, and the hydrogen content in each layer [H]up and [H]dn), the concentrations of all chemical elements are also needed as a function of depth. Most important are those of the strong neutron absorbers: Cl, Fe, Ti, S, Gd and Sm. Beside the two layers just mentioned, several layers are also needed to model the atmosphere. Although the composition and structure of the Martian atmosphere is well known [Owen, 1992], the composition and layering of the soil is not. For the sake of simplicity, no layering of an element other than hydrogen will be handled here. In addition, [H]up will be fixed at a constant value, here chosen to be one weight percent. Only two variables remain: [H]dn and D.

Our analysis procedure consists of superimposing measured thermal and epithermal currents on a thermal-epithermal grid of simulations, shown in Figure 2.36. The simulations were made for a discrete range of values of [H]dn and D. Inferred values of [H]dn and D are determined by interpolating between the points of the grid. [H]dn and D are obtained in a 2-degree gridded format through iterating the process for each map pixel of the neutron currents. A typical simulation grid (two examples given by blue and pink squares in Figure 2.36) contains the results of simulations for the following set of parameter values: [H]dn = [0.01, 0.02, 0.03, 0.06, 0.1, 0.3, 0.6, 1] WEH

mass fractions and D = [0, 10, 20, 40] g/cm². The transformation from neutron currents to hydrogen variables is seen to be strongly nonlinear. To perform a reasonably good interpolation, we have refined the grid with splines.
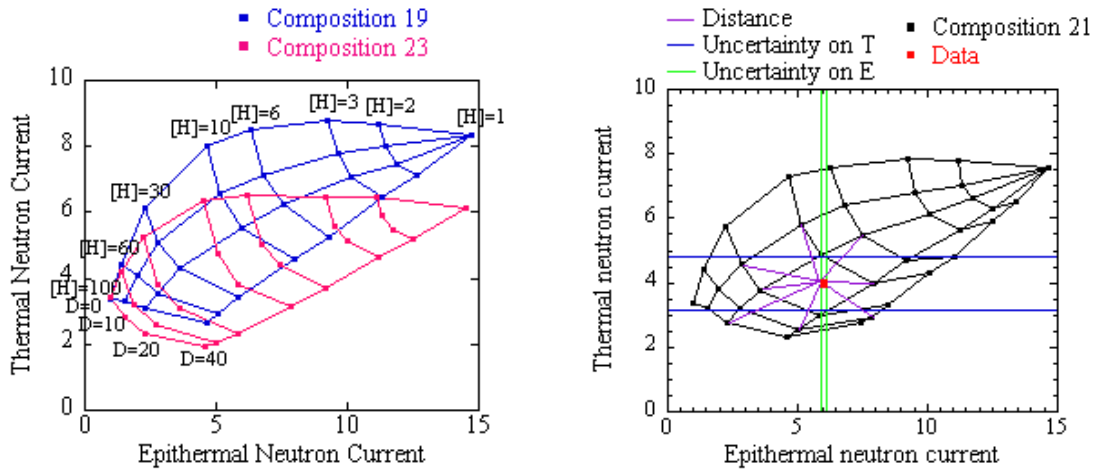

Figure 2.36: Grids of thermal counting rates as function of epithermal counting rates. (Left) Blue squares represent the simulation points obtained with composition 19 and pink squares the simulation points obtained with composition 23. (Right) Black squares represent the simulation points obtained with composition 21. Superimposed in red is a data point such as E=6 and T=4. All distances between this point and the grid are evaluated and plotted in purple (note: for sake of clearness, spline-interpolated points were omitted and only several distances have been represented). The blue line represents the error bar due to uncertainty in thermal neutron currents: 0.20*4=0.8. The green line represents the error bar due to uncertainty in epithermal neutron currents: 0.01*6=0.06.

2.3.3   Sensitivity of MONS to composition

The problem with our chosen method for determining D and [H]dn from MONS data is that some parameters of the thermal and epithermal current simulations have been set to constant values whereas they are likely to vary over the planet. They may therefore considerably affect our results. Among them, the elemental composition is the most significant. Considering separately the variations in the concentration of all chemical elements would lead to a problem of too high a complexity for the data that are available. Moreover these concentrations are only known in sufficient detail at five discrete landing sites at the present time (Viking 1 and 2, Pathfinder, Mars Exploration Rovers Opportunity and Spirit). However, transformation of measured neutron currents to hydrogen abundance and burial depths needs only a determination of the macroscopic energy-loss and absorption cross sections [Feldman et al., 1993]. The macroscopic cross section for a given reaction is the sum of elemental concentrations multiplied by the corresponding cross section for the reaction considered.

To evaluate the range of macroscopic absorption cross sections likely to be encountered on Mars, we calculated these cross sections for all compositions measured in-situ to date [Wänke et al., 2001; Gellert et al., 2004; Rieder et al., 2004]. Their distribution is shown in Figure 2.37. The sensitivity to variability in chemical compositions determined at the two Mars Exploration Rover (MER) sites is given in Table 2.6. These results determine the influence of each elemental concentration on neutron absorption of the soil. The most important elements are seen to be iron, chlorine and sulfur. These fractional contributions may not be very representative of what can be seen by MONS because they reflect the variability of compositions within a very small area, in comparison to the spatial resolution of MONS: 600 km diameter.

	Δ MER in %wt	$\Delta \sum abs$ in m^{-1}	$\Delta \sum abs$ in %
Na2O	2,07	0,02	1,9
MgO	5,29	0,01	0,5
Al2O3	7,7	0,02	2
SiO2	27	0,04	4,1
SO3	27,6	0,11	10,4
Cl	0,55	0,31	29,5
K2O	0,4	0,01	1
CaO	2,21	0,01	1
TiO2	1,34	0,06	5,5
FeO	20,77	0,44	41,6

Table 2.6: Variation of macroscopic absorption cross sections as a function of elemental concentration variation on different measures of soil compositions measured by the MER.

The Gamma Ray Subsystem provides an estimate of composition that is more representative of the MONS spatial scale. Although present GRS results do not cover all chemical elements, the macroscopic cross section can be estimated approximately through knowledge of Cl and Fe which correspond to the largest two absorbing major elements. Th, K and Si are also measured by GRS [Boynton et al., 2007], but for any other element, a constant mean abundance given by measurements made in situ, needs to be chosen. The histograms of macroscopic absorption cross sections found for the separate MER and GRS datasets generally overlap but are a little offset from one another (see Figure 2.37). These calculations provide estimates of the variability of composition on Mars but we keep in mind that they may not be representative of the whole planet because elements such as S, which contribute importantly to neutron absorption, are not presently measured by GRS.
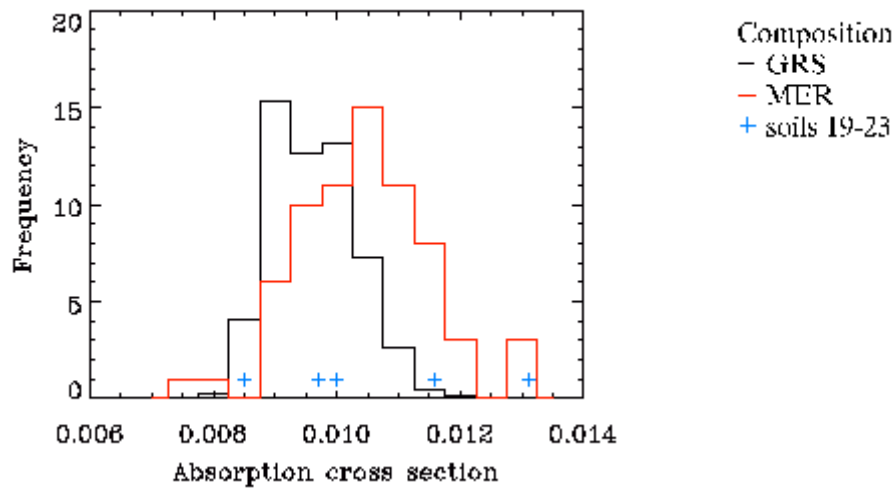
Figure 2.37: Histogram of the macroscopic absorption cross sections. The black line represents the histograms of occurrences estimated from GRS measurements. The blue line represents the histogram of occurrences from soil compositions measured by the MER: Opportunity and Spirit. Frequency scales have been normalized for data to be comparable. Red crosses represent the artificial compositions (soils 19, 20, 21, 22 and 23) created to cover the range of possible macroscopic absorption cross sections.

In order to estimate the uncertainty in determinations of [H]dn and D from neutron observations, five compositions have been created to cover the range of possible macroscopic absorption cross sections. One of these compositions represents the average composition measured at the MER, Viking, and Pathfinder landing sites. This composition (soil 21) is applied in our model to get simulations as representative as possible for the planet. The other compositions are used as benchmarks to assess the effects of the variations in composition on our results.

In order to illustrate the full range of variability in epithermal and thermal neutron currents, the grids for composition 19 and 23 are compared in Figure 2.36. Note that both grids come together at 100% of water-equivalent hydrogen and diverge more and more as the concentration in hydrogen decreases. The method we used to determine [H]dn and D from measured thermal and epithermal neutron current pairs is then applied to estimate the variations in neutron currents induced by different compositions for each pair of [H]dn and D in our simulation grid. The variation in epithermal counting rates due to composition is found to be negligible ($< 1\%$) whereas the variation in thermal counting rates reaches a maximum of 20%.

Because of the difference in magnitude of variation between epithermal and thermal neutron currents induced by the choice of composition, we need to work separately on each measured current to carry forward these variations on the calculations of depth and [H]dn. Each data point of the 2-degree gridded map was superimposed on the simulation grid obtained with composition 21. We adopt the following notation: E_X will stand for epithermal neutron current and T_X for thermal neutron current of the data point X. We define the following distances: the distance

along the epithermal neutron axis between point A and point B equals $\left| E_A - E_B \right|$ and the distance along the thermal neutron axis, $\left| T_A - T_B \right|$. The distances between the data point X and all the spline-interpolated simulation points Y are calculated in terms of distance along epithermal neutron axis and thermal neutron axis.

Unlike neutron current data points, simulation points correspond to known couples of (D, [H]dn). So the distances calculated in terms of couples (E, T) can be transformed to a representation in terms of ([H]dn, D). Figure 2.38 displays an example of the distances calculated between the data point at latitude 50° N and longitude -99° E and all simulation points. The contour color bands in the left part of Figure 2.38 displays the distances calculated along the epithermal neutron axis. The two black lines having positive slope represent the variation of 1% on epithermal neutrons due to composition. The right part of Figure 2.38 displays the distances calculated along the thermal neutron axis. The two black lines having a generally negative slope refer to the variation of 20% in thermal neutrons. These four lines allow the definition of a quadrangle that includes the authorized values of D and [H]dn at a given spatial pixel of the planet. In the example shown, the resulting range is [H]dn min = 17 % WEH, [H]dn max = 28 % WEH, Dmin = 6 g/cm², Dmax = 21 g/cm².
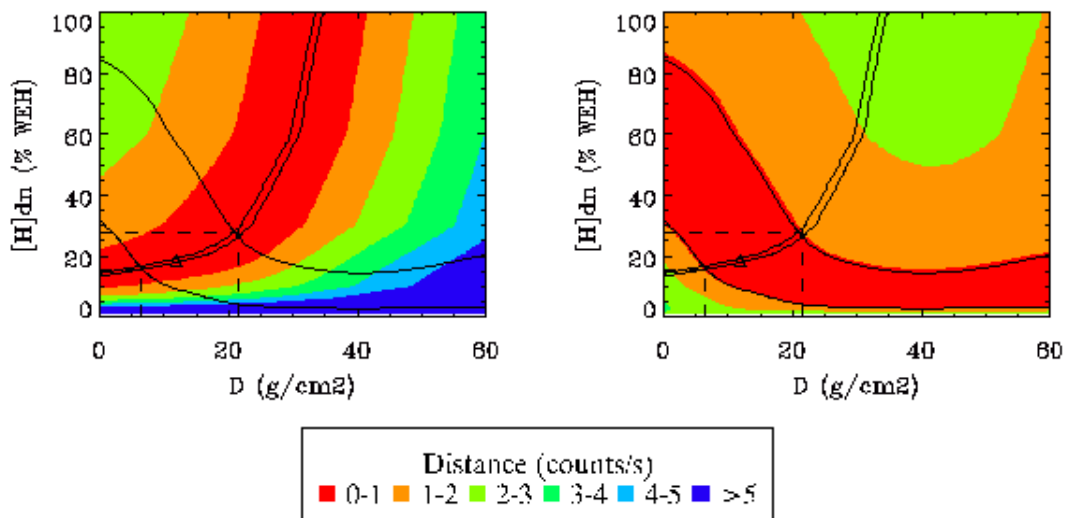

Figure 2.38: Distance between the data point of coordinates (55° N, -99° E) and the simulation points represented in the system of variables (D, [H]dn). (Left) Distance calculated in terms of epithermal neutron currents = $\left|$ Esimu – Edata $\right|$ for all simulation points. (Right) Distance calculated in terms of thermal neutron currents = $\left|$ Tsimu – Tdata $\right|$ for all simulation points. The black triangle represents the solution obtained with the average composition. Black lines represent the uncertainties in neutron currents: 1% in epithermal neutron and 20% in thermal neutron. The central quadrangle therefore represents admissible values for D and [H]dn. Dashed black lines show the definition of the minimum and maximum values of D and [H]dn.

This allows a maximal estimate of the degree of constraint on D and [H]dn due to our lack of accurate knowledge of the soil composition. But the uncertainty in these

results is not uniform over the planet. To assess the quality of the results, the best method would be to calculate the Root Mean Square of each variable D and [H]dn for a distribution of compositions representative of Mars. This method would need too many simulations. On the histogram of compositions (Figure 2.37) we can see that the difference between the absorption macroscopic cross sections of the compositions 20 and 22 give a rough idea of the FWHM (Full Width at Half Maximum) of the composition distribution. Therefore we have calculated the uncertainties on the basis of the parameters obtained with the hypotheses of compositions 20 and 22. To make them relative, we have divided by the parameters calculated with composition 21. So the definition of our relative uncertainty in a given parameter X is: $\left| X_{comp22} - X_{comp20} \right| / X_{comp21}$ with X_{comp20}, X_{comp21} and X_{comp22} standing for: X obtained with the compositions 20, 21 and 22.
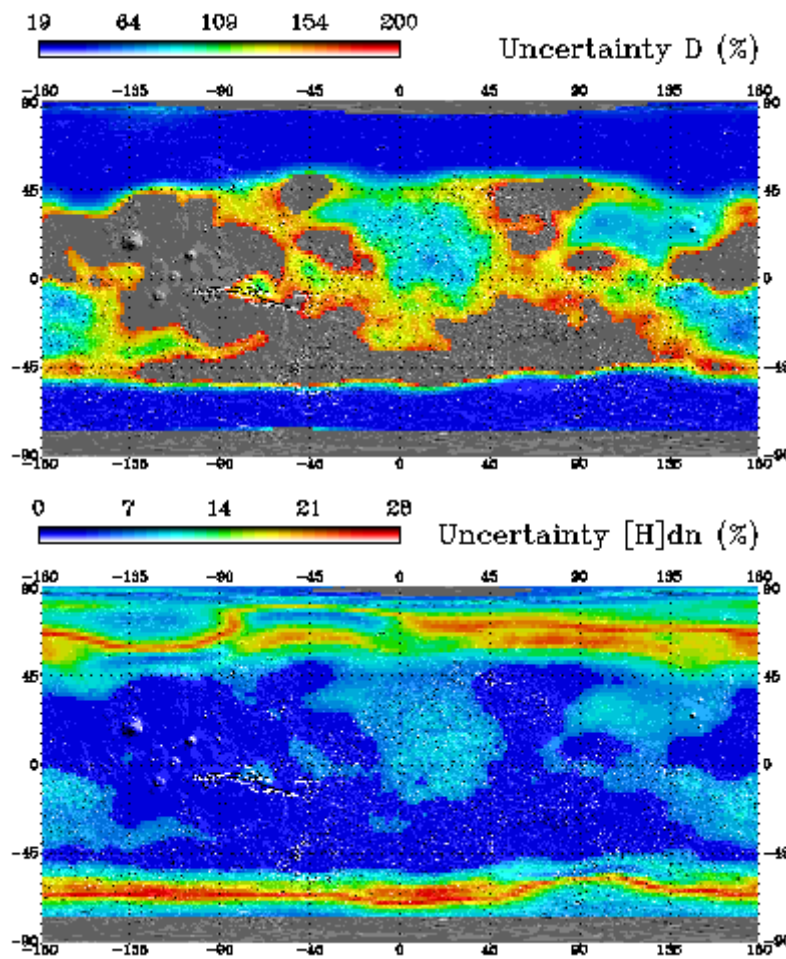

Figure 2.39: (Top) Relative uncertainty in depth = (Dcomp22-Dcomp20)/Dcomp21 for all Dcomp21 > 3 g/cm² (else undefined) in percentage. Dcomp20, Dcomp21 and Dcomp22 are the depths inferred from composition 20, 21 and 22. Whereas composition 21 is the average, the interval between 20 and 22 represents reasonably well the FWHM of the histogram of composition, which makes them appropriate compositions to evaluate the uncertainty. (Bottom) Relative uncertainty in [H]dn = ([H]dn comp22-[H]dn comp20)/[H]dn comp21 for all [H]dn comp21 > 0 (else undefined) in percentage.

The relative uncertainties plotted in Figure 2.39 are defined as $|D_{comp22}-D_{comp20}|/D_{comp21}$ for all $D_{comp21} > 3$ g/cm² (else undefined) and $|[H]dn_{comp22}-[H]dn_{comp20}|/[H]dn_{comp21}$ for all $[H]dn_{comp21} > 0.01$ WEH (else undefined). This uncertainty ranges between 0 and 28% for [H]dn and between 19 and 200% for the depth in most of the regions of the planet. The hydrogen content is seen to be generally better constrained than the depth. This result follows from the fact that the hydrogen concentration is determined mostly by the epithermal neutron counting rates when the depth is not too large, which do not depend strongly on composition. The fact that both thermal and epithermal neutron counting rates are involved in the determination of the depth makes this variable more sensitive to the variations in composition. A comparison of these two maps seems to indicate that the regions that are relatively poorly constrained in terms of [H]dn are well constrained in terms of depth.

2.3.4 Sensitivity of MONS to H content of the upper layer

Another parameter that has an impact on the determination of the layering is the H content of the upper layer. For the inversion of data, the H content of the upper layer has been set to 1% WEH. However it might be higher in some regions [Milliken et al., 2007]. We therefore evaluate the effect of a variation of this hypothesis on the determination of depth and H content of the lower layer. In order to estimate the uncertainty, we test three different values for [H]up: 1%, 2% and 5% WEH. These different hypotheses correspond to different simulation grids. We calculate an uncertainty on the basis of the results obtained with these grids. The uncertainty is defined using the same prescription as was used previously: $|X_{5\%}-X_{1\%}|/X_{2\%}$ with $X_{1\%}$, $X_{2\%}$ and $X_{5\%}$ standing for: X obtained with the [H]up contents of 1%, 2% and 5%.

These uncertainties are not defined for the whole planet. To calculate them, we need to perform the inversion with all hypotheses. However, many data points move from inside to outside the grid when the [H]up hypothesis is changed. Figure 2.40 shows an example of this problem. The simulation grid obtained with the hypothesis [H]up=1% is plotted in red triangles and that obtained with the hypothesis [H]up=5% is plotted in blue crosses. Superimposed are the measurement points comprised between latitudes -45° and 45°. Many points are outside the grid meaning that no solution can be found with the model we tested. The points that are at the right of the black line have a general H content lower than 5%. They therefore cannot be modeled with an upper layer containing 5% WEH. The points that are above the grid have a higher thermal neutron current than our simulations, which means that the composition they leak from is depleted in strong absorbers in regard to the composition we used in the simulations. We also see that many points that were inside the grid for [H]up=1% go out of the grid with the hypothesis [H]up=5%. While we cannot determine layering at these locations, we can at least give constraints expressed by the fact that the hypotheses chosen for a certain model give results comparable to what is measured or not.
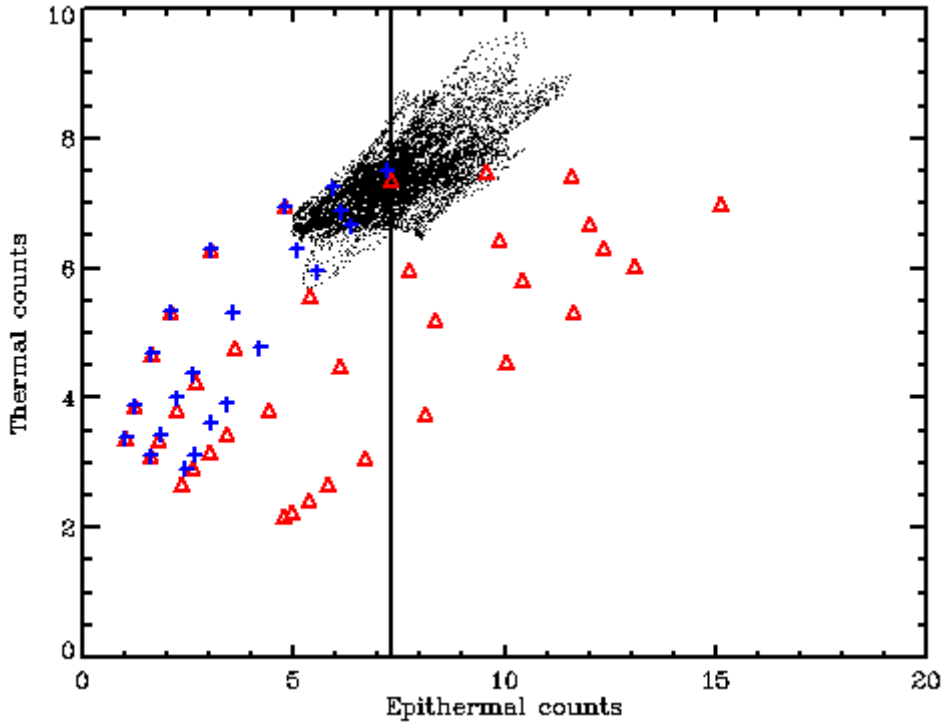
Figure 2.40: Simulation grids for (red triangles) [H]up=1% and (blue crosses) [H]up=5%. Superimposed in black dots are the data points for latitudes between -45° and 45°. The vertical line symbolizes the limit where the general H content equals 5% WEH. The points at the right of this line can therefore not be modeled with an upper layer containing 5% WEH.

The relative uncertainties plotted in Figure 2.41 are defined as $|D_{1\%}\text{-}D_{5\%}|/D_{2\%}$ and $|[H]dn_{1\%}\text{-}[H]dn_{5\%}|/[H]dn_{2\%}$. The equatorial region was removed from the map because the global hydrogen content there is low, making it difficult to define layering when [H]up and [H]dn are comparable. This uncertainty reaches 28% for [H]dn and 92% for the depth in the polar regions. This is quite a high value of uncertainty; however it is an upper limit because the H content in the upper layer on the thickness scales that match the sensitivity of neutrons (centimeters) is likely lower than 5%.

The first conclusion is that our data at equatorial regions do not allow a layering having an [H]up greater than 2%. The possible configurations are either: a single semi infinite layer or a two layers configuration with an upper layer with 1% or 2% WEH or a more complex configuration. The second conclusion is that a variation of [H]up has great impact on the results of our inversion in places. However the maximum impact is localized to a thin region of transition between polar and equatorial regions where the apparent burial depth is largest. The uncertainty at very high latitudes is very modest (lower than 7% for [H]dn and lower than 20% for the depth).
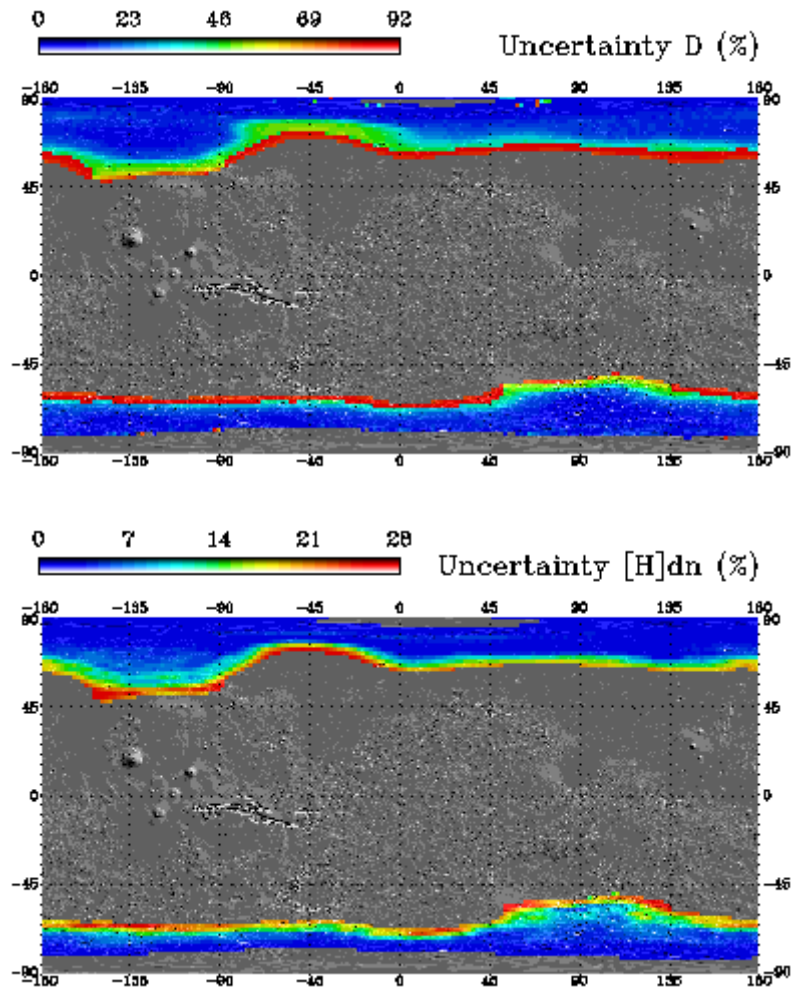
Figure 2.41: (Up) Relative uncertainty in depth = │D5%-D1%│/D2% in percentage. D1%, D2% and D5% are the depths inferred from [H]up 1%, 2% and 5%. (Down) Relative uncertainty in [H]dn = │ [H]dn5%-[H]dn1%│/[H]dn2% in percentage. Uncertainties defined where the total H content is higher than 8% WEH.

2.3.5 Sensitivity of MONS to heterogeneity

The Neutron Spectrometer of Mars Odyssey has a large spatial response function. So the signal received by the instrument is very likely a mixture of signals coming from sub regions with different characteristics, which can have: different H contents, different chemical compositions or different layering (meaning the burial depth is variable). However the transformation from epithermal neutron count rates to Water Equivalent Hydrogen content is not linear. The transformation from epithermal and thermal counting rates to layering information is also not linear. Therefore the H content interpreted from neutron currents from a heterogeneous region will not be the linear combination of the H contents of the sub regions. We want to estimate how large the difference between real H content and measured H content can be, and which area subdivisions are the most badly estimated.
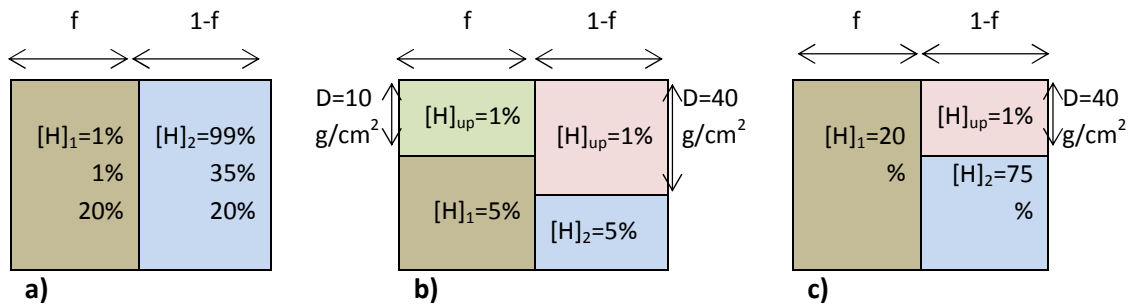
85

Figure 2.42: Scheme of the different configurations tested in part 4.

We first test the behavior of the signals in the case of single semi infinite layer. The configuration tested is made of the mix of a region with a low H content $[H]_1$ and a region with a high H content $[H]_2$. Figure 2.42a provides a schematic illustration of this configuration. The composition is set constant except for the H content that is allowed to vary. The mixing ratio f is the fraction of $[H]_1$ over $[H]_2$ and varies from 0 to 1. We evaluate the epithermal neutron currents emitted by the different sub regions and the resulting signal seen by the instrument. We define the "seen" H content as the H content obtained with inversion of this resulting epithermal neutron signal. We define the "real" H content as the average H content of the sub regions of the area. The error is defined as the difference between the seen and real H content. For each configuration we calculate the seen H content, the real H content and the error. These variables are plotted on Figure 2.43a for a configuration where $[H]_1=1\%$ and $[H]_2=99\%$ and with the fraction f varying between 0 and 1.
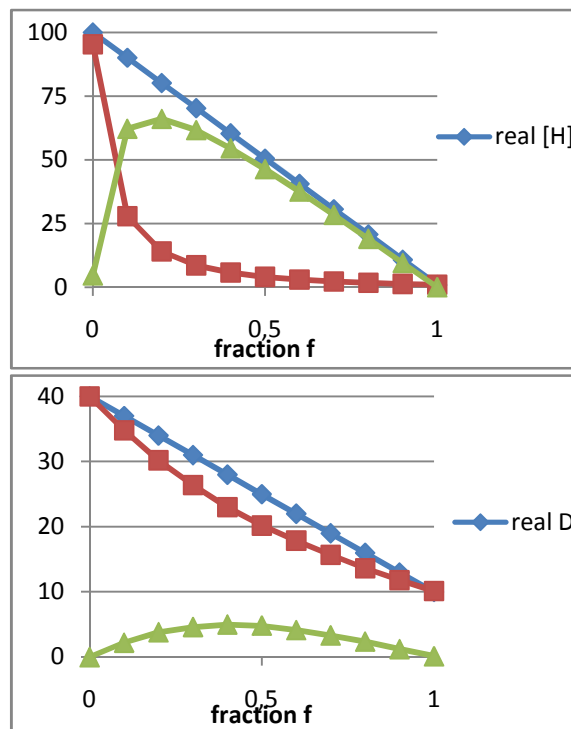

Figure 2.43: a) Real H content, seen H content and error for configuration a. b) Real depth, seen depth and error for configuration b.

86

After testing several configurations, we can draw some general conclusions. Regions made of a mix of different H contents systematically underestimate the real H content. The error made in this underestimation depends on the ratio between the different sub regions as well as the H content of these regions. It reaches a maximum at a ratio of 0.30. The error also depends on the difference between the H contents of the sub regions. The larger the gap between the H contents, the larger the error. A higher error is obtained in the case where the smaller fraction corresponds to the lower H content. Figure 2.43 displays the worst case of the studied configurations, and shows that the error can reach a maximum of 65%.

To evaluate the effects of heterogeneity on the estimation of the layering the process is less straight forward. We will model an area with a two layer model. The parameters of this model are the H content of the layers and the thickness of the upper layer. They are obtained by inversion of the epithermal and thermal count rates in making assumptions about the last parameter. Here the H content of the upper layer is set to 1%. We evaluate the effects of heterogeneity on depth (we do not need to reevaluate the effects on the H content because the preceding case already gives an upper limit of the error). The region seen by the instrument is subdivided into 2 regions. They both are made of two layers and have the same H contents (a dry layer with 1% WEH over a layer rich in H). Figure 2.42b shows a schematic diagram of this configuration. We define a "real" depth as the linear combination of the depths of the sub regions of an area. Both thermal and epithermal neutrons are evaluated in the sub regions and in the total area. The "seen" depth is obtained on the basis of an inversion performed with the resulting thermal and epithermal count rates. These variables are plotted in Figure 2.43b for a configuration where $[H]_1 = 1\%$ and $[H]_2 = 5\%$ and with the fraction f varying between 0 and 1.

The new conclusions drawn by these cases are the following. The error on depth is maximum for the lowest H content and for different fraction values. This can be explained by the fact that the layering is harder to detect by the instrument. The real depth tends to be underestimated most of the time. However the error is lower than 5 g/cm². Regarding our uncertainties on depth, this type of error is quite negligible. A mixing of depth seems to induce lower errors than a mixing of H content.

The largest region of heterogeneity known on the planet is the transition between the polar regions made of water ice rich material and the equatorial regions made of desiccated material with hydrated minerals (or hydrogen with another molecular association than ice). We investigate a configuration that mimics this transition: an area subdivided into a simple semi infinite region with a quite low H content (the equatorial region) and a region with 2 layers of different H content (the polar region). We test a wide gap between $[H]_1$ and $[H]_2$ to evaluate the upper bound of error. Figure 2.42c displays a schematic representation of this configuration. We calculate the real depth, the seen depth and the error for different fractions of these materials. We also calculate the real H content, the seen H content and the error for this variable. In agreement with the preceding conclusions, the depth seen by the instrument is lower than the real depth. The error reaches a maximum of little more than 10 g/cm².
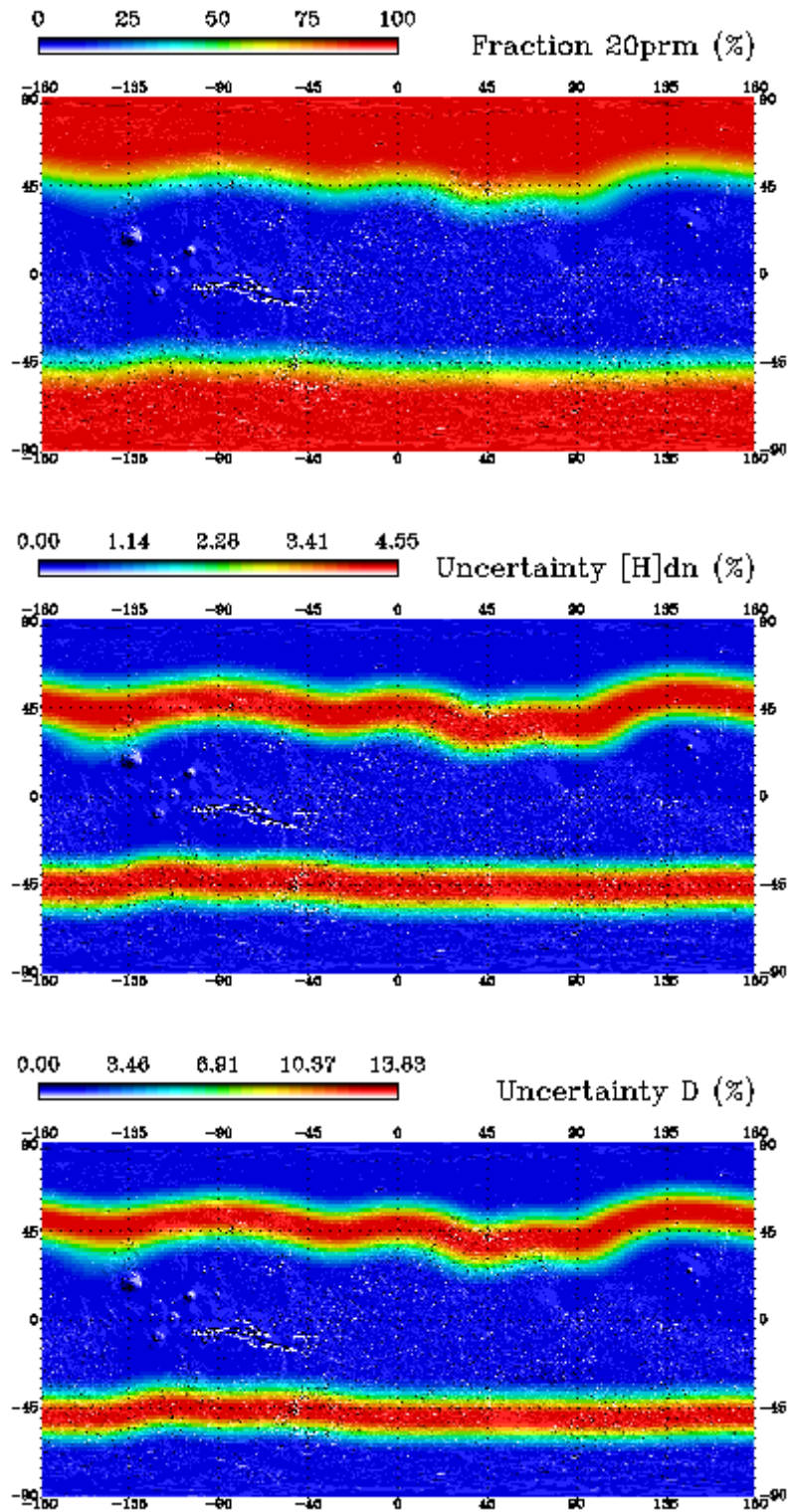
Figure 2.44: a) Fraction of soil occupied by a layered material rich in H as seen by the neutron spectrometer. b) Relative error due to heterogeneity on H content in percentage. c) Relative error due to heterogeneity on depth in percentage.

We now need to estimate which fraction of the two different materials is seen by our instrument when flying over the transition between the polar regions and the equatorial regions. Mellon et al. [2004] implement a model that determines the equilibrium ice table depth as a function of temperature and humidity. In addition to this depth, a fraction evaluating how much area of the ground could sustain water ice was calculated. Both depth and fraction were calculated for two different values of mean content of water vapor in the atmosphere (10 pr µm and 20 pr µm) at zero km altitude. To estimate the fractional weight actually occupied by each of the sub regions we have defined, we use Mellon's estimation of the fraction of soil where water ice is stable for the hypothesis 20 pr µm. We keep in mind that it doesn't mean necessarily that water ice is sustained in those locations. However it gives an idea of what could be the fraction of ice rich soil if the ground of Mars is occupied by ice where the model predicts its stability.

The FWHM spatial resolution of the instrument is about 10°. In order to make the 1 degree gridded fraction calculated by Mellon et al. [2004] comparable to the field of view seen by our instrument, we need to convolve the theoretical fraction with a function that models the response of the MONS instrument. We define this response function as a two dimensional Gaussian function of the size of our resolution. The fraction of area where ice is stable obtained after the convolution by the response function of the instrument is mapped in Figure 2.44a. This fraction corresponds to an error in the H content and in the depth. We have previously calculated the relationship between the fraction of soil occupied by a sub region and these errors. These results are interpolated for all values of fraction found on the map. We obtain maps of the error in depth and in H content due to heterogeneity. Finally, errors are converted in relative errors for easier comparison with the preceding sections. We have chosen a configuration describing the worst case, so those errors are upper bounds.

Figure 2.44b shows that the relative error in the estimation of the global amount of H in the soil is systematically lower than 4.6 %. This value is very reasonable compared to the other sources of uncertainty. The H content is systematically underestimated; therefore it could be generally higher than what is estimated in the region of transition around 45° of latitude. The estimation of depth can be more affected by the heterogeneity: Figure 2.44c shows that the error on depth can reach 13.8%.

2.3.6 Results and discussion

We have analyzed the different sources that could account for uncertainty. The uncertainty due to composition is high in the equatorial regions and modest-to-low at high latitudes. The uncertainty due to the H content of the upper layer is not defined at equatorial regions because the total H content is not high enough to define properly a layering with a high H content in the upper layer. However it is modest-to-low at high latitudes. It increases as latitude decreases. The uncertainty due to heterogeneity is high in the region of transition between equatorial regions and polar regions. However it is not completely unknown. It has been shown that the depth is underestimated. Consequently the variables determined with our procedure can be considered of high

quality near the poles, of reasonable quality at latitudes around 45° (with a high probability that the estimated depth is lower than the true depth) and cannot be trusted at equatorial latitudes.

The confidence in the estimated depth may appear quite low in many regions. However this has to be qualified. Having a poorly constrained depth in the equatorial regions (latitudes lower than ±45°) where the hydrogen content is low is to be expected because the boundary between desiccated and water rich layers is not pronounced. Near the poles the determination of the depth is more certain because the non-hydrogen component of the soil mass fraction is sufficiently small that details of its composition are not important.

Upon completion of the analysis presented in part 2, we generated maps of the apparent depth (Figure 2.45) and H content of the water-rich layer (Figure 2.46) with a model made of an average composition (soil 21) and an H content of the upper layer of 1% WEH. Our inferred depth exhibits a sharp latitudinal pattern. For latitudes poleward of ± 60° the behavior is that expected for buried water ice: the depth follows qualitatively the latitudinal variations predicted by Farmer and Doms in 1979. For the latitudes equatorward of ± 60° the depth is not sensitively defined. When the H content is too low, our uncertainties grow high and the depth cannot be constrained. It has therefore not been represented on the map.

Our inferred H content of the lower layer has a behavior very similar to that of the general H content previously published [Feldman et al., 2004]. This is not surprising considering the fact that the H content of the upper layer was set to a constant value. However it is likely to change over the planet, which would change our interpreted H content of the lower layer.

Because of the uncertainties, our procedure fails to provide a numerical value for depth or H content of the lower layer within the equatorial latitudes. We compare the measured data to the simulated data. Simulations are available for the following hypotheses: [H]up of 1, 2 and 5% WEH. We superpose the equatorial measurements on these simulation grids. We infer from this superposition which of the models can reasonably describe the material in which the neutron signal is produced. We synthesize the values of [H]up that suit the observation in Figure 2.47. The map only qualifies the adequacy between our measurements and chosen simulations, and does not provide unique solutions.
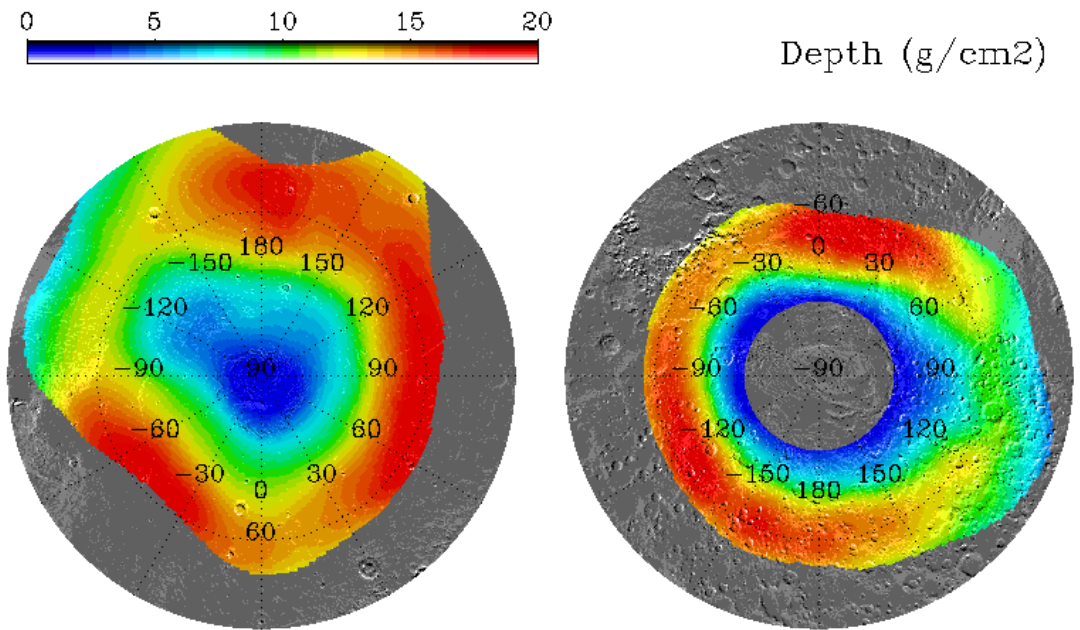
Figure 2.45: Depth of water-rich layer in g/cm² on stereographic projection. Note: the regions where the H content is lower than 8% WEH were excluded due to their high uncertainties. The South Pole is not represented due to the presence of a permanent CO_2 ice cap which contaminates the thermal neutron signal.

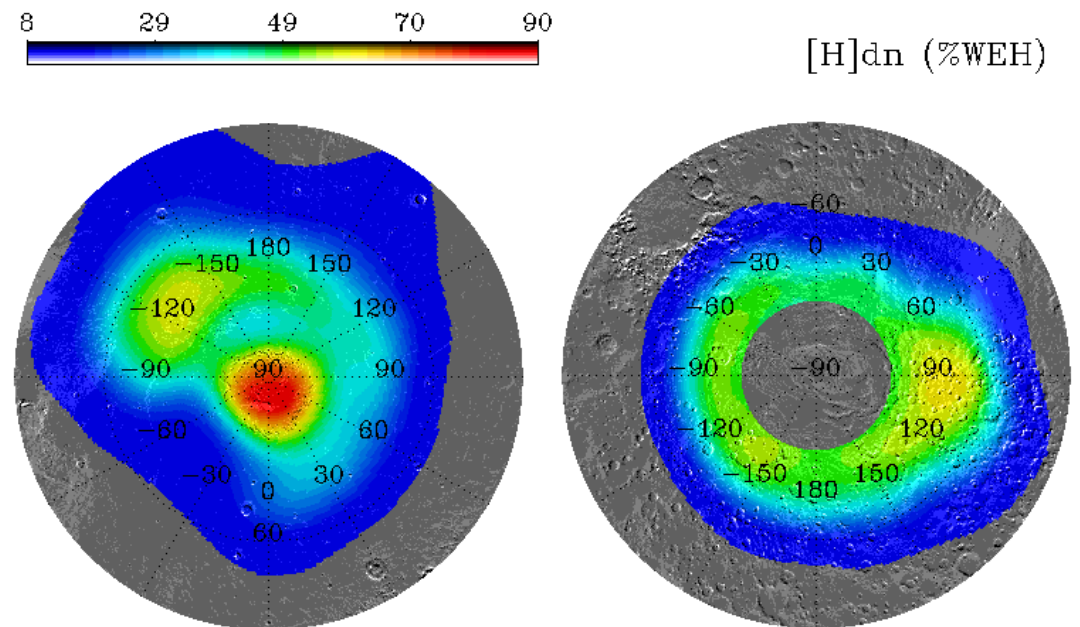Figure 2.46: H content of the water-rich layer in %WEH (mass fraction of Hydrogen when assumed to consist in H_2O) on stereographical projection. Note: the regions where the H content is lower than 8% WEH were excluded due to their high uncertainties. The South Pole is not represented due to the presence of a permanent CO_2 ice cap which contaminates the thermal neutron signal.
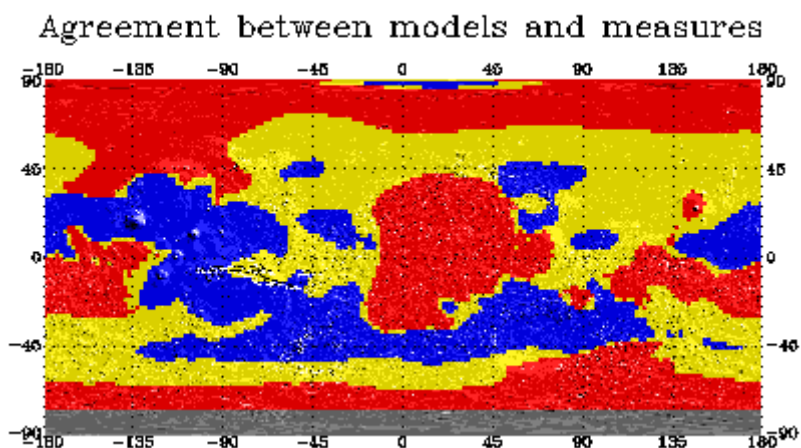
Figure 2.47: Schematic representation of the constraints on [H]up provided by the neutron data. Blue regions cannot be described by a two layer model. Yellow region do not admit the 5% WEH hypothesis but allow the 1% and 2% WEH hypotheses. Red regions admit layering with all [H]up hypotheses.

The blue regions represented in this map do not lend themselves being modeled with the two-layer model tested. The first conclusion is that these regions have probably no H layering. The layering might also be more complicated than in the tested model. Another interpretation could be that the composition hypothesis is not valid: the high thermal neutron current indicates that the composition is likely depleted in strong absorbers (such as chlorine, iron or sulfur). The yellow regions can be modeled with a two-layer model only if [H]up is 1% or 2% WEH. The conclusion is therefore that they are either not layered, or layered with an upper layer depleted in H. The red region can be modeled with a two layer model. In this last case, we can conclude our measurement is permissive of all [H]up hypotheses tested. However if the H content of the two layers are too similar, the layering will not be detected by our method of data inversion.

A byproduct of our procedure is the evaluation of the minimum and maximum values of D and [H]dn allowed by the compositional uncertainties. We set the H content of the upper layer to 1% WEH in this analysis. These constraints are important to help determine the nature of the buried hydrogen measured by MONS. The knowledge of the minimum and maximum concentration of water contained in the region equatorward of 60° is particularly important considering the fact that water ice is not expected to be stable equatorward of about 45° latitude [e. g. Feldman et al., 2005 and references therein]. This information can indeed discriminate between whether or not hydrated minerals can be sustained. Providing complete data of minimum and maximum H content and depth would not be possible. We only provide several examples here: Arabia Terra and Medusae Fossae are found to have [H]dn possibly ranging between 8% and 11.6% WEH; the Cerberus Plains, Chryse Planitia and Argyre Planitia have an H content as low as 1.8% to 3%.

2.3.7 Comparison of the neutron results with theoretical models

Whereas the nature of the hydrogen measured at equatorial latitudes remains uncertain (adsorbed water, hydrated minerals?), the nature of the hydrogen polar reservoirs is known to be mostly water ice because the hydrogen abundance there is so large [e.g. Boynton et al. 2002; Feldman et al., 2002b; Mitrofanov et al., 2002]. We now focus on these high-latitude water ice deposits.

The stability of volatiles on Mars was first studied in 1966 by Leighton and Murray. Afterwards many studies have brought considerable insight into the mechanisms that determine ground ice stability [e. g. Fanale, 1976; Farmer and Doms, 1979]. Longitudinal dimension has since been added to the original latitudinal studies [Paige, 1992], and finally, latitude-longitude theoretical maps of the ice table depth and abundance have been made [Mellon and Jakosky, 1993]. They have been compared to the measurements provided by MONS [Boynton et al., 2002; Prettyman et al., 2004b; Mellon et al., 2004; Schorghofer and Aharonson, 2005]. The comparisons of MONS to the vapor diffusion models were largely qualitative and mostly take into account the ice content determined thanks to the Neutron data. We now compare our maps of burial depths to those predicted by these models.

We extend the work of Prettyman et al. [2004b] at high southern latitudes using our transformation technique. The intercomparison between measurements and theoretical models is difficult in part because of the large spatial response function of the MONS instrument. In addition, the models only pertain to water ice and do not account for hydrated mineralogies. The Neutron Spectrometer does not discriminate between the different forms of hydrogen. We have therefore used a boundary value of [H]dn that splits the reservoirs in three (high northern latitudes, equatorial latitudes, high southern latitudes). A limit of 11% was chosen because it corresponds roughly to the location where the variation of depth with increasing latitude changes sign. These regions correspond to relatively low uncertainties, which means our depth data is of good quality.

Two theoretical sets of ice table depths are used for the intercomparison between theory and experiment [Mellon et al., 2004; Schorghofer and Aharonson, 2005]. The Mellon et al. [2004] model provides the ice table for two different values of mean content of water vapor in the atmosphere (10 pr µm and 20 pr µm) at zero km altitude. This dataset is gridded with a resolution of 1×1 degree (longitude × latitude). The Schorghofer and Aharonson [2005] model is gridded with a resolution of 5×1 degrees globally and a refined resolution of 5×0.25 degrees at latitudes between 45° and 65° in both hemispheres. Both models determine the equilibrium ice table depth as a function of temperature and humidity. They determine whether ice is stable or unstable irrespective of how the ice was emplaced. The two models differ in their treatment of the atmosphere and in the implementation of diurnal cycles.

In order to intercompare datasets, we need to convolve the theoretical models with a function that models the response function of the MONS instrument. The spatial response function of the instrument is about the same for thermal and epithermal neutron currents. In order to simplify the problem, we make the assumption that this function can be applied directly to the depth. The results should be satisfactory in the

case of little geographic variations. The FWHM spatial resolution of the instrument is about 10° (and 10° divided by cosine of latitude along the longitudinal axis on a cylindrical projection) but using such a large value eliminates too many theoretical points (which drop off sharply equatorward of about ±60° latitude in both theoretical models). To simplify the definition of the kernel, we neglect the change of the longitudinal width with latitude and take the FWHM along the longitudinal direction to be 20 degrees, the value appropriate at 60 degree latitude. Therefore, all theoretically simulated depth tables have been convolved by a two-dimensional Gaussian function having 20°×10° FWHM (longitude × latitude), the tails of which being cut to keep values greater than 30% of the maximum. This compromise allows smoothing the theoretical depths with a function that models quite well the response function of the instrument while keeping more points available for comparison than with the true response function.

The experimental-theoretical intercomparison is implemented by a chosen set of meridional cuts. The depth values have been averaged over 5 degree large bands of longitude and are shown in Figure 2.48. Original theoretical depths are superposed upon the convolved ones in order to see the effects of the process applied to them. To perform the convolution, a square of data is needed around each point. Therefore we do not have convolved depth values equatorward of about ±60°. Moreover there can be no determination of depth with the neutron spectrometer poleward of about -75° because of the perennial presence of the CO_2 ice cap near the south pole and poleward of +85° because of the inclination of the spacecraft orbit. No theoretical depths were calculated poleward of ±75° so we have arbitrarily set these depth predictions to 0 during convolution.

The error bars correspond to the compositional uncertainties on the latitudinal cuts, which are used to determine the agreement of the theoretical models to the MONS depths. A comparison of the MONS depth profiles with the two models display a wide variety of results. Several examples are presented in the form of three meridional cuts in Figure 2.48. They illustrate the different cases encountered:

- agreement of MONS depth with the two models (e.g., high southern latitudes for longitude 60°)
- agreement of MONS depth with the model of Schorghofer and Aharonson [2005] (e.g., high southern latitudes for longitude -110°, high northern latitudes for longitudes 20° and 60°)
- agreement of MONS depth with the model of Mellon et al. [2004] (e.g., high northern latitudes for longitude -110°)

In terms of variation along the same meridional cut, the fits between MONS and theoretical depths seems to get worse equatorward of about ±65° because MONS depths turn over and then decrease while all model depths increase.
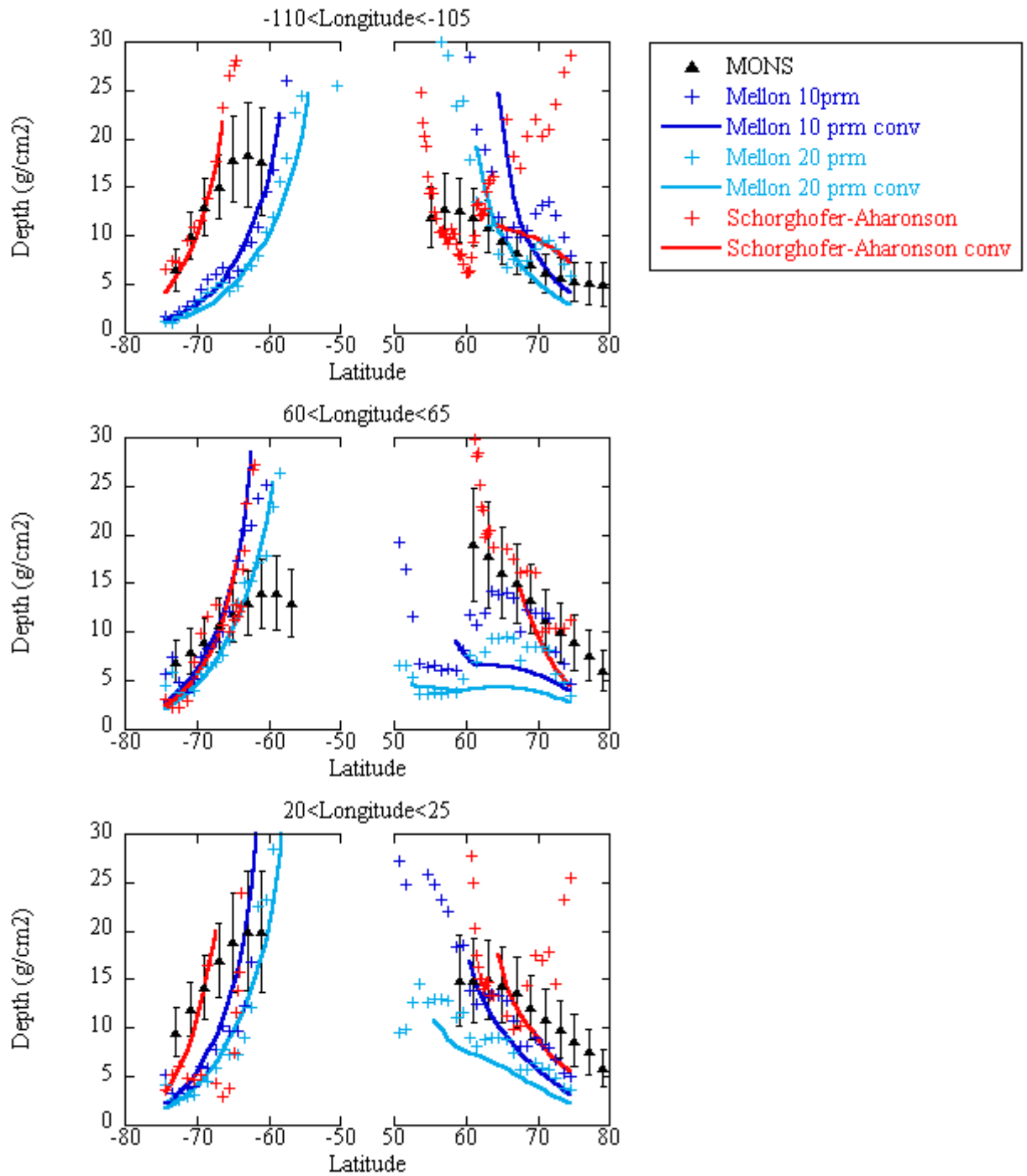
Figure 2.48: Depth of water-rich layer in g/cm² along 3 latitudinal cuts corresponding to different longitudes zones. Triangles represent the depth inferred from MONS and black lines their error bars associated. Red lines are convolved depth data from Schorghofer and Aharonson [2005]. Blue lines (two tinges for two water vapor content hypothesis) are convolved depth data from Mellon et al. [2004]. Red crosses are depth data from Schorghofer and Aharonson [2005] in the longitude zone considered. Blue crosses are depth data from Mellon et al. [2004] averaged in the longitude zone considered (5 data points averaged to 1).

Figure 2.49: Relative error in percentage between depths inferred from MONS and ice table depths from (Top) Schorghofer and Aharonson [2005] and (Bottom) Mellon et al. [2004] for the water vapor content hypothesis 10 prm. Green to red represents regions of bad agreement between the MONS measures and the models.
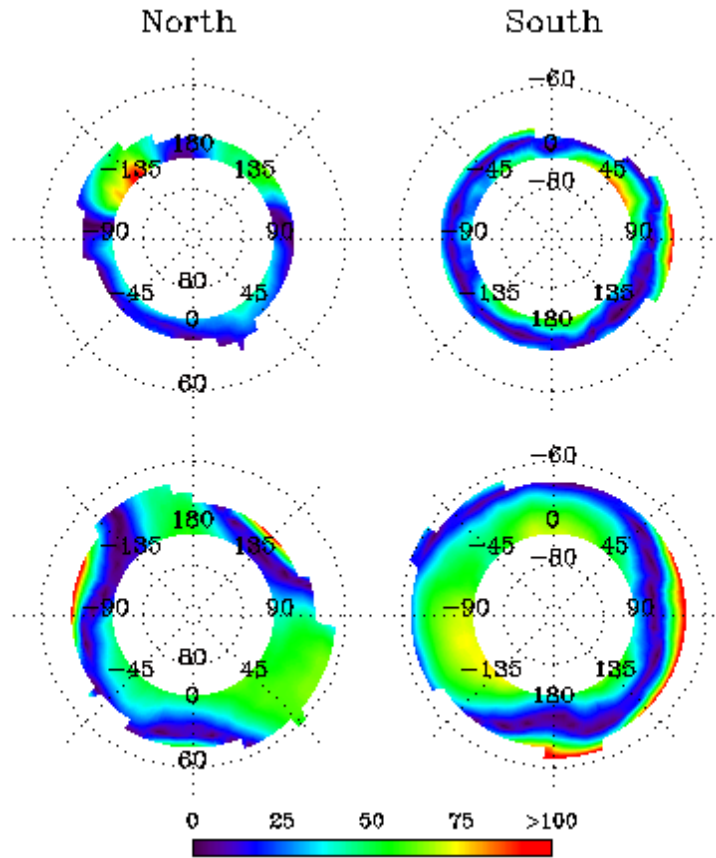
The variety of cases shown in Figure 2.48 highlights the necessity for mapping a quantitative measure of the difference between the measured depths and the models. We have therefore calculated the relative difference between the depths inferred from MONS and the three prediction datasets. Figure 2.49 shows respectively │MONS – Schorghofer and Aharonson│/ MONS and │MONS – Mellon 10 pr μm │/ MONS. These maps give a global representation of the quality of agreement between depths inferred from MONS and the ice table depth determined by the three models. The comparison of the two theoretical models was also performed and revealed that the predicted ice table depths of Mellon et al. are consistently shallower than those of Schorghofer and Aharonson.

As a general rule, the fits with Mellon et al. and Schorghofer and Aharonson get worse equatorward of about ±65°. This statement can be interpreted as due to the convolution of the MONS signal with regions where the ice is not stable. The modeled depths generally display a monotonic increase with decreasing latitude because they only refer to the ice reservoir. The neutron depths decrease with decreasing latitude as

expected for the addition of a reservoir of hydrogen having another molecular association than ice. The latitudinal transition boundary of MONS depths is broad, partly because of the broad spatial response function of the instrument. A likely explanation of the fact that the depth we observe with MONS is not comparable to that calculated in terms of ice stability at mid latitudes is that the hydrogen measured by MONS may consist of a mix of water ice and hydrated minerals at these locations.

At southern latitudes poleward of -65°, the MONS depths are very close to those of Schorghofer and Aharonson [2005]. Their differences are generally larger at a few specific longitudes: between 20° and 80°. In contrast, the depths calculated by Mellon et al. [2004] and those measured by MONS display the same general trend with latitude but their differences are globally larger. These fits are generally good but questionable between longitudes -140° and -90° and between -20° and 20°.

At high northern latitudes, the agreement between MONS results and the models is more variable regarding longitude. Several reasons may be responsible for the differences observed. The first has already been mentioned: if the water ice reservoir detected by MONS is contaminated by hydrated minerals the depth interpreted from neutron data using a simple two-dimensional model will not be correct. For example, a layering of composition could change dramatically the results of the inversion of neutron currents. The neutron depth inferred would then be erroneous. Another interpretation would be that the theoretical model used by Mellon et al. and Schorghofer and Aharonson does not reflect the reality. A complex layering of rock, dust and partially cemented soils in the ground would change the behavior of thermal inertia and give different results in terms of ice table depth. Up to now, no information allows us to discriminate between these hypotheses.

2.3.8 Conclusion

We have proposed a method to evaluate two major parameters in the characterization of the layering of soil hydrogen content: the hydration content of a lower, water-rich layer and its burial depth. This method provides us with global maps of these two parameters. These results have been assessed by estimating the effects of uncertainties in chemical composition on the transformation of the measured neutron currents to burial depths and [H] abundances, and by inter-comparison with theoretically predicted depths of water ice at high latitudes. The first step was the evaluation of the impact of the most important hypothesis involved in the model that is required to interpret the neutron currents: the composition. This process has enabled us to estimate an uncertainty index associated with the variables of interest. During the last part of our study, we have shown that the depth inferred from MONS proves to be generally close to that predicted by models of stability of water ice at high latitudes. However the fits between the data and the models are not uniformly excellent and the interpretation of the cause for the differences remains uncertain.

2.4 Contribution of Mars Odyssey GRS at Central Elysium Planitia

[1]CESR, Université Paul Sabatier, CNRS, Toulouse, France
[2]Planetary Science Institute, Tucson, AZ
[3]IDES, Université Paris Sud, CNRS, Orsay, France
[4]LDTP, Observatoire Midi-Pyrénées, Université Paul Sabatier, CNRS, Toulouse, France

2.4.1 Introduction

The comparison of neutron signals measured by the Neutron Spectrometer to geological maps [Scott and Tanaka, 1986; Greeley and Guest, 1987] highlights a particular correlation in the region of Central Elysium Planitia. By Central Elysium Planitia we refer to the flat and smooth area south east of Elysium Mons, also known as the Cerberus Plains. The most recent volcanic unit within Central Elysium Planitia indeed corresponds to a local maximum of neutron emission in all three ranges of energy. This correlation makes this region an especially interesting object regarding neutron interpretation. Such a maximum constrains the chemical composition and H content of the material in which the signal is produced.

As the gamma subsystem onboard Mars Odyssey also constrains the composition, this study aims to inter-compare the compositional constraints provided by these two instruments. The first step is the identification of the geological unit from where the anomaly originates. Particular attention will be paid to two lines of evidence: the geologic knowledge of this region built from other experiments and the difference of spatial structures seen by the GRS GS and GRS NS instruments. This analysis will lead us to deepen our understanding of the actual structure of the region through integration of the information collected by these two instruments.

2.4.2 Central Elysium Planitia

Early work [Plescia, 1990 and references herein] suggested that the Cerberus Plains have a volcanic origin and a large number of volcanic features have been documented subsequently. In addition to these features, a large variety of geological structures indicate a complex history, also involving tectonic and fluvial processes [Tanaka, 1986]. Most studies focus on the analysis of volcanic episodes involved in the formation of the different geologic units of the area [i.e.: Plescia, 1990; Lanagan et al., 2001a] or on the recent water flows and their interaction with the lavas [i.e.: Burr et al., 2002; Berman and Hartmann, 2002; Head et al., 2003; Plescia, 2003]. The low viscosity of these lavas partially explains the exceptional surface smoothness of this region. This

smoothness results also from the young ages, some of them below a few millions of years, as determined by crater counts [Hartmann et al., 2000; Burr et al., 2002; Vaucher et al., 2008, in revision].

Alternative scenarios of formation have been proposed. Murray et al. [2005] and Page [2008] defend the hypothesis of a frozen sea. However this theory would imply a high concentration of hydrogen at shallow depth, which is not consistent with the observations of the neutron spectrometer. This latter data reveal a very dry surface (among the driest regions of the planet). And as will be seen in the discussion, the compositional information retrieved from the GRS states in favor of basaltic origins, in agreement with Jaeger et al. [2007, 2008] conclusions.

The topography of Elysium Planitia as revealed by the MOLA experiment (Figure 2.50) shows that the volcanic unit is very flat and very smooth at three different scales: 0.6 km, 2.4 km and 19.2 km [Kreslavsky and Head, 2000]. At a smaller scale (decimeter scale), the region is shown to be very rough by earth-based 12.6 cm Arecibo radar data [Harmon et al., 1992]. These observations are consistent with a lava flow texture, while the smoothness at large scale suggests the widespread occurrence of low viscosity lavas. The possible emplacement styles of the flows have been extensively discussed [i.e.: Keszthelyi et al., 2000; Plescia, 2003] and include both flood lavas and plains style volcanism.

The map derived from MGS-TES data [Putzig et al., 2005] reveals that Elysium Planitia generally has a thermal inertia below 100 J m^{-2} s$^{-1/2}$ K^{-1} (Figure 2.51). Such a low inertia implies an at least partial dust or sand covering. This mantling probably results from the deposition of surficial material over the fresh lavas by atmospheric processes [Mellon et al., 2000, Putzig et al., 2005].
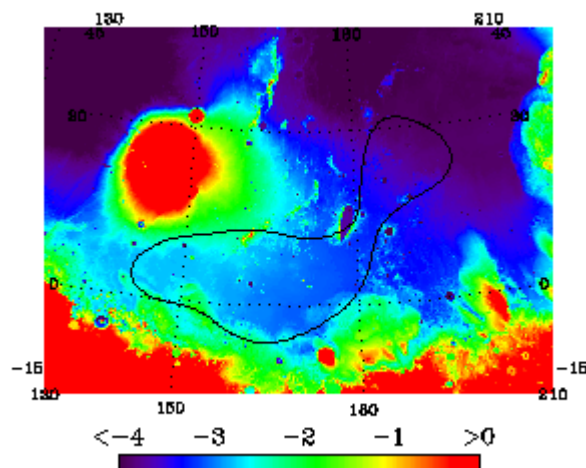

Figure 2.50: Topography measured by MOLA. Cylindrical projection centered on the coordinates: latitude 15° and longitude 170° (note: parallels and meridians appear curved because the projection is not centered on the equator). Superimposed are contours of our region of interest.
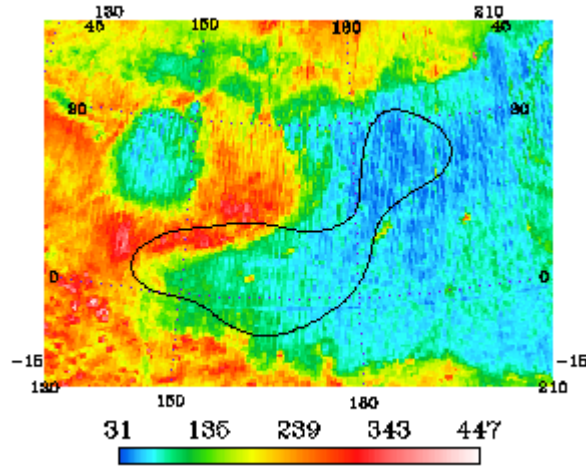
Figure 2.51: Thermal inertia map in J m-2 K-1 s-½ derived from the MGS-TES dataset [Putzig et al., 2005] (same projection as in Figure 2.50). Superimposed are contours of our region of interest.

Elysium Planitia has a uniformly bright albedo (among the highest of the planet, except for the bare ice at high latitudes), likely a result of this mantling. The analysis of a sample of HiRISE images of the region provides evidence of this mantling. At HiRISE resolution (Figure 2.52), we see that this albedo is also generally high for small objects. Figure 2.52 displays samples of HiRISE images taken at three geographic locations (see the green squares in Figure 2.53). The first image shows platy flows that are part of Central Elysium Planitia. Two types of terrains can be identified: a homogeneous smooth surface at the top and hummocky terrains formed by rocks contributing to meter scale roughness usual in lava flows at the bottom. The second image shows sand dunes formed on a smooth terrain at the north edge of the Central Elysium Planitia. The third image is a region of contact between Elysium Planitia and the Highlands marked by debris aprons.

The apparent smoothness of the different observed terrains and the relatively high thermal inertia of the entire region suggest the presence of a general mantling of superficial material. In the upper part of the first image of Figure 2.53, we observe that rocks poorly crop out whereas they are clearly visible in the lower part. This can be explained by three theories: the two geological units consist in lava flows of originally different surface roughness, or the age of the units is different, leading to a dust mantling of variable thickness, or the flows were initially emplaced at different elevations, which led the lower regions to trap a larger amount of dust. The presence of nearby dunes in the second image also indicates that a global mantling hypothesis is reasonable. It also indicates that at least part of the surficial material is sand rather than dust. These different images tend to prove the presence of a layering of surficial material of variable thickness.
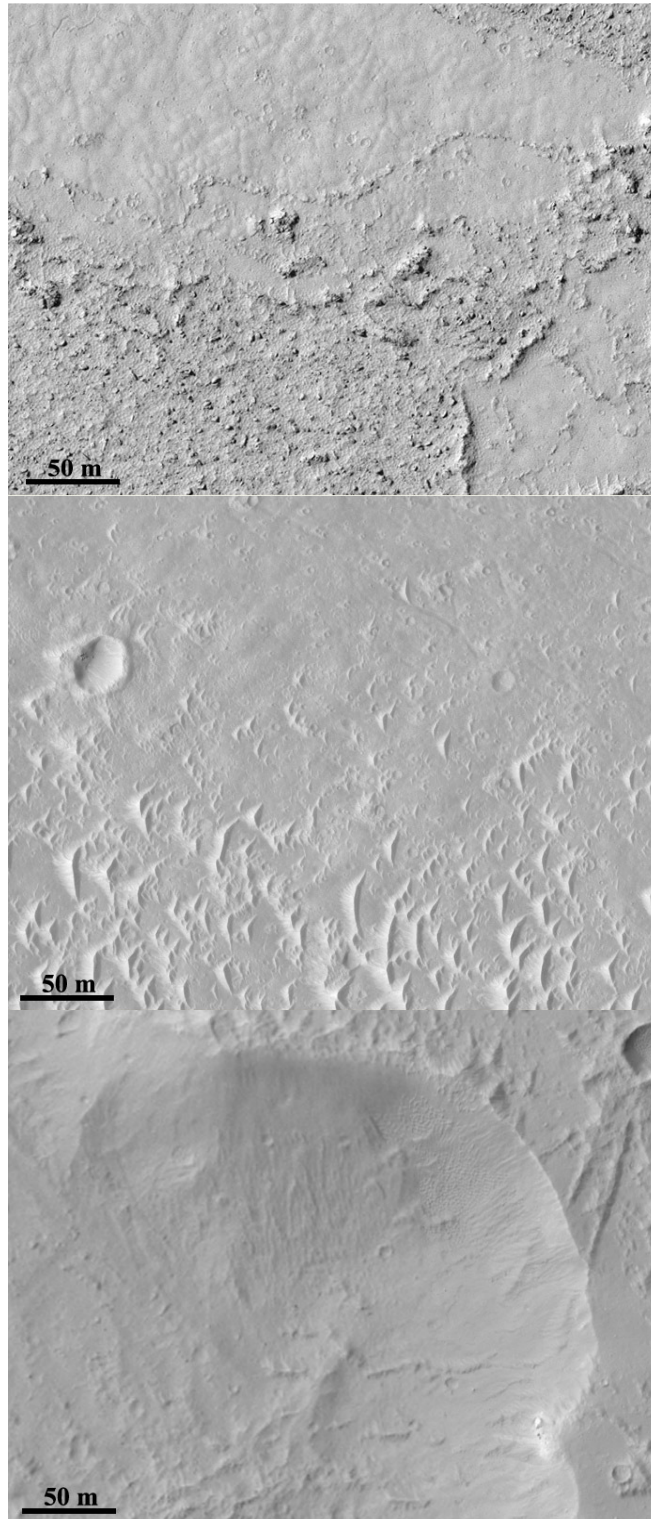
Figure 2.52: Several MRO HiRISE images extracts (see light green squares in Figure 2.53 for positioning). (a) Elysium Planitia platy flows (image TRA_000854_1855 centered on coordinates latitude 5.5° north and longitude 152.2° east). (b) Many small Zunil secondary craters (image PSP_001342_1910 centered on latitude 10.7° north and longitude 158.5° east). (c) Cerberus Plains and uplands contact (image TRA_000840_1810 centered on latitude 1° north and longitude 174.6° east).
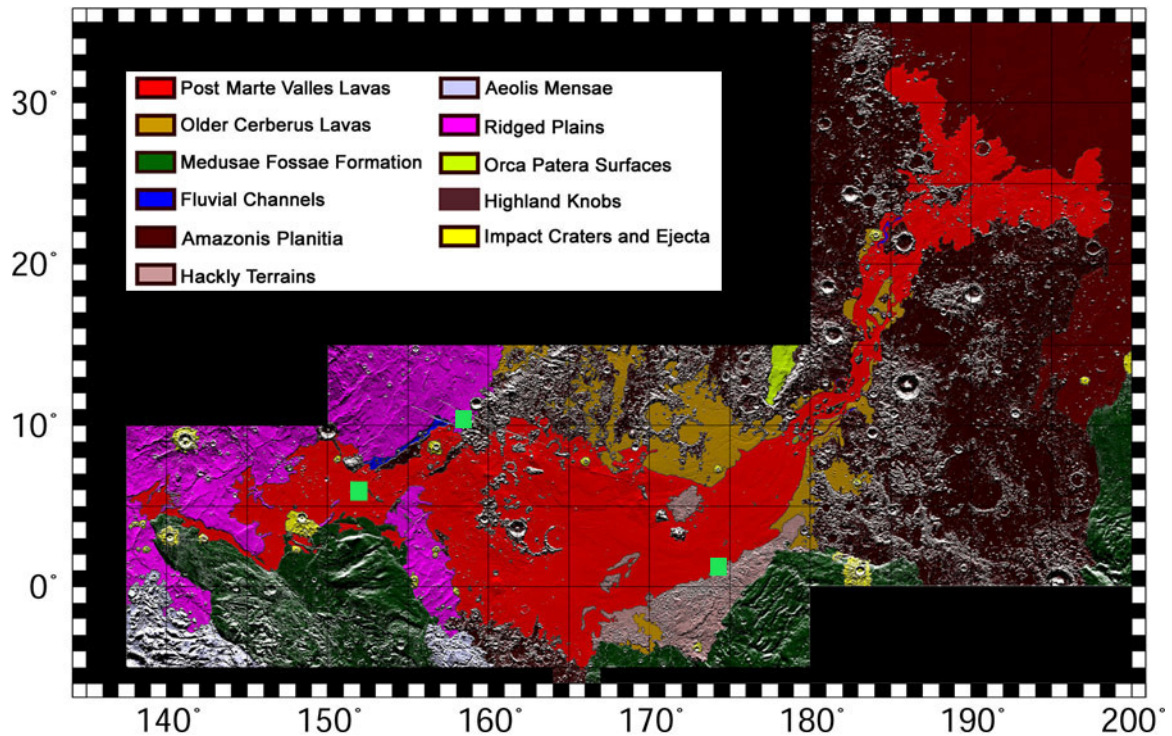
Figure 2.53: Geomorphic map of Central Elysium Planitia [Lanagan, 2004]. Surfaces in red have been interpreted as lava flows emplaced after the incision of Marte Valles.

Geological maps of the region were achieved by Scott and Tanaka [1986] and Greeley and Guest [1987]. More detailed studies were performed by Lanagan et al. [2001a, 2001b], Lanagan and McEwen [2003], Lanagan [2004] and Vaucher et al. [2008, in revision]. The geological map from Lanagan's dissertation (Figure 2.53) is used for comparison with the neutron signals. There is a strong resemblance between the boundary of the young lava flow unit (referred to as post Marte Valles lavas, in red in Figure 2.53) and the region where the maximum neutron currents are emitted (the region is the same for all three ranges of neutron energy).

2.4.3   Neutron signals at Cerberus

The neutron data used in this study extends between Feb 2002 and Sep 2005. The raw data has been processed with the reduction scheme described in part 2.2. These data have been adjusted for satellite altitude, cosmic ray variations and atmospheric pressure. After gridding the measurements using a cylindrical projection, we obtain maps of all three neutron currents at a 2-degree latitude and longitude sampling resolution. However the actual spatial resolution of the instrument is roughly 600km. Uncertainties in measured thermal, epithermal and fast neutron currents have been estimated previously [Prettyman et al., 2004b; Feldman et al., 2004b, Maurice et al., 2007]. The absolute calibration of the instrument has been identified as the data reduction step contributing the most to the uncertainty. Calibration uncertainties in fast neutrons can reach ±10% and that in thermal and epithermal neutrons, ±5%.

Because of the large spatial response function of the instrument, the neutron maps do not have a resolution as good as that of the geological map, and the comparison between them must be done with caution. The objective of the following is to determine whether the neutron high emission area can be associated with the area of recent lava flows (referred to as the post Marte Valles lavas shown in red in Figure 2.53). Neutron maps have thus been simulated by attributing hypothetical neutron emission intensity to the different geologic units.

In order to reproduce the measurements, the recent lava flows are assumed to emit a high epithermal signal whereas the rest of the region emits a low epithermal signal (see discussion for justification). Simulated neutron currents are presented in Figure 2.54a. As will be shown, the choice of an epithermal neutron emission of 12 within the recent lava flows and of 5 in the rest of the region provides the best fit to observations.

The neutron currents of the model are then convolved with a function that models the spatial response function of the neutron spectrometer. We approximate this function with a two-dimensional 10° FWHM Gaussian (both in longitude and latitude). The result of the convolution (Figure 2.54b) is compared with the measured epithermal neutron currents plotted in cylindrical projections using a 2-degree latitude and longitude sampling resolution in Figure 2.54c.

In order to evaluate the quality of the fit, a correlation coefficient is calculated between the modeled and measured epithermal counting rates. We use the Pearson correlation coefficient which is defined as the sum of the products of the standard scores of the two measures divided by the degrees of freedom. This coefficient is a measure of how well two populations vary jointly. For each pixel of an area of interest, a sample of pixels distant by less than or equal to 10° is defined. This sample allows an evaluation of the correlation coefficient for each pixel of the map. Figure 2.54d shows the resulting correlation coefficient obtained between the measured epithermal currents and the model after convolution. A value close to 1 indicates a high degree of correlation. Central Elysium Planitia is largely covered in red (coefficient greater than 0.9) and green (coefficient greater than 0.7), which provides evidence that the model closely matches the data.

We therefore conclude that the geological unit corresponding to the local maximum of neutron emission is consistent with the recent lava flows. The same investigation for fast and thermal neutron currents leads to the same conclusion: the maximum in all emissions is consistent with the recent lava flows in Central Elysium Planitia. Having made this association, we now determine the geochemical constraints provided by the neutron currents at this location.
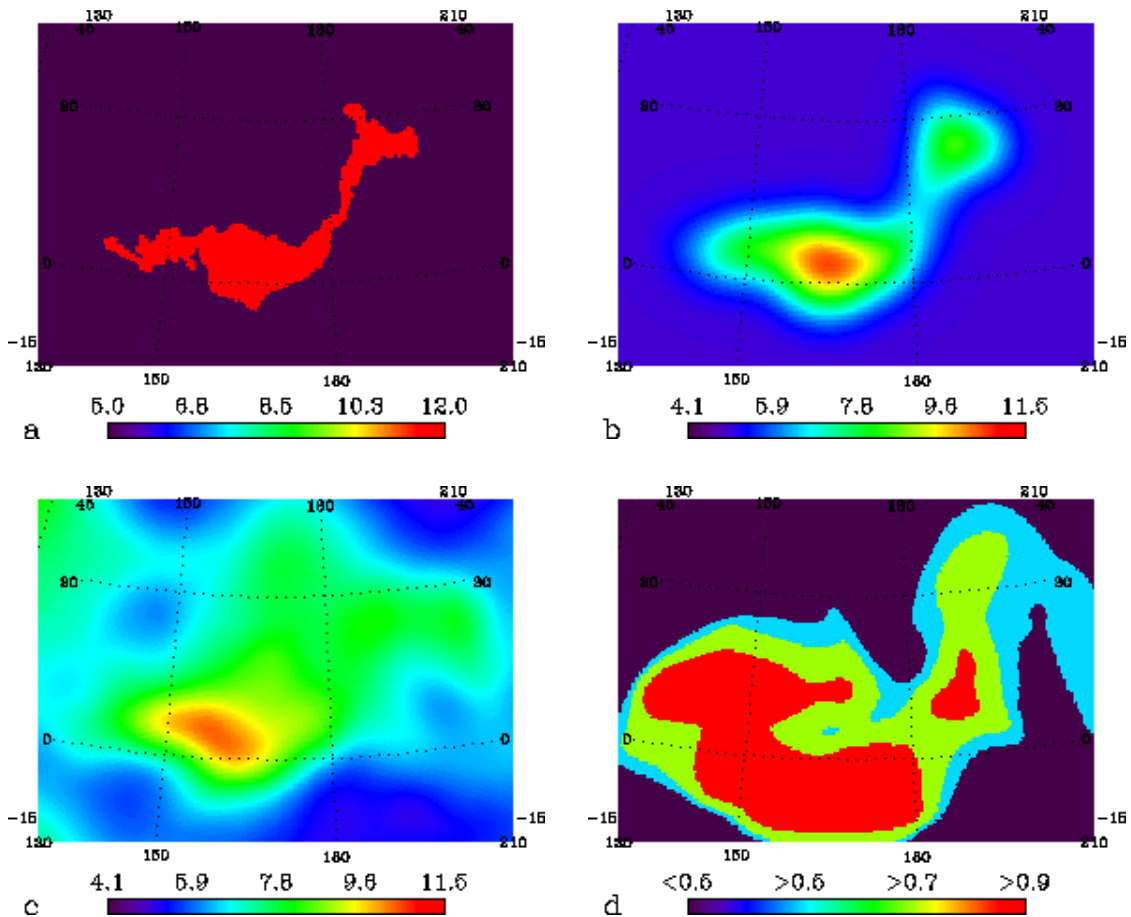
Figure 2.54: (a) Model of geological units used for comparison with the measured neutron currents for recent lavas. (b) Same model after convolution with a two dimensional Gaussian function, which approximates the point-spread function of the NS. (c) Epithermal neutron currents as measured by the neutron spectrometer. (d) Correlation coefficient between the modeled currents after convolution and the measured currents. All maps are in cylindrical projections centered on Central Elysium Planitia (same projection as in Figure 2.50).

2.4.4 Effects of the chemical composition on the neutron currents

The chemical composition of surface material considerably affects the neutron currents. Predicted relationships between elemental composition and neutron currents stems from simulations [Drake et al., 1988; Prettyman et al., 2004b]. The production of neutrons and their transport to the top of the atmosphere is simulated using the Monte Carlo Neutral Particle Code, MCNPX [Waters, 1999]. A second code is used to map these currents from the top of the atmosphere to an orbiting spacecraft and then convert them to counting rates using the energy-angle sensor response function of the NS [Prettyman et al., 2004b].

Such simulations have been carried out to determine the influence of hydrogen and carbon dioxide on the neutron currents. The results are detailed in Feldman et al. [2004b] and Prettyman et al. [2004b]. Further simulations have been performed to

figure out the dependence of the neutron currents with the absorption ability of the soil (part 2.3). Only information useful for the present article is reported here. The Martian surface is modeled with a relatively desiccated overburden material above a lower layer that is semi-infinite in depth and extending uniformly to the horizon. The atmosphere is modeled with multiple layers of constant composition but decreasing density with altitude above the planet.

In order to determine the influence of the composition in this context, five compositions have been created to cover the range of possible macroscopic absorption cross sections encountered on Mars. The abundances of all chemical elements (save hydrogen and chlorine) have been set to constant values, taken as the averages of in situ measurements of the first 630 Sols of the MER mission. Because of the high absorption cross section of chlorine, the variation of macroscopic absorption cross section from one composition to another is obtained through the variation of chlorine abundance. The compositions have been given the following chlorine concentrations: 0.25, 0.517, 0.6, 0.783 and 1.042 %.

However neutron currents are known to be very sensitive to the presence of hydrogen in the soil. It is important to determine the boundary conditions where the effects of composition can be observed. Simulations have therefore been run for different hydrogen abundances in the lower semi-infinite layer. Our present study being restricted to the equatorial latitudes where the general amount of water is lower than 10%, we restricted simulations to the following hydrogen abundances: 1, 2, 3, 6 and 10 %.

The results of the simulations consist of estimates of the neutron currents in the three different energy ranges: fast, epithermal and thermal neutrons. The different values are plotted in Figure 2.55 as a function of the chlorine abundance of the synthesis compositions. Different shapes have been used for the different hydrogen content to also track the influence of this parameter on the results.

In agreement with preceding experiments, epithermal and fast neutrons are found to be very sensitive to the hydrogen concentration. However they are not noticeably affected by the variations in chlorine concentration. On the contrary, thermal neutron currents are strongly influenced by the variations in chlorine concentration. Hydrogen content variations trigger a much smaller variability in simulations of these currents.

In conclusion, fast and epithermal neutron currents can be used to provide a measure of hydrogen content independent of knowledge of the elemental composition. In contrast, the thermal neutron currents can be used in regions of poor hydrogen abundance to determine the absorption ability of the soil. This ability is often closely correlated to the chlorine concentration of the material for Mars. However the results of the simulations are subjected to the hypotheses used in the model. Precedent assertions will therefore only be applicable in regions where the composition of the near surface ground is constant with depth and extends uniformly throughout the instrumental field of view.
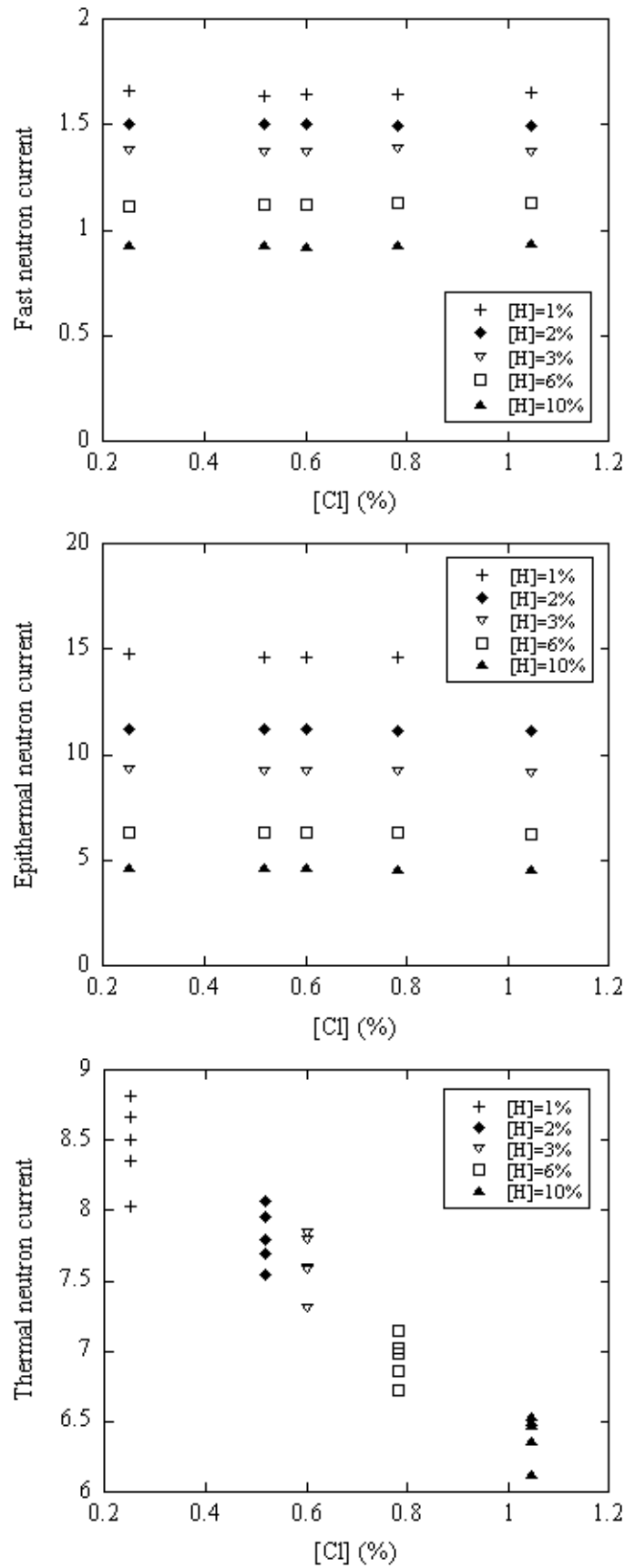
Figure 2.55: Fast, epithermal and thermal neutron currents obtained from different simulations (see text for description of hypotheses used in the models) as a function of chlorine concentration.

2.4.5 Chemical constraints from the Neutron Spectrometer

The high intensity of neutrons in the three energy ranges constrains the chemical composition of the material sampled by the instrument. The Neutron Spectrometer is limited to three measurable parameters, obviously precluding a precise determination of chemical abundances. After neutron data reduction, contributions from atmosphere, cosmic rays, and instrument background, are removed. Consequently, neutron currents essentially depend on the composition and structure of the subsurface. Macroscopic cross sections are appropriate tools to characterize the dependence on the composition.

The macroscopic cross section is the weighted sum of all chemical elements' cross section for the reaction considered. These cross sections allow predicting the behavior of neutron currents for a certain composition under the assumption that this composition is constant with depth and uniformly fills the instrumental field of view. The different energy ranges correspond to different reactions that shape the neutron spectrum. The ratio of fast neutron to epithermal neutron currents is directly related to the macroscopic energy-loss cross section. The ratio of fast neutron to thermal neutron currents is correlated to the macroscopic absorption cross section [Feldman et al., 1993]. These variables respectively refer to the reactions of elastic scattering and absorption.

The fast and epithermal neutron currents do not depend very strongly on the elemental composition except for hydrogen. Therefore we focus on the thermal neutron currents which depend mostly on the composition. The ratio of fast neutron to thermal neutron currents is mapped in Figure 2.56. Inspection shows the region of Central Elysium Planitia exhibits a very low ratio.
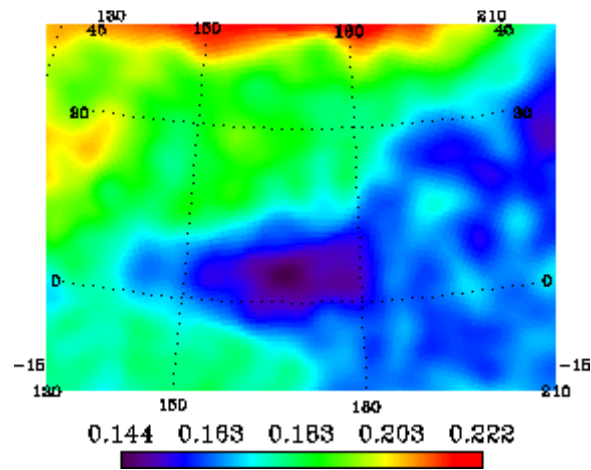
Figure 2.56: Fast over thermal neutron currents. Cylindrical projection centered on Central Elysium Planitia.

Because the ratio of fast neutron to thermal neutron currents is directly related to the macroscopic absorption cross section, this result indicates that the recent lava flows consist of low neutron absorbing material. As previously mentioned, this conclusion is correct only under the assumption that near-surface materials are not layered. In the region of Central Elysium Planitia, the hydrogen content is generally lower than 5% [Feldman et al., 2004b] and no hydrogen layering is detected (part 2.3). Under the

assumption of no layering, the macroscopic absorption cross section of Cerberus-Plains lava should be high.

2.4.6 Chemical constraints from the Gamma Subsystem

The gamma-ray data presently available extends between June 2002 and Apr 2005. Gamma ray spectra are accumulated between 0.1 and 10 MeV. The elemental abundances are estimated using the counts in several peaks of interest using a model of the regolith that is uniform with depth. Details of the data acquisition and of the steps of processing can be found in the work by Boynton et al. [2007].

We now evaluate constraints of the macroscopic absorption cross section of Central Elysium Planitia material using the composition made available by the Gamma Subsystem. This instrument provides measures of the abundances of Cl, Fe, Si, K, H and Th under the assumption of a composition that is constant with depth. However, calculation of the macroscopic absorption cross section requires a knowledge of the abundances of all chemical elements:

$$\sum\nolimits_{abs} = \sum \sigma_{absi} f_i N_A / A_i$$

where σ_{absi} is the absorption cross section of constituent i, f_i is its mass fraction, A_i is its atomic mass and N_A is Avogadro's number [Elphic et al., 1998].

All chemical elements are not equal regarding neutron absorption. The absorption abilities of the most common elements are given in Table 2.7. In the martian context, the major absorbing elements are iron and chlorine. Although the GRS GS does not measure all elements, the Gamma Subsystem, it detects those making the largest contribution to $\sum\nolimits_{abs}$: Fe and Cl. Therefore it is possible to obtain a reasonable estimate for $\sum\nolimits_{abs}$ of the martian surficial material using the GS.

Na$_2$O	0.00983
MgO	0.000947
Al$_2$O$_3$	0.00272
SiO$_2$	0.00161
SO$_3$	0.00399
Cl	0.5693
K$_2$O	0.026479
CaO	0.00495
TiO$_2$	0.04379
Cr$_2$O$_3$	0.02457
MnO	0.1122
FeO	0.02124

Table 2.7: Absorption abilities of the most common oxides ($\sigma_{absi} N_A / A_i$) in cm^{2}g^{-1}.

We define an estimated value of macroscopic absorption cross section which only takes into account Cl, Fe, Si and K. All other elements are set to constant values:

$$\sum\nolimits_{abs}{}^* = \sum \sigma_{absi} f_i N_A / A_i + \sum\nolimits_0$$

where i refers to Cl, Fe, Si and K. $\sum_0$ is the macroscopic cross section defined using average abundances of the remaining elements.

To evaluate the ability of $\sum_{abs}^*$ to trace $\sum_{abs}$, we calculate both for the full range of soils (types SU, SD, SF and SW) measured using the Alpha Particle X-ray Spectrometer aboard the Mars Exploration Rovers during the first 630 Sols of the missions [Gellert et al., 2004; Rieder et al., 2004]. Figure 2.57 shows that the relative error between the two definitions is consistently lower than 18%, and is lower than 3% for 95% of the samples. The 5% samples with high errors have very high titanium or sulfur abundances which, although possible on local scales, are unlikely on a hundreds of km scale. Therefore the error between the definitions can be considered lower than 3%.
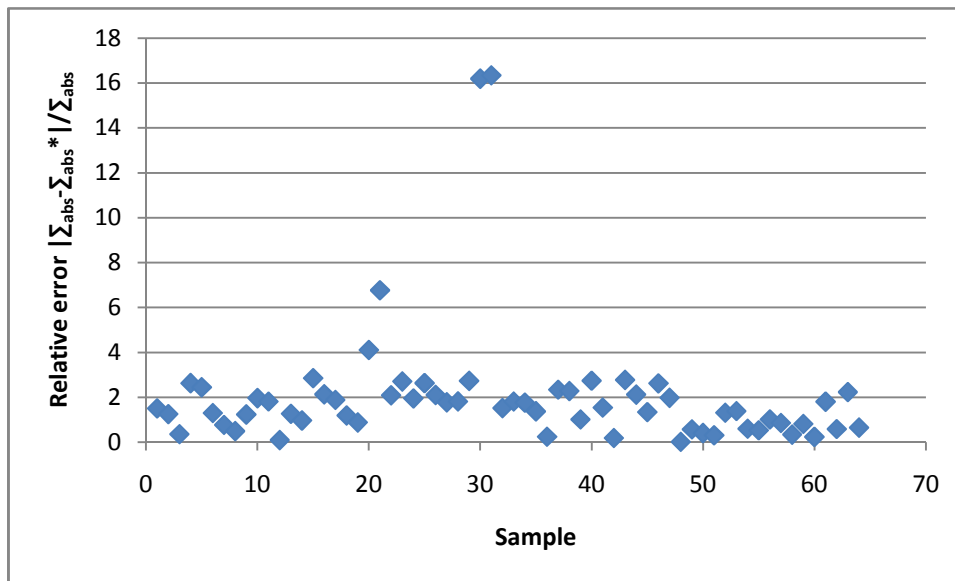

Figure 2.57: Relative error in % between real and estimated macroscopic absorption cross section for soil samples measured using the APXS of the Mars Exploration Rovers Opportunity and Spirit.

The foregoing error is low enough to give us confidence in our constructed macroscopic absorption cross section using the GRS GS data. In other words, we can evaluate the absorption ability of martian surficial material without knowing the detailed concentrations of Na, Mg, Al, S, Ca, Ti, Cr and Mn. The use of the preliminary Ca map [Newsom et al., 2007a] derived from the Gamma Subsystem dataset would not significantly improve the results due to the low impact of Ca on neutron absorption (absorption ability of 0.00495 cm^2 g^{-1} as shown in Table 2.7). Only Ti and S might contribute to a measurable error but these elements are likely to have reasonably low variation rates on a global scale. Therefore we use the definition of $\sum_{abs}^*$ to estimate $\sum_{abs}$ in the region of Central Elysium Planitia. The resulting cross section is mapped in Figure 2.58a.
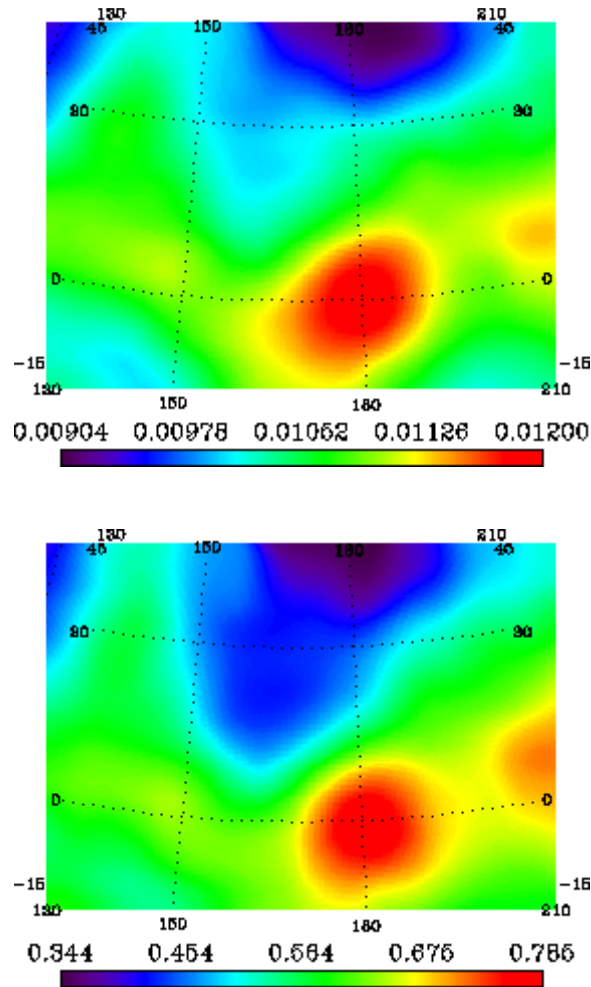
Figure 2.58: (a) Macroscopic absorption cross section estimated with abundances of Fe, Cl, K and Si measured by the Gamma Subsystem. (b) Chlorine concentration measured by the Gamma Subsystem. Cylindrical projections centered on Central Elysium Planitia.

Central Elysium Planitia is seen to have a high absorption cross section. Therefore the information about composition given by the Gamma Subsystem is inconsistent with the observations by the Neutron Spectrometer. However the local maximum of this cross section does not coincide with the recent lava flows, as did the ratio of fast over thermal neutrons. It coincides with the geological unit known as the Medusae Fossae Formation. So does the abundance of chlorine [Keller et al., 2006]. A map of the chlorine concentration as measured by the Gamma Subsystem is provided in Figure 2.58b.

Comparison between Figure 2.58a and b shows that chlorine may be the most important contributor to the absorption ability of the martian material at Elysium Planitia. Our calculated macroscopic absorption cross section for GRS data is seen to be closely similar to the chlorine abundance inferred from the Gamma Subsystem. Because the absorption cross section of this element is very high: 0.5693, it still contributes importantly to $\sum_{abs}$ even though its abundance is relatively low.

2.4.7 Discussion

The noticeable correlation between the neutron signals in all three energy ranges and the recent lavas geological unit begs for an explanation. A possibility is that the age of the unit is young, < 10 Ma [Hartmann and Berman, 2000]. The contours of the geological unit could than be sufficiently preserved from weathering and gardening processes to be detected by our instrument. We therefore attempt to determine the geologic formation processes that may yield the observations that were described previously, and also derived from other experiments.

Plescia [1990] gives examples of terrestrial analogues for the Cerberus Plains lava flows. We study the absorption abilities of these different basalts. Among them are the Columbia Plateau flood basalts and the Snake River plains basalts. Detailed compositions and their associated macroscopic absorption cross sections are collected in Table 2.8. Compositions and macroscopic absorption cross sections are also given for average soil samples at Gusev and Meridiani for comparison.

	Na_2O	MgO	Al_2O_3	SiO_2	K_2O	CaO	TiO_2	FeO	Cl	$\sum_{abs}$
Columbia Plateau 1	2.85	4.57	14.27	50.94	1.25	8.56	3.12	13.5	-	0.0069
Columbia Plateau 2	2.23	7.19	15.04	52	0.65	10.39	1.62	10.45	-	0.0054
Snake River Plains 1	2.7	6.6	15	51	1.3	10	2	11	-	0.0056
Snake River Plains 2	2.4	5	14	51	0.5	10	4	13	-	0.0066
Gusev soils	2.92	8.53	9.87	44.67	0.42	5.43	0.90	16.0	0.72	0.0106
Meridiani soils	2.84	8.06	9.17	43.58	0.41	5.06	0.83	21.6	0.63	0.0118

Table 2.8: Concentration (wt%) in major oxides and chlorine for 4 typical basalt samples from the Columbia Plateau and Snake River Plains [Shervais et al., 2005] and for average soil samples at Gusev Crater [Gellert et al., 2004] and Meridiani Planum [Rieder et al., 2004]. Last column is the macroscopic absorption cross section for these samples (in cm^2g^{-1}).

We notice that the macroscopic cross sections of these basalts are very low (with respect to the average macroscopic cross sections measured at Meridiani Planum and Gusev Crater), consistent with the measurements made using the GRS NS. The reason for this low value is the absence of Cl and SO_2 in unaltered basalts. The martian recent lava flows, which should not have undergone significant weathering, are very likely to also have a low chlorine concentration. The typical chlorine content for recent basalts is not likely to exceed 0.2 wt%. Addition of chlorine leads to an increase of the macroscopic absorption cross sections by about 20%. The high absorbing material deduced from the GS measurements, which is consistent with a moderately high Cl abundance, is therefore not consistent with these Earth-analog compositions, but rather with a soil composition.

The difference between interpretations of the GRS GS and GRS NS observations can be explained by the convolution of both signals with their spatial response functions. The large response function of both instruments causes their signals to contain a large fraction of spatial autocorrelation [Haining, 2003]. In other words, the signal in a pixel is the result of the signal really produced in this pixel plus a

contribution from surrounding pixels. We have previously said that the maximum absorption ability measured by the gamma subsystem coincides with the Medusae Fossae Formation. The presence of this geological unit in the vicinity of Elysium Planitia results in an increased measured absorption ability by the GS.

Keller et al. [2006] have noticed a similar correlation between the maximum in chlorine abundance and the Medusae Fossae Formation. Medusae Fossae Formation is a light toned layered unit eroded by long and deep grooves usually interpreted as yardangs, i.e. erosion by wind [Ward, 1979]. This texture is consistent with duricrust strongly eroded by recently occurring winds [Bradley et al., 2002]. The thermal inertia of the material (about 100 J m^{-2} s$^{-1/2}$ K^{-1}) suggests that it is highly porous and of low thermal conductivity. These characteristics suggest a partially indurated basaltic ash deposits or duricrust (which is more porous than basaltic flows). However it does not exclude other hypotheses such as a dust and water matrix [Watters et al., 2007] which may also have very low density. Volcanic exhalations would have enriched this finely grained material with substantial quantities of Cl [Keller et al., 2006].

The thermal inertia maps suggest the presence of a fine grained mantle but provide only a minimum estimate of few millimeters for its thickness. These surficial materials do not necessarily have the same chemical composition as the underlying bedrock, because they could have been brought from other regions by aeolian processes. Simulations of GCM models attribute a net annual deflation to the region [Kahre et al., 2006] over the past 72 000 years. However the region is still covered in dust. The dust reservoir therefore must have been recharged, either by occasional events (massive ash deposit during eruptions) or by a continuous process (progressive erosion of the underlying material). The young age of the geological unit favors occasional events, because progressive erosion would not have been sufficient to produce such quantities of dust.

We have reported previously the strong role of chlorine in the absorption of neutrons. Having different concentrations of chlorine in the different layers might also explain why the neutron spectrometer and the gamma subsystem do not see the same absorbing properties at this location. The analysis of the chlorine measurements of the gamma subsystem can be found in Keller et al. [2006]. They explain the Cl enrichment seen by GS (global mean of 0.49 wt%) relative to the martian meteorites (0.0014-0.11 wt%) by the fact that the GS is sensitive to the upper few tens of centimeters of Mars, which consist in soil rather than bedrock. However, because the GS observes significant variations across the martian surface, surficial materials have been inferred to be at least partly representative of the underlying bedrock, rather than a homogeneous global dust component [Newsom et al., 2007b]. The use of GS data alone fails to provide conclusive evidence of a large scale Cl layering [Keller et al., 2006], but the conjoint use of neutron and gamma ray datasets analysis points to such layering.

Mobile components have higher concentrations of chlorine in comparison to basalts. In his comparison of the gamma ray abundances to the surface age, Hahn et al. [2007] reports the average Cl abundances for different landing sites analyses [Clark et al., 1982; Brückner et al., 2003; Gellert et al., 2004; Rieder et al., 2004]. The average concentration of Cl calculated for soil samples (Viking 1: 0.8 wt%; Spirit - Gusev: 0.7

wt%; Opportunity - Meridiani: 0.64 wt%; Pathfinder: 0.6 wt%) is higher than that for basaltic rock (rocks abraded by the Rock Abrasion Tool at Gusev: 0.15 wt%). Hahn et al. [2007] highlights the fact that the GRS averages are lower than the soil averages and higher than the rock averages, probably due to the fact that the instrument measures a mixture of both. Possible explanations for the differences observed between in situ and satellite composition measurements have been discussed in Karunatillake et al. [2007]. We also keep in mind that sulfur is not measured yet by GRS and might also play a significant role. S has indeed been revealed to correlate with Cl by the in situ measurements, in particular in the airborne dust [Gellert et al., 2006].

However the effects of a mixing of material on the gamma ray fluxes and neutron currents are far from linear. The effects of the mixing of rocks and soil on gamma ray production have been studied [Kim et al., 2006]. An interesting future work would be to test the effects of a chlorine layering both on neutron and gamma ray production in order to better understand the differences between the two instruments.

The foregoing discussion suggests the scenario schematically represented in Figure 2.59. During degassing of recent eruptions, the geological unit of Medusae Fossae Formation behaves like a chlorine sink because of its finely grained structure. The wind afterwards mobilizes part of the Cl rich dust made available by the erosion of this easily erodible formation. Some of this dust ends up in the recent lava flows forming Elysium Planitia and Amazonis Planitia.

Reasons for the preferential deposition on long term in this region include the pronounced roughness of the recent lava flows which helps trapping the dust and the local topography (see Figure 2.50). The Medusae Fossae Formation has a higher altitude than Central Elysium Planitia, which favors a transfer of dust transfer from Medusae Fossae down to Central Elysium Planitia. The sequence of processes shown in Figure 2.59 might have happened several times, which is suggested by the presence of older lavas under the recent lava flows (see Figure 2.53).

With this scenario, the most recent lava flows would be the less covered by Cl rich dust, which explains the distinction detected by the Neutron Spectrometer. The region could be roughly divided into three different units. The first unit consists of the Medusae Fossae Formation. Very likely partly formed before the other units, but frequently recharged with new material from recent eruptions. The second unit consists of older lava flows. They have been progressively covered by Cl-rich dust. The thickness of this mantle depends both on the time of emplacement of the lava flows and on the deposition rate of dust. The last unit consists of recent lava flows (post Marte Valles lava flows), covered only by a very thin dust layer (on the order of a few centimeters) because of their young age.
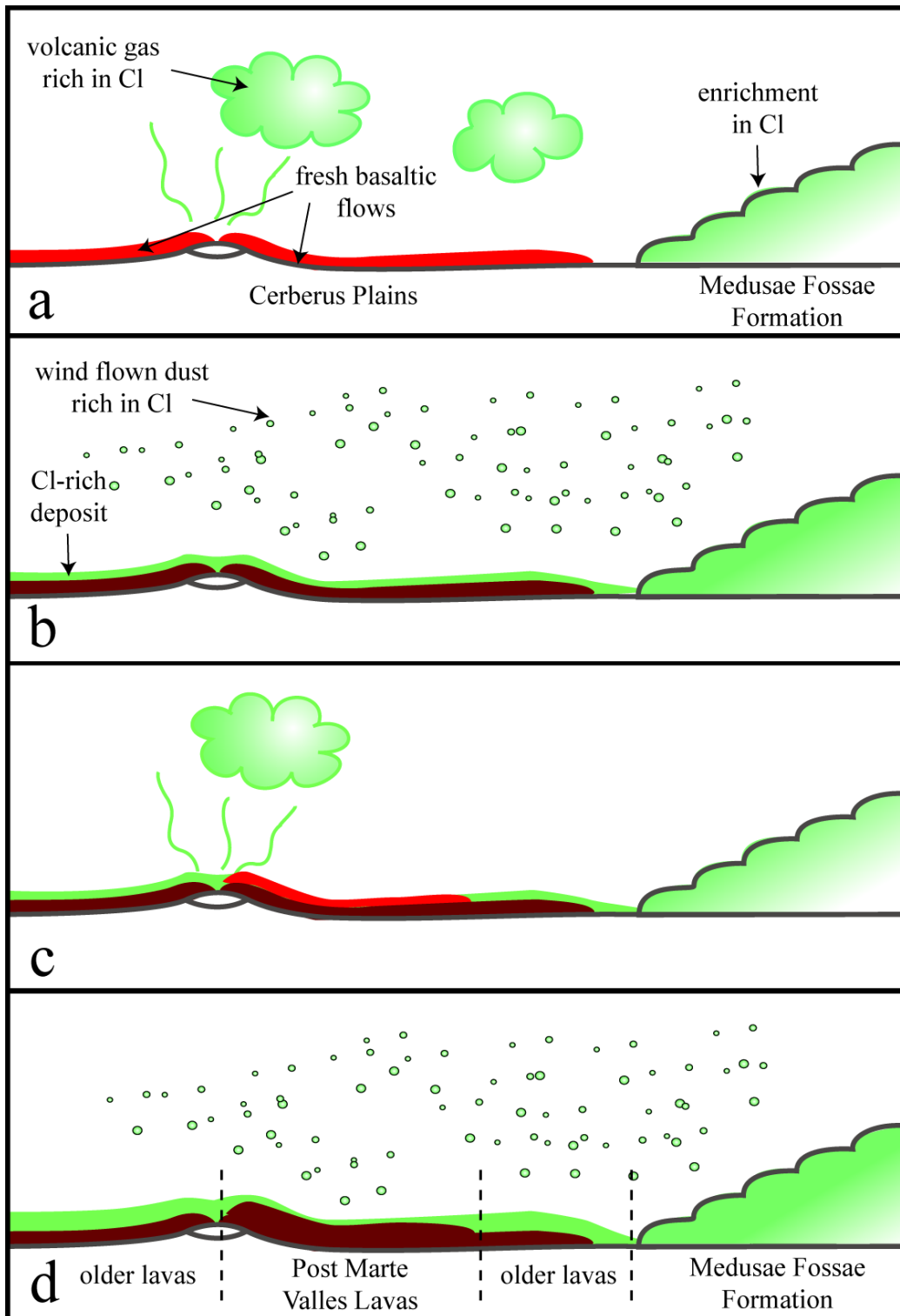
Figure 2.59: Scheme of the sequence of events explaining the present configuration as determined using results from both neutron and gamma ray datasets. (a, c) Episode of volcanism resulting in the deposition of a fresh basaltic flow and in degassing; enrichment of the Medusae Fossae Formation in chlorine. (b, d) Erosion of the Medusae Medusae Fossae Formation; mobilization of the eroded material by the wind and transport to surrounding areas.

2.4.8 Conclusion

Recent works have used the epithermal energy range of neutron data acquired by the Mars Odyssey mission to infer the H distribution on Mars. The combined use of epithermal and thermal energy ranges has also helped to reveal the vertical distribution of hydrogen at high latitudes. This part has shown how the combined use of thermal and fast energy ranges allows the geochemistry of regions with moderate hydrogen content to be inferred. However the geochemistry cannot be expressed in elemental chemical abundances, but through estimation of the absorption ability of the material.

Our attempt to reconcile the chemical insight provided the Gamma Subsystem and the Neutron Spectrometer lead us to important inferences with regard to Central Elysium Planitia. Gamma rays indicate a high neutron absorption potential centered on the Medusae Fossae Formation. However thermal neutrons are not absorbed strongly in Central Elysium Planitia, suggesting a low neutron absorption potential for the recent lava flows, northwest of Medusae Fossae.

We infer that the apparent disparity is caused by surficial heterogeneities of Cl-rich deposits. Two types of heterogeneity have been identified: vertical layering and horizontal structure, which is mixed by the relatively large area point-spread functions of both instruments. Chlorine is the key element in the chemical mixing due to its high absorption ability. However we keep in mind that sulfur, which is not measured yet by GRS, might also play a significant role.

A scenario that may explain the chlorine configuration inferred from the NS and GS datasets is proposed. An interesting conclusion of this article is that the joint use of gamma and neutron datasets allows discrimination between effective measurement and contamination by surrounding pixels and might therefore be helpful for deconvolution in other areas of the planet.

Chapter 3   Determination of the composition of the lunar surface with the Selene Gamma Ray Spectrometer

In addition to developing new technologies, the Selene Japanese mission pursues the goal of collecting scientific data. The Gamma Ray Spectrometer onboard is designed to collect the elemental abundances at the surface of the Moon. This technique allows mapping many elements fundamental in constraining the geological history of the Moon: radioactive elements (potassium, thorium and uranium), major elements (iron, calcium, silicium, titanium, oxygen) and most importantly hydrogen.

This chapter explains how the raw spectra collected by the instrument can be analyzed and processed into counting rates proportional to the elemental abundances of the elements of interest. The effective mission did not start before end of December 2007, and is still currently collecting spectra. Because of this agenda, the status of the data reduction is very preliminary.

After a short presentation of the scope of the Selene mission and most particularly of the Gamma Ray Spectrometer, this chapter presents the methods used for processing the data. Several aspect of the processing are tackled: the mapping techniques, the tools developed to analyze the spectra and the analysis of the global lunar spectrum made of the accumulation of a major part of the dataset. The following parts present how the counting rates of different elements can be determined and assessed with the exposed techniques. The third part focuses on the abundance of iron, whose determination can be particularly tricky because the iron lines are either superposed with other lines or have very low statistics. The fourth part treats the radioactive elements: potassium, thorium and uranium, which are particularly well determined. The final part processes the following major elements: calcium, silicium, magnesium and titanium.

It might be noticed that the awaited determination of the hydrogen abundance does not figure in this outline. Several attempts to detect the hydrogen line in the spectra collected at the poles were carried out by both French and Japanese teams. However none of them proved successful so far.

3.1   Scope of the Selene Gamma Ray Spectrometer mission

3.1.1   The Selene mission

The Japanese lunar orbiter Kaguya (Selene) has been successfully launched from Tanagashima Space Center TNSC on September, 14th of 2007 [Kato et al., 2008]. After a phasing orbit around the Earth, Kaguya was inserted into an elliptical orbit around the Moon on October, 4th. The nominal orbit (a nearly circular polar orbit with an altitude of 100 km) was reached on October 18th. On the way, two subsatellites Okina (Rstar) and Ouna (Vstar) have been released into elliptical orbits. Performance tests were done on

each instrument during the checkout period that lasted for about a month and a half. Nominal observation then started on December 21, for an initial period of 10 months. At the end of October 2008, Selene entered an extended operation phase, which is planned to continue until August 2009, ending with a controlled collision with the lunar surface.

The major objectives of the mission are to obtain scientific data on the origins and evolution of the Moon, and to develop the technology for future lunar exploration. The three satellites carry 14 science instruments for this purpose. Data collected during a year by these instruments amount to about 10 Tbytes. Scientific goals of the mission include: the distribution of elemental abundances, the mineralogical composition, the 3-dimensional topography down to a depth of 5 km, the electromagnetic and charged particle environment of the Moon. These data contribute to solving the important questions of the lunar science: the structure of the moon interior, the dichotomy into highlands and mare, the past existence of a magma ocean, the origin of the lunar magnetic field, the evolution of the tectonics…

The specifications of all instruments are summarized in Table 3.1. The XRS and GRS instruments are complementary to provide global mapping of the elemental abundances of the lunar surface. MI and SP constrain the global mineralogical distribution by acquiring respectively one dimension and two dimensions reflectance measurements of the lunar surface. Three of the instruments contribute to the determination of the topography: TC, LRS, and LALT. LALT is a traditional altimeter. LRS sounds the lunar surface and subsurface within about 5 km. TC takes stereo images that allow realizing Digital Elevation Models of the surface.

VRAD and RSAT are onboard the Rstar, Vstar and the main orbiter to determine the gravity field of the Moon (in particular of the far side) with a renewed precision. Two radio sources emit three S-band and an X-band radio waves to determine the satellites position with an accuracy of 10 cm. They use the differential VLBI technique in between subsatellites and ground stations. The RSAT is used to relay signals when the main orbiter is flying above the farside. A 4-way Doppler technique between the main orbiter and a ground station via Rstar Okina allow determining the gravity field of the far side.

LMAG, CPS, PACE, RS, and UPI observe the environments of the Moon and the Earth. LMAG measures the magnetic field distribution or the local remnant magnetization of the Moon. The primary purpose of CPS is to measure the environment of the Moon in terms of charged particles such as protons from cosmic ray origin, or alpha-ray particles leaking outward the lunar faults presumably originating from tectonic activity. PACE is investigating energy and incident angles of environment particles (ions, electrons and neutral atoms). RS investigates the existence of a tenuous ionosphere around the Moon, which was reported by the lunar orbiter Luna 19. The S-band and Xband radio waves emitted from VRAD2 on Vstar are received on ground stations after passing through the limb of the Moon and allow detecting any possible variation in frequency of waves. The UPI instrument observes potential plasma phenomena of the terrestrial upper atmosphere.

Instrument	Description
X Ray Spectrometer (XRS)	Global mapping of Al, Si, Mg, Fe distribution at a spatial resolution of 20 km
Gamma Ray Spectrometer (GRS)	Global mapping of U, Th, K and major elements distribution at a spatial resolution of 160 km
Multi-band imager (MI)	UV-VIS-NIR imager with a spectral bandwidth ranging from 0.4 to 1.6 microns (spectral resolution of 20-30 nm and spatial resolution of 20 m)
Spectral Profiler (SP)	Continuous spectral profile ranging from 0.5 to 2.6 microns at a spectral resolution of 6-8 nm and spatial resolution of 500 m
Terrain Camera (TC)	High resolution stereo camera with a spatial resolution of 10 m
Lunar Radar Sounder (LRS)	Mapping of the subsurface structure using active sounding at a frequency of 5 MHz with a resolution of 75 m
Laser Altimeter (LALT)	Determination of the topography with a height resolution of 5 m and a spatial resolution of 1.6 km
Differential VLBI Radio source (VRAD) Relay Satellite Transponder (RSAT)	Selenodesy and determination of the lunar gravitational field, in particular of the far side
Lunar Magnetometer (LMAG)	Determination of the magnetic field with an accuracy of 0.5 nT
Charged Particle Spectrometer (CPS)	Measurement of high-energy particles, 1-14 MeV (LPD), 2-240 MeV (HID), alpha particles, 4-6.5 MeV
Plasma Analyzer (PACE)	Measurement of the charged particles energy and composition
Radio Science (RS)	Detection of the tenuous lunar ionosphere
Plasma Imager (UPI)	Observation of the terrestrial plasmasphere from lunar orbit in XUV to VIS
High Definition TV Camera (HDTV)	High definition imaging of Earth rise and lunar surface

Table 3.1: Selene science instruments (adapted from Kato et al. 2008)

3.1.2 The Selene Gamma Ray Spectrometer (GRS)

The GRS consists of three major subcomponents: a gamma ray detector, a cooler driving unit and an electronics unit. The detector is mounted on the surface of the spacecraft so as to face the moon, while the cooler and electronics units are installed inside. During observations the detector is cooled to below 90 K by the Stirling refrigerator. A precise description of the mission can be found in Hasebe et al. [2008]. Only information useful for understanding the dataset is reported here.

The detection unit consists of three radiation detectors: a cylindrical germanium crystal, surrounded by a massive bismuth germanium (BGO) detector and a thin plastic scintillator. Among these, the Ge detector is the subsystem meant to produce the gamma ray spectra. With a volume of 250 cm^3 of high purity germanium, it has successfully

achieved an energy resolution of 3 keV FWHM for the ^{60}Co line at 1.332 MeV in preflight tests.

The BGO subsystem is a shoe shaped detector of about 1250 cm^3 that faces the spacecraft. This massive detector is both passively shielding background gamma rays from the spacecraft and serving as an active anticoincidence detector to suppress Compton scattered gamma ray events and cosmic ray events in the main detector.

And finally, the plastic scintillator is a curved shaped 5 mm thick detector facing the moon and meant to reject charged particle events. The general scheme of the GRS is shown in Figure 3.1. The configuration of the detection system allows an efficient reduction of the background gamma rays coming from the satellite and scattered in the Ge detector [Okudaira et al., 2006].

The GRS has three observation modes: Ge mode, BGO mode, and burst mode [Hasebe et al., 2008]. The Ge mode is the normal observation mode with which the GRS is operated most of the time. Two energy spectra of gamma rays with different energy ranges are accumulated every 17 seconds. Each set of data is processed to a histogram of 8500 channels: low gain (0.1–12 MeV) and high gain (0.1–3.0 MeV). In addition to these histograms, counter data are stored.

The GRS is switched to BGO mode several minutes in a month in order to adjust the gains of the two photomultiplier tube (PMT) and to estimate gamma ray background level. In this mode, the energy spectra collected by the BGO detector are stored.
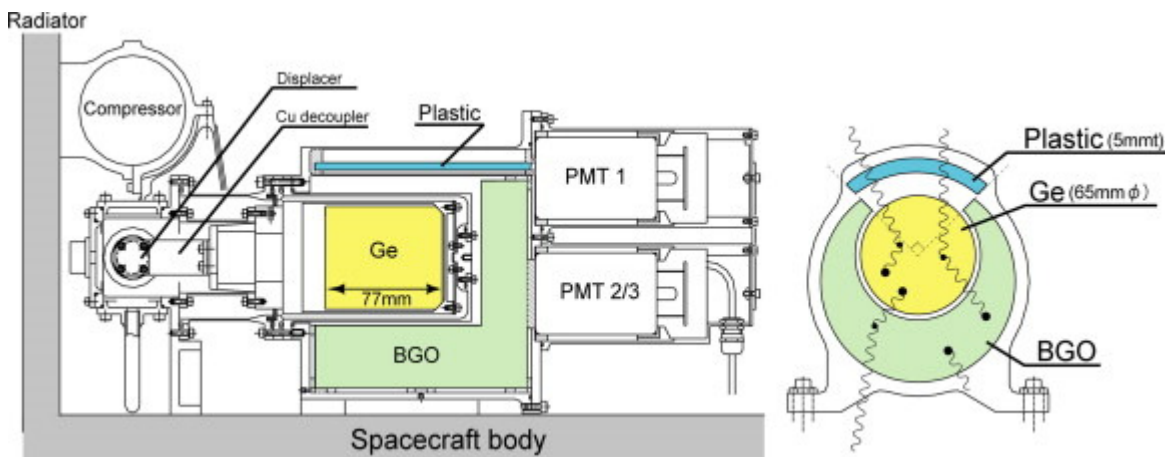

Figure 3.1: Schematic drawing of the GRS.

The counting rate of the BGO detector is monitored by the FPGA (Field Programmable Gate Array) with a 10 ms time resolution. When the counting rate of the BGO detector exceeds a threshold value during the Ge mode, the observation mode is automatically changed into the burst mode. Gamma ray bursts are characterized by a sudden increase in gamma ray intensity. The GRS observation mode of these events provides a histogram of gamma rays accumulated by the Ge detector in the short time of the event and the counting rate transition observed by the BGO detector. This mode was initially designed to collect data to better characterize gamma ray bursts and their

emission mechanisms, which are not very well understood. It has not been used during the initial mapping phase of the Selene GRS.

3.1.3 The GRS dataset

The electronics unit of the GRS contains two FPGAs and CPUs. They control the digital processing of the scientific data obtained by the detectors (including event rejection triggered by the anticoincidence system) and the associated house keeping data. They also handle the decoding and execution of ground commands. The scientific data are composed of two 8192-channel histograms and 14 counter values acquired with Ge mode during an accumulation time of 17 s.

The counter data are typically:

- discriminated events: the total number of events rejected by the anticoincidence system
- over range events in the Ge, BGO or plastic detector: events whose energy has been identified as higher than that of the highest channel
- dead time of the electronics: accumulation of time intervals following an event where the electronics cannot react to a new event
- number of events in different energy ranges of the histogram: intended to be used as proxies of the health of the instrument

The housekeeping data include the CPU status, different temperature measurements including that of the Ge crystal, of the electronics, of the base plate… These data are also collected by the second FPGA. In addition to the collection of housekeeping data, it controls the gain of the amplifiers, of the high voltages driving the detectors and the output power of the cooler unit.

About 90 lines have been fitted in this thesis work, and some of these results are presented in the following sections.

3.2 Reduction of gamma ray data from Selene GRS

3.2.1 Mapping the data

Lunar Prospector inherited methods

Individual spectra do not contain enough counting rates to allow analysis. We need to accumulate data within pixels on the lunar sphere. The dataset possesses housekeeping data such as the position of the satellite during the acquisition of the measure. The satellite is localized with the help of longitude and latitude information.

The first option to map the data consists in using the set of routines developed by the Lunar Prospector team. This method has been described in detail in part 2.2.6. The mapping toolkit allows the production of cylindrical grids of 720 x 360 pixels. Different types of geographical projection of the sphere on this grid can be used.

With the "cylindrical mapping" (Figure 3.2a), pixels have equal angular dimensions in latitude and longitude. Whereas with the ''equal area mapping'' (Figure 3.2b) pixels have the same angular dimension for the latitude, but the longitude extent is adjusted so that pixels have close to the same area. This second option offers a chance to have fluxes of gamma ray more comparable from one pixel to another.
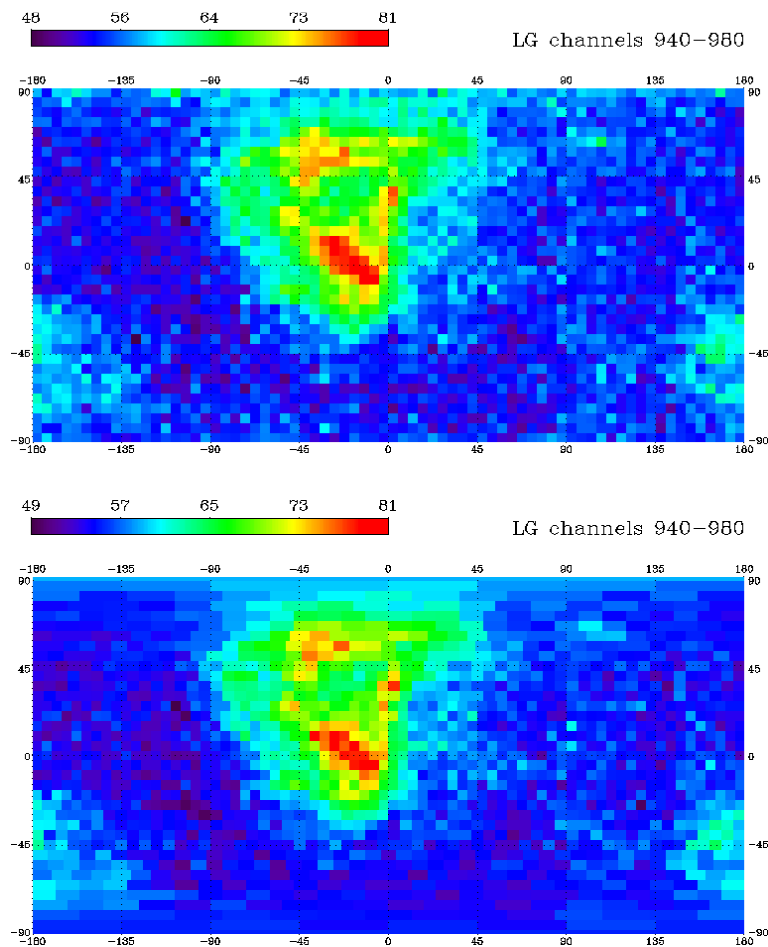

Figure 3.2: (a) Cylindrical and (b) equal area mapping at a resolution of 5° of channels 940 to 980 of the low gain histograms.

The different teams that have worked with neutron or gamma datasets did not choose the same pixelization. The gamma dataset from Lunar Prospector has been tiled with equal area mapping. The neutron and gamma datasets from Mars Odyssey are using most of all cylindrical mapping. The Selene gamma datasets is to be tiled with an improved equal area mapping which will be now described.

Healpix pixelization

The "equal area mapping" previously described provides however only approximately equally tiled pixels and leads to an irregular dissemination of the centers of the pixels on the sphere. An alternative method was therefore adopted: the Healpix pixelization [Gorski et al., 2005]. Healpix is a Hierarchical, Equal Area and isoLatitude PIXelisation of the sphere designed to handle large volume and high resolution datasets. This pixelization produces a subdivision of a spherical surface in which each pixel covers the same surface area as every other pixel [Krzysztof et al., 2008].

The Healpix base partitions the sphere in 12 pixels. Higher resolutions are subdividing pixels in 4 a given number of times (Figure 3.3). The pixelization of the lunar surface can be performed at different scales. Among the discrete resolutions that can be obtained we use the following: 14.65° (192 pixels), 7.33° (768 pixels) and 3.66° (3072 pixels). In addition to being a very useful tool to partition data on a sphere, the Healpix method provides an entire toolkit to manipulate data on the sphere.
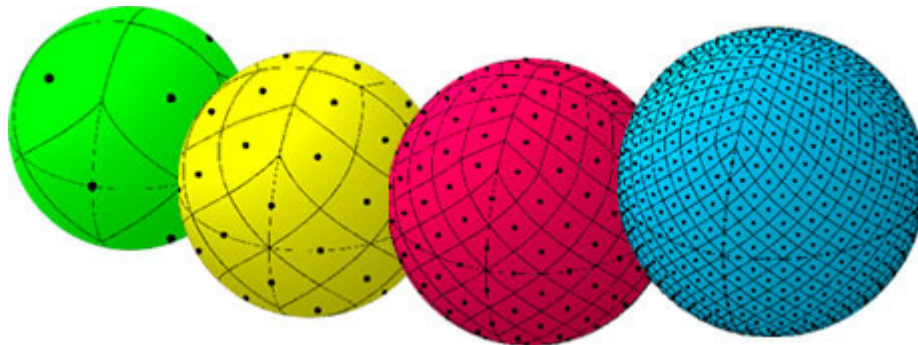

Figure 3.3: Partitioning of a sphere at progressively higher resolutions, from left to right. The green sphere represents the Healpix base partitioning of the sphere surface into 12 equal sized pixels; the yellow sphere: 48 pixels, the red sphere: 192 pixels, and the blue sphere: 768 pixels. [http://healpix.jpl.nasa.gov/index.shtml]

Figure 3.4 shows the type of map obtained with the Healpix method for comparison with the traditional partition method displayed previously in Figure 3.2. Equal area (either with Lunar Prospector toolkit or Healpix) avoids attributing a very high number of pixels to the poles, which does not have physical justification. In addition Healpix is better suited to perform multi-resolution analysis. Indeed the transformation from a resolution to the next higher resolution is made by splitting a pixel in 4. However the Lunar Prospector toolkit allows tiling the data on a wider sample of resolutions: any multiple of 0.5° can be used for mapping.
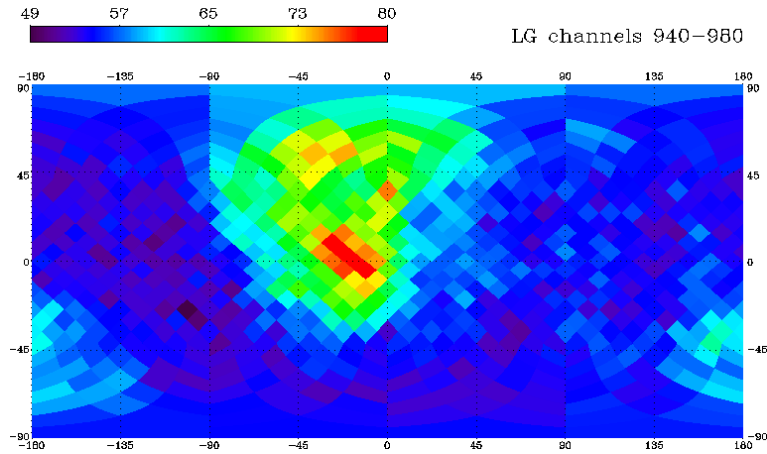
Figure 3.4: Healpix mapping at a resolution of 768 pixels (~7.33°) of channels 940 to 980 of the low gain histogram.

Wavelet Transform filtering

The signal to noise ratio is better for the spectra accumulated in pixels than for any individual spectrum, although much lower than for the global lunar spectrum. Figure 3.5a shows the map of a channel of the low gain histogram with the Healpix partition at a resolution of 768 pixels. Even though the resolution is not very high, the signal is very noisy. Therefore removal of the noise is highly recommended before any further spectral analysis is performed.

Because of its hierarchical quadrilateral tree structure, Healpix defines a partition that eases the process of passing from a scale to another scale. Once the twelve base-resolution faces are extracted, each face can be decomposed into quadrilateral blocks of a specified size. Consequently to these geometric features, the Healpix sampling scheme was used by Moudden, Starck, Abrial and Cardoso to develop a spherical data analysis software package: MRS (Multi Resolution on the Sphere). The MRS package offers an implementation of an isotropic wavelet transform on the sphere. Its properties make it very useful for data denoising and deconvolution [http://jstarck.free.fr/mrs.html]. The algorithm is directly derived from the FFT-based wavelet transform. The reconstruction process is very straightforward: the sum of all scales reproduces the original data.

A map of the counts in each channel has been drawn on the lunar surface. This map is subsequently decomposed in its different scales. The sum of these different scales allows reconstructing the initial map. The first scale, which corresponds to the highest geographical resolution, is suppressed. The signal is reconstructed after this removal. This operation degrades only slightly the resolution of the signal while removing a lot of the noise present in the data. A channel of the low gain spectrum is processed with this filtering to show its benefits. Figure 3.5b shows the resulting signal in comparison to the initial unfiltered channel (Figure 3.5a). A mere glimpse at the two figures convinces that this filtering method improves unquestionably the quality of the data.
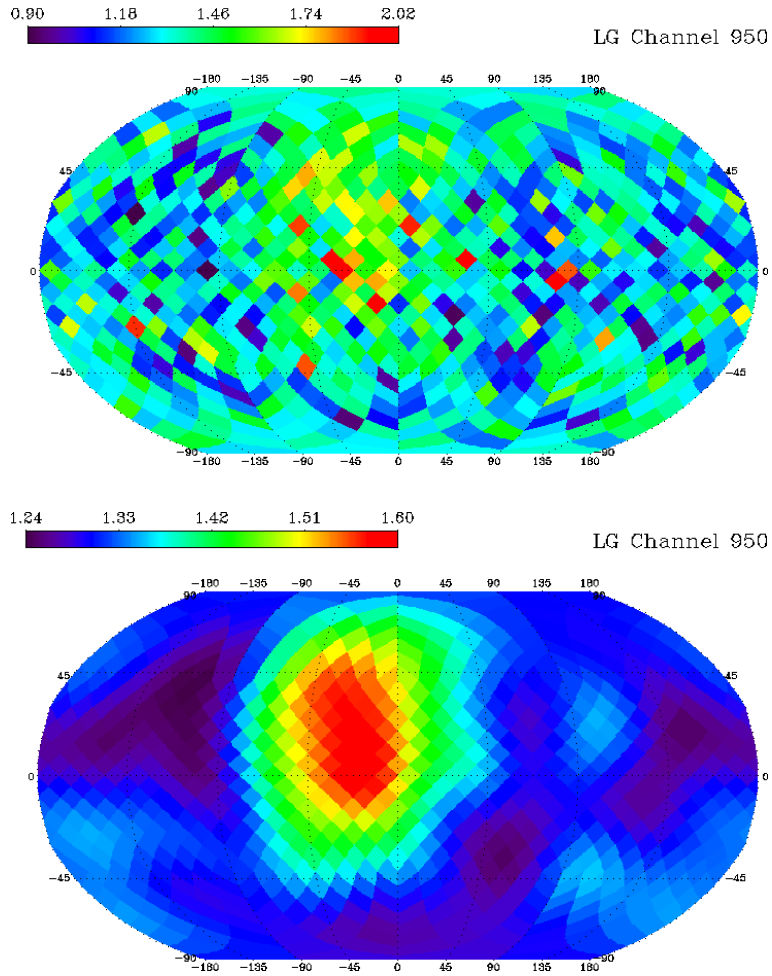
123

Figure 3.5: Comparison of maps of the channel 950 of the low gain histogram (a) before and (b) after filtering with a wavelet transform (Healpix at a resolution of 7.33°).
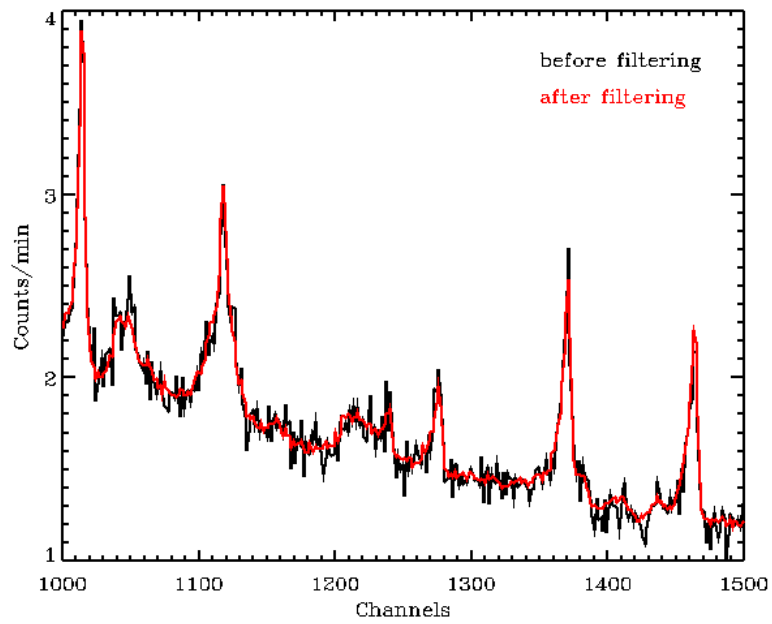

Figure 3.6: Comparison of the spectrum in one of the pixels before and after filtering.

This geographical filtering also has consequences on the quality of spectra. The wavelet filtering is applied to all channels. After this operation, a random pixel has been selected. The spectrum in this pixel is plotted before and after wavelet filtering to display the improvement on the spectrum (Figure 3.6). Part of the noise has been removed. In conclusion the removal of the higher geographical scale considerably contributes to obtaining better statistics in the spectra.

For Mars Odyssey, the smoothing of the data was performed at the very end of the data processing (part 2.2.6). However the neutron data does have much lower noise levels than gamma ray data of high spectral resolution such as those obtained with Selene. The main advantage of filtering the gamma ray data prior to doing the spectral analysis is that it removes most of the statistical noise and provides better spectra for the subsequent analysis.

3.2.2 Analysis of the spectra

Peak fitting method

Modeling the peaks of the spectra serves for two main purposes: one is to analyze the spectrum (the central energy of the peaks identifies the chemical elements that produced the gamma rays, the width informs whether the emitting nuclei were moving…) and the other is to perform a robust determination of the area. Chapter 1 exposed that the area of a line produced by a given element is proportional to the abundance of that element. However estimating this area directly on the measured spectra often fails because spectra contain noise. Modeling the lines by their known theoretical shape allows estimating their area more efficiently.

A code was developed to perform easy peak fitting of the spectra. The original concept was developed at the Max-Planck-Institut für Chemie (Mainz, Germany) under the name Ganymed [Kruse, 1979]. It was coded under IDL and renamed Aquarius by Carole Valentin at CESR in the framework of the Mars Odyssey Gamma Ray Spectrometer dataset analysis (2004). The new code is based on the *mpfit* routine of Craig B. Markwardt (http://cow.physics.wisc.edu/~craigm/idl/idl.html), which gives more control on the parameters and returns more frequently successful fits. Several new versions of Aquarius have been written, among which some integrate a graphical user interface. It was delivered to the Japanese GRS team to enable user friendly fit of the spectra.

Portions of the spectrum are fitted by summing a continuum with a given number of lines. The continuum is modeled with a linear or 2-degree polynomial function. The real continuum is more complex, but most of the time the linear approximation is very good inside a reasonably small energy range of interest. In a weakly-damaged semi-conductor detector, each peak is supposed to have a Gaussian shape, modified by an exponential low-energy tail (Figure 3.7) [Sanders and Holm, 1969]. The equations of these two functions are:

$$f(x) = A * \exp\left(\frac{-\rho}{\sigma^2} * \left(E_0 - \frac{\rho}{2} - x\right)\right) \text{ if } x \leq E_0 - \rho$$

$$f(x) = A * \exp\left(\frac{-(x - E_0)^2}{2\sigma^2}\right) \text{ if } x \geq E_0 - \rho$$

A is the amplitude of the peak, E_0 is the position (or centroid), σ is the Gaussian standard deviation and ρ is the distance from the centroid to the connecting point between Gaussian and Exponential. E_0, σ, ρ and *x* must be in the same unit. An energy in keV (rather than channels) is used by convention. *f* has the same unit as *A* (typically counts per minute). To minimize the number of free parameters, continuity of the two functions and their derivatives is imposed.
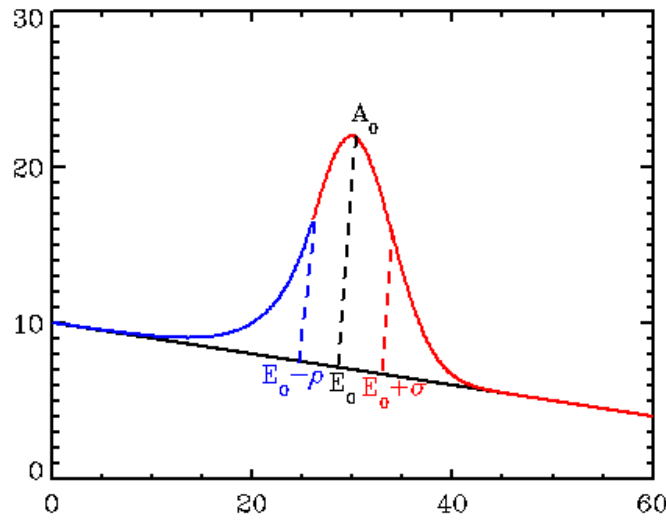

Figure 3.7: Modeled shape of a peak displaying the different parameters. The red line is the Gaussian function and the blue line is the exponential tail.

On the basis of the modeled shape that has been previously presented, the definition of the area of a line is the following:

$$Area = \int_{-\infty}^{+\infty} f(x)dx = \int_{-\infty}^{E_0 - \rho} A * \exp\left(\frac{-\rho}{\sigma^2} * \left(E_0 - \frac{\rho}{2} - x\right)\right) dx + \int_{E_0 - \rho}^{+\infty} A * \exp\left(\frac{-(x - E_0)^2}{2\sigma^2}\right) dx$$

It has been calculated to be equivalent to the following formula:

$$Area = A * \sigma * \left(\frac{\sigma}{\rho} * \exp\left(\frac{-\rho^2}{2\sigma^2}\right) + \frac{\sqrt{2\pi}}{2} * \left(1 + erf\left(\frac{\rho}{\sigma\sqrt{2}}\right)\right)\right)$$

The first step to model a region of the spectrum consists in estimating the continuum. The continuum can be evaluated on the same interval than the rest of the peak fitting, but the use of a larger interval often gives better results. The new version of Aquarius provides this dissociation between continuum and lines fitting in order to obtain a more stable determination of continuum. The user only needs to define the

126

degree of the polynomial function to perform the fit. The function resulting from the fit is plotted on top of the spectrum, enabling the user to check that the fit works. When the fitting routine fails with a two-degree polynomial, a one-degree should be imposed.

The number of peaks present in the region of interest is set by the user. The program needs initial values for the parameters of the different peaks. A run of the program is made of several iterations that tend to minimize the distance between the measured spectrum and the modeling function. If the program manages to converge, the result consists in the values of the parameters for the last iteration.

The code contains options that allow decreasing the number of degrees of freedom. The user can force any parameter to a given value. He can alternatively assign a range of values where the parameter is known to evolve. When there are several peaks in the same region of interest, they can also be attributed same ρ and σ.

Finally Aquarius offers plotting routines that allow visualizing the results. The code holds the ability to plot the measured spectra, the modeled function and the separate continuum and peaks that compose it. There is also a functionality to perform fits of multiple spectra and store the resulting parameters, thus allowing the production of maps of the area (or any other chosen parameter) of a line.

The graphical user interface of Aquarius is meant to provide all the described features in a user-friendly tool. The main window of the program contains a menu bar, a commands section and a plot area (Figure 3.8). The menu bar consists of 3 items. *File* enables to: open a spectrum (.txt and .dat formats), load a session, save a session and quit the application. *Graph* enables to: plot a spectrum and save it in different formats (jpeg, png and ps). *Batch* enables to: load and fit multiple spectra, plot the results (continuum parameters, peak(s) parameters, peak(s) area), map the results (peak(s) area, uncertainty on the determination of this area).
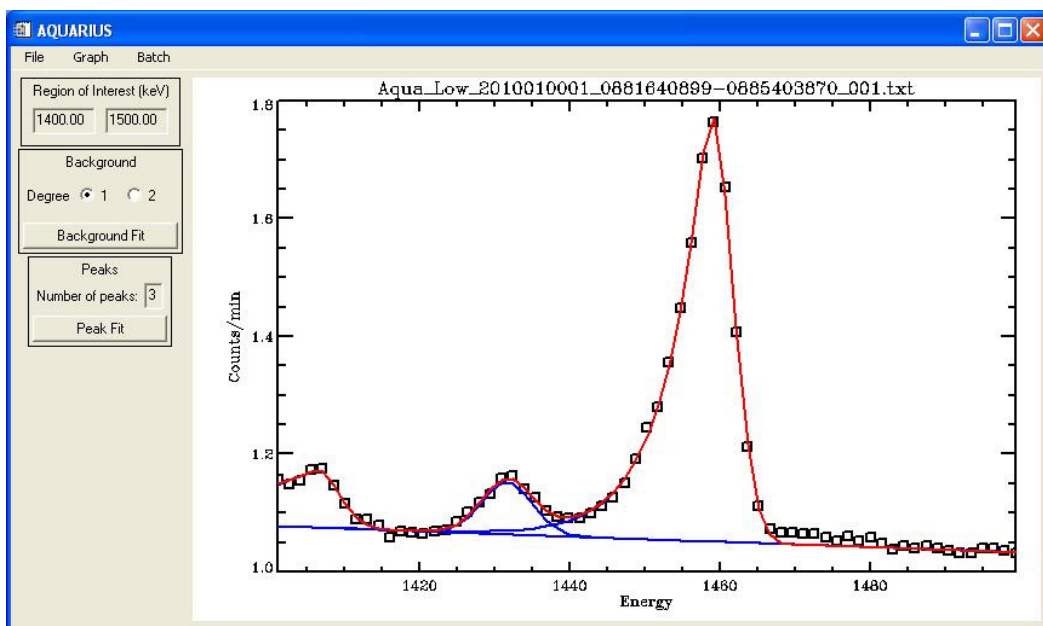

Figure 3.8: Main window of the Aquarius program displaying the fit of the potassium line at 1460 keV on a low gain histogram.

127

In the left side panel of commands, the user can define the region of interest, launch a continuum fitting routine (linear or 2-degree polynomial), set the number of peaks in this region and launch the peak determination routine. Before launching the determination of the peaks, it is recommended to perform a fit of the continuum. Once the continuum is determined, the region of interest can be redefined. The peak determination routine opens a new window dedicated to the parameters of the lines of the region of interest (Figure 3.9).
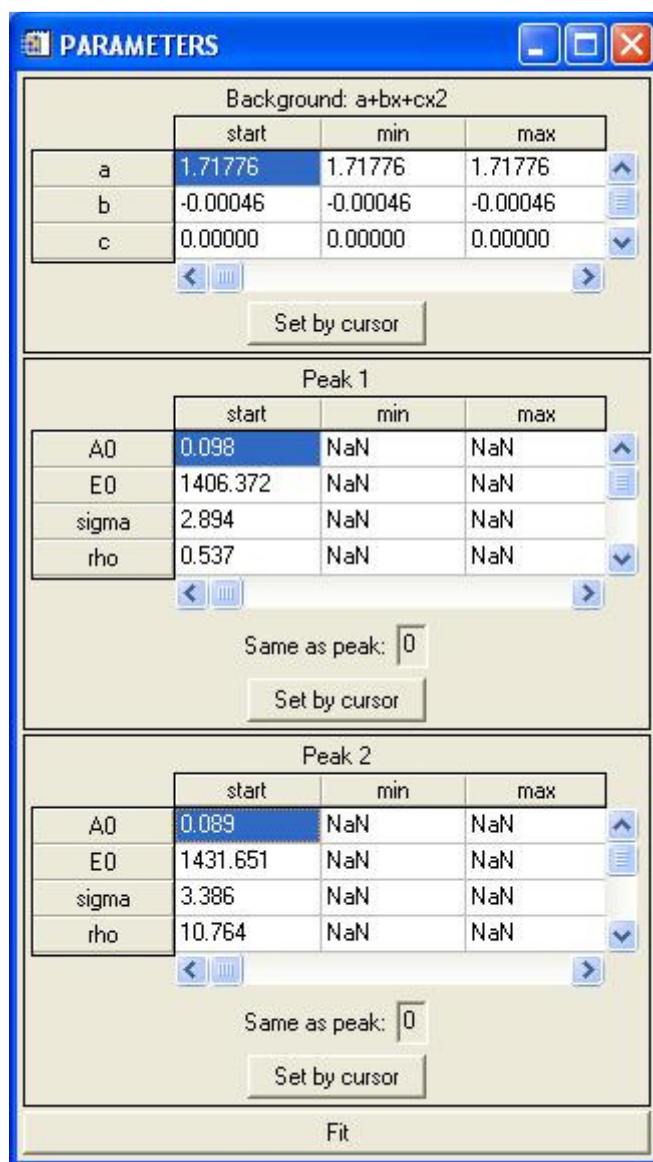

Figure 3.9: Parameters window of the Aquarius program.

Thanks to this parameters window, the user can either enter the initial values for the fitting method or set them on the plot with a cursor. At the top the window contains a table dedicated to the continuum parameters and successive tables dedicated to the peak parameters. Constraints on the parameters of the lines can be applied here. Once all parameters are settled, the fitting method can be launched. It provides the resulting

parameters in a separate window and plots the peaks with the initial and final parameters in the plot area.

This manual fitting of a spectrum can be automated with the batch mode. It is however recommended to do a preliminary analysis of the region of interest using an accumulated spectrum with good statistics (global lunar spectrum for instance). The parameters resulting from that fit can be saved and used as starting values for fitting a high number of spectra (the spectra accumulated in a grid of pixels for instance). As for regular fits, the program outputs a table of results for the batch mode (Figure 3.10).

Fit results of Low0881640899-0885403870

File

	E0(keV)	A0(cpm/keV)	sigma(keV)	rho(keV)	area(cpm)	FWHM(keV)	FWTM(keV)	uncertainty
0300010001	1459.304	0.619	2.690	1.437	5.637	8.415	24.615	0.010
0300010002	1459.094	0.597	3.151	1.889	6.045	9.178	26.103	0.008
0300010003	1458.665	0.718	2.507	1.156	6.563	8.691	26.187	0.010
0300010004	1458.634	0.914	2.158	0.786	8.242	9.000	28.072	0.010
0300010005	1458.636	1.227	3.111	2.424	11.097	7.960	20.815	0.008
0300010006	1458.768	1.438	2.251	0.975	12.221	8.182	24.918	0.009
0300010007	1459.431	1.259	2.718	1.412	11.745	8.666	25.510	0.007
0300010008	1458.998	0.944	2.950	1.879	8.716	8.297	23.198	0.007
0300010009	1458.448	0.740	2.669	1.398	6.753	8.463	24.867	0.009
0300010010	1458.208	0.770	2.436	1.223	6.551	7.948	23.562	0.012
0300010011	1458.562	0.573	3.923	3.383	6.338	9.691	24.339	0.013
0300010012	1459.047	0.674	2.236	1.056	5.429	7.622	22.867	0.013
0300020001	1459.828	0.480	2.064	0.870	3.802	7.658	23.420	0.012
0300020002	1459.586	0.439	2.847	1.446	4.335	9.216	27.257	0.010
0300020003	1458.388	0.601	2.725	1.679	5.203	7.810	22.044	0.010
0300020004	1458.363	1.167	1.995	0.741	9.617	8.190	25.487	0.009
0300020005	1458.799	1.519	3.046	1.972	14.389	8.494	23.638	0.008
0300020006	1458.681	1.469	2.406	1.235	12.204	7.734	22.824	0.009
0300020007	1459.406	1.382	2.564	1.434	11.747	7.790	22.549	0.007
0300020008	1458.945	0.832	2.888	1.846	7.511	8.110	22.654	0.008
0300020009	1458.423	0.731	2.631	1.772	5.892	7.188	19.765	0.010
0300020010	1457.953	0.634	2.633	1.753	5.135	7.237	19.972	0.013
0300020011	1458.931	0.434	3.683	2.759	4.713	9.574	25.397	0.015
0300020012	1459.205	0.491	2.273	0.818	4.699	9.575	29.909	0.014
0300030001	1458.818	0.371	3.415	3.260	3.480	8.218	19.731	0.013
0300030002	1459.073	0.384	3.305	2.719	3.632	8.288	21.220	0.011
0300030003	1458.734	0.475	2.186	0.861	4.142	8.560	26.437	0.012
0300030004	1458.641	0.911	2.229	0.973	7.635	8.053	24.493	0.010
0300030005	1458.844	1.353	3.180	2.088	13.309	8.805	24.401	0.008

Figure 3.10: Results window of the Aquarius program for the batch mode.

Although it does not offer as much flexibility as a manual code, Aquarius is a good tool for first analysis studies of spectra. When it comes to fitting difficult portion of the spectrum or working with higher resolutions, manual coding is compulsory. Aquarius is rather dedicated to non coding-proficient users to fit and plot spectra. It was developed in close collaboration with the Japanese team so that their specifications and comments were progressively incorporated to the code.

Band passing method

Lines have not only been examined with the peak fitting method, but also with the energy band summing. This very basic method consists in summing the spectra in a window containing the line of interest. The continuum is adjusted with a linear or 2-degree polynomial function and removed. Such a method was used for the low-energy resolution gamma ray spectra collected by Lunar Prospector [Lawrence et al., 1999]. It is especially robust for isolated lines, such as those of K and Th mentioned above, or with very low statistics. It can therefore be a very useful tool for very high resolution

mapping, where the statistics are often too low to allow fitting the spectra in the different pixels.

The main drawback of this method is that when two lines are very close, the counts accumulated in one band are likely to be produced by the other line. Figure 3.11 shows a portion of the low gain histogram accumulated on the entire lunar surface. This region has been both processed with the peak fitting code of Aquarius and with energy band passing. The proximity of the Mg and Ti lines makes it very hard to define energy bands that do contain only photons produced by one of the two elements. The band passing method is therefore not adapted to such cases.
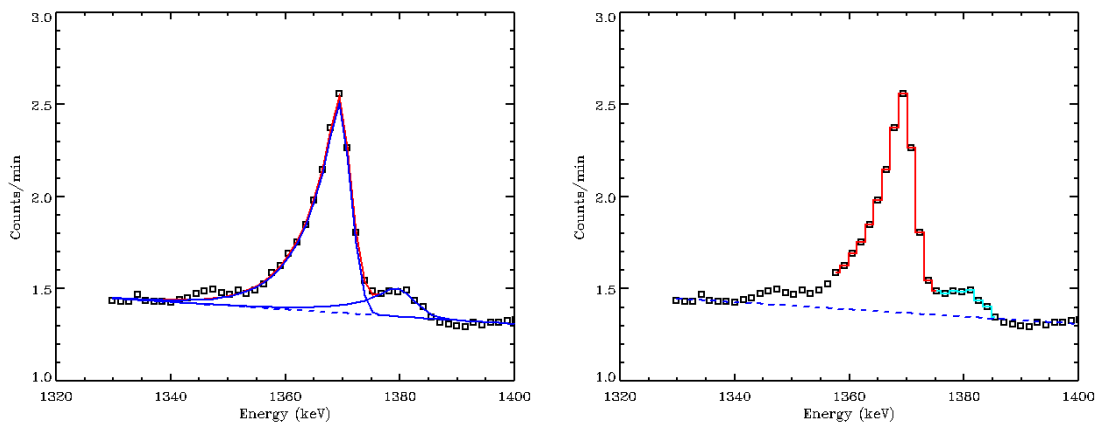

Figure 3.11: Line analysis performed in the [1320 keV; 1400 keV] region of interest. Superposition of data (black squares) with modeled linear continuum (blue dashed line) (a) Individual peaks (blue line) and fitting function (red line) issued from Aquarius. (b) Delimitation of the window of data to sum for the Mg peak (red line) and for the Ti peak (turquoise line).

Statistical analysis

The two methods of analysis previously described are very traditional processing tools of the gamma-ray spectra and were both used for the previous missions [Lawrence et al., 2004; Boynton et al., 2006]. The data can also be processed with a multivariate technique, the Independent Component Analysis (ICA) [Comon, 1994; Hyvärinen and Oja, 2000]. We now present this method and the results obtained on the Selene GRS dataset.

The Independent Component Analysis is a computational method that separates a multivariate dataset into additive subcomponents. The framework for this segmentation consists in assuming the data variables to be linear mixtures of some unknown latent variables, and the mixing system is also unknown. The latent variables are assumed non-Gaussian and mutually independent and they are called the independent components of the observed data. These independent components, also referred to as sources or factors, can be found by ICA. This is done by maximising a non-gaussianity criterion of the sources.

As in [Forni et al., 2005], we have used the JADE algorithm developed and described in [Cardoso, 1997] for analysing our gamma-ray spectra. The ICA has been run with datasets of increasing resolution. Only 1500 channels of the low gain spectra have been used for analysis. This corresponds to the energy range from 750 to 3000 keV. The number of components has been set to 5.

Two of the five sources extracted from the ICA have been identified as meaningful for elemental composition. The first one is correlated to the radioactive elements: Th, U and K (Figure 3.12a). It also contains a small contribution of Al (very likely consisting in gamma rays created in the spacecraft material) and Si. The second source is mostly correlated with Fe (Figure 3.12b) with contributions from K, Si, Mg and Al.
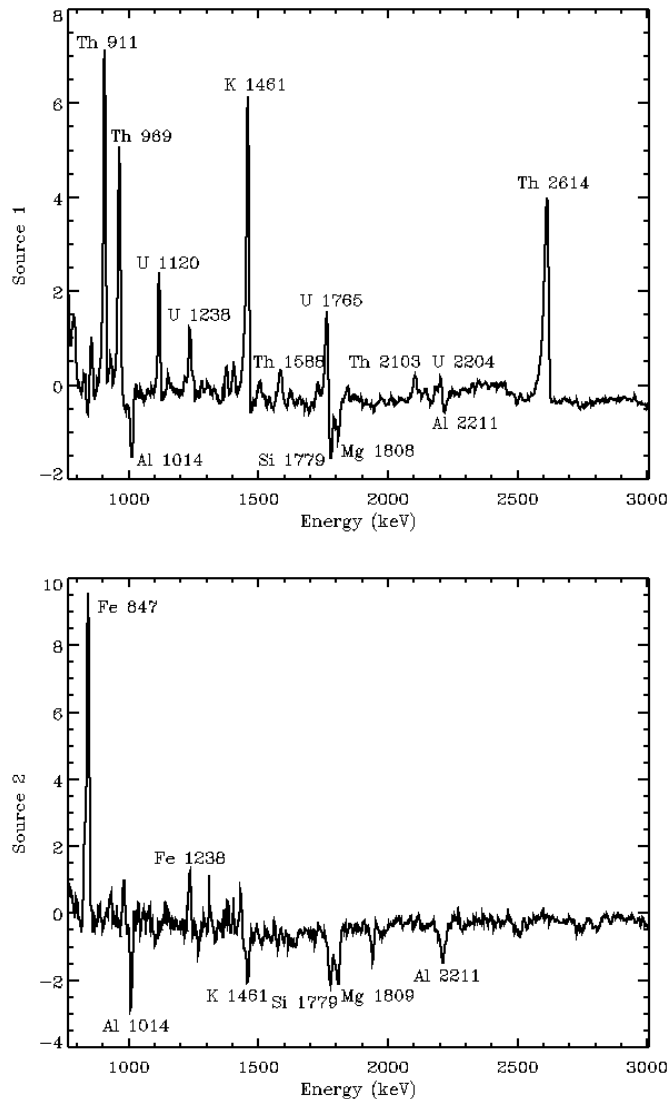

Figure 3.12: (a) Source 1 and (b) source 2 obtained with the ICA.

The other sources contain a large portion of continuum and display lines that are considerably weaker than that of source 1 and 2. When mapped, source 3 and source 4 display a partially dipolar distribution, which is correlated to the altitude of the

spacecraft. The remaining sources therefore do not contain information significant for geochemistry analysis, and are on the contrary correlated to geometric characteristics and continuum. This result sounds very promising because it means that these contributions have been extracted from the two sources containing the interesting signal.

Maps of the source are constructed by calculating the correlation coefficient between the spectrum accumulated in each pixel and the source. Maps of source 1 and source 2 (Figure 3.13) have been thus obtained. Because of its features, the first source exhibits a map correlated to the radioactive elements K, Th and U. The second source map contains a mix of Fe and of other elements within a smaller extent. The ICA has been run with datasets of increasing resolution: 192 pixels, 768 pixels and 3072 pixels to show the capability of the method to extract information, even with datasets of poor statistics.
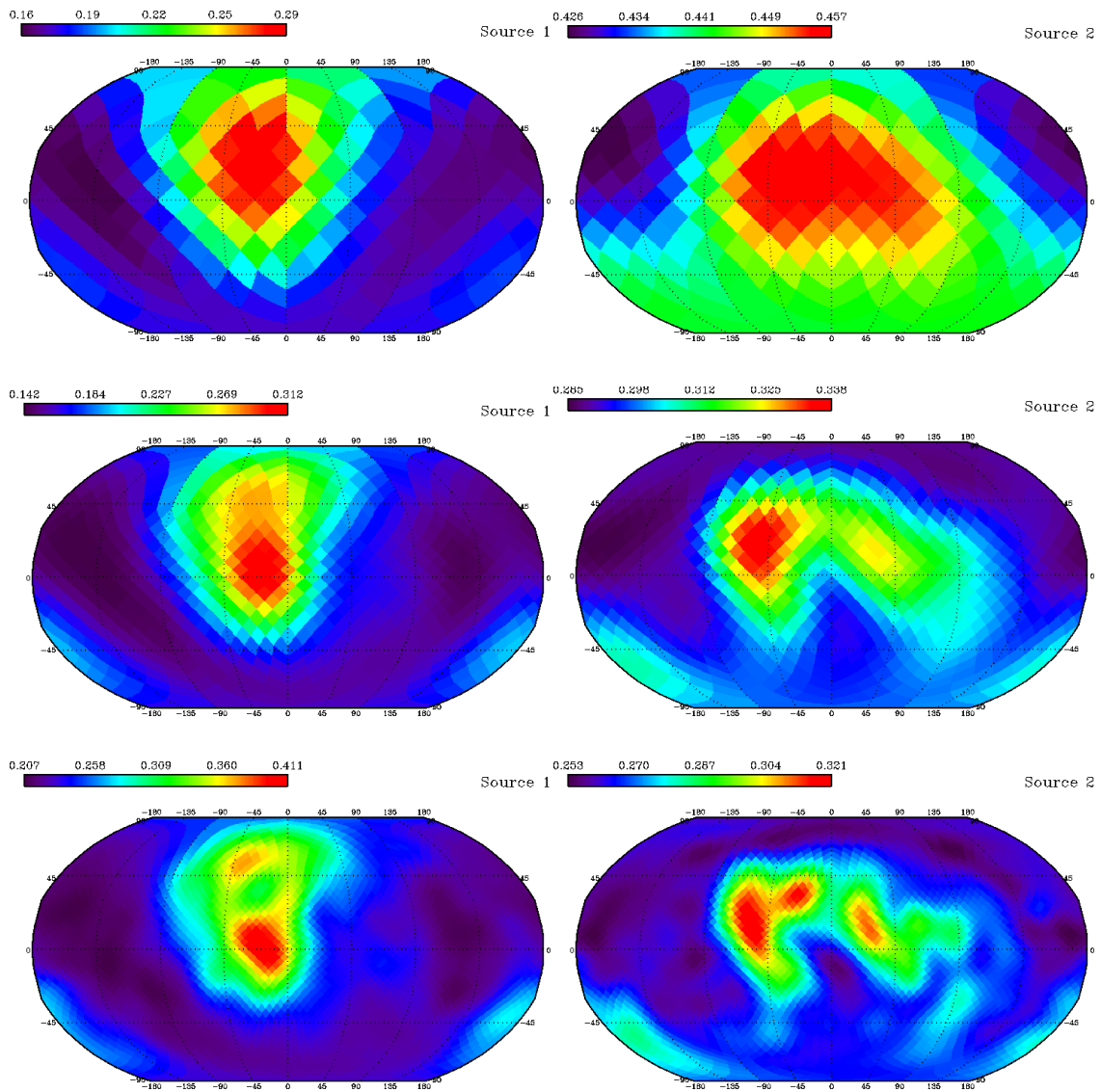

Figure 3.13: Component 1 and 2 obtained with the ICA at the following resolutions: (a) 14.65° (192 pixels) (b) 7.33° (768 pixels) and (c) 3.66° (3072 pixels).

Because of the low accumulation time so far obtained, innovative methods of spectrum analysis as the Independent Component Analysis prove especially successful at increasing the resolution of the results in spite of the low-statistics. Another advantage of this method is to separate the interesting signal (variations in elemental abundances) from other contributions (variations in the spacecraft height). On the other hand we do not extract elements but a combination of covarying elements.

Estimation of statistical errors

The statistical errors associated with the counting rates maps can be estimated on the basis of Poisson counting statistics. The fractional uncertainty is defined as follow:

$$\sigma = \frac{1}{\sqrt{S N_{spectra}}}$$

where *S* is the mean number of counts in a spectrum and $N_{spectra}$ the number of spectra measured within a pixel. The uncertainty therefore primarily depends on the resolution of the map and on the intensity of the signal. It also depends on the method chosen to acquire the counts because peak fitting and energy band summing do not provide the same counting rates for a given line.

The generation of error maps therefore requires the use of the time series data in addition to that of the gridded data. Once accumulated into pixels, accumulation time in a pixel is lost. So either the number of acquisitions or the accumulated time duration of the measurement have to be stored. The accumulation time is approximately 17 seconds times the number of acquisitions, however uncertainties in clocks and dead time can introduce a slight difference.
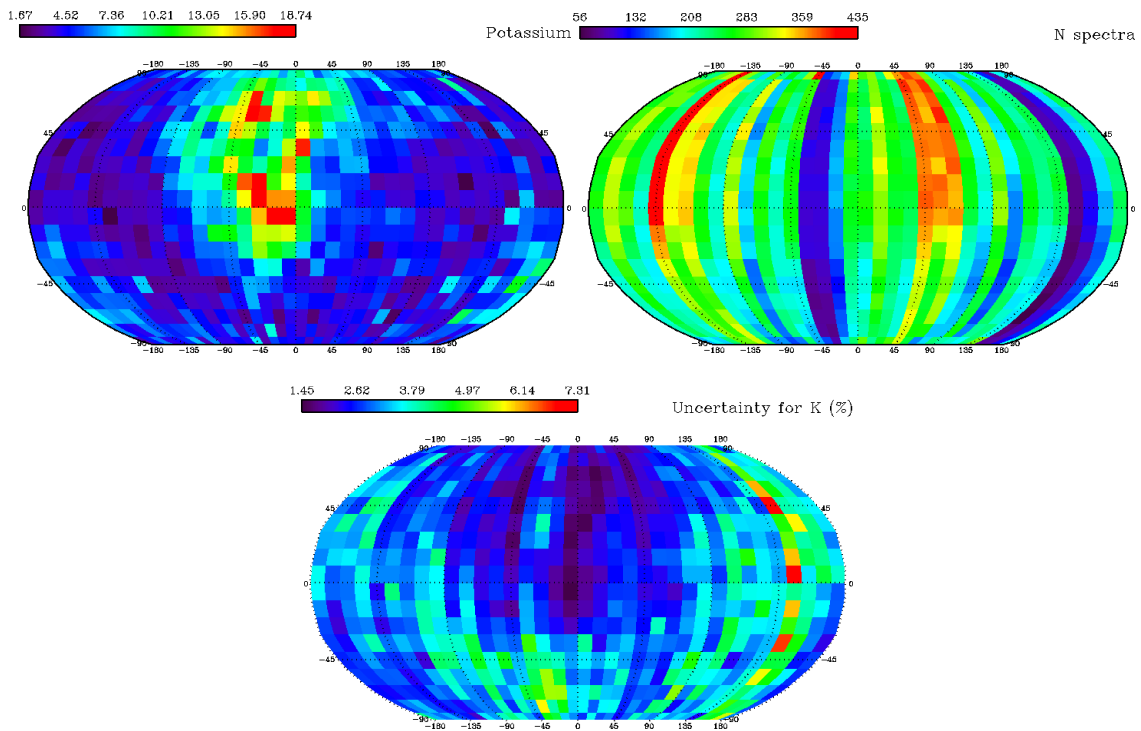

Figure 3.14: (a) Counts in the potassium peak at 1460 keV determined with peak fitting. (b) Number of spectra accumulated on a cylindrical grid with a 10° geographic resolution. (c) Statistical uncertainty associated with the determination of the K counts.

Here is a quick demonstration of an error calculation for the peak of potassium (1460 keV). We first estimate the uncertainty for a map of potassium obtained with the peak fitting method. The data has been accumulated in a cylindrical grid with a 10° geographic resolution. We first calculate the mean number of counts in each pixel S (which is simply the potassium map in counting rates) (Figure 3.14a). We then estimate the number of spectra acquired in each pixel $N_{spectra}$ (Figure 3.14b). The uncertainty is finally obtained by inverting the square root of the product of the two (Figure 3.14c).

The uncertainty is calculated in percentages. It ranges between 1.45 and 7.31 % for the potassium map at a resolution of 10°. It is generally lower than 5 % outside the band of longitudes 140° that has been very poorly covered by the spacecraft. As a second example we estimate the uncertainty associated with a map of Thorium obtained by summing the counting rates within an energy band around the line at 2614 keV. The data has been accumulated in an equal area grid with a 3° geographic resolution.
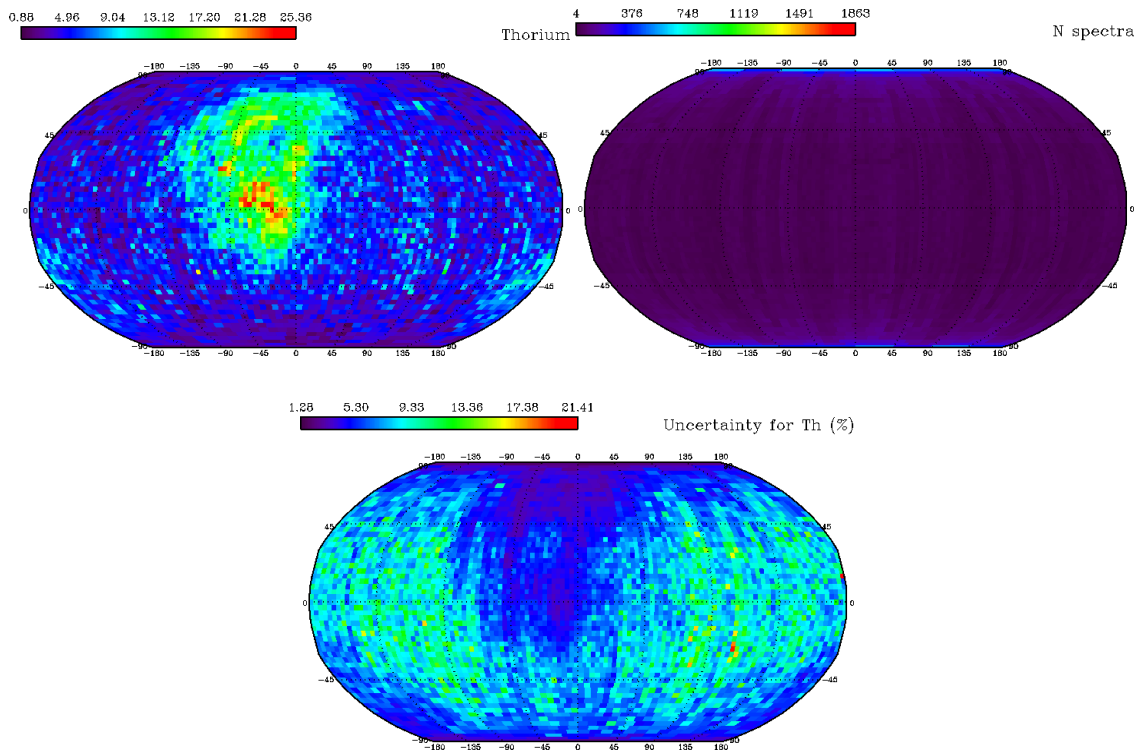

Figure 3.15: (a) Counts in the thorium peak at 2614 keV determined with energy band passing. (b) Number of spectra accumuled on an equal area grid with a 3° geographic resolution. (c) Statistical uncertainty associated with the determination of the Th counts.

The uncertainty is higher, in conformity with what can be expected when increasing the geographic resolution. However only several pixels have a very high uncertainty which is due to the low number of spectra acquired over these regions (as low as 4 spectra for some pixels). On the other side, the equal area projection provides a very significant improvement of the statistical quality of the data at the high latitudes due to the larger number of acquisitions in these regions.

3.2.3 Global lunar spectrum

Overview of the global spectrum

In order to obtain spectra with counting statistics sufficient for peak analysis, we accumulate all observations. The addition of all spectra collected in between December 21, 2007 and February 17, 2008 allows obtaining about 860 hours. This global spectrum provides the best signal to noise ratio to perform identification of lines.
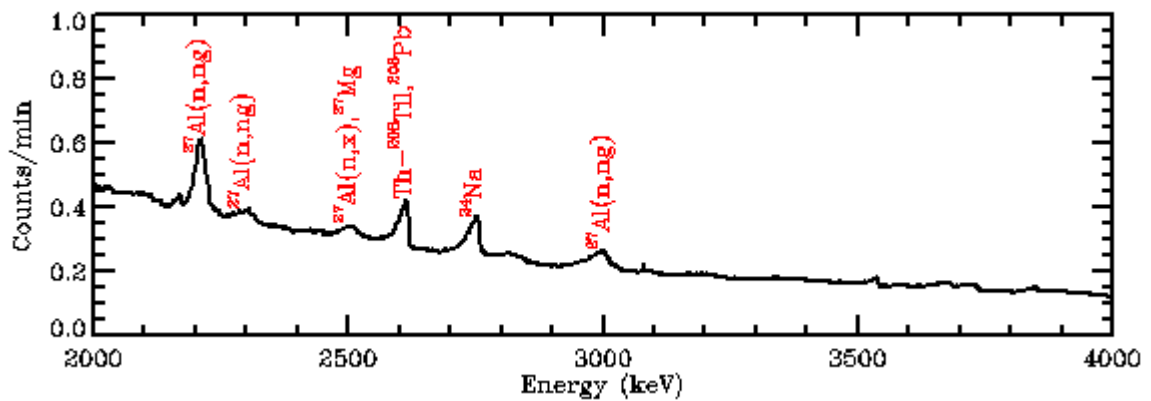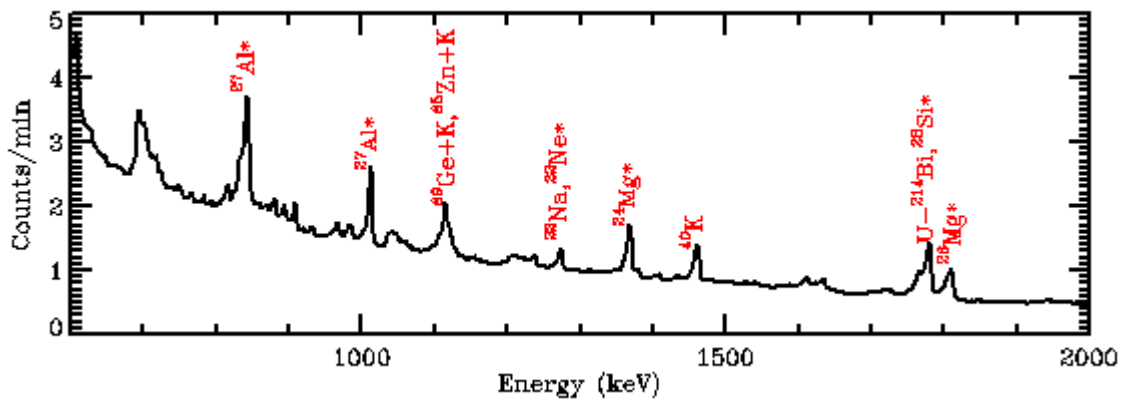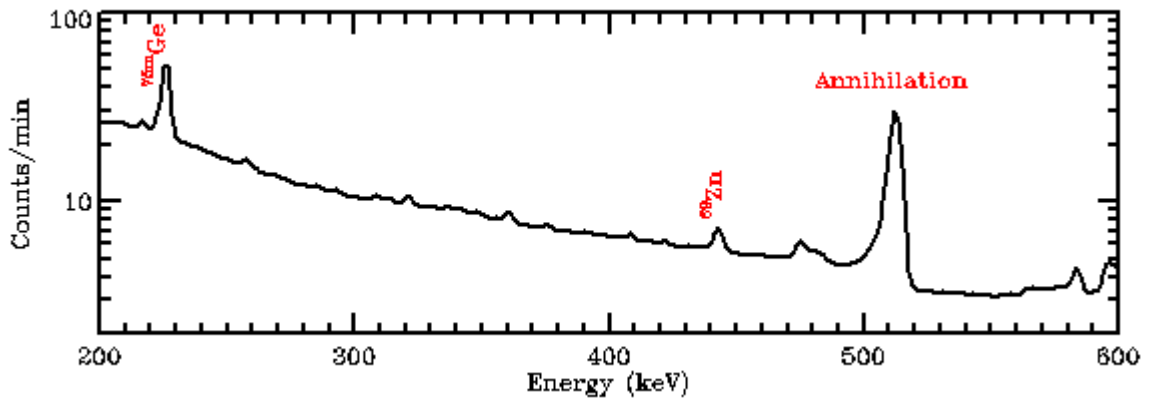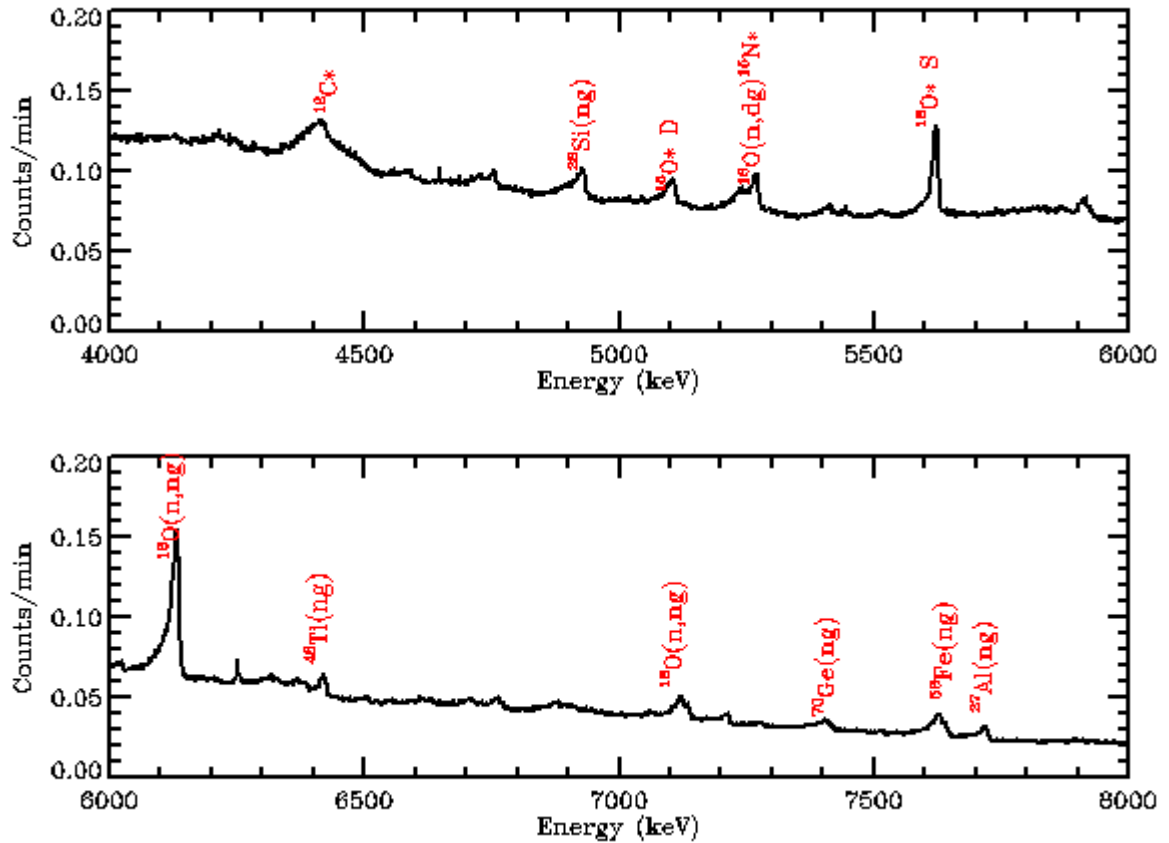
Figure 3.16: Global lunar spectrum (low gain mode).

The spectrum (Figure 3.16) consists in various lines of interest superposed on a continuum. Many elements of interest for constraining the geology of the Moon have been identified: O, Mg, Al, Si, K, Ca, Ti, Fe, U and Th. The gamma ray lines that arise from the decay of longlived radioactive species are among the easiest to analyze.

The abundance of three species has already been published thanks to such lines: potassium, thorium and uranium [Yamashita et al., 2008]. Secondary neutrons from cosmic ray interactions also produce gamma ray when reacting with the planetary material, according to scattering or absorption reactions. However these lines need substantial corrections before an interpretation in terms of abundance can be performed.

Analysis of the global spectrum

The peak fitting method has been run on the global lunar spectrum to define the parameters of the major lines with the best signal possible. Many of the lines previously identified on Figure 3.16 as well as additional lines were analyzed.

Table 3.2 displays the main parameters of the fitted peaks: central energy, area and width of the line. Additional information such as the proposed source for the line and its corresponding energy has been added. Finally we calculate the difference between the energy measured in the fit and the reference energy (Figure 3.17). This provides us an estimation of the quality of the calibration function we have used.

136

Energy (keV)	Area (cpm)	FWHM (keV)	Source	Ref Energy (keV)	Diff (keV)
512,4	160,31	5,4	annihilation	511	-1,4
583,5	6,43	4,8	Th-228Ac	583,2	-0,3
842,1	11,97	7	27Al*	843,7	1,6
879,9	1,31	4,6	69Ge+K	882,5	2,6
908,8	2,05	4,6	Th-228Ac	911,2	2,4
1012,6	8,49	6,3	27Al*	1014,4	1,8
1107,1	1,51	6,6	69Ge+L	1108	0,9
1115,6	5,21	6,6	69Ge+K	1117,1	1,5
1122,8	1,5	6,6	65Zn+K	1124,5	1,7
1273,8	2,52	8,1	22Na 22Ne*	1274,5	0,7
1368,6	6,43	8,4	24Mg*	1368,6	0
1461,2	4,63	7,1	40K	1460,8	-0,4
1610,2	1,61	10	40K	1611,7	1,5
1633,4	1,66	10	25Mg*	1633,6	0,2
1765,9	2,3	11,6	U-214Bi	1764,5	-1,4
1779,9	9,59	11,6	28Si*	1779	-0,9
1809,7	5,34	11	26Mg*	1808,7	-1
2210,3	5,33	23,3	27Al(n,ng) Dop	2211	0,7
2503,2	1,1	33,1	27Al(n,x)27Mg Dop	2505,9	2,7
2614,3	3,47	24,7	Th-208Tl 208Pb*	2614,5	0,2
2752,2	3,49	29,7	24Na	2754	1,8
2994,5	3,07	49,9	27Al(n,ng) Dop	3004	9,5
4408,3	1,36	66,5	12C* Dop	4438	29,7
4930	0,62	39,6	28Si(ng)	4933,9	3,9
5240,4	0,24	30,1	15O*	5239,9	-0,5
5270,1	0,68	30,1	16O(n,dg)15N*	5269,2	-0,9
5623,9	0,98	17,4	16O* S	5617,6	-6,3
6133,2	2,1	25,4	16O(n,ng) 16N	6128,6	-4,6
6421,4	0,19	13,9	48Ti(ng)	6418,4	-3
6890,6	0,35	73,9	16O(n,ng) Dop	6915	24,4
7407,5	0,22	40	70Ge(ng)Sum	7415,5	8
7628,5	0,26	29,9	56Fe(ng)	7631,1	2,6
7642,1	0,23	29,9	56Fe(ng)	7645,5	3,4
7720,5	0,19	29,9	27Al(ng)	7724	3,5

Table 3.2: Analysis of the global lunar spectrum.

There are little discrepancies between the energy of the fits and the reference energies. Most of the lines have central energy within 5 keV of the reference energies. However some of the lines are quite distant from the reference energies. The gap is often due to the fact that the lines are Doppler broadened [Brückner et al., 1991], which makes it harder to determine the precise center of the peak. This effect happens when a gamma ray is emitted while the parent nucleus is moving.
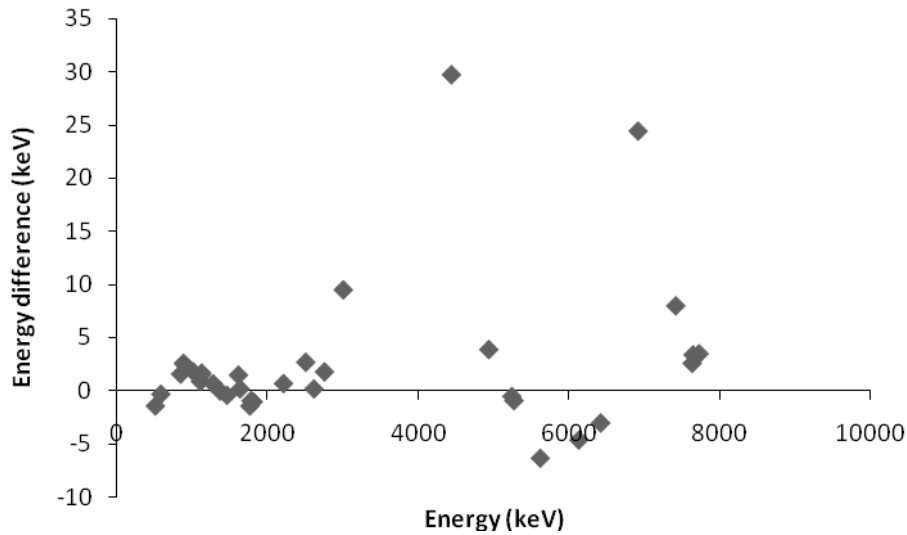
Figure 3.17: Difference between measured and reference energy as a function of energy.
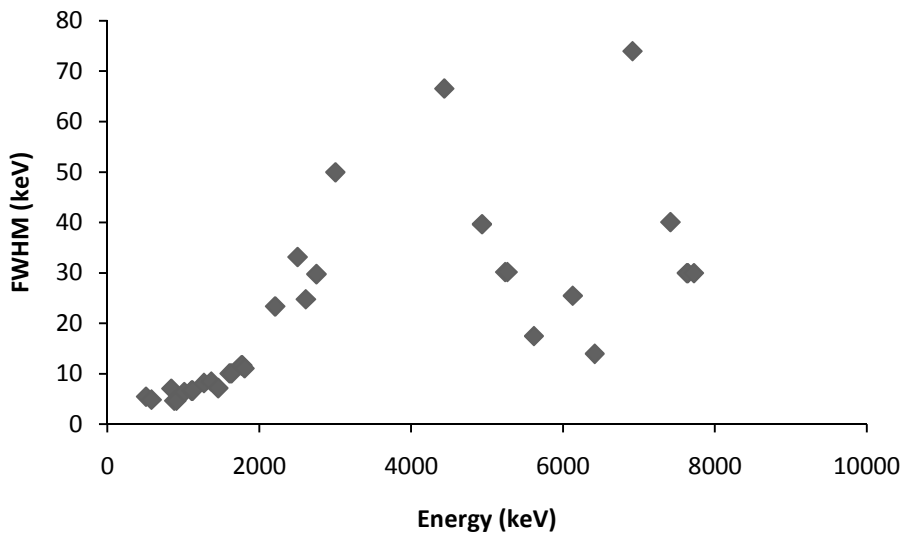

Figure 3.18: Full Width at Half Maximum of the fitted peaks as a function of energy.

The width of the lines is evaluated with the FWHM (Figure 3.18). Lines are fitted with the theoretical line shown in Figure 3.7. However this model does not suit perfectly all lines. Only narrow peaks are in conformity with this model. The width of the peaks increases systematically with energy. For low energies, the peaks are quite narrow and the increase is slow and regular. Above 2000 keV, the variations of the width of peaks are more erratic. As we previously mentioned, some of the lines are Doppler broadened which explains why they have unusually large FWHM. In addition to this effect, the signal to noise ratio decreases with the increasing energy. Therefore the quality of the fit is not as good at high energies. Some of the large rays identified in Figure 3.18 might be due to this effect.

3.3   Determination of the Fe concentration of the Moon

3.3.1   Fe lines in the global lunar spectrum

In order to obtain spectra with counting statistics sufficient for peak analysis, we accumulate all observations. To date the dataset consists of two periods respectively extending from December 21, 2007 to February 17, 2008 and from July 7, 2008 to December 11, 2008. The addition of all spectra collected within each of these periods allows obtaining a total accumulation time of about 1050 and 2143 hours. The spectral resolution of the instrument has been slightly degraded during the interval separating the two periods. Therefore we perform separate accumulation to preserve the shape of the lines.

The global spectrum of the first period provides the best conditions: good signal to noise ratio and good resolution. Many elements of interest for constraining the geology of the Moon have been identified: O, Mg, Al, Si, K, Ca, Ti, Fe, U and Th. We report here (Table 3.3) the lines that have been identified as produced by isotopes of Fe.

Source	Processus	Eref (keV)
^{56}Fe	*	1238.3
^{56}Fe	(ng)	1612.8
^{56}Fe	(ng) single escape	5409.4
^{56}Fe	(ng) single escape	5507.5
^{56}Fe	(ng)	5920.4
^{56}Fe	(ng)	6018.4
^{56}Fe	(ng) double escape	6623.5
^{56}Fe	(ng) single escape	7120.1
^{56}Fe	(ng) single escape	7134.5
^{56}Fe	(ng)	7278.8
^{56}Fe	(ng)	7631.1
^{56}Fe	(ng)	7645.5
^{54}Fe	(ng) single escape	8786.7
^{54}Fe	(ng)	9297.7

Table 3.3: Reference energy of the gamma ray lines identified as produced by Fe in the global lunar spectrum measured by the Selene GRS. * stands for multiple processes and (ng) stands for neutron capture.

These lines have been fitted with the use of Aquarius (described in part 3.2). For each Fe line, a region of interest has been defined to restrict the analysis to a smaller portion of spectrum. This region of interest might or might not contain other lines in addition to the selected Fe lines. Each portion is fitted by summing a continuum with a given number of lines. The continuum is modeled with a linear function, which is a generally very good approximation inside a reasonably small energy range. Lines are modeled with a standard Gaussian shape modified with an exponential tail. The parameters describing this model (A_0, E_0, σ and ρ) are saved and an area is calculated for

these ideal lines. The Fe lines presented in Table 3.3 offer a variety of configurations that can be encountered in the spectra.

Many are narrow peaks sitting on a continuum: lines at 1238.3 keV, 7278.8 keV and 8786.7 keV. Those lines are the simplest to fit. Other lines are very hard to fit (lines at 5409.4 keV and 5507.5 keV; lines at 5920.4 keV and 6018.4 keV) because they are close or even overlapping with lines produced by other elements. They are consequently harder to fit. Other lines can be more complicated than the standard Gaussian function. Some peaks are Doppler broadened (lines at 6623.5 keV and 9297.7 keV). This phenomenon is due to the fact that the gamma rays were emitted while the excited nucleus was moving [Evans et al., 2006].

And finally some lines are formed by the doublet of two regular-shaped lines both produced by an iron nucleus (lines at 7120.1 – 7134.5 keV and 7631.1 – 7645.5 keV). The fit is not necessarily more complicated than a single line because the parameters of the lines of the doublets are not independent: these lines have identical shapes and widths. Besides, only the estimation of the area will be helpful for chemical abundances analysis. Fortunately the estimation of that area is not significantly affected by the fact that the line is a doublet.

Some of the lines that have been analyzed are very poorly fitted. When the signal to noise ratio decreases, the quality of the fit decreases. The lines at 5920.4 keV, 6018.4 keV, 8786.7 and 9297.7 keV are not well modeled. The line at 6018.4 keV thus ends up with an erroneous σ.
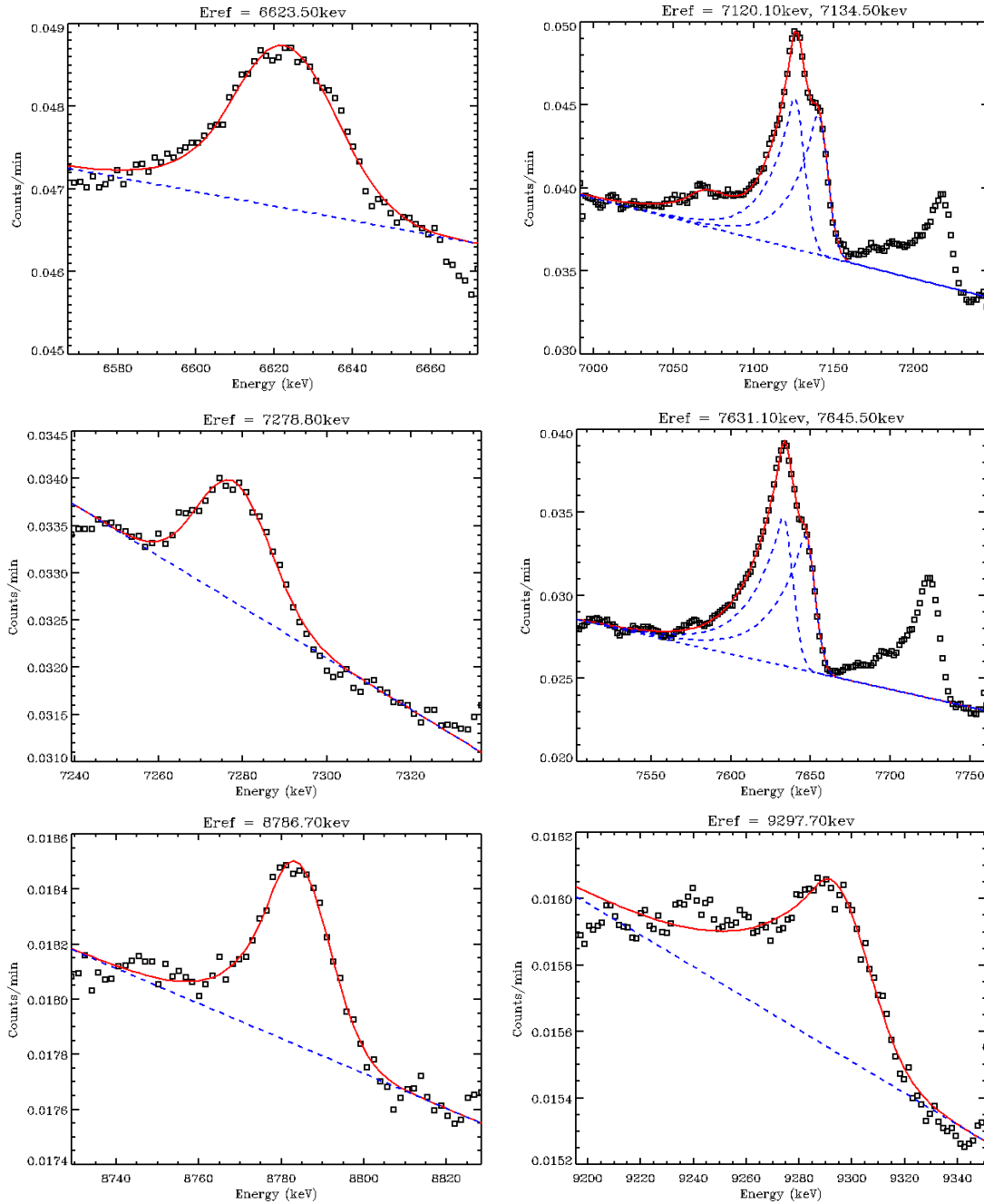

140
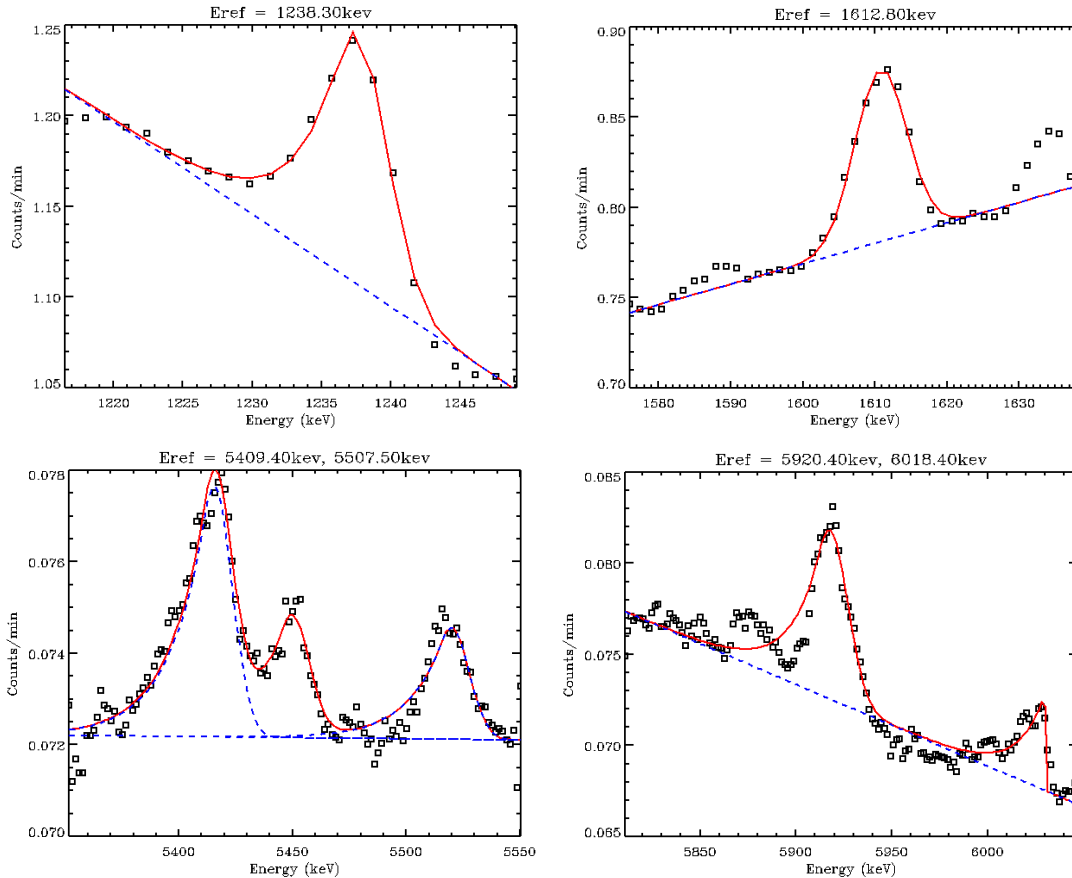
Figure 3.19: Global lunar spectrum as a function of energy in keV in regions of the spectrum containing Fe lines. Black squares are data points, red lines are analysis functions that best fit the data, blue dotted lines are background and individual peaks.

The parameters of the lines fitted in Figure 3.19 are displayed in Table 3.4. As mentioned earlier the lines have very variable parameters depending on their shape. Some of the lines have a quite small area: the lines at 5507.5, 6018.4, 6623.5, 7278.8, 8786.7 and 9297.7 keV. These are not adapted for mapping because the signal within tiled spectra is too faint. The two doublets seem to also have low counts, but thanks to the addition of the area of the two lines, they finally reach reasonably good statistics.

Eref (keV)	A₀ (cpm)	E₀ (keV)	Sigma (keV)	Rho (keV)	Area (cpm)
1238.3	0.1407	1237.5	2.36	1.56	1.026
1612.8	0.0954	1610.8	3.61	12.62	0.864
5409.4	0.0055	5415.5	7.87	3.83	0.153
5507.5	0.0024	5519.7	7.87	3.83	0.068
5920.4	0.0098	5918.1	8.94	16.91	0.219
6018.4	0.0057	6029.5	0.34	0.007	0.088
6623.5	0.0019	6622.5	13.48	16.52	0.069
7120.1	0.0091	7125.6	6.05	2.09	0.238
7134.5	0.0085	7140.1	6.05	2.09	0.221
7278.8	0.0013	7277.9	8.79	49.75	0.028
7631.1	0.0089	7632.7	5.99	1.64	0.270
7645.5	0.0081	7646.5	5.99	1.64	0.244
8786.7	0.0007	8783.5	8.21	7.07	0.015
9297.7	0.0005	9292.6	13.81	5.74	0.027

Table 3.4: Fitting parameters of the gamma ray lines identified as produced by Fe in the global lunar spectrum measured by the Selene GRS.

The variation of the width of the line is constrained by the sigma parameter. As shown in Table 3.4, the width of the lines is generally increasing with increasing energies. However some exceptions occur: the Doppler broadened lines previously mentioned. This first analysis of the Fe lines present in the global lunar spectrum allow identifying which lines are the most appropriate for mapping. After removing the lines that do not have sufficient statistics, only the line at 1238.3 keV, the doublet at 7120.1-7134.5 keV and the doublet at 7631.1-7645.5 keV have been kept for mapping purpose.

3.3.2 Fe counting rates mapping

Peak fitting

The spectra have been tiled according to the Healpix pixelisation with the following resolutions 14.65° (192 pixels), 7.33° (768 pixels) and 3.66° (3072 pixels). All channels of the datasets have been filtered with the wavelet transform described in part 3.2, thus augmenting the signal to noise ratio in spectra. Choosing the resolution for a given peak is a compromise between obtaining the best resolution as possible and sufficient statistics in the pixels to extract the information from the background. In addition to that, the lines attributed to Fe that were previously described have different signal to noise ratio. Some of them are too faint to provide sufficient counts once the spectra are tiled in pixels.

Of the above mentioned lines, the following have been identified as the most appropriate for mapping: the single line at 1238.3 keV and the doublets at 7120.1-7134.5 keV and at 7631.1-7645.5 keV. All these lines have been analyzed to figure out the best region of the spectrum to constrain the Fe abundance. The map obtained with the 1238.3 keV line (not shown here) and maps obtained with the doublets show very different features. Further analysis of the spectrum revealed that this line could be

alternatively interpreted as being produced by uranium (line at 1238.1 keV). However the map does not correlate perfectly well with U either. A very likely explanation is that the line measured by the instrument is a mix of lines produced by these two elements.
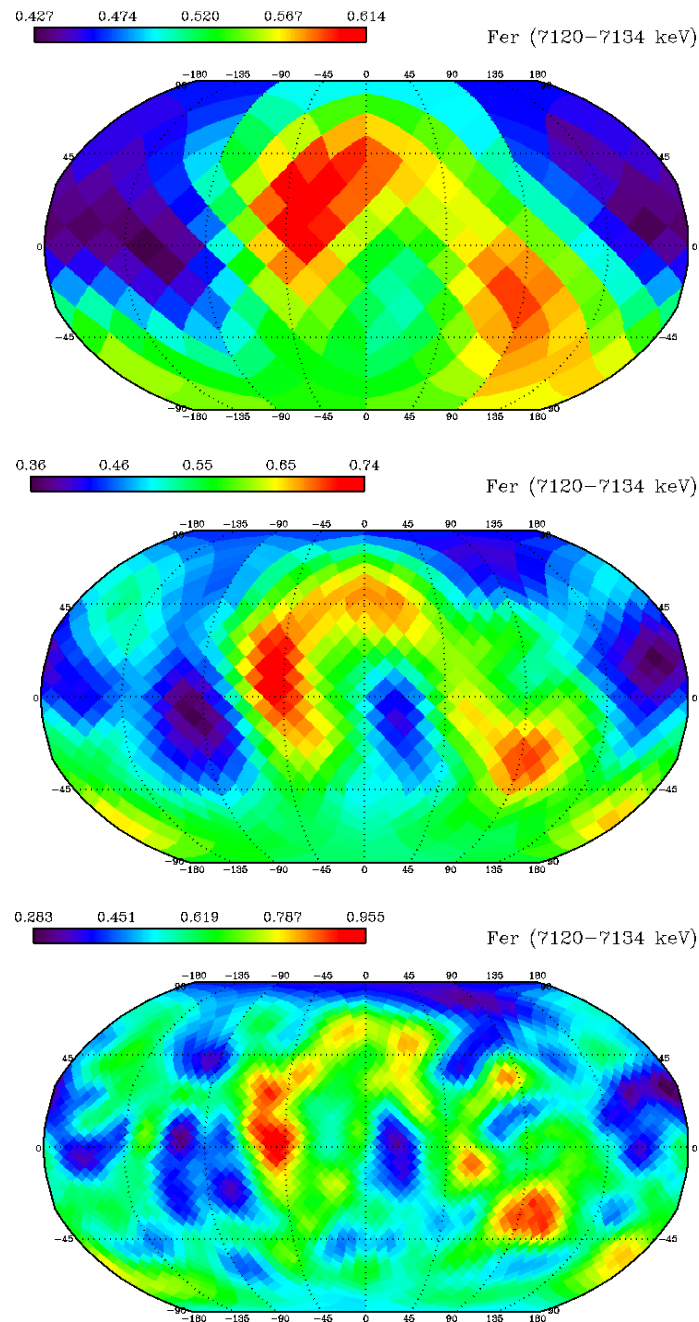

Figure 3.20: Map of Fe counting rates obtained with peak fitting of the doublets at 7120.1-7134.5 keV at resolution (a) 14.65°, (b) 7.33° and (c) 3.66°.

Therefore, only maps obtained with the doublets can be trusted. The peak fitting has been performed on three different datasets: resolution 14.65°, 7.33° and 3.66°. Maps obtained with the peak fitting of the doublet at 7120.1-7134.5 keV are shown in Figure 3.20 and maps obtained with the doublet at 7631.1-7645.5 keV in Figure 3.21. The maps obtained with a resolution of 3.66° are very noisy and not trustable.
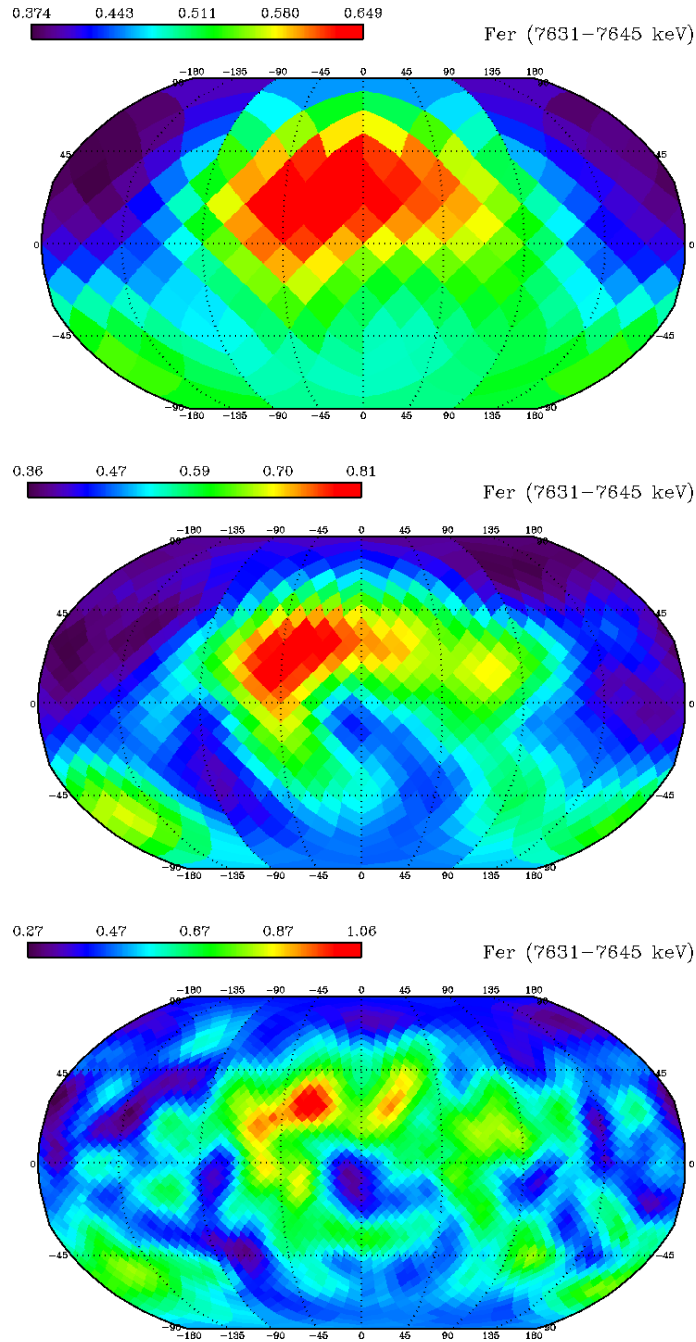
Figure 3.21: Map of Fe counting rates obtained with peak fitting of the doublets at 7631.1-7645.5 keV at resolutions (a) 14.65°, (b) 7.33° and (c) 3.66°.

Band passing

To try to improve the resolution of the maps, the spectra are analyzed with a more robust method: the band passing analysis. This method consists in summing the counts in a window containing the line of interest. The continuum is adjusted with a linear function and removed. This method was used to analyze the gamma ray spectra collected by Lunar Prospector [Lawrence et al., 1999]. The doublets at 7120.1-7134.5 keV and 7631.1-7645.5 keV were analyzed at the different resolutions.
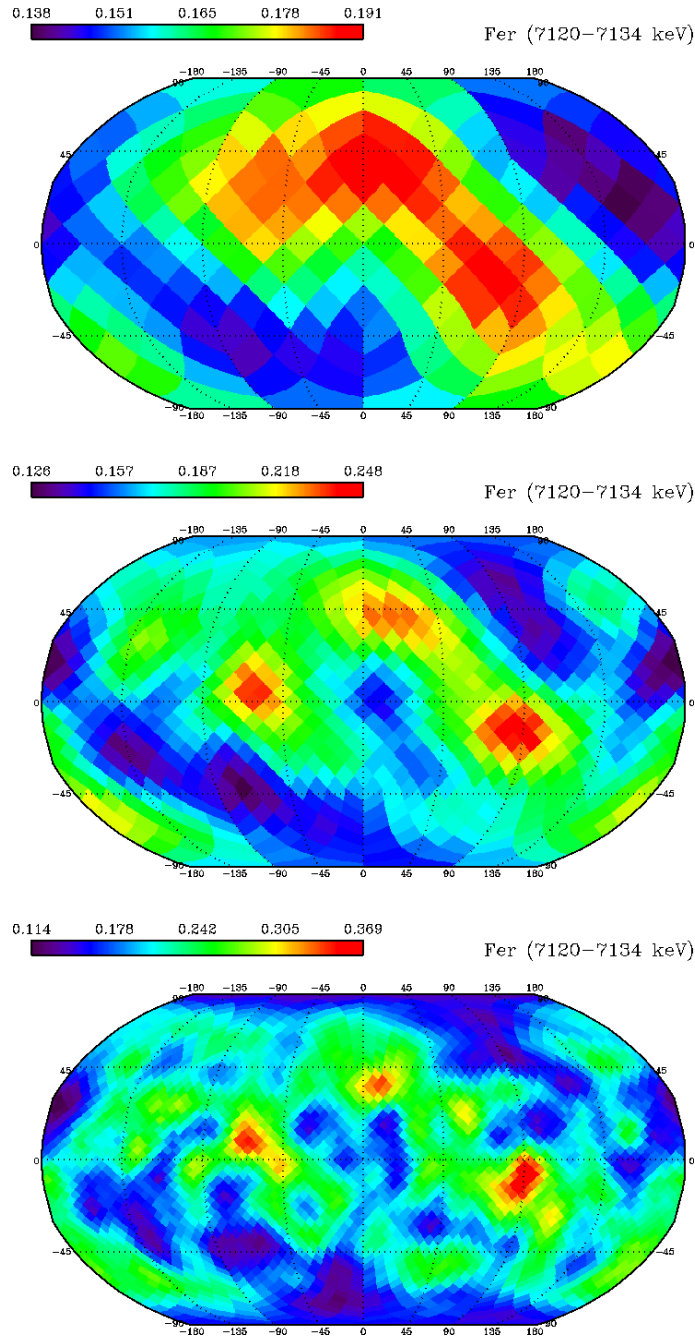
Figure 3.22: Map of Fe counting rates obtained with band passing of the doublets at
7120.1-7134.5 keV at resolutions (a) 14.65°, (b) 7.33° and (c) 3.66°.

Maps obtained with the doublet at 7120.1-7134.5 keV (Figure 3.22) are
reasonably alike maps obtained with the peak fitting method (Figure 3.20), but with an
emphasized second local maximum. An attentive observation of the spectrum shows
that there is a small line centered on 7070 keV that mingles with the doublet. Therefore
the maps realized with this doublet certainly contain a fraction of counts due to gamma
rays produced by nuclei other than Fe. The discrepancy is emphasized by the band
passing method in comparison with the peak fitting method. It could also be due to the
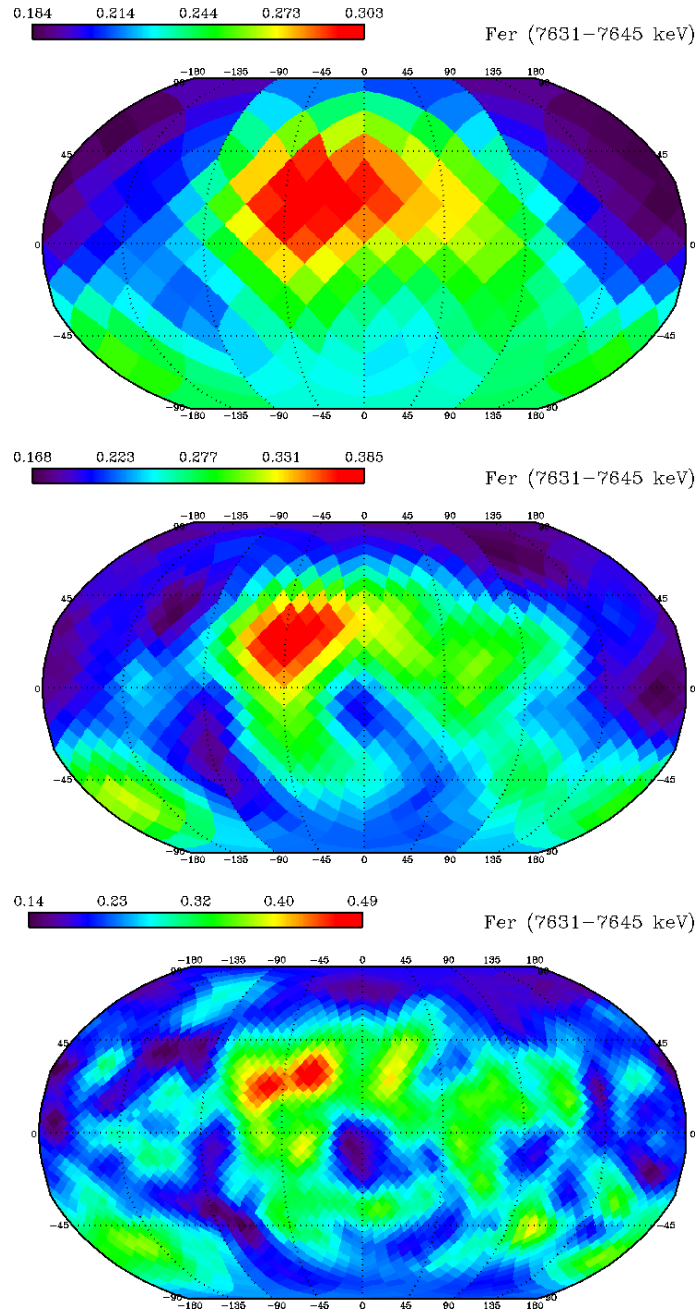fact that the doublet at 7120.1-7134.5 keV sits on an oxygen Doppler broadened line.

145

Figure 3.23: Map of Fe counting rates obtained with band passing of the doublets at 7631.1-7645.5 keV at resolutions (a) 14.65°, (b) 7.33° and (c) 3.66°.

Maps at a resolution of 14.65° do not bring any advantageous information in comparison to that previously obtained with the peak fitting method. Maps obtained with a resolution of 3.66° are very noisy so only maps with a resolution of 7.33° are trustable. Maps obtained with band passing on the basis of the doublet at 7631.1-7645.5 keV (Figure 3.23) are in very good agreement with maps obtained with the peak fitting method. However these maps are not in exact agreement with those obtained with the doublet at 7120.1-7134.5 keV. The parasite line at 7070 keV can also explain the discrepancy between the maps produced by the different doublets. In conclusion the doublet at 7631.1-7645.5 keV is the best energy range to determine the Fe abundance.

146

3.3.3 Statistical uncertainties

As described in part 3.2, the statistical errors associated with the counting rates maps can be estimated on the basis of the Poisson counting statistics. The fractional uncertainty is obtained by inverting the square root of the product of the mean number of counts in a spectrum by the number of spectra measured within a pixel. This uncertainty is calculated for all maps obtained in the present part.
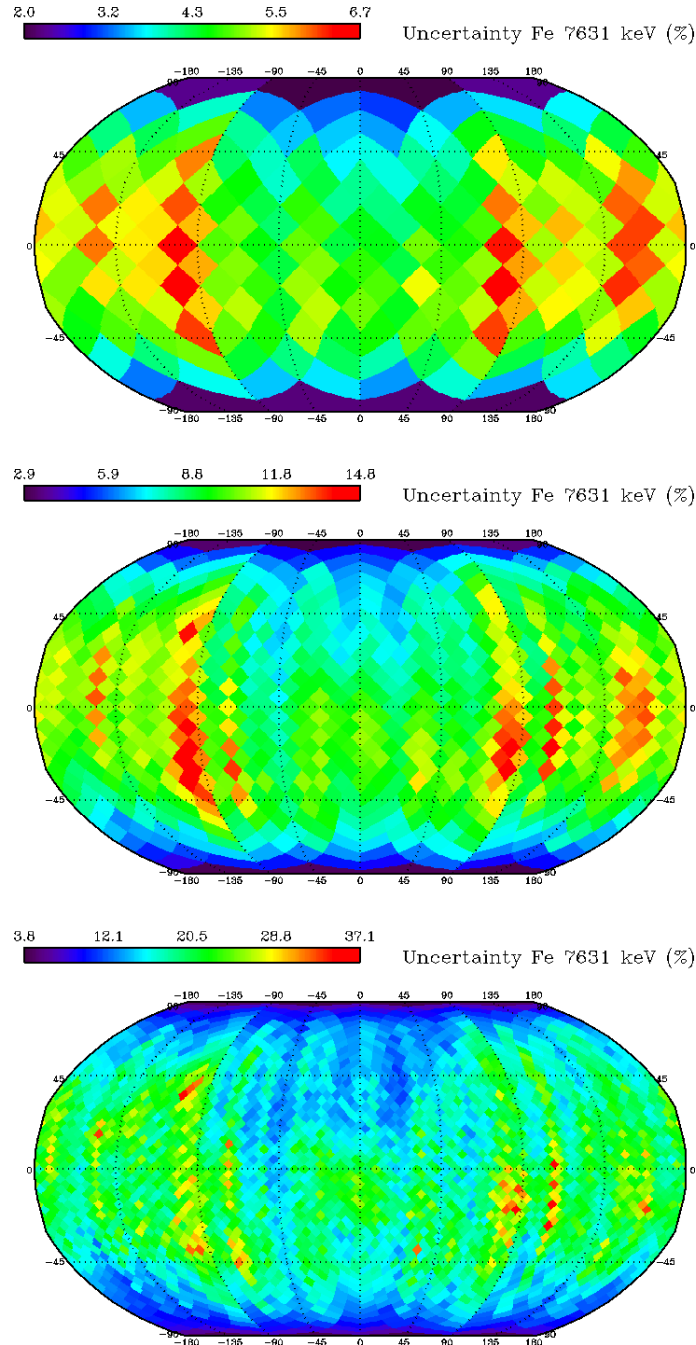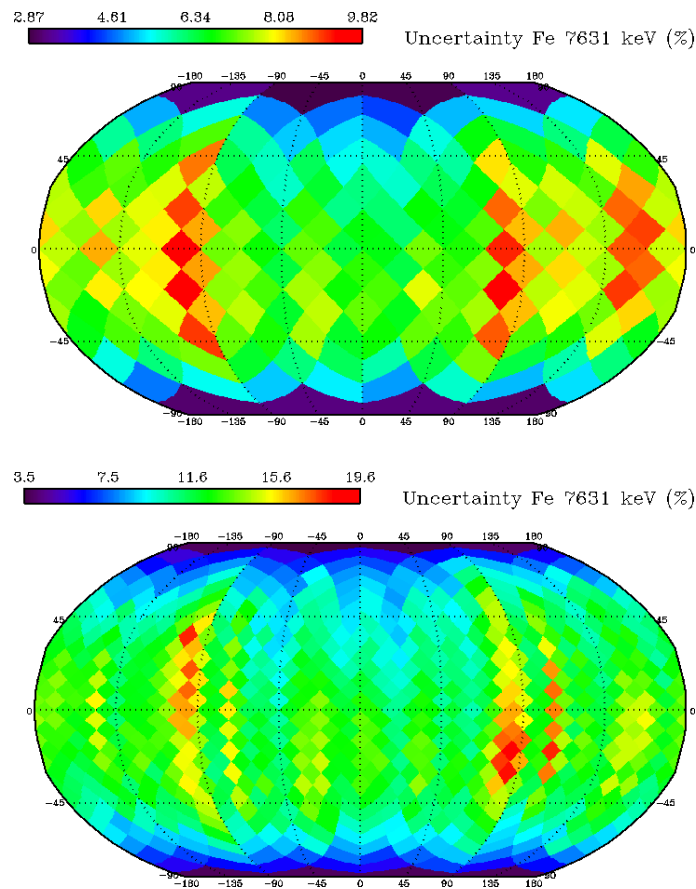

Figure 3.24: Map of statistical uncertainty associated with Fe counting rates obtained with peak fitting at resolutions (a) 14.65°, (b) 7.33° and (c) 3.66°.

The Fe abundance evaluated on the basis of the doublet at 7120.1-7134.5 keV has been ruled out because it contains a contribution from another line. Therefore we only display the uncertainties associated with the Fe abundance determined with the doublet at 7631.1-7645.5 keV. First the uncertainties associated with the peak fitting method are displayed (Figure 3.24).

As expected, uncertainties grow higher as the resolution is increased. At coarser resolution, the uncertainties range between 2 and 6.7 %. At intermediate resolution they range between 2.9 and 14.8 %. And finally at higher resolution they range between 3.8 and 37.1 %. This effect is due to the lower number of acquisitions in pixels of decreasing size. The very high uncertainties at the 3.66° resolution confirms that this dataset is very noisy and not recommended for future use, because further steps in the analysis (from counting rates to weight fractions) will add additional errors (partly statistical through the neutrons and partly systematic).

Because of the use of an equal area projection, the quality of the data at high latitudes is much better due to the larger number of acquisitions in these regions. We notice that there is also a strong longitudinal pattern, which is due to the poor coverage of some longitude bands by the spacecraft. And finally uncertainties are generally higher in highlands because counting rates there are lower.

The same evaluation has been done for counting rates determined with the use of the band passing method (still with the doublet at 7631.1-7645.5 keV). The resulting uncertainties are shown for increasing resolution in Figure 3.25.
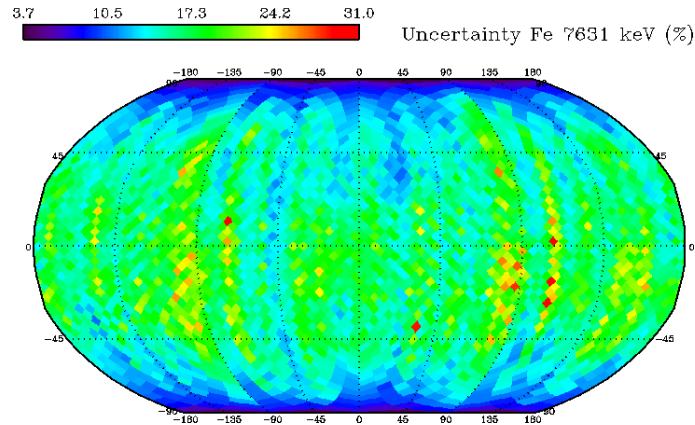
Figure 3.25: Map of statistical uncertainty associated with Fe counting rates obtained with band passing at resolutions (a) 14.65°, (b) 7.33° and (c) 3.66°.

As for peak fitting, uncertainties grow higher as the resolution is increased. At coarser resolution, the uncertainties range between 2.87 and 9.82 %. At intermediate resolution they range between 3.5 and 19.6 %. And finally at higher resolution they range between 3.7 and 31 %. For low and intermediate resolutions, the uncertainty associated with the band passing method is higher than that obtained for peak fitting. The peak fitting method is therefore recommended. For the highest resolution though, uncertainties tend to be lower with band passing.

Following the analysis done in the previous paragraph and the estimation of uncertainties, the determination of the Fe abundance is done with the use of the peak fitting method on the doublet at 7631.1-7645.5 keV. The uncertainties associated with this dataset guarantee good quality results up to a resolution of 7.33°.

3.3.4 Independent Component Analysis

One of the five sources extracted from the ICA in part 3.2 has been found to be meaningful for iron mapping. The second source is mostly correlated with Fe, but also contains contributions from K, Si, Mg and Al. The detailed analysis of these sources provides very interesting information concerning the Fe lines. For instance we can observe the presence of a line around 1238 keV in both first and second sources. We previously observed that this line provided a map partially correlated to uranium and partially correlated to iron. This conclusion is confirmed by discovering this line in a source correlated to radioactive elements and in a source correlated to Fe. The ICA seems able to separate the contribution due to Fe and that due to U.

The absence of the line at 1613 keV in the second source provides an extra argument to not consider this line as produced by Fe. The Selene spectrum shows a line around this energy that could be interpreted as Fe (1612.8 keV). The line is quite faint and therefore hard to observe in tiled data. However when tiled on a very coarse resolution, the area of the line shows a variation very distinct from the maps realized with other Fe lines. The line was therefore attributed to an alternate source: Mg (1611.7

149

keV). A brief observation of the synthesis spectrum of source 2 shows that this line should indeed not be considered as produced by Fe.

The map of source 2 (Figure 3.26a) has been obtained by calculating the correlation coefficient between the spectrum accumulated in each pixel and the source. Because of its features, the second source map contains a mix of Fe and other elements to a smaller extent. Although it does not allow deriving straightforwardly Fe counting rates, the second source map is highly correlated to Fe as determined by previous missions. Therefore it provides a very good indication of the variations of Fe. In conclusion, the ICA is a powerful tool for analyzing the spectrum and constraining the variations of the Fe abundance at very high resolution.

3.3.5 Construction of Fe maps by multi-resolution analysis

Each method that we have used to extract the geochemical information from the data has different advantages and drawbacks. The peak fitting and band passing methods provide an unquestionable counting rate of an element, but cannot be performed at a very high resolution because of the lack of statistics. On the contrary, the ICA allows an analysis at high resolution, while it does not give straightforwardly an elemental abundance, only a vector very well correlated to Fe. To benefit from the advantages of each method, it was decided to merge the results obtained at different scales into one map. Multi-resolution fusion of images is originally used in space imagery to combine high-resolution panchromatic images and low-resolution multispectral images [Nunez et al., 1999]. Peak fitting is considered as the most trustable method to make a map at intermediate resolution. The result of the ICA is used as an a priori information on the variations of Fe at high resolution to deconvolve a map produced by peak fitting.

The pyramidal wavelet transform allows decomposing a signal into different scales. Contrary to the classic wavelet transform, the scales have a progressively lower number of pixels than the initial image. An isotropic pyramidal wavelet transform algorithm can be found in the MRS (Multi Resolution on the Sphere) package.

A pyramidal wavelet transform is applied to the second source of the ICA. The map is decomposed in two scales (Figure 3.26b and Figure 3.26c). According to the definition of the pyramidal transform, the first scale has the same resolution than the initial image (3.6°), while the second scale has a coarser resolution (7.33°), which is the double of the initial resolution.

The doublet at 7631.1-7645.5 keV was identified as the most efficient region of the spectrum to map Fe. Peak fitting and band passing analysis have both produced maps at a resolution of 7.33°, so data obtained with peak fitting will be used preferentially. The coarser scale issued from the decomposition of the ICA map is replaced by the map obtained with peak fitting at 7.33° (Figure 3.21b). The homogeneity of the images that are exchanged is guaranteed by a normalization of their histogram prior to this exchange. After this switch, a final map is reconstructed with an inverse pyramidal transform (Figure 3.26). Thanks to this operation, the final image

maximizes the use of the information contained in the different tiled dataset: each scale has been calculated with the dataset that provides the higher signal to noise ratio.
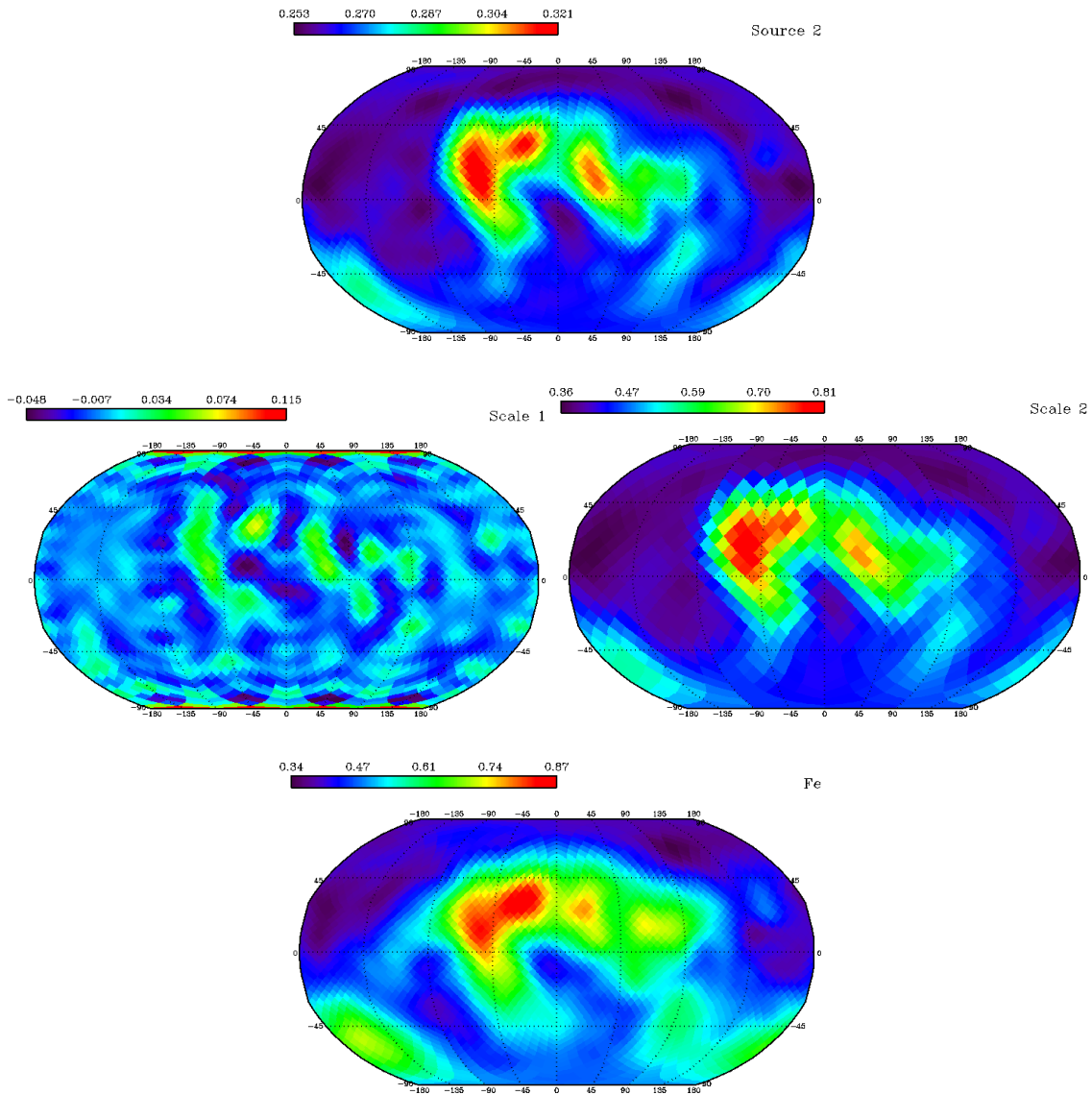

Figure 3.26: (a) Source 2 obtained with ICA at the resolution 3.66°. (b) Scale 1 and (c) scale 2 issued from the pyramidal wavelet of source 2. (d) Fe map reconstructed with an inverse pyramidal transform.

3.3.6 Comparison with Lunar Prospector results

The gamma ray data acquired by Lunar Prospector were used to determine global maps of the elemental composition of the lunar surface. Maps of the abundance of major oxides, MgO, Al_2O_3, SiO_2, CaO, TiO_2, and FeO, and trace incompatible elements K and Th have thus been determined and are presented in Prettyman et al. [2006]. Maps of the FeO abundance determined with Lunar Prospector are available in rectangular grids of 2° equal area pixels, 5° equal area pixels, and 20° equal area pixels. The Fe abundance has been retiled with the Healpix pixelisation to be comparable to that

obtained with Selene (Figure 3.27). The resolution was set at 7.33°. Once this operation has been performed, the Fe abundances determined with the GRS onboard Lunar Prospector have the appropriate format for comparison with Selene.
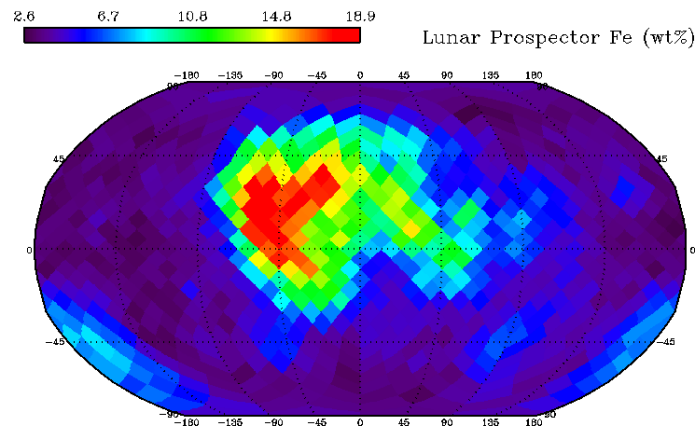

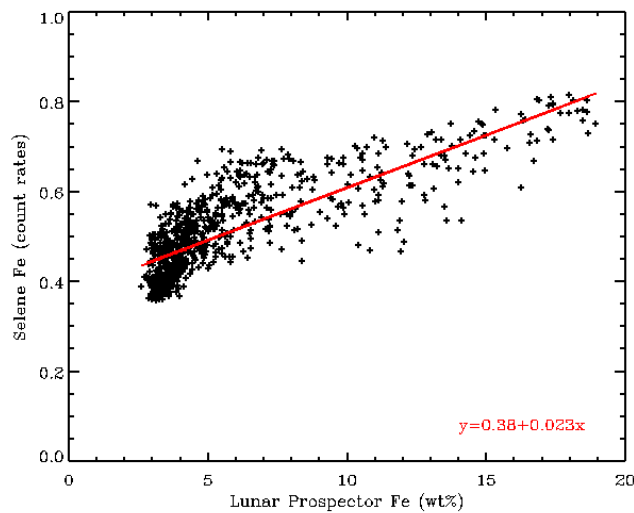Figure 3.27: Map of FeO abundance (wt%) tiled with Healpix on a 7.33° resolution.

Figure 3.28: Comparison of the Fe obtained with Selene with Lunar Prospector. Superposed in red is the linear regression function that fits the data.

Figure 3.28 shows the counting rates determined with Selene as a function of the abundances determined with Lunar Prospector. There is a generally good linear tendency. A linear regression was performed in between the two datasets. This regression yields a reasonably good correlation coefficient: 0.81. The resulting function is the following:

$[Fe]_{Selene} = 0.38 + 2.34 \, [Fe]_{LunarProspector}$

In spite of the generally good agreement, there seems to be a branching for lower values of counting rates: Selene Fe counting rates are higher than Lunar Prospector abundances. The explanation for this difference is not clear yet. It might be due to the fact that Selene gamma ray spectra have not been corrected for neutron abundances yet.

152

3.3.7 Conclusion

This initial processing has provided the identification of many Fe lines in the global spectrum. All lines have been studied in detail to determine the regions of the spectrum most appropriate for mapping. Traditional methods of spectrum analysis such as peak fitting and band passing have been applied to the gamma ray spectra measured by the Selene GRS instrument. It was subsequently concluded that the best spot to map Fe was the doublet at 7631.1-7645.5 keV.

The statistical uncertainties associated with the maps obtained with the different lines, different methods and different resolutions have been calculated. These uncertainties have validated the quality of the results obtained with the doublet at 7631.1-7645.5 keV up to a resolution of 7.33°. Finally the peak fitting method has been assessed as providing better results than the band passing method.

Because of the low accumulation time so far obtained, innovative methods of spectrum analysis have been tested. The Independent Component Analysis has proved very successful in increasing the resolution of the results in spite of the low-statistics. A multi resolution analysis has also been performed. This method proved successful in providing a map of counting rates with higher resolution. However further investigation and testing need to be done.

Finally the results were compared with the Fe abundances determined with Lunar Prospector. The map obtained with peak fitting of the doublet at 7631.1-7645.5 keV compares quite well with the Fe abundances calculated by Prettyman. However some discrepancies at low counting rates remain unexplained.

3.4 Determination of the concentration in radioactive elements

3.4.1 Th, U and K lines in the global lunar spectrum

As in part 3.3, the global spectrum accumulated during the period extending from December 21, 2007 to February 17, 2008 is used for identifying lines produced by radioactive elements. We report here (Table 3.4) the lines that have been identified as produced by isotopes of Th, U and K. We fit these lines with the use of Aquarius as in part 3.3. For each line, a region of interest has been defined to restrict the analysis to a smaller portion of spectrum. Each portion is fitted by summing a continuum with a given number of lines. The continuum is modeled with a linear function. Lines are modeled with a standard Gaussian shape modified with an exponential tail. The parameters describing this model (A_0, E_0, σ and ρ) are saved and the area of the lines. All these parameters are shown in Table 3.4.

Most of the lines are narrow peaks well fitted by the model line defined earlier. The width of the lines is generally increasing with increasing energies like formerly noticed for the Fe lines. However some of the lines, such as the lines at 609.3 keV and 1729.6 keV, appear to be enlarged or slightly deformed. Many lines have very high values of ρ (which means they can be modeled mainly as Gaussian functions). However the lines with high ρ often correspond to lines with little areas. Therefore their modeling is rendered harder by the low statistics. The parameters ρ and σ resulting from the fit of these lines have been found to be variable. The general area though, which is the important parameter, is quite stable.

Source	Eref (keV)	A_0 (cpm)	E_0 (keV)	σ (keV)	ρ (keV)	Area (cpm)
U-^{235}U	185.7	14.604	179.0	1.49	1.84	56.715
Th-^{212}Pb	238.6	37.073	225.2	1.16	0.84	128.401
U-^{214}Pb	295.2	0.577	284.5	1.12	1.86	1.644
Th-^{212}Pb	300.1	0.486	292.0	1.12	1.86	1.385
Th-^{228}Ac	583.2	1.166	583.2	1.59	1.20	5.439
U-^{214}Bi	609.3	1.296	606.9	3.30	8.91	10.720
U-^{214}Bi	768.4	0.120	766.2	2.46	3.00	0.776
Th-^{228}Ac	794.9	0.068	792.8	1.20	0.72	0.261
Th-^{228}Ac	911.2	0.399	908.8	1.75	1.34	2.036
Th-^{228}Ac	969.0	0.203	966.0	3.14	1.66	2.171
U-^{214}Bi	1377.7	0.100	1380.5	2.19	0.97	0.813
U-^{214}Bi	1408.0	0.078	1409.0	3.17	1.26	0.977
^{40}K	1460.8	0.607	1462.0	2.10	0.84	5.042
Th-^{212}Bi	1620.5	0.067	1623.8	4.09	21.47	0.692
U-^{214}Bi	1729.6	0.073	1722.1	6.80	15.37	1.246
U-^{214}Bi	1764.5	0.208	1766.9	2.92	1.16	2.408
Th-^{208}Tl ^{208}Pb*	2614.5	0.160	2616.2	3.47	0.68	3.575

Table 3.5: Fitting parameters of the gamma ray lines identified as produced by Th, U and K in the global lunar spectrum measured by the Selene GRS.

Lines with very small area are not suitable for mapping because the signal within tiled spectra is likely to be too faint. The lines at 768.4, 794.9, 1377.7, 1408.0 and 1620.5 keV have therefore not been kept on the list of lines suitable for mapping purpose. Lines in the lower energy ranges of the spectrum are traditionally not used for elemental mapping because the continuum is very high. The underlying continuum is subjected to many sources of variations. Among the lines produced by Th at energies greater than 700 keV, the line with the larger area is that at 2614.5 keV. And for U, the line with the larger area is that at 1764.5 keV.

3.4.2 K counting rates mapping

The spectra have been tiled according to the Healpix pixelisation with the following resolutions 14.65° (192 pixels), 7.33° (768 pixels) and 3.66° (3072 pixels). All channels of the datasets have been filtered with the wavelet transform described in part 3.2, thus augmenting the signal to noise ratio in spectra. Only one line is produced by K. Fortunately this line has a very good signal to noise ratio and is therefore adapted for mapping purpose.

The analysis of the 1460.8 kev line is performed on the following region of interest: [1420 keV, 1480 keV] (Figure 3.29). This energy range possesses another line with significant counts at 1434.1 keV interpreted as produced by ^{52}Mn. The peak fitting method is therefore recommended (however band summing could be alternatively used by excluding the left part of the K line if the resolution obtained with peak fitting is not sufficient). The spectrum is modeled by summing two lines with a continuum. Lines are assumed to have the same shape but different energy centers and amplitudes.

The parameters obtained when fitting the global spectrum are used to fit individual spectra of the tiled data. Only the continuum parameters and the amplitudes of the peaks are allowed to vary across the planet. Fits are performed on datasets of increasing resolution. The resulting maps are presented in Figure 3.30.
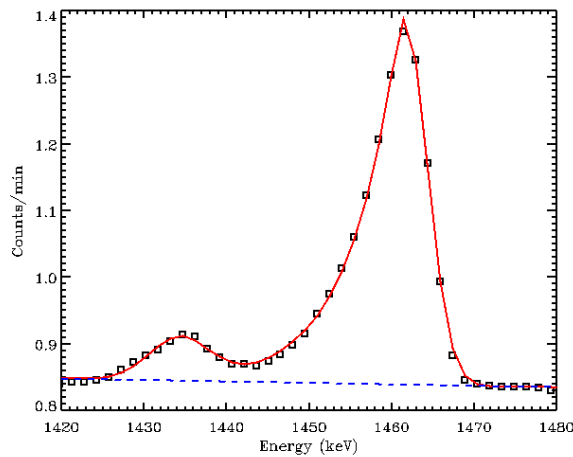

Figure 3.29: Analysis of the line at 1460.8 keV. Superposition of data (black squares) with modeled linear continuum (blue dashed line) and fitting function (red line).
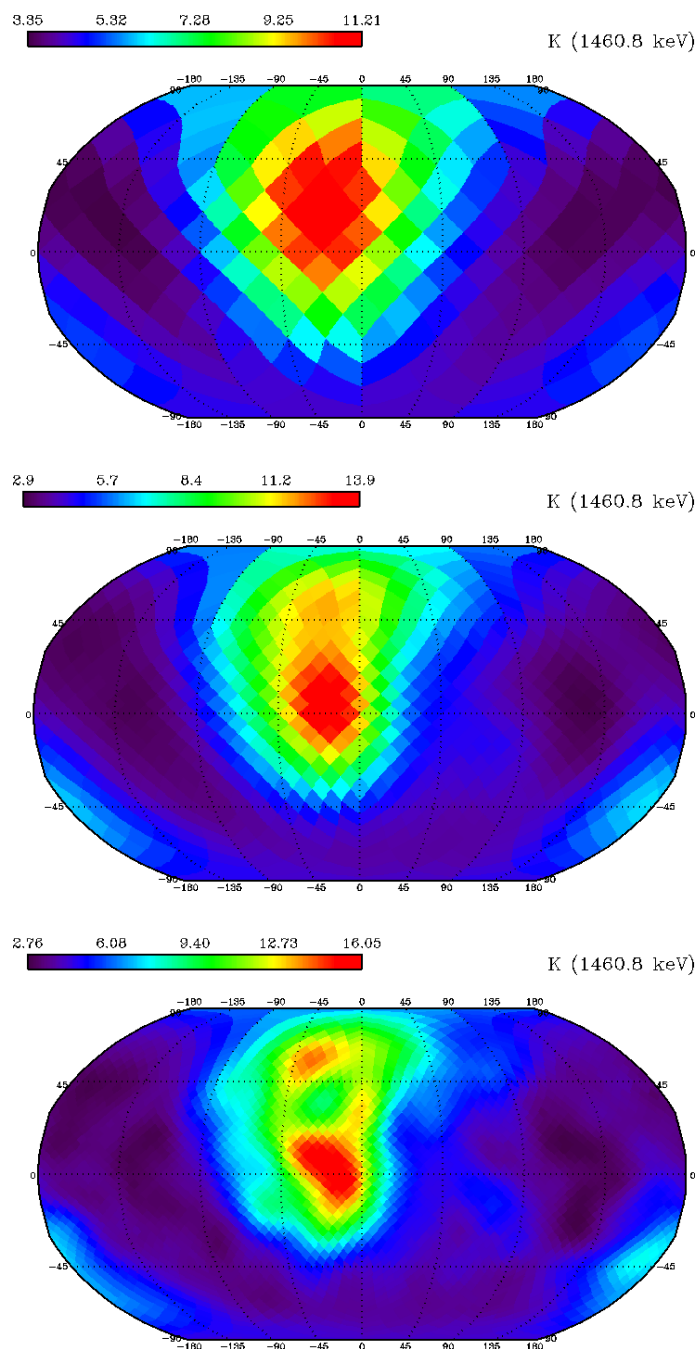
Figure 3.30: Map of K counting rates obtained with peak fitting of the line at 1460.8 keV at resolution (a) 14.65°, (b) 7.33° and (c) 3.66°.

3.4.3   Th counting rates mapping

The 2615.5 keV line has been identified as the most appropriate for mapping purpose. The analysis of this line is performed on the following region of interest: [2540 keV, 2650 keV]. This portion of the spectrum only possesses the Th line (Figure 3.31) so that peak fitting or band summing can be alternatively used. We preferentially use peak fitting. The spectrum is modeled by summing one line with a continuum.

Therefore all parameters are allowed to vary across the planet. Only areas are saved to be used for future mapping. The parameters obtained when fitting the global spectrum are used to fit individual spectra of the tiled data. Fits are performed on datasets of increasing resolution. The resulting maps are presented in Figure 3.32.
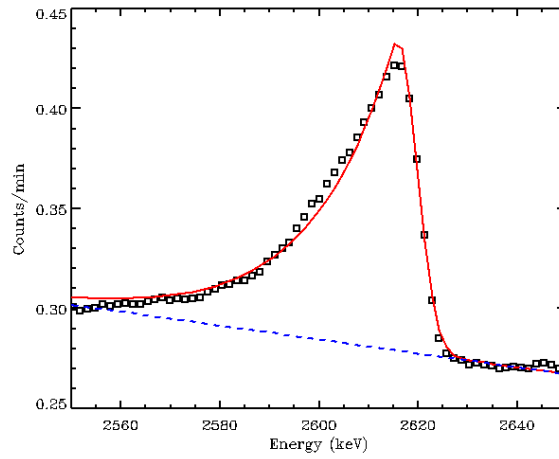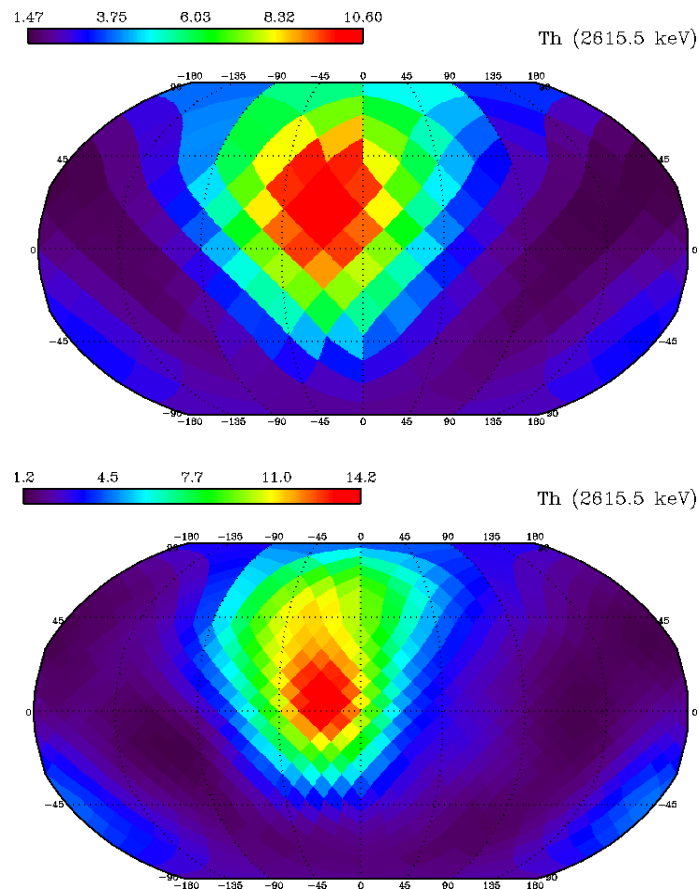

Figure 3.31: Analysis of the line at 2615.5 keV. Superposition of data (black squares) with modeled linear continuum (blue dashed line) and fitting function (red line).
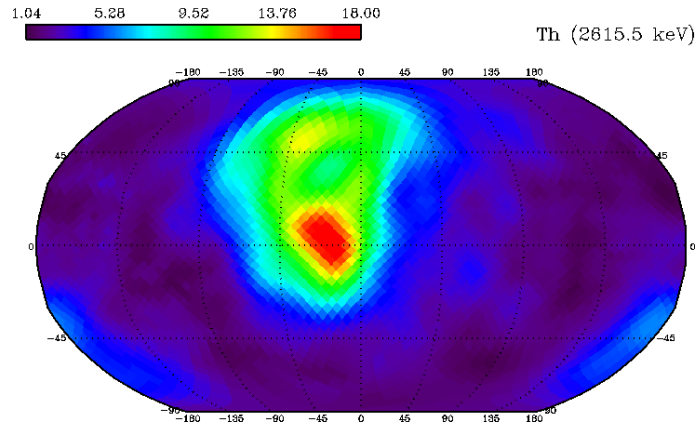
Figure 3.32: Map of Th counting rates obtained with peak fitting of the line at 2615.5 keV at resolution (a) 14.65°, (b) 7.33° and (c) 3.66°.

3.4.4 U counting rates mapping

The 1764.5 keV line has been identified as the most appropriate for mapping U. The analysis of this line is performed on the following region of interest: [1735 keV, 1790 keV]. This portion of the spectrum possesses another line with significant counts at 1779 keV interpreted as produced by ^{28}Si (Figure 3.33). The peak fitting method is preferentially used because the two lines are closely mingled. The spectrum is modeled by summing two lines with a continuum.

None of these lines are Doppler broadened so they have been assumed to have the same shape. The parameters obtained when fitting the global spectrum are used to fit individual spectra of the tiled data. Only the continuum parameters and the amplitudes of the peaks are allowed to vary across the planet. The calculated areas are saved for future mapping. Fits are performed on datasets of increasing resolution. The resulting maps are presented in Figure 3.34.
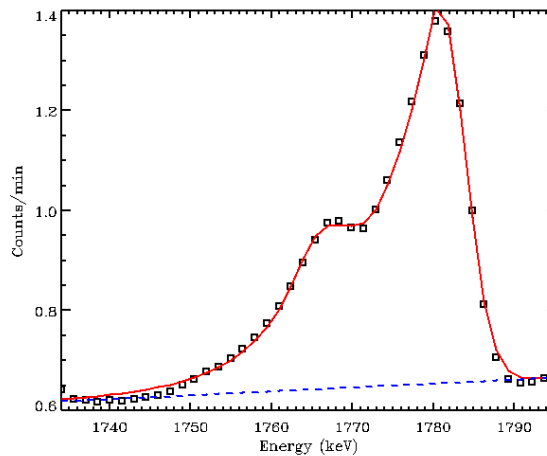

Figure 3.33: Analysis of the line at 1764.5 keV. Superposition of data (black squares) with modeled linear continuum (blue dashed line) and fitting function (red line).
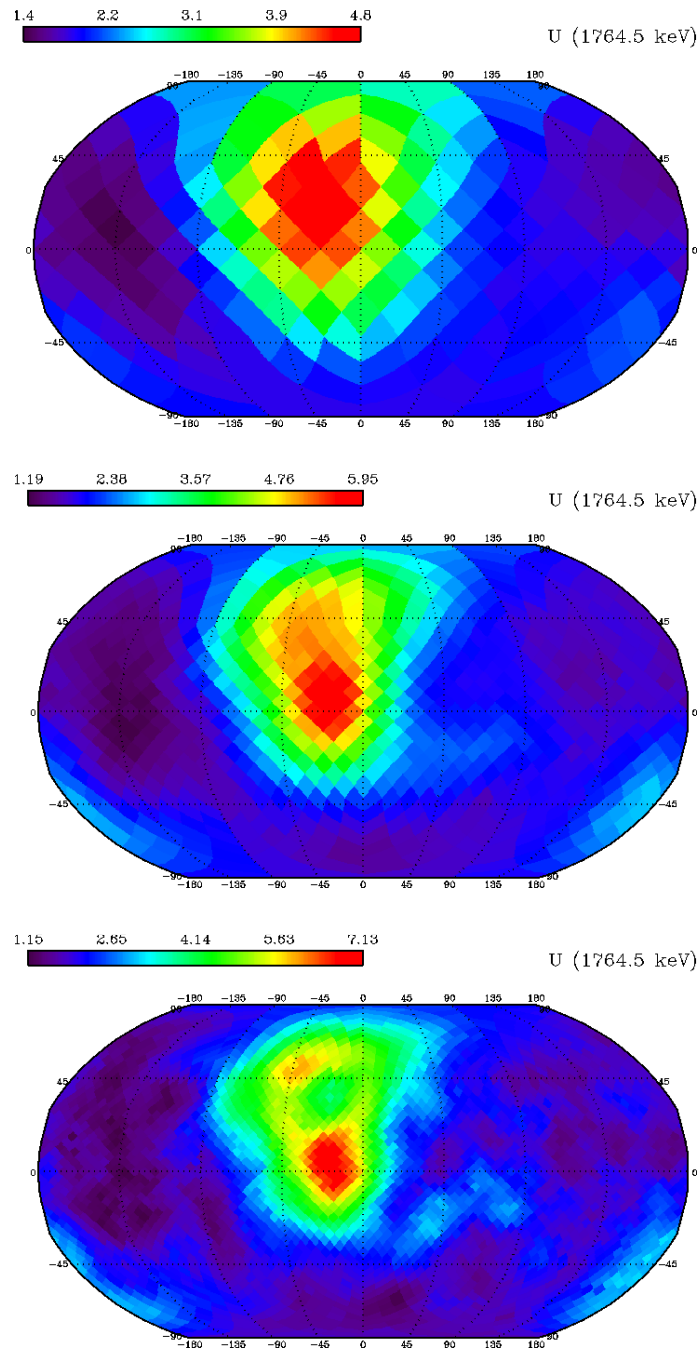
158

Figure 3.34: Map of U counting rates obtained with peak fitting of the line at 1764.5 keV at resolution (a) 14.65°, (b) 7.33° and (c) 3.66°.

3.4.5 Statistical uncertainties

As described in part 3.2, the statistical errors associated with the counting rates maps can be estimated on the basis of the Poisson counting statistics. The fractional uncertainty is obtained by inverting the square root of the product of the mean number of counts in a spectrum by the number of spectra measured within a pixel. This uncertainty is calculated for all maps obtained in the present part. We only display the

uncertainties associated with the highest resolution: 3.66°. They constitute an upper limit, because uncertainties associated with coarser resolution are expected to be lower.

The uncertainties associated with K counting rates obtained by peak fitting of the line at 1460.8 keV are shown in Figure 3.35. They range between 0.95 and 14.11 %. These uncertainties are significantly smaller than those calculated for Fe. A quick comparison reveals that the uncertainties on K counting rates at high resolution have a magnitude comparable to the uncertainties on Fe counting rates at intermediate resolution.
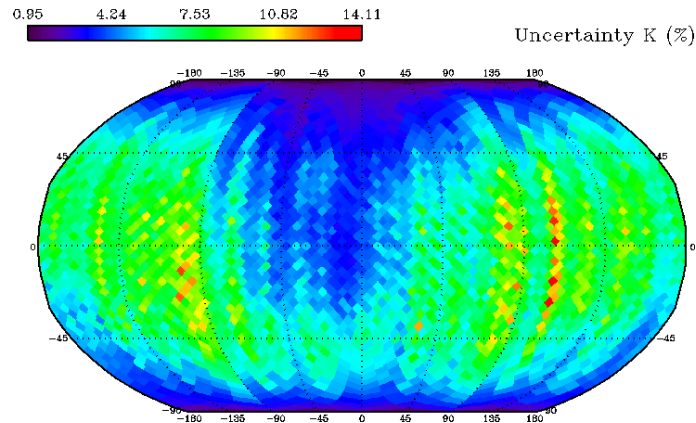

Figure 3.35: Map of statistical uncertainty associated with K counting rates obtained with peak fitting at resolution 3.66°.

The same features as in Fe uncertainty maps are found in the K uncertainties: lower uncertainties at high latitudes, longitudinal pattern and higher uncertainties in highlands. The uncertainties associated with Th counting rates obtained by peak fitting of the line at 2615.5 keV are shown in Figure 3.36. They range between 1.28 and 20.54 %. These uncertainties are slightly higher than those on K abundances, but are still quite reasonable. This map also shows the same features as for Fe uncertainties.
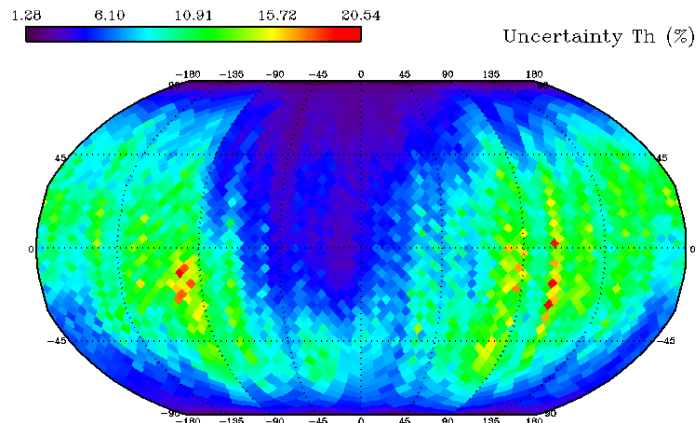

Figure 3.36: Map of statistical uncertainty associated with Th counting rates obtained with peak fitting at resolution 3.66°.

The uncertainties associated with U counting rates obtained by peak fitting of the line at 1764.5 keV are shown in Figure 3.37. They range between 1.6 and 20 %. They are therefore of the same order of magnitude as those on Th. In conclusion, the maps of counting rates of K, Th and U can be trusted up to a resolution of 3.66°.
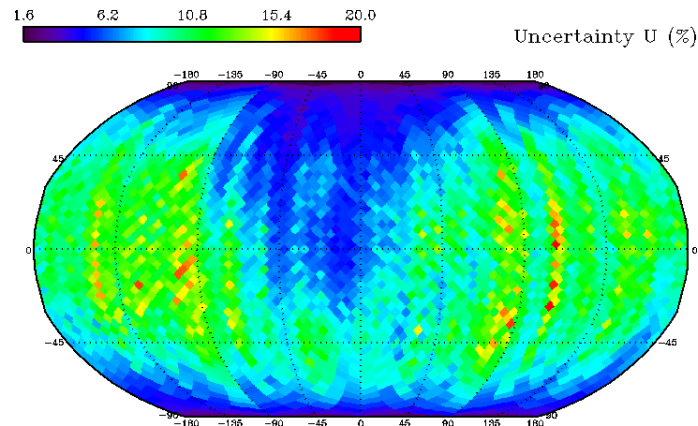

Figure 3.37: Map of statistical uncertainty associated with U counting rates obtained with peak fitting at resolution 3.66°.

3.4.6 Independent Component Analysis

One of the five sources extracted from the ICA in part 3.2, one has been found to be meaningful for mapping of radioactive elements. The first source is correlated with to the radioactive elements: Th, U and K and contains a small contribution of Al and Si. Contributions from the following lines have been detected in the spectrum of the first source: 911.2 (Th), 969 (Th), 1238.1 (U), 1460.8 (K), 1588.2 (Th), 1764.5 (U), 2614.5 (Th). Some of these lines were not clearly identified with a simple analysis of the global spectrum. The ICA is therefore a powerful tool to analyze the spectrum. Although it cannot discriminate between the different elements, it provides a useful tool to map the general behaviour of radioactive elements at a very high resolution.

3.4.7 Comparison with Lunar Prospector results

Maps of the abundance of trace incompatible elements K and Th have been determined with the Lunar Prospector gamma ray data and are presented in Prettyman et al. [2006]. Maps of K and Th abundances are available in rectangular grids of 2° equal area pixels, 5° equal area pixels, and 20° equal area pixels. These abundances have been retiled with the Healpix pixelisation to be comparable to our maps (Figure 3.38). The resolution was set at 7.33°. Once this operation has been performed, the K and Th abundances determined with the GRS onboard Lunar Prospector have the appropriate format for comparison with Selene.
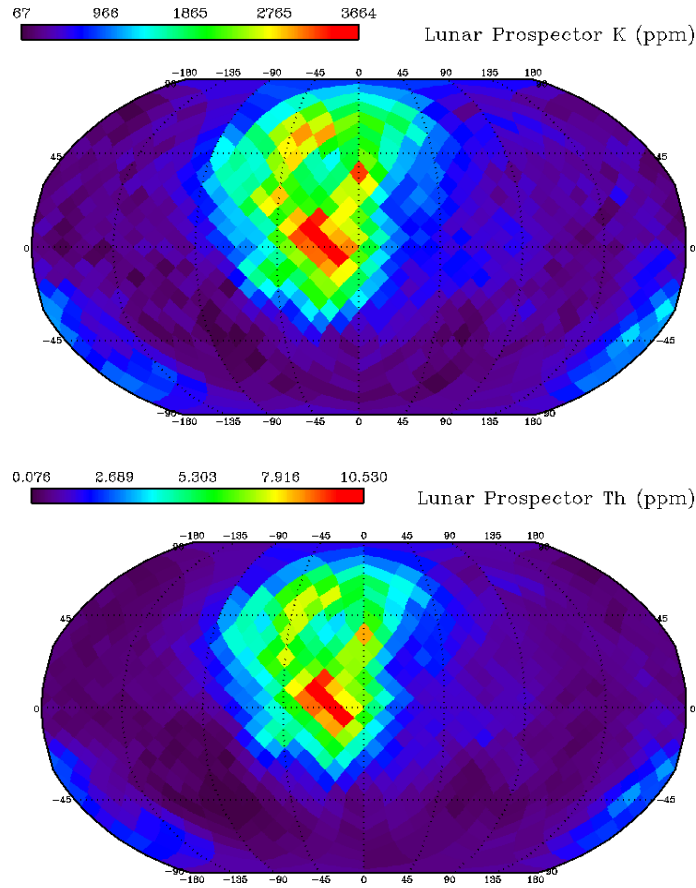
Figure 3.38: Map of (a) K and (b) Th abundances (ppm) tiled with Healpix on a 7.33°
resolution.

Figure 3.39a shows the K counting rates determined with Selene as a function of
the abundances determined with Lunar Prospector. There is a very nice agreement
between the two datasets. A linear regression was performed between the two datasets.
This regression yields a very good correlation coefficient: 0.95. The resulting function
is the following:

$$[K]_{Selene} = 2.85 + 0.0035 \, [K]_{LunarProspector}$$

Figure 3.39b shows the Th counting rates determined with Selene as a function
of the abundances determined with Lunar Prospector. Again the agreement between the
two datasets is very good. A linear regression was performed between the two datasets.
This regression yields a very good correlation coefficient: 0.96. The resulting function
is the following:

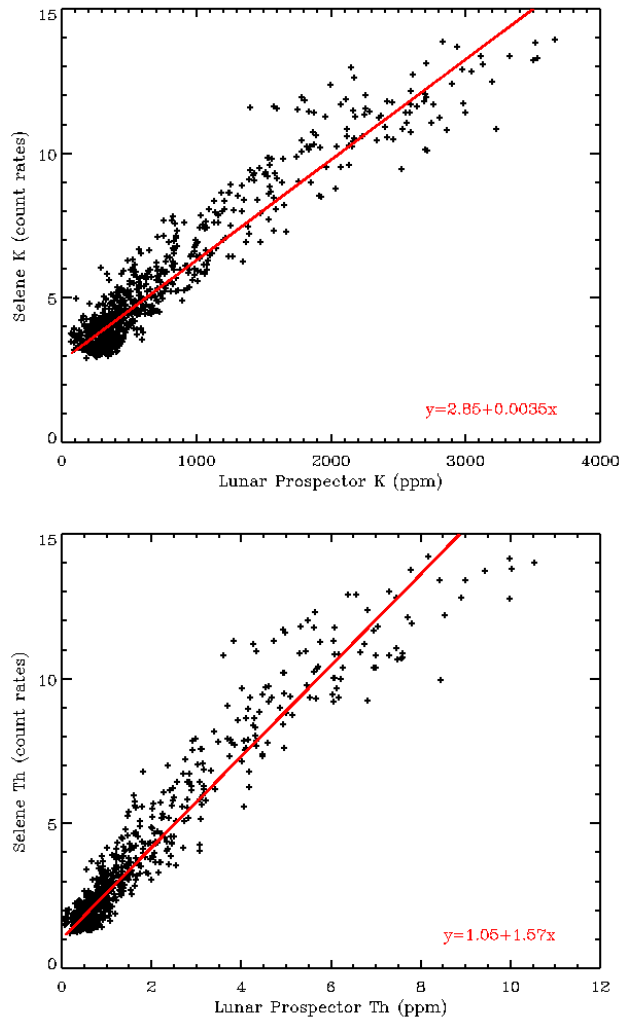$$[Th]_{Selene} = 1.05 + 1.57 \, [Th]_{LunarProspector}$$

Figure 3.39: Comparison of (a) K and (b) Th obtained with Selene with Lunar Prospector. Superposed in red are the linear regression functions that fit the data.

3.4.8 Conclusion

This initial processing has provided the identification of many lines produced by radioactive elements in the global spectrum. All lines have been studied in detail to determine the regions of the spectrum most appropriate for mapping. It was concluded that the best regions of the spectrum to map K, Th and U were respectively the lines at 1460.8 keV, 2615.5 keV and 1764.5 keV. These lines have been analyzed with traditional methods of spectrum analysis such as peak fitting and band passing to map the concentration of K, Th and U at variable resolution (from 14.65° to 3.66°).

The statistical uncertainties associated with the maps at different resolutions have been calculated. These uncertainties have validated the quality the K, Th and U abundances up to a resolution of 3.66°. The Independent Component Analysis proved successful in confirming our results, but did not bring any increase of the resolution because the resolution reached with peak fitting is already maximum. Finally the results were compared with the K and Th abundances determined with Lunar Prospector. They compare very well, as demonstrated by a correlation coefficient around 0.95.

163

3.5 Determination of the Ca, Si, Mg and Ti concentrations

The spectra have been tiled according to the Healpix pixelisation with the following resolutions 14.65° (192 pixels), 7.33° (768 pixels) and 3.66° (3072 pixels). All channels of the datasets have been filtered with the wavelet transform described in part 3.2, to have a better signal to noise ratio.

As in part 3.3, we proceed with line fitting using Aquarius. For each line, a region of interest has been defined to restrict the analysis to a smaller portion of spectrum. Each portion is fitted by summing a continuum with a given number of lines. The continuum is modeled with a linear function. Lines are modeled with a standard Gaussian shape modified with an exponential tail. The parameters describing this model (A_0, E_0, σ and ρ) are saved and an area is calculated for these ideal lines.

3.5.1 Ca counting rates mapping

Two lines have been identified as produced by calcium in the global spectrum accumulated during the period extending from December 21, 2007 to February 17, 2008. The parameters and areas obtained when fitting those lines are reported in Table 3.4. The line at 1942.7 keV is a narrow peak whereas that at 3736.5 keV is enlarged and not so well modeled by the Gaussian function modified with an exponential tail. The reason for this low quality fit is very likely the low statistics associated with this line: the line has a very small area, though it is large. The line at 1942.7 keV possesses higher counting rates. The calcium concentration is therefore preferentially determined with the analysis of the line at 1942.7 keV.

Source	Eref (keV)	A_0 (cpm)	E_0 (keV)	σ (keV)	ρ (keV)	Area (cpm)
^{40}Ca (nγ)	1942.7	0.058	1944.9	2.49	0.80	0.654
^{40}Ca (n,nγ)	3736.5	0.016	3730.3	7.42	19.77	0.299

Table 3.6: Fitting parameters of the gamma ray lines identified as produced by Ca in the global lunar spectrum measured by the Selene GRS.

The analysis is performed on the following region of interest: [1850 keV; 2050 keV]. This interval contains lines produced by elements other than Ca. Because of the complexity of the region, Aquarius fails to fit it with regular lines. Therefore it was decided to use the band passing method for mapping purpose. The band passing is performed on datasets of increasing resolution.

The resulting maps are presented in Figure 3.41. Only maps obtained at resolutions 14.65° (192 pixels) and 7.33° (768 pixels) are displayed here. The band passing method failed to provide a map at higher resolution because the signal to noise ratio is too low to extract the information properly (the resulting map appears to be very noisy).
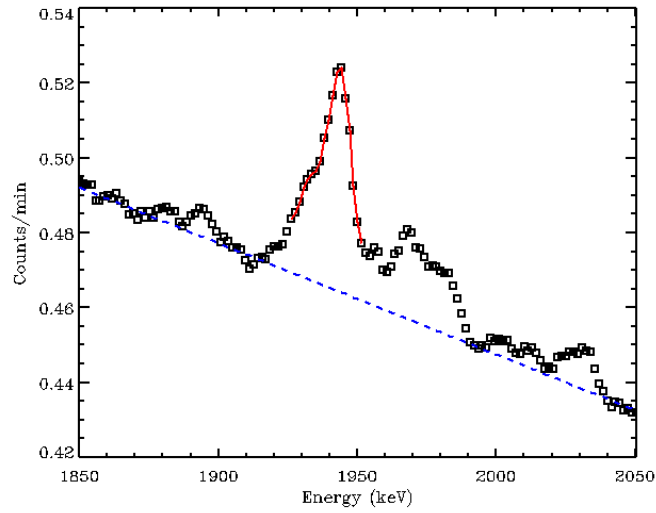
Figure 3.40: Analysis of the line at 1942.7 keV. Superposition of data (black squares) with modeled linear continuum (blue dashed line) and band passing region (red line).
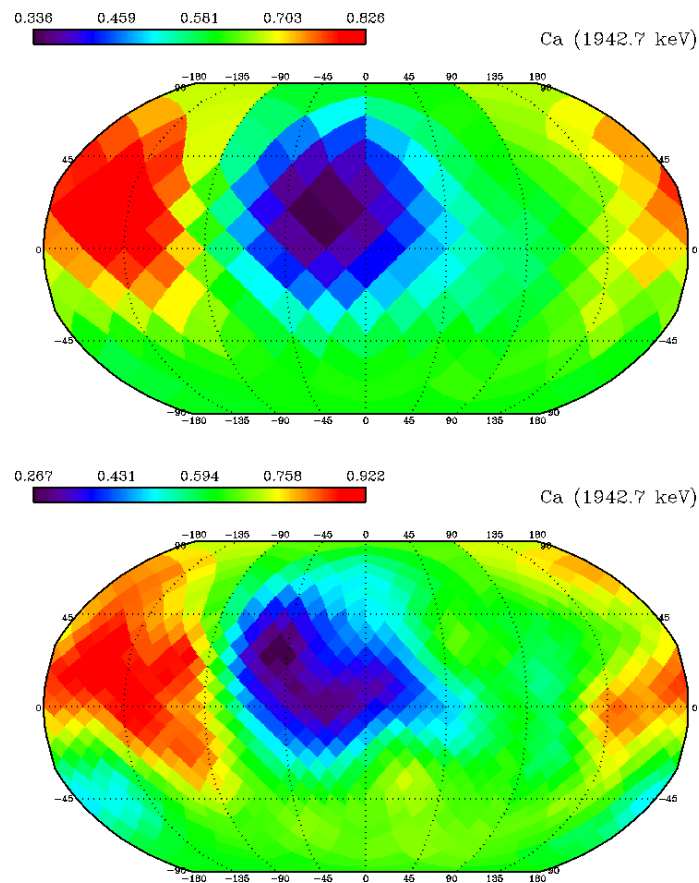

Figure 3.41: Map of Ca counting rates obtained with band passing of the line at 1942.7 keV at resolution (a) 14.65° and (b) 7.33°.

3.5.2 Si counting rates mapping

Nine lines have been identified as produced by silicium in the global spectrum. The parameters and areas obtained when fitting those lines are reported in Table 3.7. The lines at 2838.7 keV and 3200.7 keV are Doppler broadened, which causes their shape to be not very well fitted by a model line. Besides, these lines have very low counting rates. Consequently they are not recommended for mapping.

The lines at 3539.0 keV, 4422.9 keV and 4933.9 keV have reasonably high statistics but are unfortunately sitting next to Doppler broadened lines or more generally in very complex regions of the spectrum. They have therefore been qualified as inappropriate for mapping. The lines at 4588.3 keV, 6379.8 keV and 6877.9 keV have too low counting rates for mapping. So finally, the most appropriate line for mapping purpose is the line at 1779.0 keV. This line has high statistics, is not Doppler broadened or sitting next to Doppler broadened lines. Being a nice narrow peak, it will be among the easiest lines to fit.

Source	Eref (keV)	A_0 (cpm)	E_0 (keV)	σ (keV)	ρ (keV)	Area (cpm)
^{28}Si*	1779.0	0.797	1781.2	2.52	0.76	9.462
^{28}Si (n,nγ) dop	2838.7	0.013	2837.7	8.14	10.06	0.277
^{28}Si (n,nγ) dop	3200.7	0.008	3197.9	8.48	4.27	0.232
^{28}Si (nγ)	3539.0	0.023	3536.9	5.01	1.71	0.493
^{28}Si (nγ) SE	4422.9	0.012	4417.3	9.28	2.68	0.524
^{28}Si* SE	4588.3	0.003	4588.4	8.48	8.27	0.079
^{28}Si (nγ)	4933.9	0.017	4932.0	7.47	1.88	0.671
^{28}Si (nγ)	6379.8	0.006	6377.7	14.05	5.42	0.348
^{28}Si (n,nγ)	6877.9	0.003	6880.7	8.96	4.53	0.100

Table 3.7: Fitting parameters of the gamma ray lines identified as produced by Si in the global lunar spectrum measured by the Selene GRS.

The silicium concentration is therefore determined with the analysis of the line at 1779.9 keV. The analysis is performed on the following region of interest: [1735 keV; 1795 keV] (Figure 3.42). This interval contains another important line produced by U at 1764.5 keV. The two lines are largely overlapping. Therefore the use of band passing is not recommended because some photons produced by uranium are likely to be counted when summing around the silicium peak.

Therefore, the peak fitting method is used for mapping the counting rates of Si. As for calcium, only maps obtained at resolutions 14.65° (192 pixels) and 7.33° (768 pixels) are displayed here (Figure 3.43). The noise is too important at higher resolutions.
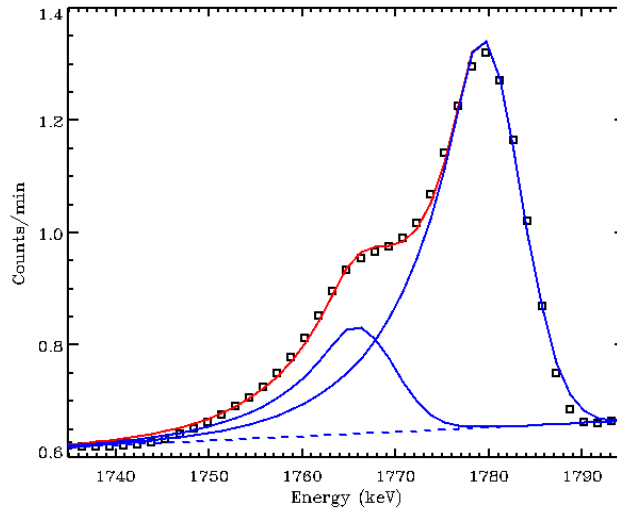
Figure 3.42: Analysis of the line at 1779.9 keV. Superposition of data (black squares) with modeled linear continuum (blue dashed line) and band passing region (red line).
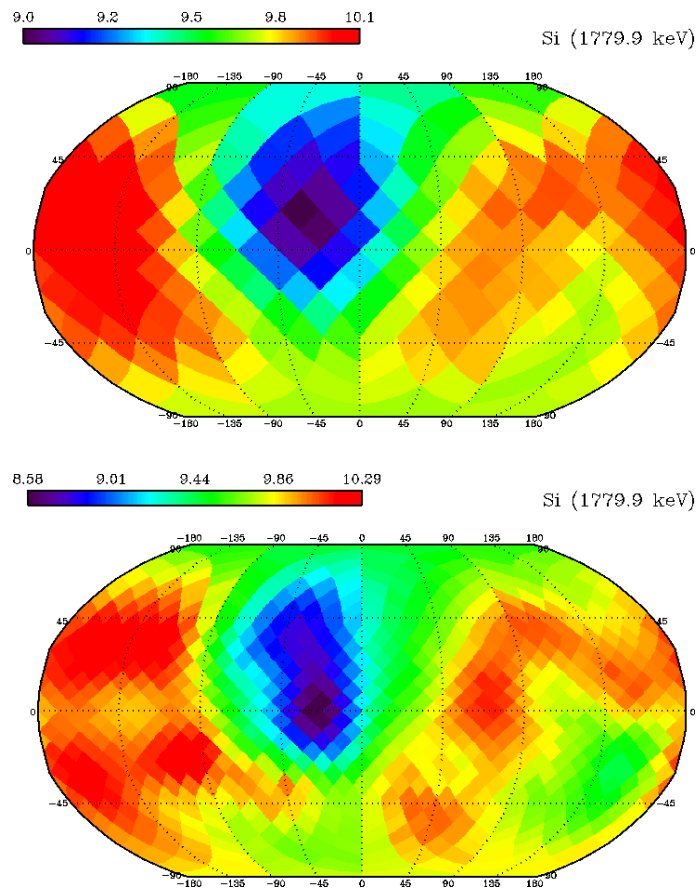

Figure 3.43: Map of Si counting rates obtained with peak fitting of the line at 1779.9 keV at resolution (a) 14.65° and (b) 7.33°.

3.5.3 Mg counting rates mapping

Nine lines have been identified as produced by magnesium in the global spectrum. The parameters and areas obtained when fitting those lines are reported in Table 3.8. The lines at 974.7 keV, 984.6 keV and 989.9 keV are very complex to fit because they are largely overlapping. The window of interest around these lines indeed contains at least 4 lines (there is an additional line produced by Th at 969 keV) which makes it too complex to be used for mapping. The line at 1002.4 keV is overlapping with the line produced by aluminium at 1014.4 keV. This line has therefore also been eliminated. Among the remaining lines, only the line at 1368.6 keV has sufficient statistics to allow mapping.

Source	Eref (keV)	A_0 (cpm)	E_0 (keV)	σ (keV)	ρ (keV)	Area (cpm)
^{25}Mg*	974.7	0.103	968.4	3.08	1.61	1.079
^{27}Mg*	984.6	0.088	981.6	3.08	1.61	0.923
^{25}Mg*	989.9	0.101	986.0	3.08	1.61	1.062
^{26}Mg*	1002.4	0.139	1003.8	3.35	8.37	1.165
^{26}Mg*	1129.6	0.025	1131.5	4.06	2.20	0.337
^{24}Mg*	1368.6	0.527	1367.7	5.12	4.25	7.689
^{25}Mg*	1611.7	0.075	1610.7	4.57	17.86	0.854
^{27}Mg*	1697.9	0.025	1700.4	5.61	14.02	0.357
^{26}Mg*	1808.7	0.019	1699.6	4.98	15.62	0.232

Table 3.8: Fitting parameters of the gamma ray lines identified as produced by Mg in the global lunar spectrum measured by the Selene GRS.
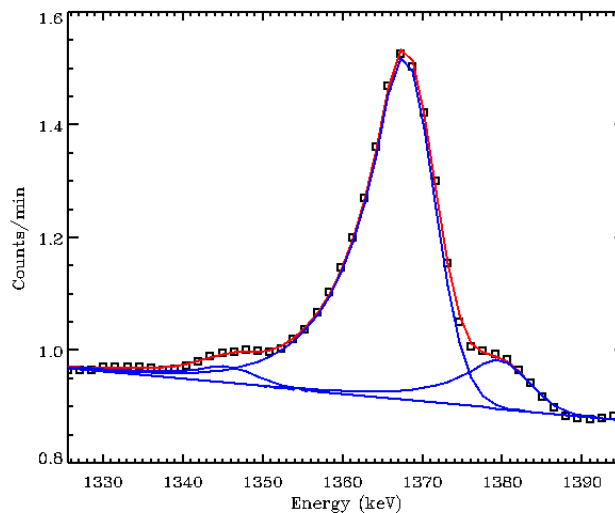

Figure 3.44: Analysis of the line at 1368.6 keV. Superposition of data (black squares) with modeled linear continuum (blue dashed line) and band passing region (red line).

The magnesium concentration is therefore determined with the analysis of the line at 1368.6 keV. The analysis is performed on the following region of interest: [1325 keV; 1395 keV] (Figure 3.44). This interval contains two other lines: a line produced by Ge at 1347 keV and a line produced by Ti at 1381.7 keV. These two lines are overlapping the Mg line, so that the use of band passing is not recommended. The peak fitting method is therefore used for mapping the counting rates of Mg. Again, only maps obtained at resolutions 14.65° (192 pixels) and 7.33° (768 pixels) are displayed here (Figure 3.45).

Figure 3.45: Map of Mg counting rates obtained with peak fitting of the line at 1368.6 keV at resolution (a) 14.65° and (b) 7.33°.

3.5.4 Ti counting rates mapping

Five lines have been identified as produced by titanium in the global spectrum. The parameters and areas obtained when fitting those lines are reported in Table 3.9. Almost all these lines have very low statistics and are therefore not appropriate for mapping. Only the line at 1381.7 keV has sufficient statistics to be used for mapping. The titanium concentration is therefore determined with the analysis of the line at 1381.7 keV.

Source	Eref (keV)	A₀(cpm)	E₀(keV)	σ (keV)	ρ (keV)	Area (cpm)
^{48}Ti*	1312.1	0.014	1313.1	3.27	10.23	0.112
^{48}Ti (nγ)	1381.7	0.049	1380.6	5.13	4.38	0.710
^{48}Ti (nγ)	6249.1	0.005	6256.4	4.97	12.97	0.065
^{48}Ti (nγ)	6418.4	0.011	6425.4	5.72	3.74	0.188
^{48}Ti (nγ)	6760.1	0.006	6765.6	8.71	4.88	0.178

Table 3.9: Fitting parameters of the gamma ray lines identified as produced by Ti in the global lunar spectrum measured by the Selene GRS.

The analysis is performed on the following region of interest: [1325 keV; 1395 keV]. This interval contains two other lines: a line produced by Ge at 1347 keV and a line produced by Mg at 1368.6 keV. It was used previously for determining the concentration in Mg (Figure 3.44). The same peak fitting treatment that was used for Mg is used for mapping the counting rates of Ti. Again, only maps obtained at resolutions 14.65° (192 pixels) and 7.33° (768 pixels) are displayed here (Figure 3.46).
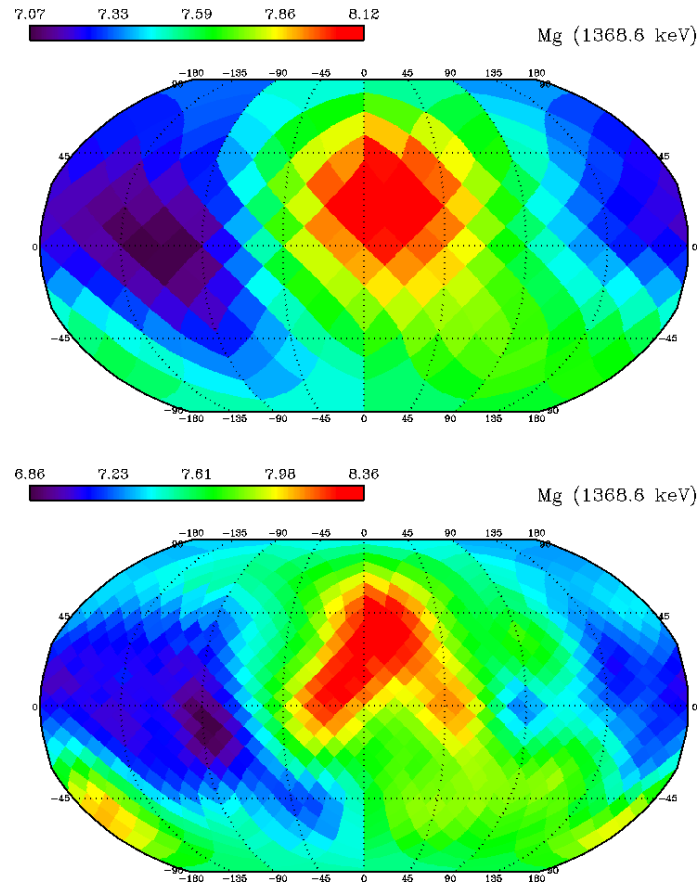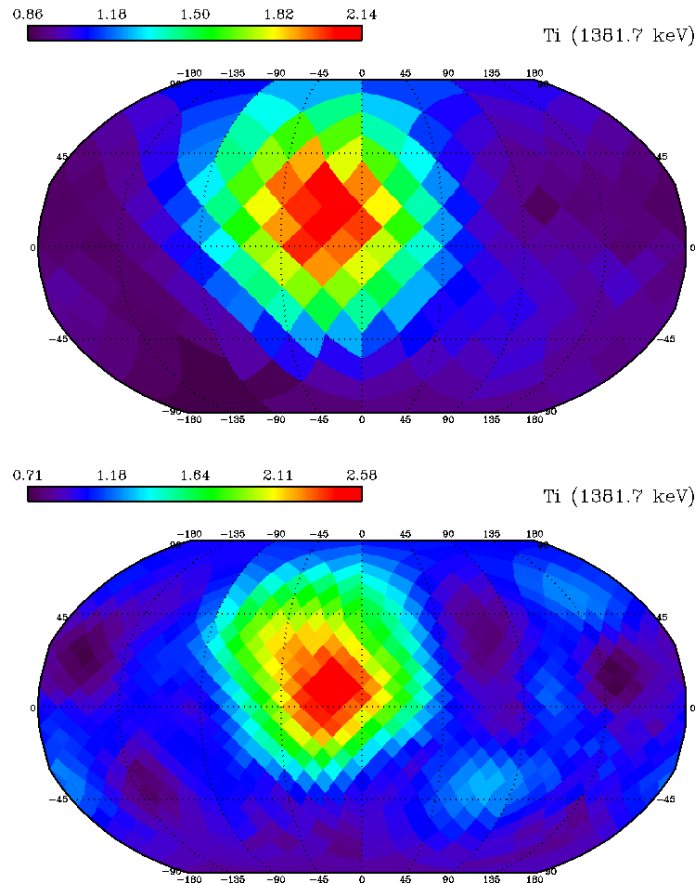

Figure 3.46: Map of Ti counting rates obtained with peak fitting of the line at 1381.7 keV at resolution (a) 14.65° and (b) 7.33°.

170

3.5.5 Statistical uncertainties

As described in precedent parts, the statistical errors associated with the counting rates maps can be estimated on the basis of the Poisson counting statistics. This uncertainty has been calculated for all maps obtained in the present part. We only display here the uncertainties associated with the highest resolution. They constitute an upper limit, because uncertainties associated with coarser resolution are expected to be lower. Statistical uncertainties associated with Ca counting rates are displayed first (Figure 3.47).

Figure 3.47: Map of statistical uncertainty associated with Ca counting rates obtained with peak fitting at resolution 7.33°.

The uncertainties associated with Ca counting rates range between 2.25 and 14.87 %. These uncertainties are significantly above that calculated for radioactive elements at comparable resolution but are similar to that calculated for Fe counting rates. The latitudinal and longitudinal patterns are found again. However contrary to iron and radioactive elements, the highest uncertainties are obtained for mare because they have lower counting rates.

Figure 3.48: Map of statistical uncertainty associated with Si counting rates obtained with peak fitting at resolution 7.33°.

Statistical uncertainties associated with Si counting rates are displayed in Figure 3.48. The uncertainties associated with Si counting rates range between 0.61 and 3.49 %. These uncertainties are slightly lower than that calculated for radioactive elements at comparable resolution. The latitudinal and longitudinal patterns and higher values in mare are found again.
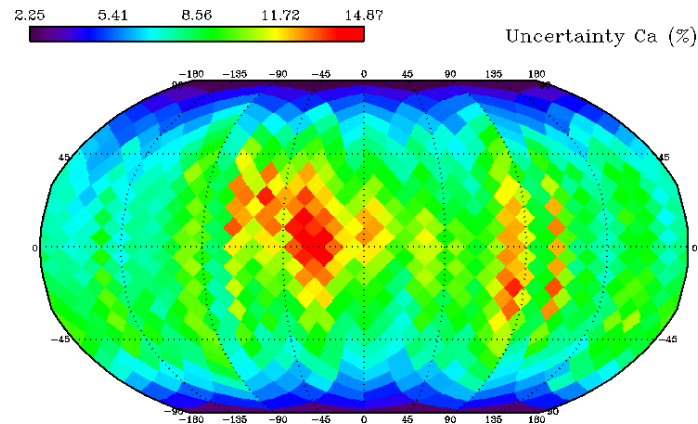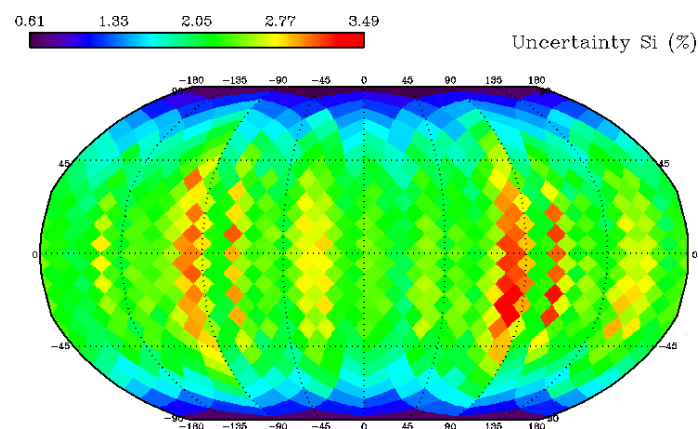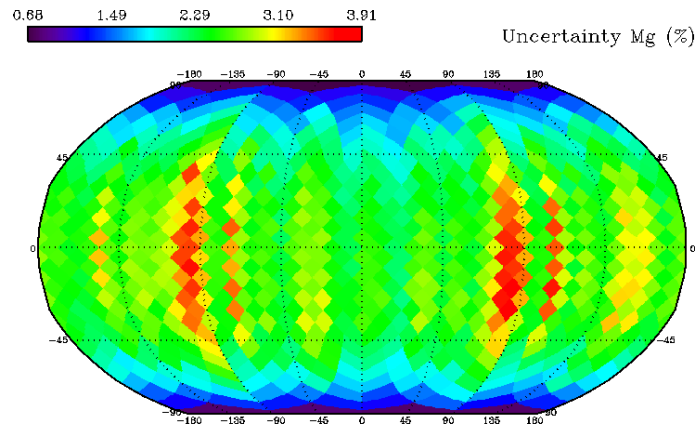

Figure 3.49: Map of statistical uncertainty associated with Mg counting rates obtained with peak fitting at resolution 7.33°.

Statistical uncertainties associated with Mg counting rates are displayed in Figure 3.49. They range between 0.68 and 3.91 %. These uncertainties are of the same magnitude as that calculated for Si counting rates. As for iron and radioactive elements, the highest uncertainties are obtained for highlands.
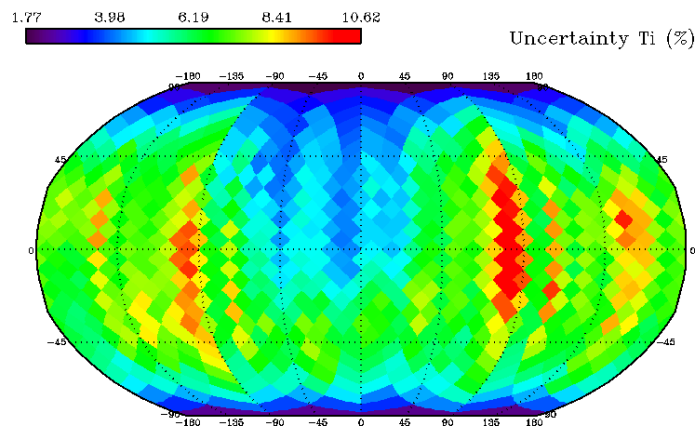
Figure 3.50: Map of statistical uncertainty associated with Ti counting rates obtained with peak fitting at resolution 7.33°.

Statistical uncertainties associated with Ti counting rates are displayed in Figure 3.50. They range between 1.77 and 10.62 %. These uncertainties are larger than that calculated for Si counting rates but lower than that calculated for Ca counting rates. As for iron and radioactive elements, the highest uncertainties are obtained for the highlands.

172

3.5.6 Comparison with Lunar Prospector results

Maps of the abundance of Mg, Ti, Si and Ca have been determined with the Lunar Prospector gamma ray data and are presented in Prettyman et al. [2006]. Maps of the Ti abundance are available in rectangular grids of 2° equal area pixels, 5° equal area pixels, and 20° equal area pixels. Maps of the Mg abundance are available in rectangular grids of 5° equal area pixels and 20° equal area pixels. Maps of the Si and Ca abundances are available in rectangular grids of 20° equal area pixels. These abundances have been retiled with the Healpix pixelisation to be comparable to that obtained previously. The resolution of the Ti and Mg maps has been set to 7.33°. The resolution of the Si and Ca maps has been set to 14.65°.

Figure 3.51: Map of Ca abundance (wt%) tiled with Healpix on a 14.65° resolution.
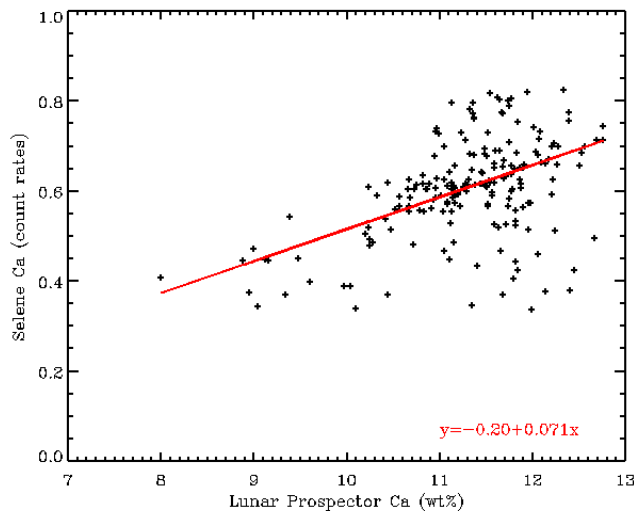
Figure 3.52: Comparison of Ca from Selene with Ca from Lunar Prospector. Superposed in red is the linear regression function that fits the data.

Once this operation has been performed, the abundances determined with the GRS onboard Lunar Prospector have the appropriate format for comparison with Selene. The map of Ca abundances determined with Lunar Prospector is shown in Figure 3.51. It appears very noisy. Figure 3.52 shows the Ca counting rates determined

with Selene as a function of the abundances determined with Lunar Prospector. There is a large dispersion of the data, and the agreement between the datasets appears to be not so good. Because of the noisy aspect of the Ca map determined by Lunar Prospector, it is not surprising to find such dispersion in the results. A linear regression was performed between them. This regression yields a poor correlation coefficient: 0.47. The resulting function is the following:

$$[Ca]_{Selene} = -0.20 + 0.071 \ [Ca]_{LunarProspector}$$
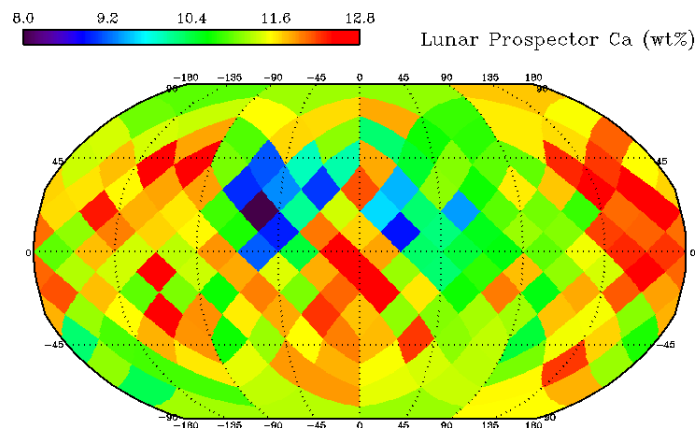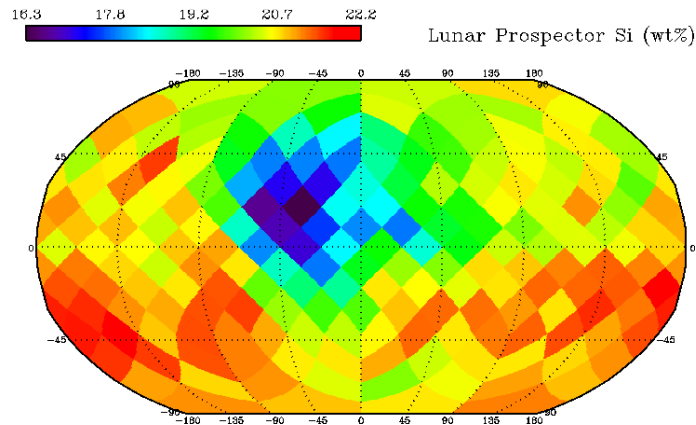

Figure 3.53: Map of Si abundance (wt%) tiled with Healpix on a 14.65° resolution.

Figure 3.54: Comparison of Si from Selene with Si from Lunar Prospector. Superposed in red is the linear regression function that fits the data.

The map of Si abundances determined with Lunar Prospector is shown in Figure 3.53. Figure 3.54 shows the Si counting rates determined with Selene as a function of the abundances determined with Lunar Prospector. There is a very nice agreement between the two datasets. A linear regression was performed between them. This regression yields a reasonably good coefficient: 0.83. The resulting function is the following:

$$[Si]_{Selene} = 5.32 + 0.20 \ [Si]_{LunarProspector}$$

Figure 3.55: Map of Mg abundance (wt%) tiled with Healpix on a 7.33° resolution.

Figure 3.56: Comparison of Mg from Selene with Mg from Lunar Prospector.
Superposed in red is the linear regression function that fits the data.

The map of Mg abundances determined with Lunar Prospector is shown in Figure 3.55. Figure 3.56 shows the Mg counting rates determined with Selene as a function of the abundances determined with Lunar Prospector. There is a reasonable agreement between the two datasets. A linear regression was performed between them. This regression yields a quite weak coefficient: 0.72. The resulting function is the following:

$$[Mg]_{Selene} = 6.70 + 0.19\ [Mg]_{LunarProspector}$$

The map of Ti abundances determined with Lunar Prospector is shown in Figure 3.57. Figure 3.58 shows the Ti counting rates determined with Selene as a function of the abundances determined with Lunar Prospector. There is a nice agreement between the two datasets. A linear regression was performed between the two datasets. This regression yields a quite good coefficient: 0.82. The resulting function is the following:

$$[Ti]_{Selene} = 0.90 + 0.47\ [Ti]_{LunarProspector}$$

175
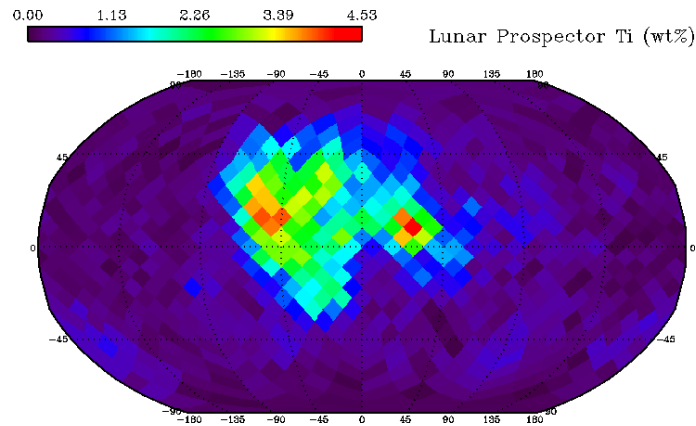
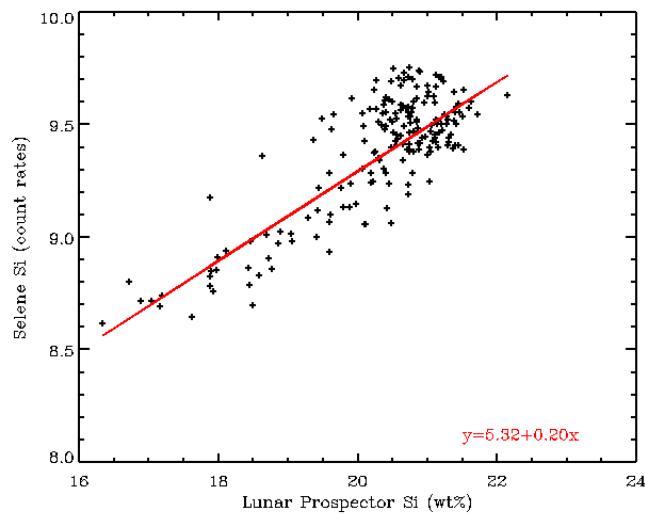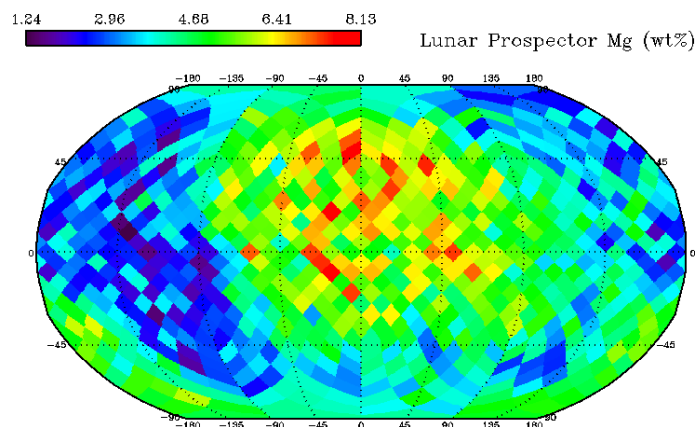Figure 3.57: Map of Ti abundance (wt%) tiled with Healpix on a 7.33° resolution.
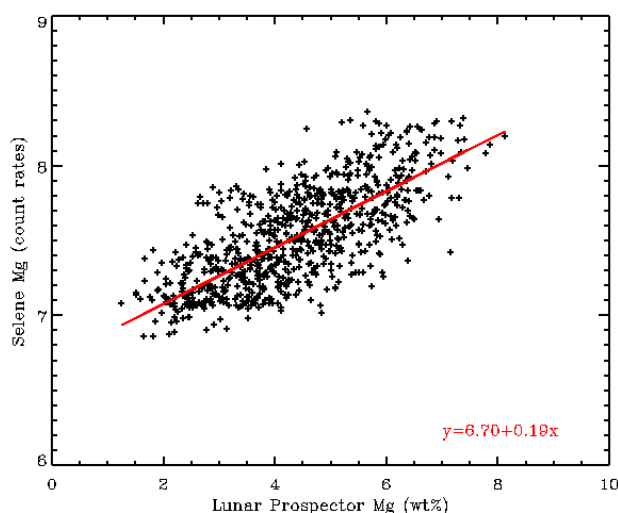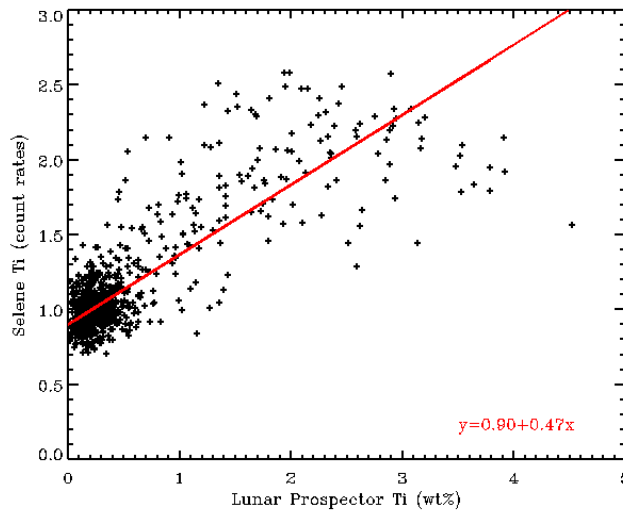

Figure 3.58: Comparison of Ti from Selene with Ti from Lunar Prospector. Superposed in red is the linear regression function that fits the data.

3.5.7 Conclusion

This initial processing has provided the identification of the following major elements: Ca, Si, Mg and Ti in the global spectrum. The following lines were selected to map respectively Ca, Si, Mg and Ti: 1942.7 keV, 1779.9 keV, 1368.6 keV and 1381.7 keV. These lines have been analyzed with traditional methods of spectrum analysis such as peak fitting and band passing to map at two different resolutions (14.65° and 7.33°).

The statistical uncertainties associated with the maps at different resolutions have been calculated. These uncertainties have validated the quality of the results up to a resolution of 7.33°. Finally the results were compared with the abundances determined by Lunar Prospector. All counting rates determined with the GRS data of Selene compare quite well with the abundances determined by Lunar Prospector at the exception of Ca.

176

Conclusion

This manuscript presented how gamma and neutron spectroscopy work, and how they were used for constraining the geochemistry of planetary surfaces. This work was done in line with two experiments, the Mars Odyssey Neutron Spectrometer and the Selene Gamma Ray Spectrometer. The combine study of the two planets was a nice opportunity to probe different objects with similar techniques. The surfaces of these bodies inherited very different compositions due to the processes at stakes in their formation. The surface of the Moon is shaped by primary processes: the crust was formed by cooling of basaltic lavas, whereas the surface of Mars has known a more complex subsequent alteration. Many secondary processes contributed to resurfacing the red planet: water alteration, soil formation (by gardening processes), wind erosion, recent volcanism, tectonic activity… Because of the agenda of the missions (Mars Odyssey was launched in 2001 and Selene in September 2007), data reduction, modeling and interpretation could not be achieved in as in depth for the Moon as for Mars. Although some simulations were carried out, the results of the data modeling were not presented here because they are very preliminary. Additional work would be needed before a perfectly operational model of the interactions between galactic cosmic rays and planetary surfaces is produced. The present manuscript therefore focused on data reduction and interpretation for each separate object.

The determination of the elemental composition of Mars, and most particularly of the abundance of water, is a necessary preliminary step to understand its formation and evolution. Neutron spectroscopy is used to survey the surface for hydrogen and constrain the abundances in elements with high affinities of reaction with neutrons. Several directions were examined to infer information from the Mars Odyssey Neutron Spectrometer data.

A method to evaluate the hydration content of a lower, water-rich layer and its burial depth was proposed. The amount of hydrogen detected by MONS increases with the latitude. The burial depth of the water-rich layer was determined for regions with hydrogen contents greater than 8%. Water ice deposits get more and more buried with decreasing latitude: from a depth of 0 at poles down to a depth of about 20 g/cm^2 near the 60° and -60° latitude rings. The global maps of these two parameters were assessed by estimating the effects of uncertainties in different parameters and by inter-comparison with theoretically predicted depths of water ice. It was shown that the depth inferred from MONS proves to be generally close to that predicted by models of water ice stability at high latitudes.

Our attempt to reconcile the chemical insight provided the Gamma Subsystem and the Neutron Spectrometer led to important inferences with regard to Central Elysium Planitia, a region chosen for its moderate hydrogen content and recent volcanic activity. Gamma rays indicated a high neutron absorption potential centered on the Medusae Fossae Formation. However thermal neutrons are not absorbed strongly in Central

Elysium Planitia, suggesting a low neutron absorption potential for the recent lava flows, northwest of Medusae Fossae. This apparent disparity was interpreted to be caused by surficial heterogeneities of chlorine-rich deposits. The concentration in chlorine varies from 0.34% to as high as 0.79% in this region. These drastic variations cause the macroscopic absorption cross section to vary between 0.009 and 0.0012, which impacts quantitatively neutron emissions. Two types of chlorine heterogeneity were identified: vertical layering and geographical distribution. A scenario that may explain the chlorine configuration inferred from the NS and GS datasets was proposed: the alternation of periods of fresh basalt emplacement and chlorine-rich dust deposition explains the complexity of the observations.

Studying the elemental composition of the surface of the Moon is fundamental to both understand its geology and develop new observation techniques and processing tools. The Selene mission carried the first germanium crystal flown to the Moon. The initial processing of the data acquired by the Gamma Ray Spectrometer onboard Selene provided the identification of different lines due to many target elements in the global spectrum: Fe, K, Th, U, Ca, Si, Mg and Ti.

All lines were studied in detail to determine the energy range of the spectrum most appropriate for mapping each element. Traditional methods of spectrum analysis such as peak fitting and band passing were applied. Because of the low accumulation time, innovative methods of spectrum analysis were tested. The Independent Component Analysis proved very successful in analyzing the geochemical content hidden in spectra and also increasing the resolution of the results in the case of iron.

The statistical uncertainties associated with the maps obtained with the different lines, different methods and different resolutions were calculated. These uncertainties validated the quality of the Fe, Ca, Si, Mg and Ti abundances up to a resolution of 7.33° and that of the K, Th and U abundances up to a resolution of 3.66°. In most cases, the peak fitting method was determined to provide better results than the band passing method. All results were compared with the abundances determined with Lunar Prospector when possible (the uranium map is a brand new result). Results compared generally well, except when the noise in the Lunar Prospector data was too high.

The interpretation of the Selene gamma data would need further corrections of the spectra and a complete modeling of the production of counting rates by the instrument. These steps implicate detaining respectively more in depth housekeeping and background data across the mission and sufficiently detailed information on the instrument to achieve a numeric model of it, neither of which is in our possession right now. However the likely arrival of a Japanese GRS team member in our French team suggests that many improvements in the level of achievement of these data are to be soon expected!

And finally, thought this work was carried out in the context of the Mars Odyssey Neutron Spectrometer and Selene Gamma Ray Spectrometer, the knowledge developed for studying these datasets can be used for future missions. Next missions carrying this type of instruments include Dawn, which was launched in 2007 and should visit two

asteroids: Vesta and Ceres in respectively 2011 and 2015. Another mission carrying gamma ray and neutron spectrometers is the Messenger spacecraft launched by NASA in direction of Mercury in 2004 and which should be inserted in orbit in 2011. Its European analogue BepiColombo, whose launch is planned for 2014, should also carry a gamma ray instrument. After these missions, following experiments including gamma ray or neutron spectrometers might be in a quite distant future. The use of these technologies is indeed adapted to bodies deprived of atmosphere, so the next targets after the Moon, Mars and Mercury, will likely be satellites of the external solar system.

Conclusion (en français)

Ces travaux de thèse ont présenté les principes de la spectroscopie gamma et neutron, et comment ces techniques permettent de contraindre la géochimie des surfaces planétaires. Ils ont été réalisés dans le cadre de deux missions : le spectromètre neutron embarqué sur Mars Odyssey et le spectromètre gamma embarqué sur Selene. L'étude parallèle de deux planètes a été une belle occasion de sonder des objets différents au moyen de techniques similaires. Les surfaces de ces corps ont hérités de compositions différentes selon les processus entrant en jeu dans leur formation. La surface de la Lune a été formée par des processus primaires : la croûte est issue du refroidissement de laves basaltiques, alors que la surface de Mars a connu une altération complexe. De nombreux processus secondaires ont contribué à modifier la surface de la planète rouge : érosion par l'eau, formation d'un régolite, érosion par le vent, volcanisme récent, activité tectonique... A cause du calendrier (Mars Odyssey a été lancée en 2001 et Selene en Septembre 2007), la réduction, la modélisation et l'interprétation des données n'ont pas pu être réalisées à des niveaux de détail similaires pour chacune des missions. Des simulations ont été réalisées, mais leur degré d'aboutissement n'était pas suffisant pour faire l'objet d'une partie. Beaucoup d'heures de travail seraient nécessaires avant qu'un modèle complet et opérationnel des interactions du rayonnement cosmique galactique avec les surfaces planétaires ne soit achevé. Ce manuscrit a donc mis l'accent sur la réduction et l'interprétation des données pour chacune des deux planètes.

La détermination de la composition élémentaire de Mars, et plus particulièrement de la concentration en eau, est un préliminaire indispensable à la compréhension de sa formation et de son évolution. La spectroscopie neutron est utilisée afin de sonder la présence d'hydrogène et contraindre les abondances en éléments susceptibles d'interagir fortement avec les neutrons dans la surface martienne. Plusieurs pistes ont été explorées pour montrer comment l'information peut être extraite des données du spectromètre neutron de Mars Odyssey.

Nous avons proposé une méthode permettant d'évaluer l'hydratation de la couche riche en eau du sol, ainsi que sa profondeur sous la surface martienne. La quantité d'hydrogène détecté par le spectromètre neutron augmente avec la latitude. La profondeur de la couche riche en eau a été déterminée dans les régions contenant plus de 8% d'eau. Les dépôts de glace d'eau s'enfoncent de plus en plus profondément sous la surface à mesure que la latitude décroit : d'une profondeur 0 aux pôles jusqu'à environ 20 g/cm^2 au niveau des cercles de latitude 60° et -60°. La qualité des cartes de ces deux paramètres a été évaluée via l'estimation des incertitudes dues à différents paramètres et la comparaison avec les profondeurs d'eau déterminées par la théorie. Il a été démontré que la profondeur issue des données MONS est généralement en bon accord avec celle prédite par les modèles de stabilités de la glace d'eau aux hautes latitudes.

En essayant de réconcilier les connaissances issues des données gamma avec celles issues des données neutron, nous avons abouti à d'importantes conclusions concernant Central Elysium Planitia, une région sélectionnée pour son contenu modeste en hydrogène et son activité volcanique récente. Les données gamma de la région indiquent un fort potentiel d'absorption des neutrons centré sur Medusae Fossae Formation. Cependant les neutrons thermiques sont peu absorbés dans cette région, ce qui suggère que les récents écoulements de lave au nord ouest de Medusae Fossae ont un faible potentiel d'absorption des neutrons. Cette différence notoire a été interprétée comme issue des hétérogénéités des dépôts riches en chlore présents en surface. La concentration en chlore varie de 0,34% à 0,79% dans cette région. Ces importantes variations font évoluer la section efficace macroscopique d'absorption des neutrons entre 0,009 et 0,0012 ; ce qui impacte significativement les émissions de neutrons. Deux types d'hétérogénéité ont été identifiés : la stratigraphie verticale et la distribution géographique. A l'issue de cette conclusion, nous avons proposé un scénario qui permet de reconstituer la configuration des dépôts de chlore déduite des données neutron et gamma. L'alternance de périodes où des basaltes frais sont mis en place et de périodes où la poussière se dépose en surface explique la complexité des observations.

L'étude de la composition élémentaire de la surface de la Lune est fondamentale pour à la fois comprendre sa géologie et développer de nouvelles techniques d'observations et outils de traitement des données. La mission Selene a transporté le premier spectromètre gamma doté d'un cristal de germanium à destination de la Lune. Le traitement primitif des données acquises par le spectromètre gamma a permis l'identification de nombreux éléments cibles dans le spectre global : Fe, K, Th, U, Ca, Si, Mg and Ti.

Toutes les raies ont été étudiées en détail afin de déterminer les régions du spectre les plus appropriées pour cartographier chacun des éléments. Les spectres ont été analysés à l'aide de méthodes traditionnelles de traitement telles que l'interpolation de raies par fonction gaussienne modifiée et l'intégration des données par bandes d'énergie. En raison du faible temps d'accumulation atteint pour l'instant, des méthodes d'analyse innovantes ont été investiguées. L'Analyse en Composantes Indépendantes s'est avérée très utile pour révéler le contenu géochimique des spectres et augmenter la résolution spatiale des résultats dans le cas du fer.

Les incertitudes statistiques ont été calculées pour toutes les cartes obtenues avec différentes raies, différentes méthodes de calcul et à différentes résolutions. Ces incertitudes ont permis de valider la qualité des abondances de Fe, Ca, Si, Mg et Ti jusqu'à une résolution de 7,33° et de K, Th et U jusqu'à 3,66°. Dans la majeure partie des cas, la méthode de l'interpolation de raies par fonction gaussienne modifiée a donné les meilleurs résultats. Tous les résultats ont été comparés avec les abondances déterminées par Lunar Prospector lorsque c'était possible (la carte de l'uranium est un tout nouveau résultat). Nos résultats s'avèrent très proches de ceux de Lunar Prospector, sauf dans certains cas où le bruit présent dans ces derniers était trop important.

Avant d'envisager d'interpréter les données gamma de Selene, des corrections des spectres plus abouties ainsi qu'une modélisation complète de la production des taux de comptage de l'instrument seraient nécessaires. Ces étapes supplémentaires impliquent

de détenir des paramètres instrumentaux détaillés et des données de bruit de contamination, que nous ne possédons actuellement que de manière très fragmentée. Cependant, la venue très probable d'un membre japonais de l'équipe GRS dans notre équipe française laisse présager que de nombreuses améliorations vont pouvoir être apportées aux données !

Enfin, en dépit du fait que ce travail a été mené dans le cadre du Spectromètre Neutron de Mars Odyssey et du Spectromètre Gamma de Selene, les connaissances acquises au cours de l'étude de ces jeux de données peuvent être utilisées pour des missions futures. Parmi les missions prochaines qui comportent de tels instruments on trouve Dawn, qui a été lancée en 2007 et devrait atteindre deux astéroïdes : Vesta et Ceres (respectivement en 2011 et 2015). Le satellite Messenger lancé en par la NASA en direction de Mercure en 2004 comporte aussi des spectromètres neutron et gamma et devrait être insérée en orbite courant 2011. Son analogue européen BepiColombo, qui fera l'objet d'un lancement courant 2014, comportera également un spectromètre gamma. Après ces missions, le vol de spectromètres neutron ou gamma se fera certainement dans un futur plus lointain. L'utilisation de ces technologies est en effet adaptée aux corps dépourvus d'atmosphères, aussi les prochaines cibles (après la Lune, Mars et Mercure) seront très certainement les satellites du système solaire externe.

References

[Arnold et al., 1962] Arnold, J. R., Metzger, A. E., Anderson, E. C. et Van Dilla, M. A. (1962). Gamma Rays in Space, Ranger 3. Journal of Geophysical Research, 67(12):4878-4880.

[Badhwar et al., 2004] Badhwar, G. D.: 2004; Martian Radiation Environment Experiment (MARIE), Space Science Reviews, 110, 131–142.

[Bandfield, 2002] Bandfield, J. L. (2002), Global mineral distributions on Mars, J. Geophys. Res., 107(E6), 5042, doi:10.1029/2001JE001510.

[Bandfield et al., 2000] Bandfield, J. L., V. E. Hamilton, and P. R. Christensen 2000, A global view of Martian surface composition from MGS-TES, Science, 287, pp. 1626-1630.

[Bertini, 1969] Bertini, H. W. (1969), Intranuclear-cascade calculations of nucleon spectra from nucleon-nucleus interactions in the energy range 340 to 29000 MeV and comparison with experiment, Phys. Rev., 188, 1711 - 1730.

[Berman and Hartmann, 2002] Berman, D. C., and W. K. Hartmann 2002, Recent Fluvial, Volcanic and Tectonic Activity on the Cerberus Plains on Mars, Icarus 159, pp. 1-17, doi:10.1006/icar.2002.6920.

[Bibring et al., 2005] Bibring, J.-P., Langevin, Y., Gendrin, A., Gondet, B., Poulet, F., Berthé, M., Soufflot, A., Arvidson, R., Mangold, N., Mustard, J., Drossart, P., and the OMEGA team, 2005, Surface diversity as revealed by the OMEGA/Mars Express observations: Science, v. 307, p. 1576–1581, doi:10.1126/science.1108806.

[Boynton et al., 2007] Boynton, W. V., G. J. Taylor, S. Karunatillake, R. C. Reedy, and J. M. Keller (2007), Concentration of H, Si, Cl, K, Fe, and Th in the low- and mid-latitude regions of Mars, J. Geophys. Res., 112, E12S99, doi:10.1029/2007JE002887.

[Boynton et al., 2004] Boynton, W. V., et al. (2004), The Mars Odyssey Gamma-Ray Spectrometer Instrument Suite, Space Science Reviews, 110:37-83.

[Boynton et al., 2002] Boynton, W. V., Feldman,W. C., Squyres, S.W., Prettyman, T. H., Bruckner, J., Evans, L. G., Reedy, R. C., Starr, R., Arnold, J. R., Drake, D. M., Englert, P. A. J., Metzger, A. E., Mitrofanov, Igor, Trombka, J. I., d'Uston, C., Wanke, H., Gasnault, O., Hamara, D. K., Janes, D. M., Marcialis, R. L., Maurice, S., Mikheeva, I., Taylor, G. J., Tokar, R. and Shinohara, C. (2002), Distribution of Hydrogen in the Near Surface of Mars: Evidence for Subsurface Ice Deposits, Science 297, 81-85.

[Boynton et al., 1992] Boynton, W. V., Trombka, J. I., Feldman, W. C., Arnold, J. R., Englert, P. A. J., Metzger, A. E., Reedy, R. C., Squyres, S. W., Wänke, H., Bailey, S. H., Brückner, J., Callas, J. L., Drake, D. M., Duke, P., Evans, L. G., Haines, E. L., McCloskey, F. C., Mills, H., Shinohara, C. et Starr, R. (1992). Science Applications of the Mars Observer Gamma Ray Spectrometer. Journal of Geophysical Research, 97:7681-7698.

[Bradley et al., 2002] Bradley, B. A., S. E. H. Sakimoto, H. Frey, and J. R. Zimbelman, Medusae Fossae Formation: New perspectives from Mars Global Surveyor, J. Geophys. Res., 107(E8), 5058, doi:10.1029/2001JE001537, 2002.

[Brückner et al., 2003] Brückner, J., G. Dreibus, R. Rieder, and H. Wänke 2003, Refined data of Alpha Proton X-ray Spectrometer analyses of soils and rocks at the Mars Pathfinder site: Implications for surface chemistry, J. Geophys. Res., 108(E12), 8094, doi:10.1029/2003JE002060.

[Brückner et al., 1991] Brückner, J., M. Koerfer, H. Wänke, A. N. F. Schroeder, D. Filges, P. Dragovitsch, P. A. J. Englert, R. Starr, and J. I. Trombka (1991), Photon-induced radiation damage in germanium detectors, IEEE Trans. Nucl. Sci., 38, 209-217.

[Burr et al., 2002] Burr, D. M, A. S. McEwen, S. E. H. Sakimoto 2002, Recent aqueous floods from the Cerberus Fossae, Mars, Geophys. Res. Lett. 29.

[Cardoso, 1997] Cardoso, J. F., Infomax and maximum likelihood for source separation. IEEE Letters on Signal Processing, 4, pp.112–114. 1997.

[Christensen et al., 2004] Christensen, P. R., et al. (2004), The Thermal Emission Imaging System (THEMIS) for the Mars 2001 Odyssey Mission, Space Sci. Rev., 110, 85– 130.

[Christensen et al., 2003] Christensen, P. R. et al, Morphology and Composition of the Surface of Mars: Mars Odyssey THEMIS Results, Science 300, 2056 (2003), DOI:10.1126/science.1080885

[Christensen et al., 2000] Christensen, P. R., et al., Detection of crystalline hematite mineralization on Mars by the Thermal Emission Spectrometer: Evidence for near-surface water, J. Geophys. Res., 105, 9632– 9642, 2000.

[Clark et al., 1982] Clark, B. C., A. K. Baird, R. J. Weldon, D. M. Tsusaki, L. Schnabel, and M. P. Candelaria 1982, Chemical composition of Martian fines, J. Geophys. Res., 87, pp. 10,059-10,067.

[Comon, 1994] Comon, P., Independent component analysis, a new concept?, Signal Processing, v.36 n.3, p.287-314, April 1994 , doi :10.1016/0165-1684(94)90029-9

[Drake et al., 1988] Drake, D. M., W. C. Feldman, B. M. Jakosky (1988), Martian neutron leakage spectra, Journal of Geophysical Research, Vol. 93., p. 6353-6368

[d'Uston et al., 1989] d'Uston, C., Atteia, J. L., Barat, C., Chernenko, A., Dolidze, V., Dyatchkov, A., Jourdain, E., Khariukova, V., Khavenson, N., Kozlenkov, A., Kucherova, R., Mitrofanov, I., Moskaleva, L., Niel, M., Pozanenko, A., Scheglov, P., Surkov, Y. et Vilchinskaya, A. (1989). Observations of the gamma-ray emission of the Martian surface by the APEX experiment. Nature, 341:598-600.

[Elphic et al., 1998] Elphic, R. C., D. J. Lawrence, W. C. Feldman, B. L. Barraclough, S. Maurice, A. B. Binder, P. G. Lucey 1998, Lunar Fe and Ti Abundances: Comparison of Lunar Prospector and Clementine Data, Science 281, pp. 1493-1496.

[Evans et al., 2006] Evans, L. G., R. C. Reedy, R. D. Starr, K. E. Kerry, and W. V. Boynton (2006), Analysis of gamma ray spectra measured by Mars Odyssey, J. Geophys. Res., 111, E03S04, doi:10.1029/2005JE002657.

[Evans et al., 2001] Evans, L. G., Starr, R. D., Brückner, J., Reedy, R. C., Boynton, W. V., Trombka, J. I., Goldstein, J. O., Masarik, J., Nittler, L. R., McCoy, T. J., Elemental composition from gamma-ray spectroscopy of the NEAR-Shoemaker landing site on 433 Eros, Meteoritics & Planetary Science, vol. 36, no. 12, pp. 1639-1660 (2001).

[Evans et al., 1993] Evans, L. G., Reedy, R. C. et Trombka, J. I. (1993). Introduction to planetary remote-sensing gamma-ray spectroscopy. In Pietersand, C. and Englert, P. A. J., edited by: Remote Geochemical Analysis: Elemental and Mineralogical Composition, pages 167-198. Cambridge University Press, New York.

[Fanale, 1976] Fanale, F. 1976, Martian volatiles - Their degassing history and geochemical fate, Icarus, 28, 179-202.

[Farmer and Doms, 1979] Farmer, C. B., and P. E. Doms (1979), Global and seasonal variation of water vapor on Mars and the implications for permafrost, J. Geophys. Res., 84, 2881-2888.

[Feldman et al., 2005] Feldman, W. C., et al. (2005), Topographic control of hydrogen deposits at low latitudes to midlatitudes of Mars, J. Geophys. Res., 110, E11009, doi:10.1029/2005JE002452.

[Feldman et al., 2004a] Feldman, W. C., Ahola, K., Barraclough, B. L., Belian, R. D., Black, R. K., Elphic, R. C., Everett, D. T., Fuller, K. R., Kroesche, J., Lawrence, D. J., Lawson, S. L.,

Longmire, J. L., Maurice, S., Miller, M. C., Prettyman, T. H., Storms, S. A. et Thornton, G. W. (2004). Gamma-Ray, Neutron, and Alpha-Particle Spectrometers for the Lunar Prospector mission. Journal of Geophysical Research, 109(E7).

[Feldman et al., 2004b] Feldman,W. C., et al. (2004), Global Distribution of near-surface hydrogen on Mars, J. Geophys. Res., 109, E09006, doi:10.1029/2003JE002160.

[Feldman et al., 2002a] Feldman, W.C., et al., Fast neutron flux spectrum aboard Mars Odyssey during cruise, JGR. 107, #A6, 10.1029/2001JA000295, 2002.

[Feldman et al., 2002b] Feldman,W. C., W. V. Boynton, R. L. Tokar, T. H. Prettyman, O. Gasnault, S. W. Squyres, R. C. Elphic, D. J. Lawrence, S. L. Lawson, S. Maurice, G. W. McKinney, K. R. Moore, and R. C. Reedy: 2002, Global Distribution of Neutrons from Mars: Results from Mars Odyssey, Science 297, 75-78.

[Feldman et al., 2001] Feldman, W. C., Maurice, S., Lawrence, D. J., Little, R. C., Lawson, S. L., Gasnault, O., Wiens, R. C., Barraclough, B. L., Elphic, R. C., Prettyman, T. H., Steinberg, J. T. et Binder, A. B. (2001). Evidence for water ice near the lunar poles. Journal of Geophysical Research, 106:23231-23252.

[Feldman et al., 1999] Feldman, W. C., B. L. Barraclough, K. R. Fuller, D. J. Lawrence, S. Maurice, M. C. Miller, T. H. Prettyman, and A. B. Binder (1999), The Lunar Prospector Gamma-Ray and Neutron Spectrometers, Nucl. Instrum. Methods, Sect. A, 422, 562– 566.

[Feldman et al., 1993] Feldman, W. C., Boynton, W. V. et Drake, D. M. (1993). Planetary Neutron Spectroscopy from Orbit, in Remote geochemical analysis: elemental and mineralogical composition, pages 213-234, edited by C.M. Pieters and P.A.J. Englert, Cambridge University Press, New York.

[Feldman and Drake, 1986] Feldman, W. C., and D. Drake (1986), A Doppler filter technique to measure the hydrogen content of planetary surfaces, Nucl. Instrum. Methods, 245, 182– 190.

[Forget et al., 2002] Forget, F., Hourdin, F., Talagrand, O. (2002), CO_2 Snowfall on mars: simulation with a general circulation model, Icarus 131, doi:10.1006/icar.1997.5874

[Forget et al., 1999] Forget, F., Hourdin, F., Fournier, R., Hourdin, C., Talagrand, O., Collins, M., Lewis, S. R., Read, P. L., Huot, J.-P. (1999) Improved general circulation models of the Martian atmosphere from the surface to above 80 km, J. Geophys. Res. 104, E10, doi:10.1029/1999JE001025

[Forni et al., 2005] Forni, O., F. Poulet, J.-P., Bibring et al. 2005, Component Separation of OMEGA Spectra with ICA, LPS XXXVI, 1623.

[Gasnault et al., 2003] Gasnault, O., S. Maurice, and D. J. Lawrence (2003), Low resolution planetary experiments: Gridding and mapping routines using IDL, paper presented at ISPRS Workshop: Advances in Planetary Mapping, Int. Soc. for Photogramm. and Remote sens., Houston, Tex.

[Gellert et al., 2006] Gellert, R., et al. 2006, Chemical diversity along the traverse of the rover Spirit at Gusev Crater, Lunar and Planet. Sci. Conf. XXXVII, abstract #2176.

[Gellert et al., 2004] Gellert, R., et al. 2004, Chemistry of Rocks and Soils in Gusev Crater from APXS, Science, 305, 829-832.

[Gendrin et al., 2005] Gendrin, A., Mangold, N., Bibring, J.-P., Langevin, Y., Gondet, B., Poulet, F., Bonello, G., Quantin , C., Mustard, J., Arvidson, R., and LeMouélic, S., 2005, Sulfates in Martian layered terrains: The OMEGA/Mars Express View: Science, v. 307, p. 1587–1591, doi: 10.1126/science.1109087.

[Gold et al., 2001] Gold, R. E., et al. (2001), The MESSENGER mission to Mercury: scientific payload, Planetary and Space Science, 49:1467-1479.

[Gorski et al., 2005] Gorski, K.M., E. Hivon, E, A.J. Banday, et al. 2005, HEALPix: A Framework for High-Resolution Discretization and Fast Analysis of Data Distributed on the Sphere, The Astrophysical Journal, 622, 2, pp. 759-771.

[Greeley and Guest, 1987] Greeley, R., and J. E. Guest 1987, Geologic map of the eastern equatorial region of Mars, 1:15000000, U.S. Geol. Surv. Misc. Invest. Ser., Map I-1802-A.

[Hahn et al., 2007] Hahn, B. C., et al. 2007, Mars Odyssey Gamma Ray Spectrometer elemental abundances and apparent relative surface age: Implications for Martian crustal evolution, J. Geophys. Res., 112, E03S11, doi:10.1029/2006JE002821.

[Haining, 2003] Haining, R. (2003), Spatial Data Analysis: Theory and Practice, Cambridge Univ. Press, New York.

[Harmon et al., 1992] Harmon, J. K., M. P. Sulzer, P. J. Perillat, and J. F. Chandler 1992, Mars Radar Mapping - Strong Backscatter from the Elysium Basin and Outflow Channel, Icarus 95, pp. 153-156.

[Harrington et al., 1974] Harrington, T. M., Marshall, J. H., Arnold, J. R., Peterson, L. E., Trombka, J. I. et Metzger, A. E. (1974). The Apollo Gamma-Ray Spectrometer. Nuclear Instruments and Methods, 118:401-411.

[Hartmann et al., 2000] Hartmann, W. K. and D. C. Berman 2000, Elysium Planitia lava flows: crater count chronology and geological implications, J. Geophys. Res., 105, E6, pp. 15,011-15,025.

[Hasebe et al., 2008] Hasebe, N., N. Yamashita, O. Okudaira, S. Kobayashi, H. Yamamoto, T. Ishizaki, K. Hirano, K. Sakurai, T. Miyachi, M. Miyajima, M. Fujii, M.-N. Kobayashi, T. Takashima, E. Shibamura, O. Gasnault, S. Maurice, C. d'Uston, R. Reedy, M. Grande, The high precision gamma-ray spectrometer for lunar polar orbiter SELENE, Advances in Space Research, Volume 42, Issue 2, 18 July 2008, Pages 323-330, ISSN 0273-1177, DOI: 10.1016/j.asr.2007.05.046.

[Hasebe et al., 1999] Hasebe, N., Shibamura, E., Atarashiya, T., Doke, T., D'Uston, C., Grande, M., Kashiwagi, T., Kikuchi, J., Kobayashi, M., Kubo, K., Mitani, S., Mori, K., Narasaki, K., Nomi, K., Takashima, T., Tanibata, R. et Reedy, R. C. (1999). Gamma-ray spectrometer for Japanese lunar polar orbiter. Advances in Space Research, 23:1837-1840.

[Head et al., 2003] Head, J. W., L. Wilson and K. L. Mitchell 2003, Generation of recent massive water floods at Cerberus Fossae, Mars by dyke emplacement, cryospheric cracking, and confined aquifer, Geophys. Res. Lett. 30(11), 1577, doi:10.1029/2003GL017135.

[Hess et al., 1980] Hess, S. L., Ryan, J. A., Tillman, J. E., Henry, R. M., Leovy, C. B. (1980), The annual cycle of pressure on Mars measured by Viking landers 1 and 2, Geophys. Res. Lett. 7, 197-200.

[Hyvärinen and Oja, 2000] Hyvärinen, A., E. Oja, Independent component analysis: algorithms and applications, Neural Networks, v.13 n.4-5, p.411-430, May-June 2000, doi:10.1016/S0893-6080(00)00026-5.

[Jaeger et al., 2008] Jaeger, W. L., L. P. Keszthelyi, A. S. McEwen, T. N. Titus, C. M. Dundas, P. S. Russell, Response to Comment on "Athabasca Valles, Mars: A Lava-Draped Channel System", Science 320, 1588c (2008).

[Jaeger et al., 2007] Jaeger, W. L., L. P. Keszthelyi, A. S. McEwen, C. M. Dundas, P. S. Russell, Athabasca Valles, Mars: A Lava-Draped Channel System, Science 317, 1709 (2007).

[Jolliff et al., 2000] Jolliff, B. L., J. J. Gillis, L. A. Haskin, R. L. Korotev, and M. A. Wieczorek (2000), Major lunar crustal terranes: Surface expressions and crust-mantle origins, J. Geophys. Res., 105(E2), 4197– 4216.

[Kahre et al., 2006] Kahre, M.A., J.R. Murphy and R.M. Haberle, Modeling the martian dust cycle and surface dust reservoirs with the NASA Ames general circulation model, J. Geophys. Res. 111 (2006) 10.1029/2005JE002588 E06008.

[Karunatillake et al., 2007] Karunatillake, S. , J.M. Keller, S.W. Squyres, W.V. Boynton, J. Brückner, D.M. Janes, O. Gasnault and H.E. Newsom, Chemical compositions at Mars landing sites subject to Mars Odyssey Gamma Ray Spectrometer constraints, J. Geophys. Res. 112 (2007) 10.1029/2006JE002859 E08S90.

[Kato et al., 2008] Kato, M., S. Sasaki, K. Tanaka, Y. Iijima, Y. Takizawa, The Japanese lunar mission SELENE: Science goals and present status, Advances in Space Research, Volume 42, Issue 2, 18 July 2008, Pages 294-300, ISSN 0273-1177, DOI: 10.1016/j.asr.2007.03.049.

[Keller et al., 2006] Keller, J. M., et al. 2006, Equatorial and midlatitude distribution of chlorine measured by Mars Odyssey GRS, J. Geophys. Res., 111, E03S08, doi:10.1029/2006JE002679.

[Keszthelyi et al., 2000] Keszthelyi, L., and A. S. McEwen, T. Thordarson 2000, Terrestrial analogs and thermal models for Martian flood lavas, J. Geophys. Res., 105, E6, pp. 15,027-15,049.

[Kim et al., 2006] Kim, K., W. V. Boynton, M. J. Finch, R. M. S. Williams, R. C. Reedy, and D. M. Drake 2006, Effects of rock and soil on gamma ray production in the Martian surface, Proc. Lunar Planet. Sci. Conf. 37th, abstract #2356.

[Kreslavsky and Head, 2000] Kreslavsky, M. A., and J. W. Head III 2000, Kilometer-scale roughness of Mars: Results from MOLA data analysis, J. Geophys. Res., 105, E11.

[Kruse, 1979] Kruse, H. (1979), Spectra processing with computer-graphics, in Computers in Activation Analysis and Gamma-Ray Spectroscopy, edited by S. Carpenter, M. D. D'Agostino, and H. P. Yule, pp. 76– 84, U.S. Dep. of Energy, Washington, D. C.

[Krzysztof et al., 2008] Krzysztof M. G´orski, Benjamin D. Wandelt, Eric Hivon, Frode K. Hansen, and Anthony J. Banday, The Healpix Primer, 2008.

[Lanagan, 2004] Lanagan, P. D. 2004, Geologic history of the Cerberus Plains, Mars, Ph.D. Dissertation.

[Lanagan and McEwen, 2003] Lanagan, P. D., and A. S. McEwen 2003, Cerberus Plains volcanism: constraints on temporal emplacement of the youngest flood lavas on Mars, Sixth International Conference on Mars.

[Lanagan et al., 2001a] Lanagan, P. D., A. S. McEwen, and L. S. Link 2001, Geomorphologic mapping of Cerberus plains, Mars, LPS XXXII, abstract #2077.

[Lanagan et al., 2001b] Lanagan, P. D., A. S. McEwen, L. P. Keszthelyi, T. Thordarson 2001, Rootless cones on Mars indicating the presence of shallow equatorial ground ice in recent times, Geophys. Res. Lett. 28(12), pp. 2365-2367.

[Lawrence et al., 2004] Lawrence, D. J., S. Maurice, and W. C. Feldman (2004), Gamma-ray measurements from Lunar Prospector: Time series data reduction for the gamma-ray spectrometer, J. Geophys. Res., 109, E07S05, doi:10.1029/2003JE002206.

[Lawrence et al., 2002] Lawrence, D. J., Feldman, W. C., Elphic, R. C., Little, R. C., Prettyman, T. H., Maurice, S., Lucey, P. G. and Binder, A. B. (2002). Iron abundances on the lunar surface as measured by the Lunar Prospector gamma-ray and neutron spectrometers. Journal of Geophysical Research (Planets), 107:13-1.

[Lawrence et al., 1999] Lawrence, D. J., Feldman, W. C., Barraclough, B. L., Binder, A. B., Elphic, R. C., Maurice, S., Miller, M. C. et Prettyman, T. H. (1999). High resolution measurements of absolute thorium abundances on the lunar surface. Geophysical Research Letters, 26:2681-2684.

[Leighton and Murray, 1966] Leighton, R. B., and B. C. Murray (1966), Behavior of Carbon Dioxide and Other Volatiles on Mars, Science 153, 136-144.

[Lingenfelter et al., 1961] Lingenfelter, R. E., Canfield, E. H. and Hess,W. N. (1961), The lunar neutron flux, J. Geophys. Res. 66, 2665–2671.

[Maurice et al., 2007] Maurice S., W. C. Feldman, T. H. Prettyman, B. Diez, O. Gasnault 2007, Reduction of Mars Odyssey Data, LPS XXXVIII, Abstract #2036.

[Maurice et al., 2004a] Maurice S., D. J. Lawrence, W. C. Feldman, and R. C. Elphic, and O. Gasnault (2004), Reduction of neutron data from Lunar Prospector, J. Geophys. Res., 109, E07S04, doi:10.1029/2003JE002208

[Maurice et al., 2004b] Maurice S., O. Gasnault, W. C. Feldman, T. H. Prettyman, R. C. Elphic, D. J. Lawrence 2004, Burial depth of the reservoirs of hydrogen at equatorial latitudes on Mars, LPS XXXV, Abstract #1866.

[Mellon et al., 2004] Mellon, M., W. C. Feldman, and T. H. Prettyman 2004, The presence and stability of ground ice in the southern hemisphere of Mars, Icarus, 169, 324-340.

[Mellon et al., 2000] Mellon, M. T., B. M. Jakosky, H. H. Kieffer, P. R. Christensen 2000, High-Resolution Thermal Inertia Mapping from the Mars Global Surveyor Thermal Emission Spectrometer, Icarus, Volume 148, Issue 2, pp. 437-455.

[Mellon and Jakosky, 1993] Mellon, M., and B. Jakosky 1993, Geographic variations in the thermal and diffusive stability of ground ice on Mars, J. Geophys. Res., 98, 3345-3364.

[Metzger and Arnold, 1970] Metzger, A. E. and Arnold, J. R. (1970). Gamma ray spectroscopic measurements of Mars. Applied Optics, 9:1289-1303.

[Mitrofanov et al., 2002] Mitrofanov, I., Anfimov, D., Kozyrev, A., Litvak, M., Sanin, A., Tret'yakov, V., Krylov, A., Shvetsov, V., Boynton, W., Shinohara, C., Hamara, D. and Saunders, R. S. (2002), Maps of Subsurface Hydrogen from the High Energy Neutron Detector, Mars Odyssey, Science 297, 78-81.

[Mitrofanov et al., 1996] Mitrofanov, I. G., Anfimov, D. S., Chernenko, A. M., Dolidze, V. S., Kostenko, V. I., Isupov, O. E., Pozanenko, A. S., Ton'shev, A. K., Ushakov, D. A., Auchampaugh, G. F., Cafferty, M., Drake, D. M., Fenimore, E. E., Klebesadel, R. W., Longmire, J. L., Moss, C. E. et Reedy, R. C. (1996). High Precision Gamma-Ray Spectrometer PGS for Russian Interplanetary Mission to Mars. Advances in Space Research, 17(12):51-59.

[Murray et al., 2005] Murray, J.B., J.-P. Muller, G. Neukum, E. Hauber, W. J. Markiewicz, J. W. Head, B. H. Foing, D. P. Page, K. L. Mitchell, G. Portyankina 2005, Evidence from the Mars Express High Resolution Stereo Camera for a frozen sea close to Mars' equator, Nature 434, 352–355.

[Mustard et al., 2008] Mustard, J. F., et al. 2008, Hydrated silicate minerals on Mars observed by the Mars Reconnaissance Orbiter CRISM instrument, Nature 454, 305-309 (17 July 2008), doi:10.1038/nature07097.

[Newsom et al., 2007a] Newsom, H. E., L. S. Crumpler, R. C. Reedy, M. J. Nelson, M. T. Petersen, L. G. Evans, G. J. Taylor, J. M. Keller, D. M. Janes, W. V. Boynton, K. E. Kerry, S. Karunatillake, and the GRS team 2007, Mars Geochemistry of Martian surficial materials with Gamma Ray data from Mars Odyssey: Initial observations for Calcium, Lunar and Planet. Sci. Conf. XXXVIII, abstract #1939.

[Newsom et al., 2007b] Newsom, H. E., et al. 2007, Geochemistry of Martian soil and bedrock in mantled and less mantled terrains with gamma ray data from Mars Odyssey, J. Geophys. Res., 112, E03S12, doi:10.1029/2006JE002680.

[Nunez et al., 1999] Nunez, J., Otazu, X., Fors, O., Prades, A., Pala, V., Arbiol, R., Multiresolution-based image fusion with additive wavelet decomposition, Geoscience and Remote Sensing, IEEE Transactions on , vol.37, no.3, pp.1204-1211, May 1999.

[Okudaira et al., 2006] Okudaira, O., Yamashita, N., Hasebe, N., et al., Geant4 Monte Carlo simulation to estimate gamm-ray emissions from lunar surface and SELENE spacecraft. In: Proceedings of the 9th ICATPP Conference on Astroparticle, Particle, Space Physics, Detectors and Medical Physics Applications, vol. 9, pp. 490-494, 2006.

[Owen, 1992] Owen, T. 1992, The composition and early history of the atmosphere of Mars, in Mars, H. H. Kieffer, B. M. Jakosky, C. W. Snyder, M. S. Mathews, eds Univ. Ariz. Press, pp 818-834.

[Page, 2008] Page, D., Comment on "Athabasca Valles, Mars: A Lava-Draped Channel System", Science 320, 1588b (2008).

[Paige, 1992] Paige, D.A. 1992, The thermal stability of near-surface ground ice on Mars, Nature, 356, 43-45.

[Pirard, 2006] Pirard, B., Etude et Validation d'un spectromètre gamma pour la mesure de la composition chimique des surfaces planétaires, PhD dissertation.

[Plescia, 1990] Plescia, J. B. 1990, Young flood lavas in the Elysium region, Mars, In Lunar and Planetary Inst., Scientific Results of the NASA-Sponsored Study Project on Mars: Evolution of Volcanism, Tectonics, and Volatiles pp. 243-245.

[Plescia, 2003] Plescia, J. B. 2003, Cerberus Fossae, Elysium, Mars: a source for lava and water, Icarus 164, pp. 79-95.

[Prettyman et al., 2006a] Prettyman, T. H., Barraclough, B. L., Feldman, W. C., Baldonado, J. R., Bernardin, J. D., Dingler, R. D., Enemark, D. C., Little, C. K., Miller, E. A., Patrick, D. E., Pavri, B., Raymond, C. A., Russell, C. T., Storms, S. A., Sweet, M. R., Williford, R. L. et Wong-Swanson, B. (2006). Gamma Ray and Neutron Spectrometer for Dawn. In 37th Annual Lunar and Planetary Science Conference, pages 2231-2232.

[Prettyman et al., 2006b] Prettyman, T. H., J. J. Hagerty, R. C. Elphic, W. C. Feldman, D. J. Lawrence, G. W. McKinney, and D. T. Vaniman (2006), Elemental composition of the lunar surface: Analysis of gamma ray spectroscopy data from Lunar Prospector, J. Geophys. Res., 111, E12007, doi:10.1029/2005JE002656.

[Prettyman et al., 2004a] Prettyman, T.H., et al., Mars 2001 Odyssey neutron spectrometer processing, Version 1.3, 06/30/2004.

[Prettyman et al., 2004b] Prettyman, T.H., et al., Composition and structure of the Martian surface at high southern latitudes from neutron spectroscopy, JGR, 109, E05001, doi:10.1029/2003JE002139, 2004.

[Putzig et al., 2005] Putzig, N. E., M. T. Mellon, K. A. Kretke, and R. E. Arvidson, Global thermal inertia and surface properties of Mars from the MGS mapping mission, Icarus 173, 325-341, 2005.

[Rieder et al., 2004] Rieder, R., et al. 2004, Chemistry of Rocks and Soils at Meridiani Planum from the APXS, Science, 306, 1746-1749.

[Sanders and Holm, 1969] Sanders, W. M. and D. M. Holm, Analytical method for unfolding gamma-ray spectra (Analytical method and computer code for unfolding gamma ray spectra), Rapport LASL - 68-4030.

[Saunders et al., 2004] Saunders, R. S., Arvidson, R. E., Badhwar, G. D., Boynton, W. V., Christensen, P., Cucinotta, F. A., Gibbs, R. G., Kloss, Jr. C., Landano, M. R., Mase, R. A., Meyer, M., Pace, G., Plaut, J. J., Sidney, W., McSmith, G. W., Spencer, D. A., Thompson, T. W. and Zeitlin, C. J.: 2004, '2001 Mars Odyssey Mission Summary', Space Sci. Rev., 110, 1-36.

[Schorghofer and Aharonson, 2005] Schorghofer, N., and O. Aharonson 2005, Stability and exchange of subsurface ice on Mars, J. Geophys. Res., 110, E05003, doi:10.1029/2004JE002350.

[Schulz and Benkhoff, 2006] Schulz, R. and Benkhoff, J. (2006). BepiColombo : Payload and mission updates. Advances in Space Research, 38:572-577.

[Scott and Tanaka, 1986] Scott, D. H., and K. L. Tanaka 1986, Geologic map of the western equatorial region of Mars, 1:15000000, U.S. Geol. Surv. Misc. Invest. Ser., Map I-1802-A.

[Shervais et al., 2005] Shervais, J.W., et al., 2005, Basaltic volcanism of the central and western Snake River Plain: A guide to field relations between Twin Falls and Mountain Home, Idaho, in Pederson, J., and Dehler, C.M., eds., Interior Western United States: Geological Society of America Field Guide 6, doi: 10.1130/2005.fld006(02).

[Smith et al., 1999] Smith, D. E., et al., The Global Topography of Mars and Implications for Surface Evolution, Science 28 May 1999: Vol. 284. no. 5419, pp. 1495 – 1503, DOI: 10.1126/science.284.5419.1495.

[Surkov et al., 1989] Surkov, I. A., -arsukov, V. L., Moskaleva, L. P., Khariukova, V. P. et Zaitseva, S. E. (1989). Determination of the elemental composition of Martian rocks from Phobos 2. Nature, 341:595-598.

[Surkov et al., 1981] Surkov, I. A., Moskaleva, L. P., Manvelian, O. S. et Khariukova, V. P. (1981). Analysis of the gamma radiation of Martian rocks based on the data of the Mars 5 spacecraft. Cosmic Research, 18:623-631.

[Tanaka, 1986] Tanaka, K. L. 1986, Stratigraphy of Mars, J. Geophys. Res., 91, E139-E158.

[Tokar et al., 2003] Tokar, R. L, R. C. Elphic, W. C. Feldman, H. O. Funsten, K. R. Moore, T. H. Prettyman, R. C. Wiens 2003, Mars Odyssey Neutron sensing of the south residual polar cap, Geophys. Res. Lett., 30, NO. 13, 1677, doi:10.1029/2003GL017316.

[Tokar et al., 2002] Tokar, R.L., et al., Ice concentration and distribution near the south pole of Mars: Synthesis of odyssey and global surveyor analyses, GRL, 29, #19, 1904, doi:10.1029/2002GL015691, 2002.

[Trombka et al., 2001] Trombka, J. I., Nittler, L. R., Starr, R. D., Evans, L. G., McCoy, T. J., Boynton, W. V., Burbine, T. H., Brückner, J., Gorenstein, P., Squyres, S. W., Reedy, R. C., Goldsten, J. O., Lim, L., Hurley, K., Clark, P. E., Floyd, S. R., McClanahan, T. P., McCartney, E., Branscomb, J., Bhangoo, J. S., Mikheeva, I. et Murphy, M. E. (2001). The NEAR-Shoemaker xray/gamma-ray spectrometer experiment: Overview and lessons learned. Meteoritics and Planetary Science, 36:1605-1616.

[Trombka et al., 2000] Trombka, J. I., Squyres, S. W., Brückner, J., Boynton, W. V., Reedy, R. C., McCoy, T. J., Gorenstein, P., Evans, L. G., Arnold, J. R., Starr, R. D., Nittler, L. R., Murphy, M. E., Mikheeva, I., McNutt, R. L., McClanahan, T. P., McCartney, E., Goldsten, J. O., Gold, R. E., Floyd, S. R., Clark, P. E., Burbine, T. H., Bhangoo, J. S., Bailey, S. H. et Petaev, M. (2000). The Elemental Composition of Asteroid 433 Eros: Results of the NEARShoemaker X-ray Spectrometer. Science, 289:2101-2105.

[Trombka et al., 1997] Trombka, J. I., Floyd, S. R., Boynton, W. V., Bailey, S., Brückner, J., Squyres, S. W., Evans, L. G., Clark, P. E., Starr, R., Fiore, E., Gold, R., Goldsten, J. et McNutt, R. (1997). Compositional Mapping with the Near X-Ray / Gamma-Ray Spectrometer. Journal of Geophysical Research, 102:23729-23750.

[Van Dilla et al., 1962] van Dilla, M. A., Anderson, E. C., Metzger, A. E. et Schuch, R. L. (1962). Lunar Composition by Scintillation Spectroscopy. IEEE Transactions on Nuclear Science, 9:405-412.

[Vaucher et al., 2008] Vaucher, J., Baratoux, D., Mangold, N., Pinet, P. Kurita, K., Grégoire (2008), M., The volcanic activity at Cerberus: ages, volumes, and the relationship with other geologic processes, in revision for Icarus.

[Vinogradov et al., 1976] Vinogradov, A. P., Surkov, Y. A., Moskaleva, L. P. and Kirnozov, F. F. (1976). Measurement of the Intensity and the Spectral Structure of the Gamma Radiation of Mars by AMS 'Mars 5'. Soviet Physics - Doklady, 20:523-525.

[Vinogradov et al., 1967] Vinogradov, A. P., Surkov, Y. A., Chernov, G. M., Kirnozov, F. F. et Nazarkina, G. B. (1967). Lunar Gamma-Radiation and the Composition of the Lunar Rocks According to Results of Luna 10 Experiment. Cosmic Research, 5:741.

[Wänke et al., 2001] Wänke, H., J. Brückner, G. Dreibus, R. Rieder, I. Ryabchikov 2001, Chemical Composition of Rocks and Soils at the Pathfinder Site, Space Science Review, v. 96, Issue ¼, p. 317-330.

[Ward, 1979] Ward, A. W. 1979, Yardangs on Mars - Evidence of recent wind erosion, J. Geophys. Res., 84, 8147-8166.

[Warren, 1985] Warren, P.H., The magma ocean concept and lunar evolution, Annu. Rev. Earth Planet. Sci. 13 (1985), pp. 201–240.

[Waters, 1999] Waters, L. S. (Ed.) 1999, MCNPX User's Guide, Document LA-UR-99-6058. Los Alamos National Laboratory, Los Alamos, NM.

[Watters et al., 2007] Watters, T. R., et al., Radar Sounding of the Medusae Fossae Formation Mars: Equatorial Ice or Dry, Low-Density Deposits?, Science 318, 1125 (2007), doi:10.1126/science.1148112.

[Yamashita et al., 2008] Yamashita, N., Hasebe, N., Miyachi, T., Kobayashi, M., Okudaira, O., Kobayashi, S., Ishizaki, T., Sakurai, K., Miyajima, M., Reedy, R. C., D'Uston, C., Maurice, S., Gasnault, O. (2008), Complexities of gamma-ray line intensities from the lunar surface, Earth, Planets and Space, Volume 60, p. 313-319.

Publications

Referred journals

B. Diez, W.C. Feldman, N. Mangold, D. Baratoux, S. Maurice, O. Gasnault, L. d'Uston, F. Costard, Contribution of Mars Odyssey GRS at Central Elysium Planitia, Icarus, Volume 200, Issue 1, March 2009, Pages 19-29, ISSN 0019-1035, DOI: 10.1016/j.icarus.2008.11.011.

B. Diez, W.C. Feldman, S. Maurice, O. Gasnault, T.H. Prettyman, M.T. Mellon, O. Aharonson, N. Schorghofer, H layering in the top meter of Mars, Icarus, Volume 196, Issue 2, Mars Polar Science IV, August 2008, Pages 409-421, ISSN 0019-1035, DOI: 10.1016/j.icarus.2008.02.006.

W.C. Feldman, M.C. Bourke, R.C. Elphic, S. Maurice, J. Bandfield, T.H. Prettyman, B. Diez, D.J. Lawrence, Hydrogen content of sand dunes within Olympia Undae, Icarus, Volume 196, Issue 2, Mars Polar Science IV, August 2008, Pages 422-432, ISSN 0019-1035, DOI: 10.1016/j.icarus.2007.08.044.

Feldman, W. C., J. L. Bandfield, B. Diez, R. C. Elphic, S. Maurice, and S. M. Nelli (2008), North to south asymmetries in the water-equivalent hydrogen distribution at high latitudes on Mars, *J. Geophys. Res.*, 113, E08006, doi:10.1029/2007JE003020.

Feldman, W. C., M. T. Mellon, O. Gasnault, B. Diez, R. C. Elphic, J. J. Hagerty, D. J. Lawrence, S. Maurice, and T. H. Prettyman (2007), Vertical distribution of hydrogen at high northern latitudes on Mars: The Mars Odyssey Neutron Spectrometer, *Geophys. Res. Lett.*, *34*, L05201, doi:10.1029/2006GL028936.

Selection of abstracts

O. Forni, B. Diez, B. Munoz, C. d'Uston, R.C. Reedy, N. Hasebe and the SELENE GRS Team, Preliminary observations of the SELENE Gamma Ray Spectrometer, European Planetary Science Congress, Münster, Germany, 21 - 26 September 2008.

B. Diez, S. Maurice, O. Gasnault, L. d'Uston, W. C. Feldman, D. Baratoux and N. Mangold, Comparison of the Mars Odyssey GRS results with geological mapping at the Cerberus Plains, EGU General Assembly 2008.

B. Diez, S. Maurice, O. Gasnault, W. C. Feldman, Comparison of the Mars Odyssey GRS results with geological mapping at the Cerberus Plains, European Mars Science and Exploration Conference: Mars Express & ExoMars, ESTEC, Noordwijk, The Netherlands, 12-16 November 2007.

B. Diez, S. Maurice, W. C. Feldman, O. Gasnault, T. H. Prettyman, C. d'Uston, Stratigraphy of hydrogen in the top meter of Mars, European Planetary Science Congress, Berlin, Germany, 18 - 22 September 2006.

Abstract

Measuring the neutron and gamma ray fluxes produced by the interaction of galactic cosmic rays with planetary surfaces allow constraining the chemical composition of the upper tens of centimeters of material. Two different angles are proposed to study neutron and gamma spectroscopy: data processing and data interpretation. The present work is in line with two experiments, the Mars Odyssey Neutron Spectrometer and the Selene Gamma Ray Spectrometer. A review of the processing operations applied to the MONS dataset is proposed. The resulting dataset is used to determine the depth of the hydrogen deposits below the Martian surface. In water depleted regions, neutron data allow constraining the concentration in elements likely to interact with neutrons. The confrontation of these results to those issued from the Gamma Ray Spectrometer onboard Mars Odyssey provides interesting insight on the geologic context of the Central Elysium Planitia region. These martian questions are followed by the study of the Selene gamma ray data. Although only preliminary processing has been done to date, qualitative lunar maps of major elements (Fe, Ca, Si, Ti, Mg, K, Th, U) have already been realized.

Résumé (en français)

La mesure des flux de neutrons et de rayonnements gamma issus de l'interaction du rayonnement cosmique galactique avec les surfaces planétaires permet de contraindre la composition chimique des premières dizaines de centimètres de régolite. Deux angles d'approche de la spectroscopie neutron et gamma ont été abordés : le traitement des données et l'interprétation des résultats. Les études menées s'inscrivent dans le cadre de deux missions : le spectromètre neutron à bord de Mars Odyssey et le spectromètre gamma à bord de Selene. Une revue détaillée des opérations de réduction des données MONS est proposée. Le jeu de données résultant est utilisé pour déterminer la profondeur des dépôts d'hydrogène sous la surface martienne. Dans les régions dépourvues d'eau, les données neutron permettent de contraindre la concentration des éléments susceptibles d'interagir avec les neutrons. La confrontation de ces résultats avec ceux du spectromètre gamma à bord de Mars Odyssey permet d'éclairer le contexte géologique de la région de Central Elysium Planitia. Toutes ces problématiques martiennes sont suivies de l'étude des données gamma de Selene. Bien que seuls les traitements préliminaires aient été réalisés à ce jour, des cartes qualitatives des éléments majeurs (Fe, Ca, Si, Ti, Mg, K, Th, U) ont pu être extraites des données.